Universidade de Évora - Instituto de Investigação e Formação Avançada

Programa de Doutoramento em Engenharia Mecatrónica e Energia

Área de especialização | Energia

Tese de Doutoramento

Advances on the design of linear Fresnel solar concentrators

André Vitor de Albuquerque Santos

Orientador(es) | Diogo Canavarro

Manuel Pedro Ivens Collares-Pereira

Évora 2025

Universidade de Évora - Instituto de Investigação e Formação Avançada

Programa de Doutoramento em Engenharia Mecatrónica e Energia

Área de especialização | Energia

Tese de Doutoramento

Advances on the design of linear Fresnel solar concentrators

André Vitor de Albuquerque Santos

Orientador(es) | Diogo Canavarro

Manuel Pedro Ivens Collares-Pereira

Évora 2025

A tese de doutoramento foi objeto de apreciação e discussão pública pelo seguinte júri nomeado pelo Diretor do Instituto de Investigação e Formação Avançada:

Presidente	|	João Manuel Figueiredo (Universidade de Évora)
Vogais	|	Alberto Sanchez-Gonzalez (Universidad Carlos III de Madrid) Charles-Alexis Asselineau (Universidade Politécnica de Madrid) Diogo Canavarro (Universidade de Évora) Paulo Canhoto (Universidade de Évora) josé González Aguillar (Fundacion IMDEA Energia)

Évora 2025

To the memory of my grandmother Creuza – my eternal Dama de Vermelho.

Abstract

The design of linear Fresnel solar concentrators poses a complex challenge due to the high number of decision variables and relatively few constraints. These characteristics define a multivariate problem with a multi-objective nature, where optical, thermal, and economic components are key factors to assessing overall performance, often involving trade-off relations. This thesis advances the understanding of this design problem by introducing meaningful simplifications that either reduce it to its simplest form or clarify how such simplifications affect performance. Rather than pursuing a single optimal solution, the developments presented here offer insights into a broader generalization of the design challenge. In this work, the adopted strategy involved decomposing the problem into smaller, more manageable, and targeted sub-problems, each addressed independently. Specifically, this thesis investigates: (i) the development of an optical method, surrogate to time-intensive ray-tracing simulations (Chapter 3); (ii) curvature design of primary mirrors, comparing different shapes (Chapter 4) and design approaches (Chapter 5); (iii) secondary optics design (Chapter 6); and (iv) the assessment of cost-effectiveness relations of optimal geometric configurations (Chapter 7). Although primarily aimed at the context of solar thermal electricity generation, in which an evacuated tube serves as the absorber element, the findings presented here may also be applicable to the context of applications comprising other types of absorbers.

Keywords: Solar concentration, Linear Fresnel collector, Analysis, Design, Optimization.

Resumo

Avanços no desenho de concentradores solares do tipo Fresnel linear

O desenho de concentradores solares de tipo Fresnel linear representa um problema complexo, devido ao elevado número de variáveis e ao número reduzido de restrições. Estas características definem um problema multivariado de natureza multiobjetiva, no qual fatores ópticos, térmicos e económicos são fundamentais para uma avaliação do desempenho global, frequentemente implicando compromissos entre estes fatores. Esta tese contribui para o avanço da compreensão deste problema de desenho, através da introdução de simplificações que ou o reduzem à sua forma mais simples ou clarificam o impacto dessas simplificações no desempenho. Em vez de determinar uma única solução ótima, os desenvolvimentos aqui apresentados oferecem perspetivas sobre uma generalização deste problema. A estratégia aqui adotada consistiu na decomposição em subproblemas, menores, mais geríveis e com objetivos mais claros, tratados de forma independente. Concretamente, esta tese investiga: (i) o desenvolvimento de um método óptico alternativo às simulações de traçado de raios, operações computacionais usualmente intensivas em tempo (Capítulo 3); (ii) a curvatura dos espelhos primários, comparando diferentes formas geométricas (Capítulo 4) e abordagens de cálculo (Capítulo 5); (iii) o desenho da óptica secundária (Capítulo 6); e (iv) a avaliação das relações de custo-benefício associadas às configurações geométricas óptimas (Capítulo 7). Embora o âmbito destes desenvolvimentos seja o contexto da produção de eletricidade por via solar térmica, o que implica no uso de um tubo evacuado como elemento absorvedor, os resultados aqui apresentados poderão também ser aplicáveis às utilizações que considerem outros tipos de absorvedores.

Palavras-chave: Concentração solar, Coletor Fresnel linear, Análise, Desenho, Otimização.

Acknowledgements

I have been fortunate to always encounter wonderful people who, in one way or another, helped me along this PhD journey. I could not leave them unmentioned at this moment of completion.

To my parents, Sandra and Nininho: all that I am is the result of the almost superhuman effort and extraordinary determination you invested in the difficult task of raising the impossible and hyperactive child that I was — and you did it with great love. I owe everything to you.

To my brother, Edgar, for our conversations about Mathematics, Physics, and so many other things that connect us, beyond the love and care we have for each other. You are a constant inspiration.

To my uncles, Deize (Titia) and Cristiano: you were fundamental pillars in my personal growth — examples that I carry with me always. I will be forever grateful for all that you have done for me.

To my second family, who willingly and wholeheartedly welcomed me as one of their own: Selma, Carlos, Kayo, Kayke, you will always have a place in my heart. I will never forget you.

To Débora, for over two decades of friendship and, especially, for encouraging me at the outset of this academic path. Thank you for everything.

To the many friends I made in Évora — who are now part of yet another family I carry in my heart: Fred, Tarci, Paola, Ángeles, Cata, Gabriel, Isa, Andreia, João Oliveira, João Angrola, Francesco, Inês, Foles, Dorin, Thomas, Fran, Tiago, Elsa, Ailton, Dorivaldo, Lucas. So many people over the years. My apologies if I forgot someone. You welcomed me into this city, your homes, and your hearts — and by doing so, you helped make this work possible.

To my supervisors, Diogo Canavarro and Manuel Collares-Pereira, for the opportunities and the lessons — not only scientific and professional but also about humanity and humility.

To my co-authors Pedro Horta and Camilo Arancibia-Bulnes, for their contributions and revisions, which greatly improved this thesis. I also thank my friend Thomas Fasquelle for his thorough review of the first version of this thesis.

Finally, but by no means least, I acknowledge the Portuguese National Science Foundation (FCT - Fundação para a Ciência e a Tecnologia), through PhD grant 2021.07140.BD, and the National Research Infrastructure in Solar Energy Concentration (INIESC – Infraestrutura Nacional de Investigação em Energia Solar de Concentração), for the financial support.

Agradecimentos

Tive a sorte de sempre encontrar pessoas maravilhosas que, de uma forma ou de outra, me ajudaram nesta jornada do doutorado. Não poderia deixar de mencioná-las neste momento de conclusão.

Aos meus pais, Sandra e Nininho: tudo o que sou é fruto do esforço quase desumano e da determinação sobrenatural que vocês dedicaram à difícil tarefa de educar a criança impossível e hiperativa que eu fui. E o fizeram com muito amor. A vocês, devo tudo.

Ao meu irmão, Edgar, pelas nossas conversas sobre Matemática, Física e tantas outras coisas que nos conectam, além do amor e carinho que temos um pelo outro. Você é uma inspiração constante.

Aos meus tios Deize (Titia) e Cristiano: vocês foram pilares fundamentais no meu crescimento pessoal, exemplos que levo sempre comigo. Serei eternamente grato por tudo que já fizeram por mim.

À minha segunda família, que me acolheu de forma espontânea como parte de si: Selma, Carlos, Kayo, Kayke, vocês sempre terão um lugar no meu coração. Jamais me esquecerei de vocês.

À Débora, por mais de duas décadas de amizade e, especialmente, por me encorajar no início desta jornada acadêmica. Obrigado por tudo.

Aos muitos amigos que fiz em Évora — e que, agora, são parte de mais uma família que levo no coração: Fred, Tarci, Paola, Ángeles, Cata, Gabriel, Isa, Andreia, João Oliveira, João Angrola, Francesco, Inês, Foles, Dorin, Thomas, Fran, Tiago, Elsa, Ailton, Dorivaldo, Lucas. Foram tantas pessoas ao longo desses anos. Perdoem-me se esqueci de alguém. Vocês me acolheram nesta cidade, em suas casas e em seus corações. Assim, também tornaram possível este trabalho.

Aos meus orientadores, Diogo Canavarro e Manuel Collares-Pereira, pelas oportunidades e pelos ensinamentos — não apenas científicos e profissionais, mas também sobre humanidade e humildade.

Aos meus coautores Pedro Horta e Camilo Arancibia-Bulnes, pelos seus contributos e revisões, que muito enriqueceram esta tese. Agradeço também ao amigo Thomas Fasquelle pela leitura detalhada da primeira versão do texto.

Por fim, mas não menos importante, agradeço à Fundação para a Ciência e a Tecnologia (FCT), através da bolsa de doutoramento 2021.07140.BD, e à Infraestrutura Nacional de Investigação em Energia Solar de Concentração (INIESC), pelos apoios financeiros.

"I have found that it is the small things, everyday deeds of ordinary folk that keep the darkness at bay. Simple acts of kindness and love."

– **Gandalf the Grey**, The Hobbit: An Unexpected Journey (2012)

Written by Philipa Boyens, Guillermo del Toro, Peter Jackson, & Fran Walsh

Contents

List of Papers

This thesis incorporates verbatim excerpts from the following papers:

- A. V. Santos, D. Canavarro, P. Horta, and M. Collares-Pereira, "An analytical method for the optical analysis of Linear Fresnel Reflectors with a flat receiver," *Solar Energy*, vol. 227, pp. 203–216, 2021. DOI: 10.1016/j.solener.2021.08.085 [Chapter 3].
- A. V. Santos, D. Canavarro, P. Horta, and M. Collares-Pereira, "On the comparison of parabolical and cylindrical primary mirrors for linear Fresnel solar concentrators," *Renewable Energy*, vol. 218, p. 119 380, 2023. DOI: 10.1016/j.renene.2023.119380 [Chapter 4].
- A. V. Santos, D. Canavarro, P. Horta, and M. Collares-Pereira, "Assessment of the optimal curvature radius of linear Fresnel primary mirrors," *Solar Energy*, vol. 270, p. 112 376, 2024. DOI: 10.1016/j.solener.2024.112376 [Chapter 5].
- A. Santos, D. Canavarro, C. A. Arancibia-Bulnes, P. Horta, and M. Collares-Pereira, "A comparison of secondary optic designs for linear Fresnel collectors with a single tubular absorber," *Solar Energy*, vol. 282, p. 112 936, 2024. DOI: 10.1016/j.solener.2024.112936 [Chapter 6].
- A. Santos, D. Canavarro, P. Horta, and M. Collares-Pereira. "On optimum designs of linear Fresnel solar collectors", 2025. (Under review, *Solar Energy*) [Chapter 7].

Moreover, all these papers have excerpts included in other chapters and appendices. These inclusions are made with the permission of the co-authors and are intended to integrate the findings and discussions of our collaborative work directly into the fabric of this thesis. While these sections are presented without explicit quotation marks for seamless integration, it is important to acknowledge the significant contributions of the co-authors to the development of these ideas and findings. I assume full responsibility for including these materials and their interpretation within the context of this thesis.

During the course of the PhD, I engaged in a broad spectrum of research activities that extended beyond the scope of this thesis. This additional work, which includes papers where I have contributed as either the first author or a co-author, is closely related to the subjects explored in my doctoral research. Although these contributions have significantly enriched my understanding and expertise in the field, they have not been included as part of the main body of this thesis. The decision to exclude these works was made to maintain a focused and coherent narrative within the thesis, ensuring that each included paper directly advances the thesis statement and research objectives. These related works remain an integral part of my academic journey and contributions during my PhD studies, nonetheless. They are:

- L. Martínez-Manuel, J. Córdova-Gallegos, A. Santos, D. Riveros-Rosas, D. Canavarro, P. Horta, and C. A. Arancibia-Bulnes, "Secondary mirrors for homogenization of

parabolic trough radiative flux distributions on cylindrical receivers," *Solar Energy*, vol. 287, p. 113 209, 2025. DOI: 10.1016/j.solener.2024.113209.

- P. Horta, T. Eusébio, A. Santos, R. Cadi, and L. Fialho, "Comparison of Parabolic Troughs and Solar Photovoltaic as Solar Field Technology in Dispatchable Solar Power Plants," *SolarPACES Conference Proceedings*, vol. 2, 2024. DOI: 10.52825/solarpaces.v2i.751.

- A. Santos, "soltracepy: a Python module for the fast implementation of SolTrace ray-tracing simulations," *Zenodo*, 2023. DOI: 10.5281/zenodo.10439687.

- P. Scalco, J. Copetti, M. H. Macagnan, A. Santos, D. Canavarro, and J. Diehl de Oliveira, "OPTICAL PERFORMANCE COMPARISON OF TWO CONFIGURATIONS OF LINEAR FRESNEL COLLECTORS RECEIVERS," in *Proceedings of the 27th International Congress of Mechanical Engineering*, ABCM, 2023. DOI: 10.26678/ABCM.COBEM2023.COB2023-0552.

- A. Santos and D. Canavarro, "Geometric optimization of linear Fresnel collectors for solar thermal electricity," in *3rd SFERA-III/16th SOLLAB Doctoral Colloquium*, Zurich, September 12th – 14th, 2022, pp. 22–23. [Online]. Available: https://sfera3.sollab.eu/wp-content/uploads/2022/12/Book-of-Abstracts_2022-09-08_r.pdf.

- A. C. Montenon, A. V. Santos, M. Collares-Pereira, F. M. Montagnino, R. Garofalo, and C. Papanicolas, "Optical performance comparison of two receiver configurations for medium temperature Linear Fresnel Collectors," *Solar Energy*, vol. 240, pp. 225–236, 2022. DOI: 10.1016/j.solener.2022.05.029.

- D. Canavarro, J. Chaves, H. Borges, A. Santos, and M. Collares-Pereira, "Simultaneous Multiple Surface concentrators for large acceptance angles and gap losses control," *Optik*, vol. 242, p. 167 116, 2021. DOI: 10.1016/j.ijleo.2021.167116.

- S. C. Costa, A. Santos, D. Canavarro, I. Malico, and F. Janeiro, "Optimization of Linear Fresnel Reflector Solar Collectors Using a Genetic Algorithm," in *5th International Conference on Numerical and Symbolic Computation: Developments and Applications, SYMCOMP 2021*, Évora: European Community on Computational Methods in Applied Sciences (ECCOMAS), 2021, pp. 163–172. [Online]. Available: https://eccomas.org/wp-content/uploads/2021/04/symcomp2021_proceedings.pdf.

- A. V. Santos, D. Canavarro, and M. Collares-Pereira, "The gap angle as a design criterion to determine the position of linear Fresnel primary mirrors," *Renewable Energy*, vol. 163, pp. 1397–1407, 2021. DOI: 10.1016/j.renene.2020.09.017.

List of Figures

List of Tables

Replication Statement

All replication materials necessary to reproduce the results presented in this thesis are available in the following GitHub repository: https://github.com/andrevitoras/PhD_Studies. The repository is organized into sub-directories corresponding to each chapter, containing Python scripts, data files, and documentation. The code utilizes libraries such as NumPy and SciPy, along with custom-developed modules.

Chapter-wise resources:

- **Chapter 3**. *"An optical method"*: https://github.com/andrevitoras/PhD_Studies/tree/master/an_optical_method.
- **Chapter 4**. *"On the shape of the primary mirrors"*: https://github.com/andrevitoras/PhD_Studies/tree/master/on_the_primaries_shape.
- **Chapter 5**. *"On the radius of the primary mirrors"*: https://github.com/andrevitoras/PhD_Studies/tree/master/on_the_primaries_radius.
- **Chapter 6**. *"On secondary optics"*: https://github.com/andrevitoras/PhD_Studies/tree/master/on_secondaries.
- **Chapter 7**. *"On optimum designs"*: https://github.com/andrevitoras/PhD_Studies/tree/master/on_optimum_designs.

The `solaren` module, https://github.com/andrevitoras/PhD_Studies/tree/master/solaren, contains core functions and classes utilized throughout the thesis. It includes implementations for optical simulations, mirror design calculations, and optimization routines. Detailed documentation and usage examples are provided within the module's directory.

Chapter 1

Introduction

1.1 Background and motivation

Nowadays, the pursuit of a sustainable development is one of society's main purposes. Related to it, the energy problem is crucial: delivering clean, secure, affordable, and reliable energy to meet current and future needs.

According to the International Energy Agency (IEA), global energy demand increased by 15% between 2013 and 2023, an average annual rate of 1.4% per year. Clean energy sources, including renewables, modern bioenergy, nuclear, hydrogen-based fuels, accounted for 40% of this growth [1]. Consequently, the share of fossil fuels (oil, coal, and natural gas) in the energy mix slightly decreased during the same period, dropping from 82% to 80%. Looking ahead to 2050, projections based solely on currently stated policies (STEP scenario) suggest fossil fuels will comprise 58% of the global energy mix. However, considering announced pledges (APS scenario) and a net-zero emissions (NZE scenario), the share of clean energy could rise significantly, reaching 75% and 90%, respectively. Achieving these ambitious goals, as illustrated in Figure 1.1, will require extensive electrification across multiple sectors notably heating and cooling, mobility, on-site hydrogen production for heavy industries, and various other end-use applications. The degree of electrification and electricity consumption share will vary according to the scenario (STEP, APS, or NZE), with increased electrification also helping reduce overall energy intensity by improving energy system efficiency [1].

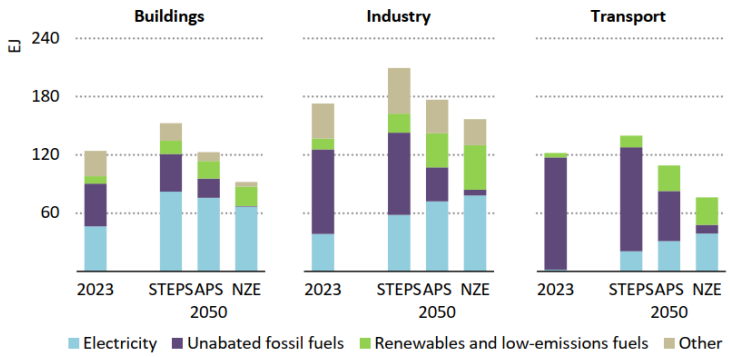

Figure 1.1: Total final consumption by energy source per sector. It shows three different projection of scenarios for 2050: Stated Policies (STEP), Announced Pledges (APS), and Net Zero Emissions (NZE). EJ = exajoules. This figure was taken from the IEA's World Energy Outlook 2024 report [1].

A prominent example of this transition is in the transport sector, where numerous countries have implemented policies to facilitate the widespread adoption of electric vehicles, including heavy-duty trucks, gradually replacing combustion engine technologies by 2050 [2].

In this context, the transition to a clean energy future relies on the widespread adoption of renewable energy to replace fossil fuels and the electrification of key economic sectors. Renewable electricity production is pivotal to this transformation, which has already begun. From 2010 to 2023, the renewable energy sector underwent significant advancements driven by technology, policy, and market dynamics. During this period, the global weighted average cost of electricity from renewables dropped sharply, making them the most cost-competitive source of new power generation in many regions. This cost decline coincided with a surge in deployment, as renewable energy capacity grew from less than 30% to over 80% of new power generation capacity by 2023. Solar photovoltaic (PV) and onshore wind have been particularly impactful. Solar PV, benefiting from scalability, adaptability, and a 90% cost reduction from 2010 to 2023, became the most affordable renewable energy source in many areas. Onshore wind, a long-standing technology, achieved a 75% cost decrease in the same period and remains a reliable and competitive electricity source. Together, these technologies have dominated recent renewable capacity growth [3].

Due to their intermittent and non-dispatchable production, PV and wind are denominated as Variable Renewable Energy (VRE) [4]. That is, their output fluctuates due to uncontrollably local meteorological conditions. This inherent feature poses challenges to the integration of larger VRE shares into the power system as it comes with additional (marginal) costs, inertia reduction, and a higher potential for imbalances between available supply and demand (e.g., net load and Duck curve) [5, 6]. Thus, VRE integration implies measures to promote flexibility to the power system to manage fluctuations in both demand and supply through grid expansion, curtailment, flexible power plants, energy storage, among others [7, 8].

Solar Thermal Electricity (STE)[1] offers a promising complement to VRE by addressing grid flexibility challenges. It makes use of Concentrating Solar Thermal (CST) technologies to collect and concentrate sunlight onto a receiver, converting it into heat, which is then used to generate electricity via a steam turbine or other engines [11]. A key feature of STE is its integration with Thermal Energy Storage (TES) systems, which allows energy to be stored and dispatched as needed, providing a reliable and dispatchable utility-scale renewable power production [12].

The most widely used concentrating technologies for STE are shown in Figure 1.2. They operate by collecting incoming solar radiation through a reflective aperture and directing it onto a receiver which comprises a significantly smaller absorber, thereby defining the concentration factor [10]. A higher concentration factor corresponds to increased operation temperature, as heat losses are proportional to the absorber's surface area. The absorber transforms concentrated sunlight into heat and then transfer it to a Heat Transfer Fluid (HTF), producing the thermal energy to drive the power cycle. The Parabolic Trough Collector (PTC), Figure 1.2a, utilizes parabolic-shaped mirrors to focus sunlight onto an absorber tube. The Central Receiver System (CRS) consists of an array of heliostats (mirrors) that reflect and concentrate sunlight onto a central receiver mounted atop a tower, as shown in Figure 1.2b. Lastly, the Linear Fresnel Collector (LFC) employs multiple flat or slightly curved linear mirrors to direct sunlight onto an elevated receiver, as illustrated in Figure 1.2c. PTC and LFC are denominated as linear-concentrating technologies, and require an one-axis tracking system to follow the Sun movement in the sky, achieving con-

[1]The term Solar Thermal Electricity (STE) differs from Concentrated Solar Power (CSP) in that only the latter includes Fresnel lens technology to drive concentrated photovoltaic cells [9, 10].

centration factors between 30 and 80 (the thermodynamic limit is 215). The CRS is a point-focus technology, requiring a two-axis tracking to reach concentration factors of 600 (the thermodynamic limit is 46,250). Due to these high values of concentration, only the beam component of the incident sunlight can be concentrated and then absorbed [9, 10, 13].

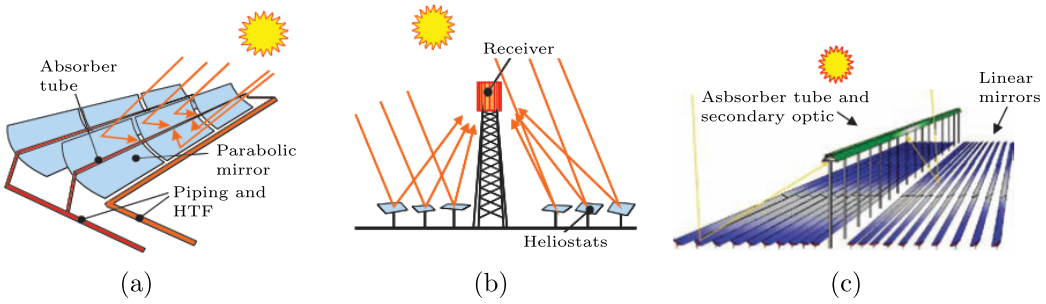

Figure 1.2: Concentrating solar thermal technologies used in Solar Thermal Electricity systems: (a) Parabolic Trough Collector (PTC), (b) Central Receiver System (CRS), and (c) Linear Fresnel Collector (LFC). Adapted from Romero and González-Aguilar [9].

STE plants have been implemented worldwide since the early 1980s. It started with the PTC technology in the United States, the so-called Solar Energy Generating System (SEGS) power plants located at the California Mojave Desert, summing more than 350 MW of installed capacity [14]. These deployments were driven by long-term power-purchase agreements that made SEGSs financially viable [15]. Then, a new rise took place after 2005, now including all technologies: PTC (Andasol 1 and 2), CRS (PS10, PS20, Gemasolar, Ivanpah) and LFC (Kimberlina, Liddell, Puerto Errado I and II) [16–18], while much of this deployment was mainly caused by the feed-in-tariffs policy in Spain [15, 19]. After 2013, a more decentralized expansion started in Morocco, China, Chile, South Africa, among others [20], with policies based on tendering schemes of long-term power-purchase agreements [15]. As of July 2023, the global cumulative installed capacity was approximately of 8.6 GW, including operating, non-operating, decommissioned, and under construction plants, however, only 6.4 GW were operational by the end of this period [21], as illustrated in Figure 1.3b. As the figure indicates, beyond differences in working principles, STE technologies highly diverge in terms of commercial maturity.

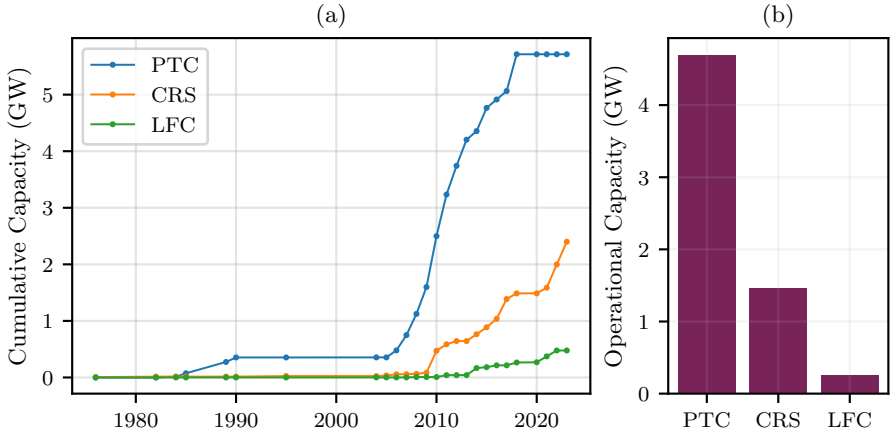

Figure 1.3: Global capacity trends of Solar Thermal Electricity (STE) plants. (a) Cumulative capacity evolution over time, distinguishing different technologies: Parabolic Trough Collector (PTC), Central Receiver System (CRS), and Linear Fresnel Collector (LFC). (b) Comparative operational capacity of these technologies as of July 2023. Elaborated based on *CSP.guru* database [21].

As a matter of comparison, onshore wind and solar PV grew fivefold and thirty-fivefold from 2010 to 2023, reaching installed capacities of 944 GW and 1,412 GW, respectively, by the end of this period [3]. The meager deployment rate of STE results in a significantly lower learning curve compared to these Variable Renewable Energy (VRE) sources, as shown in Figure 1.4. Solar PV shows a steep and consistent cost decline, as shown in Figure 1.4b, driven by economies of scale, technological innovation, manufacturing improvements, among others. On shore wind has slower but steady improvements mainly driven by turbine efficiency gains, improved project design, and stable supply chains, as depicted in Figure 1.4a. Thus, solar PV follows a very steep and predictable learning curve, continuing to achieve record-low electricity prices, while onshore wind follows a moderate learning curve, with improvements mainly driven by efficiency gains rather than drastic cost reductions [22–24].

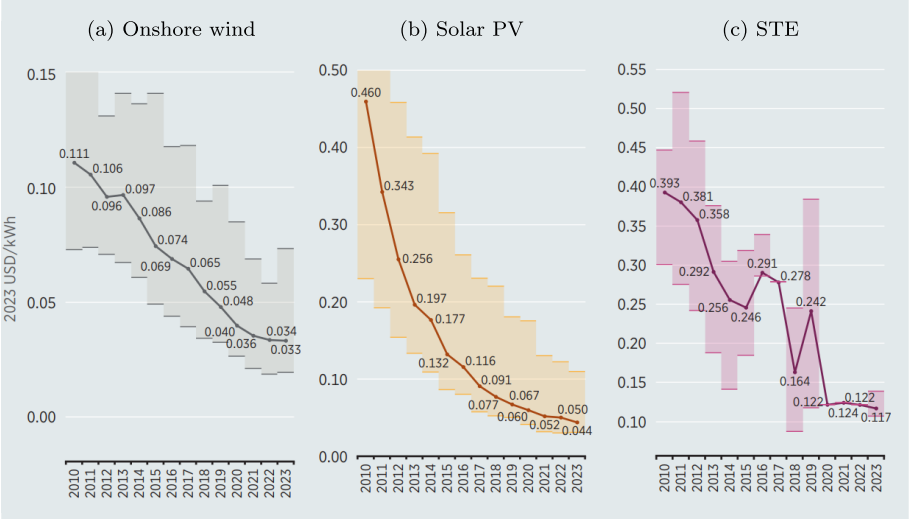

Figure 1.4: Global weighted average Levelized Cost of Electricity (LCOE) for (a) onshore wind, (b) solar PV, and (c) STE, 2010-2023. Adapted from IRENA [3].

As Figure 1.4c indicates, Solar Thermal Electricity (STE) has a much shallower learning curve than solar PV and onshore wind. This issue is primarily due to the high upfront investment required for solar field, receiver, thermal storage, and power block, which makes the technology not viable at small scales [25]. Additionally, the system complexity demands high-precision engineering and maintenance. For example, operation and maintenance costs accounts for approximately 20% of the Levelized Cost of Electricity (LCOE), which is two to four times higher than that of solar PV and onshore wind [26]. Furthermore, site selection presents an inherent challenge. The most suitable locations are in latitudes between 20°and 35°(North and South), where beam irradiance is highest. However, overall efficiency improves as sites get closer to the Equator line. In summary, STE faces challenges limiting its deployment due to high capital and operational costs, as well as geographical constraints.

On the other hand, unlike solar PV and wind, STE enhances grid flexibility in several ways. First, its thermal energy storage systems enable temporal decoupling of energy collection and electricity generation [27], directly addressing supply-demand imbalances and reducing reliance on fossil fuel-based plants to deliver firm capacity during periods of high demand or low VRE availability [12]. Second, STE contributes to grid inertia by providing synchronous generation. Additionally, its ability to operate as a baseload or dispatchable power source complements VRE sources, easing integration challenges and reducing curtailment [25].

Due to these characteristics, STE is uniquely suited for a clean energy future. Indeed, the International Energy Agency's stated policies (STEP), announced pledges (APS), and net

zero emission (NZE) scenarios project a significant increase in STE deployment by 2050. As shown in Figure 1.5, the conservative projection (STEP) estimates 68 GW, while the optimistic projection (NZE) estimates 390 GW, representing at least a tenfold increase. Although it is a major raise for STE, it is still way below to the shares of solar PV and onshore wind, which suggests that policy makers are now seeing STE more as a complimentary generation, changing from a baseload technology to a storage and balancing source [28, 29].

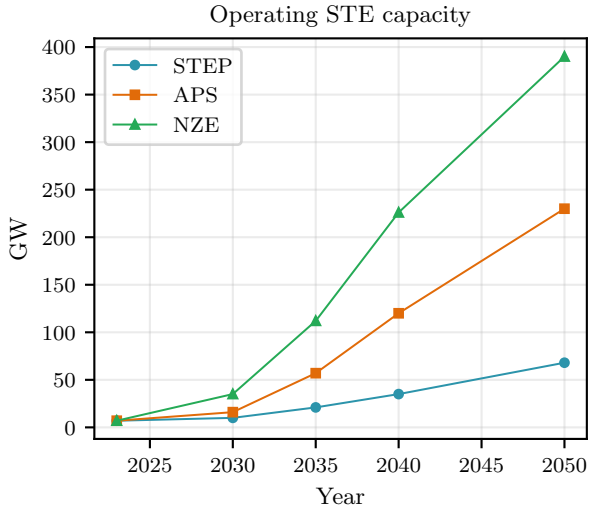

Figure 1.5: Global Solar Thermal Electricity (STE) operating capacity under different scenarios: stated policies (STEP), announced pledges (APS), and net zero emission (NZE). Elaborated based on data from IEA [1].

Whether STE will scale-up in time to achieve these projections is uncertain and depend on many factors such as supporting policies, capacity growth, industry continuity, and technological developments [15, 30]. Presenting a historically highest growth rate of 30% per year [31], the STE industry has a hard task to meet the goals of APS and NZE scenarios. Moreover, it is expected that short and medium-term deployments (2020s and 2030s) will rely mostly in already existing and mature technologies, even considering hybridization with VRE [32–35], as a ten years gap is usually the time for a new STE technology to go from a pilot to a first of a kind project [31].

The existing commercial STE technologies have evolved aiming to enhance competitiveness through cost reduction and efficiency gains. The first concept of solar thermal power plants was that of the SEGS, as shown in Figure 1.6a. It comprises a solar field of PTCs working with thermal oil as the Heat Transfer Fluid (HTF), up to temperatures of 393 °C, and not including storage systems; the solar field heats up the oil, which is then used to drive the power block by producing superheated steam. Sequential deployments of this concept presented a two-tank Thermal Energy Storage (TES) system based on a indirect heating of molten salts, as shown in Figure 1.6b; the heated oil is directed to a oil-salts heat exchanger to transfer energy to salts coming from the cold tank; the heated salts are stored in the hot tank, and are used to drive the power block and produce electricity. The addition of a TES system, as shown in Figure 1.6b, enhances the capacity factor (annual fraction at full load operation) of the power plant. On the one hand, this inclusion means an increase in overall cost and parasitic losses, but on the other hand it also means increasing power production and, consequently, revenues. Overall, the storage system yields a more competitive concept. However, both concepts have a constraint regarding the solar field working temperature: above 398 °C thermal oil starts to decompose [36], which mean the use of low-efficiency turbines and, consequently, reducing the solar-to-electricity conversion rate [37].

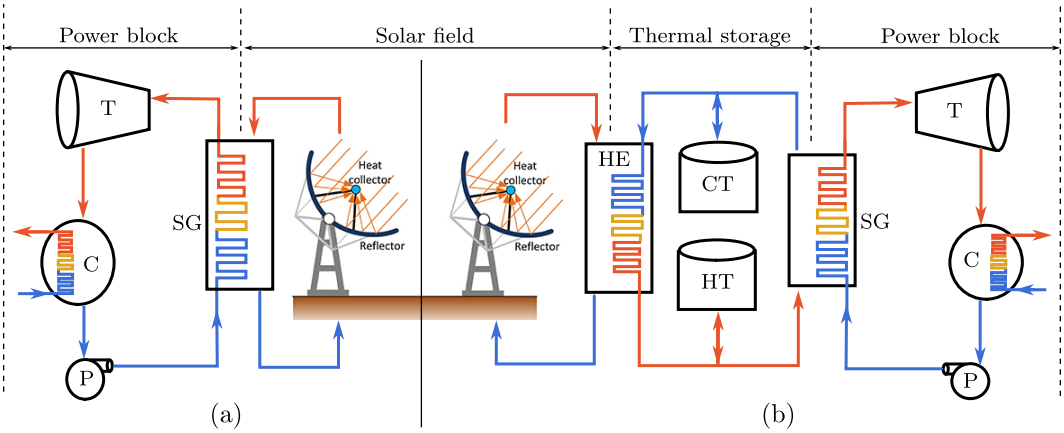

Figure 1.6: Basic schematic representation of Parabolic Trough Collector (PTC) solar thermal power plants, illustrating two configurations: (a) a thermal oil system, and (b) an indirect two-tank thermal energy storage. Key components include the turbine (T) for power generation, the condenser (C) for heat rejection, the pump (P) for fluid circulation, the steam generator (SG) for thermal energy conversion, the heat exchanger (HE) for indirect heat transfer, the cold storage tank (CT), and the hot storage tank (HT). Adapted from Belgasim et al. [38] and Dirker et al. [39].

Two other plant concepts were developed to work with different HTFs to achieve higher solar field working temperatures. These systems are depicted in Figure 1.7, and are mainly based on CRS and LFC concentrating technologies [21]. One is presented in Figure 1.7a, the Direct Steam Generation (DSG) concept, in which the solar field acts as the steam generator driving the turbine to produce electricity. The molten salts solar thermal power plant is shown in Figure 1.7b. It presents a two-tank storage system, and salts from the cold tank are directly heated up in the solar field and then stored in the hot tank. To generate electricity, the hot salt is pumped through a steam generator to drive the power block.

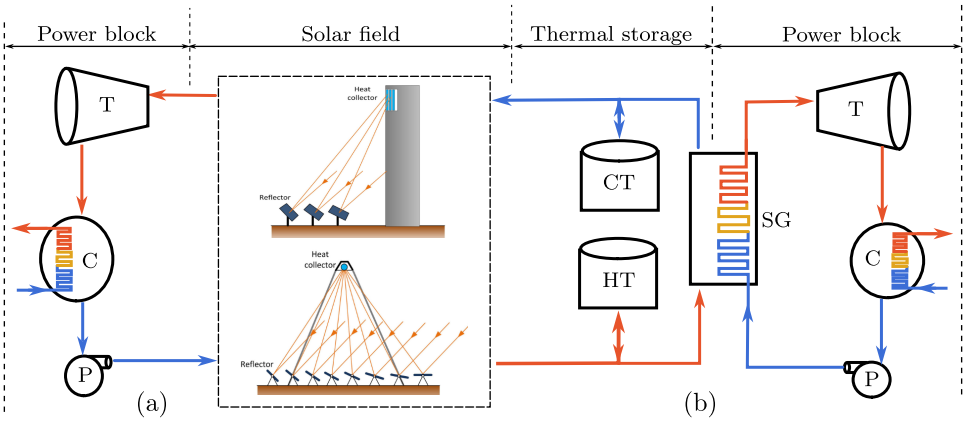

Figure 1.7: Basic schematic representation of (a) direct steam generation and (b) molten salts solar thermal power plants. The solar field can be composed of Linear Fresnel Collector (LFC) or Central Receiver System (CRS) concentrating technologies. Key components include the turbine (T) for power generation, the condenser (C) for heat rejection, the pump (P) for fluid circulation, the steam generator (SG) for thermal energy conversion, the heat exchanger (HE) for indirect heat transfer, the cold storage tank (CT), and the hot storage tank (HT). Adapted from Belgasim et al. [38] and Dirker et al. [39].

The DSG concept can reach up to 550 °C, and has the additional advantage of being a simpler design and thus reducing costs related to equipment (e.g., heat exchanger, steam generator). However, the main disadvantage is the lack of cost-effective thermal storage

solutions that can provide long hours (> 3.0) of uninterrupted production [40–42]. In the case of molten salts power plants (salts as HTF and storage medium), the concept shown in Figure 1.7b, the solar field working temperature can reach up to 565 °C [43, 44]. Beyond the higher temperature, the advantages here are due to the fact that salts are far cheaper than thermal oil and there is no need for an oil-salts heat exchanger [45]. In fact, the vast majority of recent (after 2018) developed commercial projects (> 30 MW) rely on molten salts concept, where typical storage sizes range between 4-18 hours of full load operation of the power block [21]. The PTC-based molten salts plant is already a proven concept [46], although it did not scaled up to commercial applications, even being a more competitive design than the ones shown in Figure 1.6 [47].

Besides these developments in plants concepts, advances in the system level (solar field, thermal storage, and power block) can also play a role to increase competitiveness. A core system is the solar field, where sunlight is converted into useful heat. Each concentrating technology has its own path, which is related to the depth of its commercial deployment. As the most mature technology, Parabolic Trough Collector (PTC) developments are more focused in an (detailed) engineering level than in the conceptual (basic) design, aiming for larger aperture parabolas [45, 48] improved designs to reduce the amount of supporting structure, pylons, foundations, frames, arms, as well as better assembly strategies [49, 50]. Central Receiver Systems (CRSs) have been deployed based on different solar field layouts, tower heights, and receivers [44]. Now, much effort is being made on the cost-effective design of heliostats [51], advanced calibration and control techniques [52, 53], and heliostat field performance testing [54, 55]. The Linear Fresnel Collector (LFC) presents a case rather different than those previous two. As a far less mature technology (refer to Figure 1.3), it is still in a quite early development stage, where both conceptual and engineering designs can play an important role to improve its competitiveness [43].

The combination of concentrating technologies and thermal energy storage provides dispatchable operation and underscores the potential of solar thermal systems to play a critical role in achieving a renewable power system. Nevertheless, continuous advancements in materials, storage technologies, and systems designs are expected to further enhance its economic viability and scalability [56].

1.2 Problem statement and research questions

1.2.1 Definition of the problem

Among these concentrating technologies, the Linear Fresnel Collector (LFC) has garnered increasing attention due to its compact design, simplicity of nearly flat and ground level mirrors, reduced material, lighter and fixed receiver structure, and ease of manufacturing, characteristics that in general mean cost reduction opportunities and present a path to reduce the Levelized Cost of Electricity (LCOE) of solar thermal production.

However, the linear Fresnel technology is having difficulties to improve its commercial maturity due to a rather low annual solar-to-electricity conversion efficiency, a problem mainly caused by geometrical characteristics affecting its optical performance [57–62]. For this reason, related studies deal with geometric designs to find a way around this optical efficiency problem. Unlike PTCs, which use a continuous parabolic mirror, LFCs (refer to Figure 1.2c) employ segmented mirrors arranged horizontally – the primary field – to reflect sunlight towards a fixed receiver located above them [63]. This working principle adds more losses and turns the conceptual design of LFCs a far more complex problem than that of PTCs.

On the one hand, losses in LFCs are well-known and include cosine effect, shading, blocking, spillage, end-effect, and thermal losses to the surroundings. On the other hand, the number of geometric variables that can be manipulated is large – such as receiver height; number of mirrors comprising the primary field; positions, widths and curvature of each primary mirror; and the size and shape of the receiver, which defines a secondary optic [64–68]. Furthermore, the concentrator working principle imposes few constraints on the conceptual design of geometric solutions. All of these characteristics lead to a multivariate problem with a multi-objective nature, as optical, thermal, and economic components are crucial for evaluating overall performance and can even present a cost-benefit trade-off [69, 70].

The literature on design and optimization of linear Fresnel collectors is extensive but fragmented in its approaches, methods, and results. This issue suggests that this design problem remains an open challenge, emphasizing the need for a more systematic and comprehensive approach to unresolved issues that justify further research on this topic.

1.2.2 Objectives and research questions

Given these challenges, this research aims to investigate the geometric design problem of linear Fresnel collectors. The study focuses on developing geometric configurations, assessing and comparing their optical, thermal, and economic performances to determine the most cost-effective solutions. Recognizing the complexity of the problem, this research adopts a strategy of decomposing it into simpler, manageable sub-problems. Specifically, this work aims to (i) develop an optical evaluation tool as a surrogate model to ray-tracing simulations, (ii) analyze how mirrors curvature influences optical performance, (iii) compare different secondary optics, and (iv) assess the impact of different geometric configurations on overall performance. For this matter, the following research questions are established in order to give an overall direction and guide the research:

- How to develop a simple but accurate optical evaluation tool?
- What is the effect of mirror curvature on the optical performance?
- What are the advantages and limitations of different secondary optics?
- How do geometric configurations impact the cost-effectiveness trade-off?

1.3 Outline of the thesis

This thesis is structured in eight chapters. Chapter 1 introduces the context and general motivation, and defines the problem, objectives, and research questions that guide this work. Chapter 2 holds the theoretical background on the linear Fresnel collector, defining geometric models used throughout the work, and presents a literature review detailing the design problem and the related open subjects that are analyzed in the upcoming chapters. Chapter 3 develops and validates an optical method, a surrogate but faster tool than ray-tracing simulations, to be used throughout the work. Chapters 4 and 5 discuss the curvature design problem. The former presents a comparison of different mirror shapes. The latter compares methods on how to determine the proper curvature value. Chapter 6 discuss secondary optics, comparing simple design procedures to stochastic optimized geometries. Chapter 7 presents an analysis regarding optimum geometric configurations, comparing different settings to underscore the most cost-effective solutions and further design simplifications. In Chapter 8, the conclusions are drawn, detailing findings and contributions, followed by

a description of the limitations of this investigation, and suggestions of future research activities. Lastly, two appendices support the aforementioned chapters: one holds auxiliary mathematical functions and the other details how sunlight is modeled throughout the work.

References

[1] IEA, "World Energy Outlook 2024," International Energy Agency (IEA), Paris, Tech. Rep., 2024. [Online]. Available: https://www.iea.org/reports/world-energy-outlook-2024.

[2] IEA, "Global EV Outlook 2024: Moving towards increased affordability," International Energy Agency (IEA), Paris, Tech. Rep., 2024. [Online]. Available: https://www.iea.org/reports/global-ev-outlook-2024.

[3] IRENA, "Renewable power generation costs in 2023," International Renewable Energy Agency (IRENA), Abu Dhabi, Tech. Rep., 2024. [Online]. Available: https://www.irena.org/Publications/2024/Sep/Renewable-Power-Generation-Costs-in-2023.

[4] IEA, "Integrating Solar and Wind: Global experience and emerging challenges," International Energy Agency (IEA), Paris, Tech. Rep., 2024. [Online]. Available: https://www.iea.org/reports/integrating-solar-and-wind.

[5] L. Reichenberg, F. Hedenus, M. Odenberger, and F. Johnsson, "The marginal system LCOE of variable renewables – Evaluating high penetration levels of wind and solar in Europe," *Energy*, vol. 152, pp. 914–924, 2018. DOI: 10.1016/j.energy.2018.02.061.

[6] T. Xu, W. Gao, F. Qian, and Y. Li, "The implementation limitation of variable renewable energies and its impacts on the public power grid," *Energy*, vol. 239, p. 121 992, 2022. DOI: 10.1016/j.energy.2021.121992.

[7] K. Guerra, P. Haro, R. E. Gutiérrez, and A. Gómez-Barea, "Facing the high share of variable renewable energy in the power system: Flexibility and stability requirements," *Applied Energy*, vol. 310, 2022. DOI: 10.1016/j.apenergy.2022.118561.

[8] G. N. Psarros, P. A. Dratsas, P. P. Chinaris, and S. A. Papathanassiou, "Assessing the implications of RES technology mix on curtailments, storage requirements and system economics," *Applied Energy*, vol. 381, p. 125 159, 2025. DOI: 10.1016/j.apenergy.2024.125159.

[9] M. Romero and J. González-Aguilar, "Solar thermal CSP technology," *Wiley Interdisciplinary Reviews: Energy and Environment*, vol. 3, no. 1, pp. 42–59, 2014. DOI: 10.1002/wene.79.

[10] K. Lovegrove and W. Stein, "Introduction to concentrating solar power technology," in *Concentrating Solar Power Technology: Principles, Developments, and Applications*, 2nd Edition, Cambridge: Elsevier, 2021, ch. 1, pp. 3–17. DOI: 10.1016/B978-0-12-819970-1.00012-8.

[11] IEA, "Technology Roadmap: Solar Thermal Electricity," International Energy Agency, Paris, Tech. Rep., 2014. [Online]. Available: https://www.oecd.org/en/publications/technology-roadmap-solar-thermal-electricity_9789264238824-en.html.

[12] S. Teske, J. Leung, L. Crespo, M. Bial, E. Dufour, and C. Richter, "Solar Thermal Electricity - Global Outlook 2016," European Solar Thermal Electricity Association (ESTELA), Tech. Rep., 2016. [Online]. Available: https://www.estelasolar.org/wp-content/uploads/2016/02/GP-ESTELA-SolarPACES_Solar-Thermal-Electricity-Global-Outlook-2016_Full-report.pdf.

[13] M. I. Roldán Serrano, "Concentrating Solar Thermal Technologies," in *Concentrating Solar Thermal Technologies: Analysis and Optimisation by CFD Modelling*, Cham, 2017, ch. 2, pp. 11–24. DOI: 10.1007/978-3-319-45883-0_2.

[14] H. Price and D. Kearney, "Reducing the Cost of Energy From Parabolic Trough Solar Power Plants," in *Solar Energy*, ASMEDC, 2003, pp. 591–599. DOI: 10.1115/ISEC2003-44069.

[15] J. Lilliestam, M. Labordena, A. Patt, and S. Pfenninger, "Empirically observed learning rates for concentrating solar power and their responses to regime change," *Nature Energy*, vol. 2, no. 7, p. 17 094, 2017. DOI: 10.1038/nenergy.2017.94.

[16] T. M. Pavlović, I. S. Radonjić, D. D. Milosavljević, and L. S. Pantić, "A review of concentrating solar power plants in the world and their potential use in Serbia," *Renewable and Sustainable Energy Reviews*, vol. 16, no. 6, pp. 3891–3902, 2012. DOI: 10.1016/j.rser.2012.03.042.

[17] H. Muller-Steinhagen, "Concentrating solar thermal power," *Philosophical Transactions of the Royal Society A: Mathematical, Physical and Engineering Sciences*, vol. 371, no. 20110433, 2013. DOI: 10.1098/rsta.2011.0433.

[18] D. A. Baharoon, H. A. Rahman, W. Z. W. Omar, and S. O. Fadhl, "Historical development of concentrating solar power technologies to generate clean electricity efficiently – A review," *Renewable and Sustainable Energy Reviews*, vol. 41, pp. 996–1027, 2015. DOI: 10.1016/j.rser.2014.09.008.

[19] H. Martín, J. de la Hoz, G. Velasco, M. Castilla, and J. L. García de Vicuña, "Promotion of concentrating solar thermal power (CSP) in Spain: Performance analysis of the period 1998–2013," *Renewable and Sustainable Energy Reviews*, vol. 50, pp. 1052–1068, 2015. DOI: 10.1016/j.rser.2015.05.062.

[20] S. Rodat and R. Thonig, "Status of Concentrated Solar Power Plants Installed Worldwide: Past and Present Data," *Clean Technologies*, vol. 6, no. 1, pp. 365–378, 2024. DOI: 10.3390/cleantechnol6010018.

[21] R. Thonig, A. Gilmanova, and J. Lilliestam, *Csp.guru*, version 2023-07-01, Zenodo, 2023. DOI: 10.5281/zenodo.8191855. [Online]. Available: https://csp.guru.

[22] G. Kavlak, J. McNerney, and J. E. Trancik, "Evaluating the causes of cost reduction in photovoltaic modules," *Energy Policy*, vol. 123, pp. 700–710, 2018. DOI: 10.1016/j.enpol.2018.08.015.

[23] M. Schauf and S. Schwenen, "Mills of progress grind slowly? Estimating learning rates for onshore wind energy," *Energy Economics*, vol. 104, p. 105 642, 2021. DOI: 10.1016/j.eneco.2021.105642.

[24] W. Chen and M. Han, "Quantifying the cost savings of global solar PV and onshore wind markets," *Energy Policy*, vol. 199, p. 114 521, 2025. DOI: 10.1016/j.enpol.2025.114521.

[25] P. Gauché, J. Rudman, M. Mabaso, W. A. Landman, T. W. von Backström, and A. C. Brent, "System value and progress of CSP," *Solar Energy*, vol. 152, pp. 106–139, 2017. DOI: 10.1016/j.solener.2017.03.072.

[26] M. I. Khan, R. Gutiérrez-Alvarez, F. Asfand, Y. Bicer, S. Sgouridis, S. G. Al-Ghamdi, H. Jouhara, M. Asif, T. A. Kurniawan, M. Abid, A. Pesyridis, and M. Farooq, "The economics of concentrating solar power (CSP): Assessing cost competitiveness and deployment potential," *Renewable and Sustainable Energy Reviews*, vol. 200, p. 114 551, 2024. DOI: 10.1016/j.rser.2024.114551.

[27] T. Hirsch, J. Dersch, K. Noureldin, B. Nouri, D. Maldonado Quinto, P. Schwarzbözl, R. Uhlig, and S. Wilbert, "Dynamical Behavior of CSP Plants," in *Solar Thermal Energy*, A. S. and K. S.A., Eds., New York: Encyclopedia of Sustainability Science and Technology Series. Springer Nature, 2022, pp. 187–213. DOI: 10.1007/978-1-0716-1422-8_1101.

[28] C. Augustine, C. Turchi, and M. Mehos, "The Role of Concentrating Solar-Thermal Technologies in a Decarbonized U.S. Grid," National Renewable Energy Laboratory (NREL), Golden, CO (United States), Tech. Rep., 2021. DOI: 10.2172/1820100.

[29] R. Thonig and J. Lilliestam, "Cross-technology legitimacy feedback: The politics of policy-led innovation for complementarity in concentrating solar power," *Environmental Innovation and Societal Transitions*, vol. 52, p. 100 884, 2024. DOI: 10.1016/j.eist.2024.100884.

[30] G. Resch, F. Schöniger, C. Kleinschmitt, K. Franke, R. Thonig, and J. Lilliestam, "Deep decarbonization of the European power sector calls for dispatchable CSP," in *SOLARPACES 2020: 26th International Conference on Concentrating Solar Power and Chemical Energy Systems, AIP Conference Proceedings, AIP Conference Proceedings*, vol. 2445, 2022, p. 050 006. DOI: 10.1063/5.0086710.

[31] J. Lilliestam, F. Du, A. Gilmanova, M. Mehos, Z. Wang, and R. Thonig, "Scaling up CSP: How long will it take?" In *SolarPACES SOLAR POWER & CHEMICAL ENERGY SYSTEMS: 27th International Conference on Concentrating Solar Power and Chemical Energy Systems, AIP Conference Proceedings*, vol. 2932, 2023, p. 050 003. DOI: 10.1063/5.0148709.

[32] W. J. Platzer, "Combined solar thermal and photovoltaic power plants - An approach to 24h solar electricity?" *SOLARPACES 2015: International Conference on Concentrating Solar Power and Chemical Energy Systems, AIP Conference Proceedings*, vol. 1734, 2016. DOI: 10.1063/1.4949173.

[33] R. S. Amano and A. Abbas, "Integration of Linear Fresnel Reflectors (LFR) with Conventional Power Plants," in *15th International Energy Conversion Engineering Conference*, Reston, Virginia: American Institute of Aeronautics and Astronautics, 2017. DOI: 10.2514/6.2017-4624.

[34] K. M. Powell, K. Rashid, K. Ellingwood, J. Tuttle, and B. D. Iverson, "Hybrid concentrated solar thermal power systems: A review," *Renewable and Sustainable Energy Reviews*, vol. 80, pp. 215–237, 2017. DOI: 10.1016/j.rser.2017.05.067.

[35] R. Gutiérrez-Alvarez, K. Guerra, and P. Haro, "Market profitability of CSP-biomass hybrid power plants: Towards a firm supply of renewable energy," *Applied Energy*, vol. 335, p. 120 754, 2023. DOI: 10.1016/j.apenergy.2023.120754.

[36] E. Z. Moya, "Parabolic-trough concentrating solar power systems," in *Concentrating Solar Power Technology*, K. Lovegrove and W. Stein, Eds., 2nd Edition, Cambridge: Elsevier, 2021, ch. 7, pp. 219–266. DOI: 10.1016/B978-0-12-819970-1.00009-8.

[37] K. Lovegrove and J. Pye, "Fundamental principles of concentrating solar power systems," in *Concentrating Solar Power Technology*, 2nd Edition, Cambridge: Elsevier, 2021, ch. 2, pp. 19–71. DOI: 10.1016/B978-0-12-819970-1.00013-X.

[38] B. Belgasim, Y. Aldali, M. J. Abdunnabi, G. Hashem, and K. Hossin, "The potential of concentrating solar power (CSP) for electricity generation in Libya," *Renewable and Sustainable Energy Reviews*, vol. 90, pp. 1–15, 2018. DOI: 10.1016/j.rser.2018.03.045.

[39] J. Dirker, D. Juggurnath, A. Kaya, E. A. Osowade, M. Simpson, S. Lecompte, S. M. R. Abadi, V. Voulgaropoulos, A. O. Adelaja, M. Z. Dauhoo, A. Khoodaruth, S. O. Obayopo, O. T. Olakoyejo, M. K. Elahee, M. De Paepe, J. P. Meyer, and C. N. Markides, "Thermal energy processes in direct steam generation solar systems: Boiling, condensation and energy storage," *Frontiers in Energy Research*, vol. 6, pp. 1–35, 2019. DOI: 10.3389/fenrg.2018.00147.

[40] M. Seitz, P. Cetin, and M. Eck, "Thermal Storage Concept for Solar Thermal Power Plants with Direct Steam Generation," *Energy Procedia*, vol. 49, pp. 993–1002, 2014. DOI: 10.1016/j.egypro.2014.03.107.

[41] C. Prieto, A. Rodríguez, D. Patiño, and L. F. Cabeza, "Thermal energy storage evaluation in direct steam generation solar plants," *Solar Energy*, vol. 159, pp. 501–509, 2018. DOI: 10.1016/j.solener.2017.11.006.

[42] C. Prieto, L. F. Cabeza, M. C. Pavón-Moreno, and E. Palomo, "Thermal energy storage for direct steam generation concentrating solar power plants: Concept and materials selection," *Journal of Energy Storage*, vol. 83, p. 110 618, 2024. DOI: 10.1016/j.est.2024.110618.

[43] W. J. Platzer, D. Mills, and W. Gardner, "Linear Fresnel Collector (LFC) solar thermal technology," in *Concentrating Solar Power Technology*, K. Lovegrove and W. Stein, Eds., 2nd Edition, Cambridge: Elsevier, 2021, ch. 6, pp. 165–217. DOI: 10.1016/B978-0-12-819970-1.00006-2.

[44] L. L. Vant-Hull, "Central tower concentrating solar power systems," in *Concentrating Solar Power Technology*, K. Lovegrove and W. Stein, Eds., 2nd Edition, Cambridge: Elsevier, 2021, ch. 8, pp. 267–310. DOI: 10.1016/B978-0-12-819970-1.00019-0.

[45] S. Dieckmann, J. Dersch, S. Giuliano, M. Puppe, E. Lüpfert, K. Hennecke, R. Pitz-Paal, M. Taylor, and P. Ralon, "LCOE reduction potential of parabolic trough and solar tower CSP technology until 2025," in *SOLARPACES 2016: International Conference on Concentrating Solar Power and Chemical Energy Systems, AIP Conference Proceedings*, vol. 1850, 2017, p. 160 004. DOI: 10.1063/1.4984538.

[46] A. Maccari, D. Bissi, G. Casubolo, F. Guerrini, L. Lucatello, G. Luna, A. Rivaben, E. Savoldi, S. Tamano, and M. Zuanella, "Archimede Solar Energy Molten Salt Parabolic Trough Demo Plant: A Step Ahead towards the New Frontiers of CSP," *Energy Procedia*, vol. 69, pp. 1643–1651, 2015. DOI: 10.1016/j.egypro.2015.03.122.

[47] J. Dersch, M. K. Wittmann, and T. Hirsch, "Comparison of Molten Salts and Thermal Oil in Parabolic Trough Power Plants for Different Sites and Different Storage Capacities," *Energies*, vol. 18, no. 2, p. 326, 2025. DOI: 10.3390/en18020326.

[48] K. Riffelmann, T. Richert, P. Nava, and A. Schweitzer, "Ultimate Trough® – A Significant Step towards Cost-competitive CSP," *Energy Procedia*, vol. 49, pp. 1831–1839, 2014. DOI: 10.1016/j.egypro.2014.03.194.

[49] N. Schuknecht, J. McDaniel, and H. Filas, "Achievement of the $\$100/m^2$ parabolic trough," *AIP Conference Proceedings*, vol. 2033, 2018. DOI: 10.1063/1.5067035.

[50] P. Kurup, S. Glynn, and S. Akar, "Manufacturing cost analysis of advanced parabolic trough collector," in *AIP Conference Proceedings*, vol. 2445, 2022, p. 020 006. DOI: 10.1063/5.0085663.

[51] J. B. Blackmon, "Heliostat size optimization for central receiver solar power plants," in *Concentrating Solar Power Technology*, K. Lovegrove and W. Stein, Eds., Cambridge: Elsevier, 2021, ch. 16, pp. 585–631. DOI: 10.1016/B978-0-12-819970-1.00016-5.

[52] J. C. Sattler, M. Röger, P. Schwarzbözl, R. Buck, A. Macke, C. Raeder, and J. Göttsche, "Review of heliostat calibration and tracking control methods," *Solar Energy*, vol. 207, pp. 110–132, 2020. DOI: 10.1016/j.solener.2020.06.030.

[53] Z. Zeng, D. Ni, and G. Xiao, "Real-time heliostat field aiming strategy optimization based on reinforcement learning," *Applied Energy*, vol. 307, p. 118 224, 2022. DOI: 10.1016/j.apenergy.2021.118224.

[54] G. Zhu, C. Augustine, R. Mitchell, M. Muller, P. Kurup, A. Zolan, S. Yellapantula, R. Brost, K. Armijo, J. Sment, R. Schaller, M. Gordon, M. Collins, J. Coventry, J. Pye, M. Cholette, G. Picotti, M. Arjomandi, M. Emes, D. Potter, and M. Rae, "HelioCon : A roadmap for advanced heliostat technologies for concentrating solar power," *Solar Energy*, vol. 264, p. 111 917, 2023. DOI: 10.1016/j.solener.2023.111917.

[55] A. Peña-Lapuente, M. Sánchez, C.-a. Asselineau, K. M. Armijo, M. Röger, C. Villasante, J. Fernández, R. Monterreal, A. Ávila-Marín, J. Pye, K. Milidonis, J. Gonzalez-Aguilar, G. Zhu, S. Ulmer, and G. Bern, "SolarPACES Task III Project: Analyze Heliostat Field:" *SolarPACES Conference Proceedings*, vol. 2, pp. 1–11, 2024. DOI: 10.52825/solarpaces.v2i.903.

[56] M. Imran Khan, F. Asfand, and S. G. Al-Ghamdi, "Progress in research and technological advancements of commercial concentrated solar thermal power plants," *Solar Energy*, vol. 249, pp. 183–226, 2023. DOI: 10.1016/j.solener.2022.10.041.

[57] J. D. Nixon, P. K. Dey, and P. A. Davies, "Which is the best solar thermal collection technology for electricity generation in north-west India? Evaluation of options using the analytical hierarchy process," *Energy*, vol. 35, no. 12, pp. 5230–5240, 2010. DOI: 10.1016/j.energy.2010.07.042.

[58] G. Morin, J. Dersch, W. Platzer, M. Eck, and A. Häberle, "Comparison of Linear Fresnel and Parabolic Trough Collector power plants," *Solar Energy*, vol. 86, no. 1, pp. 1–12, 2012. DOI: 10.1016/j.solener.2011.06.020.

[59] A. Giostri, M. Binotti, P. Silva, E. Macchi, and G. Manzolini, "Comparison of Two Linear Collectors in Solar Thermal Plants: Parabolic Trough Versus Fresnel," *Journal of Solar Energy Engineering*, vol. 135, no. 1, p. 011 001, 2012. DOI: 10.1115/1.4006792.

[60] G. Zhu, M. Wagner, T. Wendelin, and C. Kutscher, "Performance Evaluation and Outlook of Utility-Scale Linear Fresnel Technology," in *ASME 2013 7th International Conference on Energy Sustainability*, American Society of Mechanical Engineers, 2013, pp. 1–8. DOI: 10.1115/ES2013-18069.

[61] H. Schenk, T. Hirsch, J. Fabian Feldhoff, and M. Wittmann, "Energetic Comparison of Linear Fresnel and Parabolic Trough Collector Systems," *Journal of Solar Energy Engineering*, vol. 136, no. 4, pp. 04 101 501–04 101 511, 2014. DOI: 10.1115/1.4027766.

[62] N. Kincaid, G. Mungas, N. Kramer, M. Wagner, and G. Zhu, "An optical performance comparison of three concentrating solar power collector designs in linear Fresnel, parabolic trough, and central receiver," *Applied Energy*, vol. 231, pp. 1109–1121, 2018. DOI: 10.1016/J.APENERGY.2018.09.153.

[63] G. Zhu, T. Wendelin, M. J. Wagner, and C. Kutscher, "History, current state, and future of linear Fresnel concentrating solar collectors," *Solar Energy*, vol. 103, pp. 639–652, 2014. DOI: 10.1016/j.solener.2013.05.021.

[64] R. Abbas and J. Martínez-Val, "Analytic optical design of linear Fresnel collectors with variable widths and shifts of mirrors," *Renewable Energy*, vol. 75, pp. 81–92, 2015. DOI: 10.1016/j.renene.2014.09.029.

[65] V. Sharma, J. K. Nayak, and S. B. Kedare, "Effects of shading and blocking in linear Fresnel reflector field," *Solar Energy*, vol. 113, pp. 114–138, 2015. DOI: 10.1016/j.solener.2014.12.026.

[66] P. Boito and R. Grena, "Optimization of the geometry of Fresnel linear collectors," *Solar Energy*, vol. 135, pp. 479–486, 2016. DOI: 10.1016/j.solener.2016.05.060.

[67] Z. D. Cheng, X. R. Zhao, Y. L. He, and Y. Qiu, "A novel optical optimization model for linear Fresnel reflector concentrators," *Renewable Energy*, vol. 129, pp. 486–499, 2018. DOI: 10.1016/j.renene.2018.06.019.

[68] R. Grena, "Geometrical Aspects of the Optics of Linear Fresnel Concentrators: A Review," *Energies*, vol. 17, no. 14, p. 3564, 2024. DOI: 10.3390/en17143564.

[69] M. Moghimi, K. Craig, and J. Meyer, "Simulation-based optimisation of a linear Fresnel collector mirror field and receiver for optical, thermal and economic performance," *Solar Energy*, vol. 153, pp. 655–678, 2017. DOI: 10.1016/J.SOLENER.2017.06.001.

[70] J. Men, X. Zhao, Z. Cheng, Y. Leng, and Y. He, "Study on the annual optical comprehensive performance of linear Fresnel reflector concentrators with an effective multi-objective optimization model," *Solar Energy*, vol. 225, pp. 591–607, 2021. DOI: 10.1016/j.solener.2021.07.051.

Nomenclature

Abbreviations

APS	Announced Pledges
CRS	Central Receiver System
CSP	Concentrated Solar Power
CST	Concentrating Solar Thermal
DNI	Direct Normal Irradiance
DSG	Direct Steam Generation
HTF	Heat Transfer Fluid
IEA	International Energy Agency
IRENA	International Renewable Energy Agency
LCOE	Levelized Cost of Electricity
LFC	Linear Fresnel Collector
NZE	Net Zero Emission
PTC	Parabolic Trough Collector
PV	Photovoltaic
SEGS	Solar Energy Generating System
STE	Solar Thermal Electricity
STEP	Stated Policies
TES	Thermal Energy Storage
VRE	Variable Renewable Energy

Chapter 2

The linear Fresnel collector

2.1 Fundamentals

2.1.1 Overview

The Linear Fresnel Collector (LFC), as shown in Figure 2.1, is a solar concentrator technology mainly used for thermal applications. It is composed of a primary field of reflectors slightly elevated from the ground – hereafter denominated also by linear mirrors – whose purpose is to reflect (and concentrate) the incident sunlight on a fixed linear receiver located above the primaries [1, 2]. Each mirror performs a single-axis tracking to follow the Sun's daily movement. The receiver has an absorber element to convert the reflected radiation to thermal energy, transferring it to a heat transfer fluid (HTF).

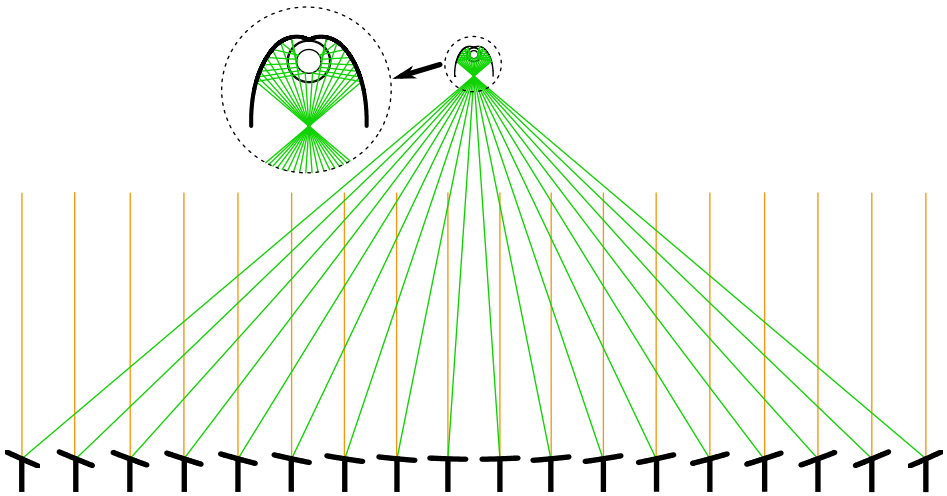

Figure 2.1: The Linear Fresnel Collector (LFC). The incident sunlight (orange lines) is reflected (green lines) by the primary mirrors towards the linear receiver above the primaries, concentrating the incoming radiation. This figure illustrates the case of receiver comprising a Compound Parabolic Concentrator (CPC) secondary optic that concentrates the reflected radiation on an evacuated absorber tube.

The receiver can also contain a secondary optic, whose shape is related to the absorber's [3]. Usually, a trapezoidal secondary is associated with a multi-tube absorber, while a Compound Parabolic Concentrator (CPC) is associated with a single tube [4]. Previous studies have

highlighted that secondary optics enhance the overall performance of LFCs. In general, it allows using larger aperture widths [1], which increases the geometric concentration [5], energy collection [6, 7], flux uniformity [8], and potentially reduce the thermal losses and the number of rows of the solar field [1].

The solar concentration working principle of the linear Fresnel technology offers several benefits over Parabolic Trough Collectors (PTCs). The fixed receiver eliminates the need of rotating joints, avoiding HTF leaks. The use of smaller and slightly bent mirrors coupled to this fixed receiver contribute to the use of lighter supporting structures. The mirrors, positioned at ground level, reduce wind loads, and their simplicity and low cost make the tracking system more affordable. Overall, these factors contribute to yield a simple but robust optical system with low capital and maintenance costs. However, LFCs present the lower solar-to-electricity conversion efficiency and commercial maturity among the concentrating technologies used for power production [9], which pose challenges for securing project financing from banking institutions [10, 11].

In the context of solar thermal power plants, today's state-of-the-art technology uses molten salts as both HTF and storage medium, allowing the solar field to operate at temperatures up to 565°C [12]. An example is the Gemasolar plant in Spain, a 20 MW Central Receiver System (CRS) that has been in operation since 2011 [13]. The first proposal for LFC-based molten salt power plants dates back to 2011 [14]. Since then, this concept has been analyzed extensively [15–17], but the first operational LFC-based plant was Lanzhou Dacheng Dunhuang, a 50 MW facility in China, which has been running since 2020 [13]. At temperatures above 300°C, radiative losses become significantly important. However, they can be minimized by applying a selective coating to the absorber surface. Existing coatings, however, tend to oxidize at high temperatures and in the presence of oxygen, making vacuum conditions necessary [1]. Therefore, in LFC systems, these high temperatures require the use of an evacuated tube — such as the PTR® tubes [18] — as the absorber, as it is the only commercially available alternative with a stable coating for these conditions [19].

2.1.2 Symmetry planes and incidence direction

Due to the linear symmetry of LFCs, their spatial geometry can be fully defined by two constitutive planes. These planes are described in an XYZ coordinate system attached to the concentrator aperture, as illustrated in Figure 2.2. They are referred to as the transversal plane (blue) and the longitudinal plane (magenta).

Within this coordinate system, the direction of incident sunlight, represented by $\vec{S}$, is fully defined by two angles: the transversal incidence angle (θ_T) and the longitudinal incidence angle (θ_L). As shown in Figure 2.2, these angles are measured between the Z-axis and the projections of $\vec{S}$ onto the transversal and longitudinal planes, denoted as $\vec{S}_T$ and $\vec{S}_L$, respectively. Consequently, $\vec{S}$ is expressed as a function of θ_T and θ_L, so that:

$$\vec{S}(\theta_T, \theta_L) = \frac{1}{\sqrt{\tan^2\theta_L \cos^2\theta_T + 1}} \begin{bmatrix} \sin\theta_T \\ -\cos\theta_T \tan\theta_L \\ \cos\theta_T \end{bmatrix}. \tag{2.1}$$

Figure 2.2 also introduces the longitudinal-solar angle (θ_{LS}), which represents the projection of θ_L onto the plane defined by $\vec{S}$ and $\vec{S}_T$. Mathematically, θ_{LS} is defined by θ_T and θ_L as expressed in Equation 2.2. This angle is particularly useful for efficiency approximations in

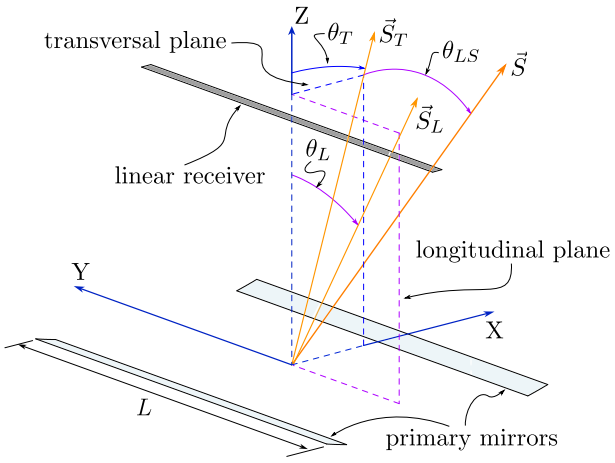

Figure 2.2: Spatial geometry of a Linear Fresnel Collector (LFC). It shows incidence planes and angles in the aperture plane of the concentrator. Transversal and longitudinal planes define angles that fully characterize the incident sunlight direction.

LFCs, as discussed in Section 2.3.

$$\theta_{LS} = \tan^{-1}\left(\tan\theta_L \cos\theta_T\right) \tag{2.2}$$

θ_T and θ_L are angles defined in mutually orthogonal planes of a coordinate system attached to the concentrator aperture. Therefore, they form a pair of generalized coordinates that describe the direction of sunlight as perceived by the concentrator. That is, they constitute the minimum number of independent variables required to fully specify sunlight direction. Further details on θ_T, θ_L, and θ_{LS}, including their relationship with solar angles such as zenith and azimuth, and how to derive Equation 2.1, are provided in Appendix B, Section B.1. These details are omitted here for the sake of conciseness.

2.1.3 A geometric model

The geometry of a linear Fresnel collector is fully defined in the transversal plane, but a three-dimensional object is obtained by extruding this plane in the longitudinal direction. Thus, the concentrator has a finite length, denoted as L in Figure 2.2. A geometric model of the concentrator is then presented in Figure 2.3, showing all related parameters.

The primary field is composed of a finite number of mirrors, where i stands for the mirror index, $i = \{1, 2, ..., n\}$, with n standing for the number of primary reflectors. The center points of the primaries are illustrated as red dots in Figure 2.3 and are represented by $\mathbf{M}$. One assumption of this model is that all center points lie on the X-axis. Thus, the center point of the i-th mirror is $\mathbf{M}_i = \{m_i, 0, 0\}$. The first mirror ($i = 1$) is the most distant from the origin in the positive direction so that $m_1 > m_2 > ... > m_n$. The distance (or shift) between two neighbor mirrors is denoted by s, so that s_i stands for the shift between mirrors of index i and $i + 1$. Therefore,

$$s_i = m_i - m_{i+1}. \tag{2.3}$$

Each primary mirror has a particular width so that w_i stands for the width of the i-th mirror. Of course, to avoid collision due to the rotation of the tracking movement, a constraint is

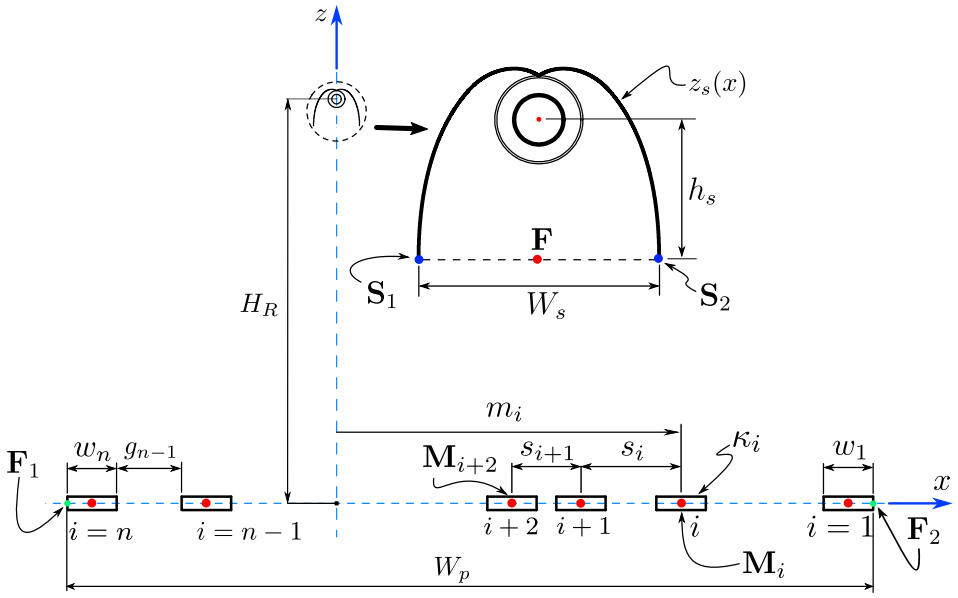

Figure 2.3: A geometric model of an Linear Fresnel Collector (LFC). The figure illustrates the main parameters of its transversal plane exemplifying the case of a Compound Parabolic Concentrator (CPC) secondary optic and an evacuated absorber tube.

then imposed and relates the mirror width and shift as the following:

$$s_i > \frac{w_i + w_{i+1}}{2}. \tag{2.4}$$

Another parameter is the gap, g, which stands for the empty space between two neighboring mirrors. Furthermore, κ stands for the curvature profile of the mirrors so that κ_i stands for the profile of the i-th mirror: it can be parabolic (κ_i varies along the mirror width), cylindrical (κ_i is constant along mirror width), or even flat ($\kappa_i = 0$).

The total width of the primary field, here denominated as W_p, is defined by the distance between the edges of the primary field, points $\mathbf{F}_1$ and $\mathbf{F}_2$ (green dots in Figure 2.3), when all mirrors are in the horizontal position. In general, W_p can be calculated by:

$$W_p = [\mathbf{F}_1, \mathbf{F}_2] = \frac{w_n + w_1}{2} + \sum_{i=1}^{n-1} s_i, \tag{2.5}$$

where $[\mathbf{F}_1, \mathbf{F}_2]$ represents the Euclidean distance between the two points.

H_R represents the receiver height regarding the primary field. For the example shown in Figure 2.3, it is the height of the absorber tube center point above the field. z_s stands for the shape function of the secondary optic, and W_s stands for the aperture width of the secondary optic. Points $\mathbf{S}_1$ and $\mathbf{S}_2$ are the edges of the receiver, and h_s for the height difference between the tube center and the aperture of the secondary optic. Moreover, $\mathbf{F}$ stands for the aim-point of the mirrors used for the tracking procedure (refer to Subsection 2.1.4), which can also be also refereed to as the tracking point of the primary mirrors.

In a LFC, the aperture area of the concentrator can be defined in two ways. A_{gross} stands for the occupied area so that it considers the empty space, the gaps, between mirrors:

$$A_{gross} = W_p \cdot L. \tag{2.6}$$

Another option is the net surface area, as represented by A_{net}, where only the available reflective area is accounted for:

$$A_{net} = \sum_{i=1}^{n} w_i \cdot L. \tag{2.7}$$

The filling factor, FF defined in Equation 2.8, is the packing measure of the primary field, defined as the ratio between net and gross aperture when all mirrors are at the horizontal position. A higher filling factor means a denser primary field, i.e., a higher number of mirrors for the same field width.

$$\text{FF} = \frac{\sum_{i=1}^{n} w_i}{W_p} \tag{2.8}$$

The model in Figure 2.3 describes a primary field non-uniform configuration, which is defined by the decision vector $\hat{x} = \{n, \{w_1, m_1, \kappa_1\}, ..., \{w_n, m_n, \kappa_n\}, H_R, z_s, W_s\}$. In this case, mirrors have their own design parameters, as indicated by the index i. On the other hand, simpler configurations involve uniform settings for specific design variables. For example, in a uniform width configuration, all mirrors have the same width: $w_1 = w_2 = w_i = w$. Analogous settings can also be defined as for curvature and shift between neighbor mirrors, and so a uniform configuration is then defined by $\hat{x} = \{n, w, s, \kappa, H_R, z_s, W_s\}$.

2.1.4 The tracking procedure

The tracking procedure, as shown in Figure 2.4, is the rotational movement that each primary mirror needs to perform to follow the Sun's apparent movement in the sky. For the i-th mirror in the primary field, the tracking is defined by the angle τ_i: the angular deviation from the horizontal position at which the normal vector at the mirror's center point, $\vec{n}_i$, bisects $\vec{S}_T$ and the focusing vector $\vec{v}_{f,i}$ [20].

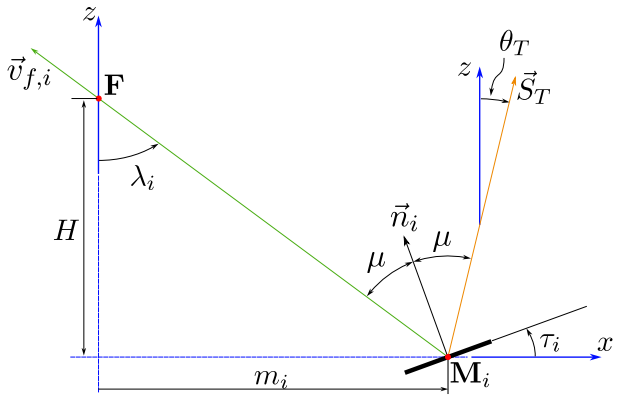

Figure 2.4: The tracking procedure of linear Fresnel primary mirrors. The tracking angle, τ_i, is the angular deviation from the horizontal position at which the normal vector at the mirror's center point, $\vec{n}_i$, bisects $\vec{S}_T$ and the focusing vector $\vec{v}_{f,i}$.

$\vec{v}_{f,i}$ is defined by the line that connects the mirror's center, $\mathbf{M}_i$, and the aim-point at the receiver, $\mathbf{F}$, so that $\vec{v}_{f,i} = \mathbf{F} - \mathbf{M}_i$. In Figure 2.4, λ_i is the angular position of the i-th heliostat regarding $\mathbf{F}$, and is defined as shown in Equation 2.9, where sign and ang are functions as defined in Appendix A, Equations A.2 and A.3, respectively.

$$\lambda_i = \text{sign}(\vec{v}_{f,i} \times \vec{I}_z \cdot \vec{I}_y)\, \text{ang}(\vec{v}_{f,i}, \vec{I}_z) \tag{2.9}$$

Therefore, the tracking angle of the i-th mirror for a particular transversal angle θ_T is

calculated as given by Equation 2.10.

$$\tau_i = \frac{\theta_T - \lambda_i}{2} \tag{2.10}$$

Thus, from Equation 2.10 one can derive that all the mirrors track the Sun with the same speed: half of the speed of the Sun in the transversal plane, as shown in Equation 2.11.

$$\frac{\mathrm{d}\tau_i}{\mathrm{d}t} = \frac{1}{2}\frac{\mathrm{d}\theta_T}{\mathrm{d}t} \tag{2.11}$$

When **F** does not change with time or mirror, the aiming strategy is denominated a fixed aim-line; when it changes, the aiming strategy is referred to as variable aim-line [8, 21].

2.2 Optical losses

2.2.1 Overview

The main sources of optical losses in a LFC are discussed in the literature, although in a separately and diverse way. This section introduces cosine effect, shading, blocking, spillage, and end-effect losses by presenting definitions, mathematical models, and some discussions. In addition to these losses, caused by the concentrator geometry, optical properties of material and surfaces also reduces the amount of the flux that is absorbed at the receiver by imperfect reflection, absorption, and transmission. However, attenuation due to optical properties are not discussed here; they are out of the scope of this work.

2.2.2 Cosine effect

The cosine effect is related to the fact that only the surface projection perpendicular to the incidence direction is used to collect sunlight. Mathematically, as shown in Equation 2.12, this effect is defined by the angle between the sunlight direction and the vector normal to the surface, as illustrated in Figure 2.5.

$$\cos\theta_i = \mathrm{ang}(\vec{S}, \vec{n}_i) \tag{2.12}$$

Considering that $\vec{n}_i$ in Figure 2.5 is given by $\vec{n}_i = \{\sin\tau_i, 0, \cos\tau_i\}$ (refer to Figure 2.4), the Cosine Loss Factor (CLF) of the i-th primary mirror, CLF_i, can be calculated as defined by Equation 2.13.

$$\mathrm{CLF}_i = 1 - \cos\theta_i = 1 - \frac{\cos(\theta_T - \tau_i)}{\sqrt{\tan^2\theta_L \cos^2\theta_T + 1}} \tag{2.13}$$

Some studies [22, 23] also derived models for cosine losses, however, they are based on sun position angles instead of θ_T and θ_L, so that their expressions for θ_i are more complicated.

2.2.3 Shading and blocking

Shading refers to the incident sunlight that would hit a mirror surface but is intercepted by another surface instead. Blocking refers to the reflected sunlight intercepted before it can hit the receiver. These losses are associated with any surface that casts a shade or blocks a specific mirror, although are usually related to the neighbors, as exemplified in Figure 2.5.

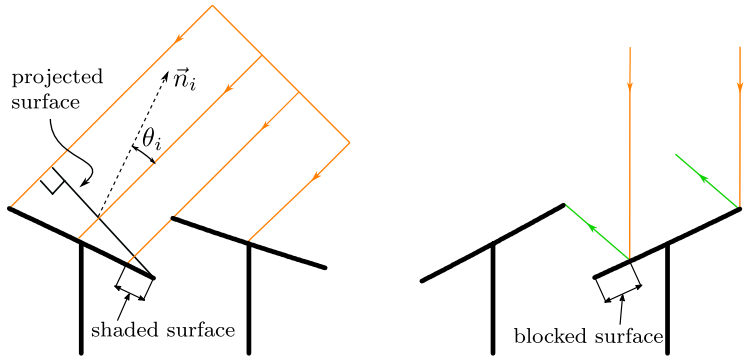

Figure 2.5: A transversal plane view of optical losses caused by shading (when one mirror intercepts the incident sunlight that would hit its neighbor), blocking (when one mirror blocks the sunlight reflected by its neighbor), and cosine effect (only the projected surface perpendicular to the incident rays plays a role in sunlight collection). $\vec{n}_i$ is the vector normal to the mirror's surface at its center point.

Sharma et al. [22] and Yang et al. [23] derived simple models for shading and blocking from the neighboring mirrors, considering flat mirrors and a transversal plane analysis, as illustrated in Figure 2.6, where the i-th mirror is shaded or blocked for a particular incidence so that a fraction of its width, w^*, is not being used to collect sunlight.

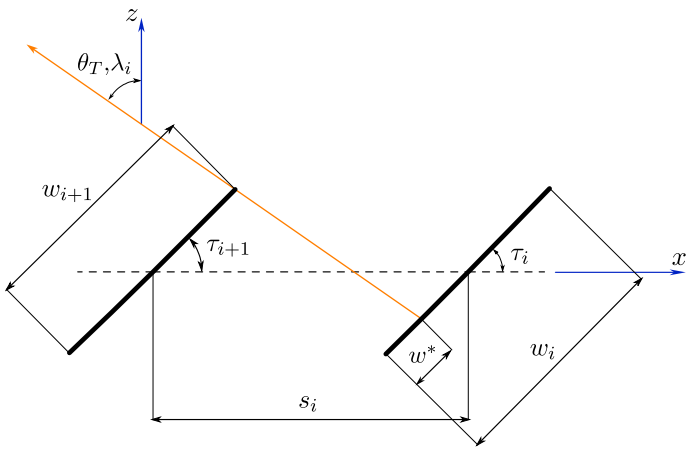

Figure 2.6: Transversal plane analysis for shading and blocking modeling. It considers flat mirrors, so all reflected rays have the same direction as given by the mirror angular position, λ_i.

For shading, the incident sunlight direction is given by θ_T, and Equation 2.14 determines the fraction of the mirror width shaded by the neighbor, defining a Shading Loss Factor (SLF), where "+" means that only positive values should be considered.

$$\text{SLF}_i = \frac{w^*}{w_i} = \left[\frac{1}{2} - \frac{2s_i \cos\theta_T - w_{i+1}\cos(\theta_T - \tau_{i+1})}{2w_i \cos(\theta_T - \tau_i)}\right]^+ \tag{2.14}$$

Blocking deals with the interception of reflected rays. For flat mirrors, due to the tracking procedure illustrated in Figure 2.4, all reflected rays have the same direction, given by the heliostat angular position λ_i. Equation 2.15 presents a mathematical model for the Blocking Loss Factor (BLF), derived from Figure 2.6, which computes the fraction of the width that is blocked by its neighbor. Of course, only the fraction not shaded can be blocked since

sunlight must first hit the mirror to be reflected and then blocked.

$$\mathrm{BLF}_i = \left[\left[\frac{1}{2} - \frac{2s_i \cos\lambda_i - w_{i+1}\cos(\lambda_i - \tau_{i+1})}{2w_i \cos(\lambda_i - \tau_i)}\right] - \mathrm{SLF}_i\right]^+ \tag{2.15}$$

Equations 2.14 and 2.15 are general models that considers variable parameters (non-uniform configuration), but simpler expressions can be derived for particular cases. For example, Bellos and Tzivanidis [24] presented a simple analysis for SLF by considering a uniform width primary field ($w_i = w_{i+1} = w$) and that $\tau_i \approx \tau_{i+1}$.

2.2.4 Spillage

Spillage refers to reflected rays missing the receiver. In a first, simpler, and ideal analysis, this effect is closely related to the shape of the mirrors. Figure 2.7 illustrates the focusing feature of flat and curved mirrors. The flat one just projects the width of the mirror on the focal plane. Curved mirrors have a parabolic or cylindrical shape to produce a smaller spot in the focal plane, allowing larger mirrors (or smaller receivers) and increasing concentration.

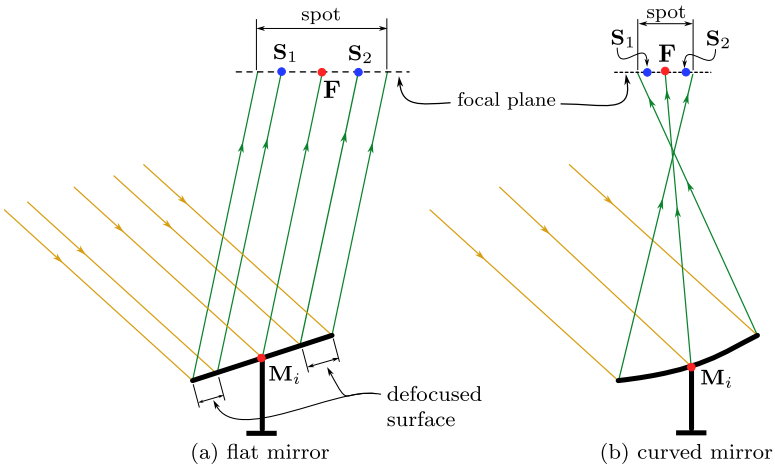

Figure 2.7: Focusing feature of (a) flat and (b) curved mirrors. It considers the incident sunlight (in orange) as collimated rays and perfect specular reflection so that reflected rays (in green) are deflected based only on Snell's law.

Due to the tracking procedure stated in Subsection 2.1.4, the reflected ray at the mirror's center, $\mathbf{M}_i$, always hits the aim point at the receiver, $\mathbf{F}$, regardless of the mirror's shape or the transversal incidence angle θ_T. However, as shown in Figure 2.7, sunlight reflected at the points far from the center might not hit the receiver if part of the spot lies out of the width defined by edge-points $\mathbf{S}_1$ and $\mathbf{S}_2$. Therefore, spillage losses are defined by the part of the mirror that does not reflect sunlight within the receiver edges – the defocused surface.

Rabl [3] and Häberle [25] presented analyses for the design of cylindrical and parabolic mirrors, respectively, that can perfectly focus all incident rays on the mirror surface onto the aim-point at the receiver, $\mathbf{F}$, for a particular transversal incidence. Thus, at least in these ideal conditions of collimated sunlight and perfect specular reflection, spillage losses do not occur for this particular incidence, i.e., the spot size is negligible compared to the receiver size. On the other hand, mirrors rotate to track the apparent sun's daily movement, and incidences out of the design are the most common conditions.

Abbas et al. [26] studied these off-design conditions. They found that reflected rays drift over the receiver, and analytically derived equations for the displacements, showing that

rays reflected at the edges of the mirror present higher drifts – the mirror surface reflecting rays out of the receiver edges was denominated as *lateral losses*. Instead of proposing an equation for the defocused surface, they used this drift analysis to establish a criterion for the maximum mirror width so that no lateral losses occur between sunrise and sunset. Later, this criterion was used by Abbas and Martínez-Val [27, 28] to study the design of LFCs.

To determine the fraction of the mirror surface not being used due to spillage, a Defocusing Loss Factor (DLF), from the drift analysis presented by Abbas et al. [26] is not straightforward. It is even harder since a due accounting of shading and blocking must be included – spillage only occurs for the mirror surface that is not under shading or blocking. Moreover, several sources of imperfections cause a ray to deviate from its ideal direction (beam spread sources) [3]: sunlight is not collimated (sunshape), the actual shape of the concentrator does not follow the desired theoretical profile (contour error), misalignment between the concentrator and the receiver (displacement error), non-specular reflection (specular error), and imperfect tracking (tracking error). Therefore, it is reasonable to assume that some spillage losses always occur, and that developing a closed-form equation for DLF is even more challenging. Section B.2 details the concepts of sunshape and optical errors.

2.2.5 End-effect

End-losses are related to reflected sunlight from the primary mirrors missing the receiver because it would require a longer receiver (in the longitudinal direction) to collect it, defining an End-effect Loss Factor (ELF). Figure 2.8 illustrates a simple end-losses analysis.

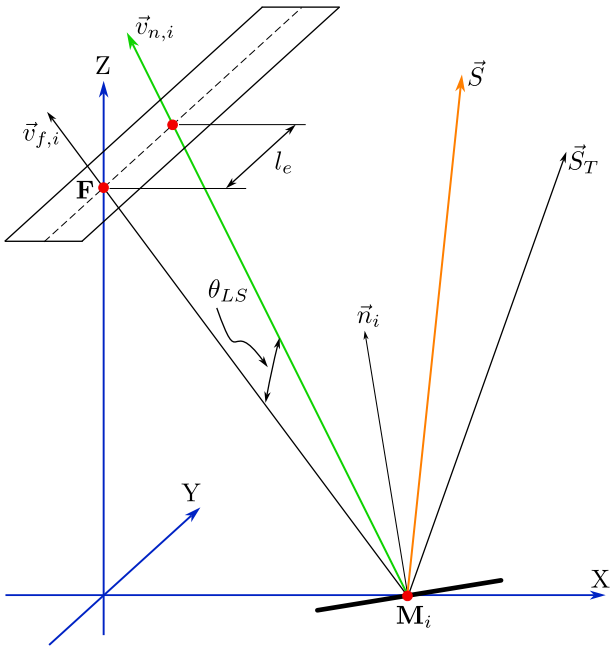

Figure 2.8: A simple geometric model for end-losses. An incident ray $\vec{S}$ is reflected as $\vec{v}_{n,i}$ at the mirror center point, $\mathbf{M}_i$, where $\vec{n}_i$ is the normal vector to mirror surface at $\mathbf{M}_i$. The longitudinal incidence deviates $\vec{v}_{n,i}$ from the transversal plane a length l_e.

The above figure shows an incident ray $\vec{S}$ reflected as $\vec{v}_{n,i}$ at the mirror center point, $\mathbf{M}_i$. $\vec{n}_i$ is the normal vector to the mirror surface at $\mathbf{M}_i$. Since $\vec{S}$ has a longitudinal component, $\vec{v}_{n,i}$ deviates from the transversal plane a length l_e in the longitudinal direction. This longitudinal displacement l_e is precisely the length of the primary mirror that reflects sunlight missing the receiver and corresponds to a fraction of its total length L.

It is quite straightforward to show that the angle between $\vec{v}_{f,i}$ and $\vec{v}_{n,i}$ is the longitudinal-solar incidence angle, i.e., $\text{ang}(\vec{v}_{f,i}, \vec{v}_{n,i}) = \theta_{LS}$, as depicted in Figure 2.8. Therefore, one can derive the following expression for the ELF for the i-th primary mirror:

$$\text{ELF}_i = \frac{l_e}{L} = \frac{|\vec{v}_{f,i}| \tan \theta_{LS}}{L}. \tag{2.16}$$

Of course, a due accounting of end-losses only occur for the fraction of the mirror that is not shaded, blocked, and that reflects sunlight within the edges of the receiver. Furthermore, although Equation 2.16 allows that $\text{ELF}_i > 1$, one must ensure that $\text{ELF}_i \leq 1$ for the model to have a physical meaning. Thus, end-losses is a longitudinal effect mainly ruled by θ_L, and it only exists for a finite-length concentrator when some energy is collected.

The analysis illustrated in Figure 2.8 is considered by some works [22–24, 29, 30] to model end-effect losses. It models sunlight as collimated rays striking only at the center of the primaries, an approach that neglects end-losses variations along mirror width due to the tracking and, therefore, the influence of θ_T on it. Rabl [3] developed a simple equation for end-losses in PTCs. On the other hand, in the case of LFCs, the modeling for the whole concentrator is not that simple due to the discrete primary reflector, although a couple of closed-form equations [24, 29] were developed for the particular case when $\theta_T = 0$.

It is important to highlight that end-losses are particularly significant for small-scale systems, as in roof-top applications, since for large-scale applications the total length of a row of concatenated individual modules is big enough so that end-losses becomes negligible: $L \gg l_e$.

2.3 Optical analysis

2.3.1 Introduction

The optical analysis of LFCs deals with the calculation of the absorbed flux at the receiver by means of the flux density distribution or the integration of such a profile to yield the total absorbed power, as represented by:

$$Q_{abs} = \int_{A_{abs}} q(u, v) \mathrm{d}u\mathrm{d}v, \tag{2.17}$$

where q is the flux density function, defined over a coordinates system attached to the absorber surface by coordinates u and v, and Q_{abs} is the total flux integrated over the absorber surface area, as denoted by A_{abs}.

Q_{abs} can be represented in a relative measure by the optical efficiency, η_{opt}, as defined in Equation 2.18: the fraction of the available flux, $A \cdot I_b$, that is actually absorbed [3], where A is the aperture area, and I_b stands for the beam irradiance.

$$\eta_{opt} = \frac{Q_{abs}}{A \cdot I_b} \tag{2.18}$$

In the case of LFCs, there are two options of aperture area to define the optical efficiency: reflective (or net) and land (or gross). In this work, when not clearly stated, A stands for the total reflective area: A_{net}.

One property of η_{opt} is that it is a function of the incident sunlight direction on the aperture plane of the concentrator, denominated as $\vec{S}$ in Figure 2.2. In short, η_{opt} is a function of

both θ_T and θ_L. This directional nature defines the Incidence Angle Modifier (IAM) as the ratio between the optical efficiency for a particular incidence and the efficiency at a standard position (here considered as the normal incidence), as shown in Equation 2.19 [3, 7].

$$\mathrm{IAM}(\theta_T, \theta_L) = \frac{\eta_{opt}(\theta_T, \theta_L)}{\eta_{opt}(0,0)} = \frac{\eta_{opt}(\theta_T, \theta_L)}{\eta_{opt0}} \tag{2.19}$$

Thus, the optical characterization of an LFC is based on the computation of η_{opt0} and the IAM as a function of θ_T and θ_L – the bi-axial model of efficiency. McIntire's factorization [31] approximates the bi-axial model by individually considering the two orthogonal planes in which θ_T and θ_L are defined, as shown in Equation 2.20.

$$\mathrm{IAM}(\theta_T, \theta_L) \approx \mathrm{IAM}(\theta_T, 0) \times \mathrm{IAM}(0, \theta_L) = K_T(\theta_T) K_L(\theta_L) \tag{2.20}$$

K_T and K_L are referred to as the transversal and longitudinal IAMs, respectively, and establish a relationship between the efficiency at positions in the correspondent planes and the one at normal incidence. For example, K_T is defined as shown in Equation 2.21.

$$K_T(\theta_T) = \frac{\eta_{opt}(\theta_T, 0)}{\eta_{opt0}} = \mathrm{IAM}(\theta_T, 0) \tag{2.21}$$

Nevertheless, it is well-known that this factorized model introduces errors in the approximation of the bi-axial IAM [32, 33]. A more accurate estimate can be achieved using the approach proposed by Bernhard et al. [32], which incorporates θ_{LS}, defined in Equation 2.2, into the longitudinal IAM function, K_L, as presented in Equation 2.22.

$$\mathrm{IAM}(\theta_T, \theta_L) \approx K_T(\theta_T) K_L(\theta_{LS}) \tag{2.22}$$

Equation 2.22 provides a more accurate approximation than Equation 2.20 as it correctly accounts for the bi-axial cosine effect from the factorized model. This can be easily demonstrated using the cosine effect model in Equation 2.12, though the proof is omitted here for the sake of conciseness.

A less common approach is to characterize the LFC directly using the efficiency as a function θ_T and θ_L. Similarly, transversal and longitudinal optical efficiencies, η_T and η_L, are defined analogously to K_T and K_L, respectively. For example, η_T is defined by Equation 2.23.

$$\eta_T(\theta_T) = \eta_{opt}(\theta_T, 0) \tag{2.23}$$

In this case, Equation 2.24 gives the factorized model for the bi-axial efficiency.

$$\eta_{opt}(\theta_T, \theta_L) \approx \frac{\eta_T(\theta_T)\, \eta_L(\theta_{LS})}{\eta_{opt0}} \tag{2.24}$$

All in all, the performance models trough IAM or directly by efficiency are analogous and are just different representations for the absorbed flux at the receiver.

2.3.2 Optical methods

An optical method encompasses the technique used to assess how a concentrator captures, redirects, and focuses sunlight onto a target area. These methods are essential for understanding and optimizing the performance of solar concentrators, as they enable a detailed analysis of light pathways, losses, and flux distributions. In the context of LFCs, two methods are commonly used: ray-tracing simulations and analytical approaches.

Ray-tracing simulations

Ray-tracing is the most used optical method due to its capability to precisely model even the most complex optical phenomena involved in the interactions of sunlight with materials and surfaces that composes the optical system such as multiple reflections and transmissions, sunshape, optical errors, total internal reflection, among others.

This method uses the concept of light rays — straight lines representing sunlight's path in the optical system [34]. It creates and follows rays throughout the optical system, simulating their interaction with surfaces and materials, calculating the reflected, transmitted, and absorbed fractions of the incident rays. The number of rays must be large enough to produce accurate results. It has the advantage of dealing with any geometry and mapping the flux distribution on the absorber. On the other hand, the computational cost can be high and the stochastic nature of the simulations introduce fluctuations in the results, issues that make its use in further optimization studies a challenging task.

Tonatiuh [35] and SolTrace [36] are two open source ray-tracing tools. Commercial computer programs are also available: TracePro [37], ASAP [38], and the Optica package for the Wolfram Mathematica® [39] are examples. Another common alternative is to develop from scratch the ray-tracing algorithm (an in-house solution), as done in many studies [10, 40–43].

Analytical methods

Analytical approaches to compute the optical analysis problem are based on the split of losses due to optical properties and geometrical characteristics to define η_{opt}. Although optical properties are functions of incidence angles [44], a common simplification in solar concentration is to consider them as constant values.

Thus, η_{opt} can be written as shown in Equation 2.25, where Π stands for the concatenation of surfaces optical properties (reflectivity, transmissivity, and absorptivity), and γ is the intercept factor, which accounts for losses due to the concentrator geometry [3].

$$\eta_{opt}(\theta_T, \theta_L) = \Pi\gamma(\theta_T, \theta_L) \tag{2.25}$$

From Equations 2.18 and 2.25, one can derive that $Q_{abs} = \Pi\gamma A I_b$, and then interpret γ as a purely geometric factor which accounts for the fraction of the aperture area being used to collect the incident radiation I_b. Thus, models like the ones defined in Section 2.2 can be used to determine the intercept factor for a particular incidence.

Analytical methods are less detailed but much faster than ray-tracing. Models in Subsection 2.2 illustrate the relationships between various geometric parameters, facilitating the identification of dimensionless terms that minimize the number of design variables, which is not achievable with ray-tracing, as its approach hides functional relationships [3].

2.4 The performance problem

Linear Fresnel Collectors (LFCs) face significant challenges in optical performance when compared to Parabolic Trough Collectors (PTCs), particularly in the context of solar thermal electricity production. The key issue lies in its lower optical efficiency [45–49].

Unlike PTCs, LFCs encounter several performance-reducing factors that are mainly related

to its working principle. First, the use of a secondary optics imposes more losses due to the additional reflections and shading on the primary mirrors. Moreover, it is quite straightforward to show that cosine effect losses occur even under normal incidence (refer to Subsection 2.2.2). PTCs commercial technologies can reach normal incidence efficiency between 75.0% and 81.0% [50, 51], while LFCs achieve between 64.0% and 67.0% [2]. Furthermore, as the sun moves out of the normal incidence, LFCs experience a faster reduction of efficiency than PTCs. In the transversal plane, cosine effect, shading and blocking (refer to Subsection 2.2.3), and also spillage (refer to Subsection 2.2.4) increase, which do not occur in PTC systems. In the longitudinal plane, LFCs have a more pronounced penalty in spillage and end-effect (refer to Subsection 2.2.5) due this its higher averaged focusing distance. This steeper efficiency reduction as the sun moves out of normal incidence is exemplified by the IAMs comparison shown in Figure 2.9.

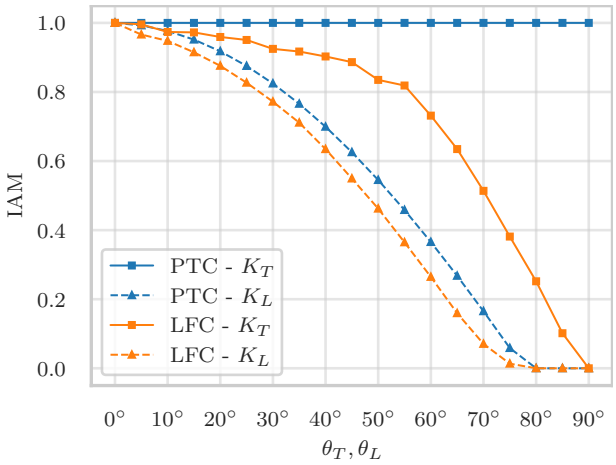

Figure 2.9: Incidence Angle Modifiers (IAMs) comparison: Linear Fresnel Collector (LFC) vs. Parabolic Trough Collector (PTC). Elaborated based on data from Morin et al. [45], collected by automeris (available at https://automeris.io).

Overall, these effects substantially reduce the amount of solar flux reaching the absorber in LFC systems, diminishing their optical efficiency in comparison to PTCs. Thus, this drawback has a notable impact on generation by first decreasing sunlight-to-heat conversion efficiency, but also by increasing part-load operation hours of the power block, ultimately reducing the system's capacity for more continuous, efficient electricity production.

Studies comparing LFC and PTC technologies [45–49] highlight these challenges, as they underscore that the lower optical performance of LFCs remains a central factor in their reduced competitiveness for utility-scale solar power generation. These comparisons have explored various power plant configurations, including systems using thermal oil [46, 49], direct steam generation [45, 46], molten salts [47, 49], as well as with [47, 49] and without [45, 46] thermal storage systems. The reduced optical performance of LFCs affects their Levelized Cost of Electricity (LCOE), often necessitating a lower solar field specific cost compared to PTCs to achieve the same competitiveness. This threshold, referred to as the break-even cost, is typically expressed as a percentage of the direct specific cost (in €/m^2) of the PTC solar field and varies across studies based on the analyzed conditions. For instance, Morin et al. [45] identified break-even costs for LFCs ranging between 53% and 55% of PTC costs. Giostri et al. [46] reported a wider range of 40% to 50%. Schenk et al. [47] estimated break-even costs between 67% and 72%, while Kincaid et al. [48] found values around 66%. These variations underscore the dependence of specific technological and operational factors on break-even costs for the LFC technology.

To address the efficiency limitations in linear Fresnel collectors, two approaches have been

explored. One was briefly investigated by Morin et al. [45] and involves structural modifications. The other relates to the design of the concentrator and how the geometric parameters are determined. The first encompasses detailed engineering adjustments, such as improvements in the steel supporting structures of the concentrator to reduce shading on the primary field, as one example. The second involves the conceptual design of this concentrator, aiming to optimize performance through a careful procedure. While improvements on the engineering project have shown potential, their impact on the overall efficiency is limited without concurrent improvements in the geometric conceptual design.

This thesis, therefore, centers on the second approach: developing geometric designs to enhance the optical performance of linear Fresnel collectors, as it aims to address one of the primary barriers to the technology's competitiveness in solar thermal electricity production.

2.5 The design problem

In view of the aforementioned performance problem, geometric designs that improves the optical performance of the linear Fresnel technology is the core objective of a vast literature. A geometric configuration (refer to Figure 2.3) presents numerous parameters to be defined, while the constraints imposed are relatively limited. Furthermore, complexity arises from the interdependence of multiple parameters in calculating optical and thermal losses, making the optimization process notably challenging. The works on this geometric design can be divided into three large groups: new concepts, design criteria, and optimization studies.

The first one comprises new concepts of concentration, whether in terms of modifications of the primary reflector or by innovative secondary optic designs. The Compact LFC (CLFC) proposed by Mills and Morison [52] considers that mirrors have two receivers to reflect the incoming sunlight, which has the purpose of reducing shading and blocking losses. Chaves and Collares-Pereira [53] incremented the CLFC and proposed an Etendue-Matched (EM-CLFC) design, in which primary mirrors position do not lie in the same horizontal line but instead has also a vertical component following a particular curve profile to achieve etendue conservation. These designs are illustrated in Figure 2.10, and were the subject of further research: CLFC studies were conducted by Montes et al. [10] and Zhu and Cheng [54], while Rungasamy et al. [55] tackle the EM-CLFC design.

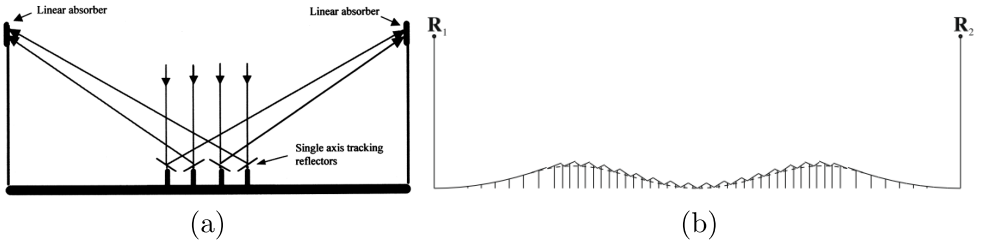

Figure 2.10: New concepts for the Linear Fresnel Collector. It shows the (a) Compact LFC (CLFC) [52] and (b) Etendue-Matched CLFC (EM-CLFC) [53] designs.

Other concepts encompass the simultaneous multiple surface design [56], a primary field composed of catoptric subsets [57], the beam-down design [58, 59], and a recently proposed rotatory linear Fresnel with tilted primaries [60, 61]. Although presenting promising results, disadvantages also arise such as the addition of more parameters to the model illustrated in Figure 2.3, so that optimum designs for each one of these new concepts are novel problems. The examples mentioned previously are only a few, and the literature encompasses much more. They are not the subject of this thesis.

The second group comprises studies that use design criteria to determine parameters of the geometric model. In these cases, models of optical losses are derived and the corresponding geometric parameters are determined to minimize those losses. As examples, Mathur et al. [62, 63] used a non-blocking criterion to determine position and width of the primary mirrors to achieve a more uniform flux distribution at the absorber. Abbas and Martínez-Val [27, 28] used a previous analysis [26] to establish the maximum width of primary mirrors so that it minimizes spillage, as well as criteria on how to determine the curvature of the primary mirrors. A non-shading criterion was used by Nixon and Davies [64] to determine the position of primary mirrors. These works usually do not include the secondary optic as part of the design problem.

The last group of studies tackle the design of a linear Fresnel collector by the approach of an optimization problem, defining decision variables, objective functions, and a heuristic to determine optimal configurations [65, 66]. The search algorithm is coupled to models that evaluate how a particular geometric configuration perform. Most of the studies consider a single-objective approach [10, 22, 67–71] by evaluating only the optical behavior, but multi-objective studies were already conducted to simultaneously accounting for optical [11, 72], thermal [11, 64, 72], and economical objectives [11, 67]. Parametric analysis [10, 22, 70], gradient-based methods [67], and computational intelligence tools [11, 68, 69, 71, 72] are used as search heuristics to determine optimum configurations. It can include [68–72] or not [10, 11, 22, 67] the secondary optic in the problem definition.

These two last group of studies provide methodologies for addressing this design challenge. The design criteria approach offers a practical way to simplify the problem. For example, Abbas and Martínez-Val [73] use a couple of criteria as a pre-design to reduce the number of decision variables before applying an optimization routine – each variable is an additional degree-of-freedom in the problem. However, the considered criteria can restrict the search space and risk convergence to local rather than global optima. Consequently, the optimization approach emerges as the more robust method for achieving optimal configurations, although insights from studies based on design criteria remain valuable, as they can provide guidance for optimization efforts.

The varied reported results in the literature reflect the inherent complexity of the problem and underscore that the geometric design of linear Fresnel collectors remains an active and open area of research. Moreover, the diversity of proposed optimal solutions, rather than convergence to a specific configuration, suggests that this problem is highly sensitive to boundary conditions such as sunshape, optical errors, and location, among others. For example, Montes et al. [10] highlight the importance of defining proper objective functions representing the actual performance to avoid trivial biased solutions.

To address the complexity of the linear Fresnel collector design problem, an alternative approach is to break it into smaller and more direct problems. Instead of viewing the design as a single, intricate challenge, focusing on specific aspects allows for the formulation of more objective research questions. This strategy is used in this thesis to advance the understanding of this design problem while uncovering opportunities to simplify and generalize its solutions. The upcoming five chapters detail the advances produced in the context of this thesis. They are structured as follows in the next paragraphs.

One key effort is related to computational evaluation methodologies. Ray-tracing is known for its time-consuming simulations [11, 68, 69] and inherent variability due to stochastic sampling algorithms [67]. Developing faster yet equally accurate methods could significantly streamline design optimization, enabling more efficient exploration of potential configurations. The development of an optical method is the subject of Chapter 3.

Other efforts comprise the curvature design, the parameter κ in Figure 2.3. It is clear that curved mirrors (parabolic or cylindrical) achieve better concentration and energy collection than flat ones, under the same conditions [5, 6, 41]. Additionally, existing evidence suggests that parabolic and cylindrical mirrors may deliver comparable performance [26, 74, 75], but the underlying reasons remain not fully exploited. Then, different methodologies for defining curvature values [3, 27, 75] have yet to be compared. Investigating these alternatives can shed light on best practices for primary mirrors design, topics discussed in Chapters 4 and 5. The former deals with the shape of the primaries, while the latter tackles the determination of the proper curvature value.

The secondary optics design presents itself as another critical area for advancement. The literature regarding this subject comprise not only proposition of secondaries [69, 71, 76, 77], but also comparison studies [8, 78, 79]. The CPC is the winner optic, although it was never compared to the Compound Elliptical Concentrator (CEC) [80] and a more recent aplanatic design [81]. Additionally, trade-offs between optimized [68, 72] and edge-ray [82] CPC-based geometries remain an open question that warrants further investigation. Understanding these dynamics can lead to more effective and versatile secondary optics solutions. This topic is the subject of Chapter 6.

Furthermore, it is essential to evaluate the effectiveness of uniform versus non-uniform optimum designs. While literature suggests that non-uniform configurations of mirror width and shift have minimal impact on energy collection efficiency [27, 67, 73], their potential cost implications could make them less attractive. This highlights the importance of balancing performance gains with practical considerations such as cost, operation, and maintenance. This discussion is addressed in Chapter 7.

In summary, important lessons from the current literature point toward breaking down the linear Fresnel collector design problem into manageable sub-problems. This approach enables the development of targeted studies that not only deepen understanding but also push the boundaries of the state of the art by addressing key challenges such as an optical method, mirror curvature, secondary optics, and optimal geometry configurations.

References

[1] M. Collares-Pereira, D. Canavarro, and L. Guerreiro, "Linear Fresnel reflector (LFR) plants using superheated steam, molten salts, and other heat transfer fluids," in *Advances in Concentrating Solar Thermal Research and Technology*, M. J. Blanco and L. R. Santigosa, Eds., Cham: Elsevier, 2017, ch. 15, pp. 339–352. DOI: 10.1016/B978-0-08-100516-3.00015-0.

[2] W. J. Platzer, D. Mills, and W. Gardner, "Linear Fresnel Collector (LFC) solar thermal technology," in *Concentrating Solar Power Technology*, K. Lovegrove and W. Stein, Eds., 2nd Edition, Cambridge: Elsevier, 2021, ch. 6, pp. 165–217. DOI: 10.1016/B978-0-12-819970-1.00006-2.

[3] A. Rabl, *Active Solar Collectors and Their Applications*. New York: Oxford University Press, 1985. [Online]. Available: https://shorturl.at/oGLX6.

[4] G. Zhu, T. Wendelin, M. J. Wagner, and C. Kutscher, "History, current state, and future of linear Fresnel concentrating solar collectors," *Solar Energy*, vol. 103, pp. 639–652, 2014. DOI: 10.1016/j.solener.2013.05.021.

[5] R. Abbas, J. Muñoz-Antón, M. Valdés, and J. Martínez-Val, "High concentration linear Fresnel reflectors," *Energy Conversion and Management*, vol. 72, pp. 60–68, 2013. DOI: 10.1016/j.enconman.2013.01.039.

[6] D. Feuermann and J. M. Gordon, "Analysis of a Two-Stage Linear Fresnel Reflector Solar Concentrator," *Journal of Solar Energy Engineering*, vol. 113, no. 4, pp. 272–279, 1991. DOI: 10.1115/1.2929973.

[7] P. Horta and T. Osório, "Optical Characterization Parameters for Line-focusing Solar Concentrators: Measurement Procedures and Extended Simulation Results," *Energy Procedia*, vol. 49, pp. 98–108, 2014. DOI: 10.1016/j.egypro.2014.03.011.

[8] G. C. Prasad, K. Reddy, and T. Sundararajan, "Optimization of solar linear Fresnel reflector system with secondary concentrator for uniform flux distribution over absorber tube," *Solar Energy*, vol. 150, pp. 1–12, 2017. DOI: 10.1016/j.solener.2017.04.026.

[9] S. Rodat and R. Thonig, "Status of Concentrated Solar Power Plants Installed Worldwide: Past and Present Data," *Clean Technologies*, vol. 6, no. 1, pp. 365–378, 2024. DOI: 10.3390/cleantechnol6010018.

[10] M. J. Montes, C. Rubbia, R. Abbas, and J. M. Martínez-Val, "A comparative analysis of configurations of linear Fresnel collectors for concentrating solar power," *Energy*, vol. 73, pp. 192–203, 2014. DOI: 10.1016/j.energy.2014.06.010.

[11] M. Moghimi, K. Craig, and J. Meyer, "Simulation-based optimisation of a linear Fresnel collector mirror field and receiver for optical, thermal and economic performance," *Solar Energy*, vol. 153, pp. 655–678, 2017. DOI: 10.1016/J.SOLENER.2017.06.001.

[12] S. Teske, J. Leung, L. Crespo, M. Bial, E. Dufour, and C. Richter, "Solar Thermal Electricity - Global Outlook 2016," European Solar Thermal Electricity Association (ESTELA), Tech. Rep., 2016. [Online]. Available: https://www.estelasolar.org/wp-content/uploads/2016/02/GP-ESTELA-SolarPACES_Solar-Thermal-Electricity-Global-Outlook-2016_Full-report.pdf.

[13] R. Thonig, A. Gilmanova, and J. Lilliestam, *Csp.guru*, version 2023-07-01, Zenodo, 2023. DOI: 10.5281/zenodo.8191855. [Online]. Available: https://csp.guru.

[14] R. Grena and P. Tarquini, "Solar linear Fresnel collector using molten nitrates as heat transfer fluid," *Energy*, vol. 36, no. 2, pp. 1048–1056, 2011. DOI: 10.1016/j.energy.2010.12.003.

[15] G. Morin, M. Karl, M. Mertins, and M. Selig, "Molten Salt as a Heat Transfer Fluid in a Linear Fresnel Collector – Commercial Application Backed by Demonstration," *Energy Procedia*, vol. 69, pp. 689–698, 2015. DOI: 10.1016/j.egypro.2015.03.079.

[16] C. Bachelier and R. Stieglitz, "Design and optimisation of linear Fresnel power plants based on the direct molten salt concept," *Solar Energy*, vol. 152, pp. 171–192, 2017. DOI: 10.1016/j.solener.2017.01.060.

[17] A. Aljudaya, S. Michailos, D. B. Ingham, K. J. Hughes, L. Ma, and M. Pourkashanian, "Techno-Economic Assessment of Molten Salt-Based Concentrated Solar Power: Case Study of Linear Fresnel Reflector with a Fossil Fuel Backup under Saudi Arabia's Climate Conditions," *Energies*, vol. 17, no. 11, p. 2719, 2024. DOI: 10.3390/en17112719.

[18] RioGlass. "RECEIVER TUBES FOR LINEAR CSP (CONCENTRATED SOLAR POWER) APPLICATIONS." (2025), [Online]. Available: https://www.rioglass.com/en/our-products/hce-tubes (visited on 03/07/2025).

[19] M. Imran Khan, F. Asfand, and S. G. Al-Ghamdi, "Progress in research and technological advancements of commercial concentrated solar thermal power plants," *Solar Energy*, vol. 249, pp. 183–226, 2023. DOI: 10.1016/j.solener.2022.10.041.

[20] R. Grena, "Geometrical Aspects of the Optics of Linear Fresnel Concentrators: A Review," *Energies*, vol. 17, no. 14, p. 3564, 2024. DOI: 10.3390/en17143564.

[21] Y. Qiu, M. J. Li, K. Wang, Z. B. Liu, and X. D. Xue, "Aiming strategy optimization for uniform flux distribution in the receiver of a linear Fresnel solar reflector using a multi-objective genetic algorithm," *Applied Energy*, vol. 205, pp. 1394–1407, 2017. DOI: 10.1016/j.apenergy.2017.09.092.

[22] V. Sharma, J. K. Nayak, and S. B. Kedare, "Effects of shading and blocking in linear Fresnel reflector field," *Solar Energy*, vol. 113, pp. 114–138, 2015. DOI: 10.1016/j.solener.2014.12.026.

[23] M. Yang, Y. Zhu, and R. A. Taylor, "End losses minimization of linear Fresnel reflectors with a simple, two-axis mechanical tracking system," *Energy Conversion and Management*, vol. 161, pp. 284–293, 2018. DOI: 10.1016/j.enconman.2018.01.082.

[24] E. Bellos and C. Tzivanidis, "Development of analytical expressions for the incident angle modifiers of a linear Fresnel reflector," *Solar Energy*, vol. 173, pp. 769–779, 2018. DOI: 10.1016/j.solener.2018.08.019.

[25] A. Häberle, "Linear Fresnel Collectors," in *Solar Energy*, C. Richter, D. Lincot, and C. A. Gueymard, Eds., Springer New York, 2013, pp. 72–78. DOI: 10.1007/978-1-4614-5806-7_679.

[26] R. Abbas, M. J. Montes, M. Piera, and J. M. Martínez-Val, "Solar radiation concentration features in Linear Fresnel Reflector arrays," *Energy Conversion and Management*, vol. 54, no. 1, pp. 133–144, 2012. DOI: 10.1016/j.enconman.2011.10.010.

[27] R. Abbas and J. Martínez-Val, "Analytic optical design of linear Fresnel collectors with variable widths and shifts of mirrors," *Renewable Energy*, vol. 75, pp. 81–92, 2015. DOI: 10.1016/j.renene.2014.09.029.

[28] R. Abbas and J. Martínez-Val, "A comprehensive optical characterization of linear Fresnel collectors by means of an analytic study," *Applied Energy*, vol. 185, pp. 1136–1151, 2017. DOI: 10.1016/j.apenergy.2016.01.065.

[29] A. Heimsath, G. Bern, D. van Rooyen, and P. Nitz, "Quantifying Optical Loss Factors of Small Linear Concentrating Collectors for Process Heat Application," *Energy Procedia*, vol. 48, pp. 77–86, 2014. DOI: 10.1016/j.egypro.2014.02.010.

[30] M. Hongn, S. F. Larsen, M. Gea, and M. Altamirano, "Least square based method for the estimation of the optical end loss of linear Fresnel concentrators," *Solar Energy*, vol. 111, pp. 264–276, 2015. DOI: 10.1016/j.solener.2014.10.042.

[31] W. R. McIntire, "Factored approximations for biaxial incident angle modifiers," *Solar Energy*, vol. 29, no. 4, pp. 315–322, 1982. DOI: 10.1016/0038-092X(82)90246-8.

[32] R. Bernhard, S. Hein, J. LaLaing, M. Eck, M. Eickhoff, M. Pfaender, G. Morin, and A. Häberle, "Linear Fresnel collector demonstration on the PSA Part II - Commissioning and first performance tests," in *14th International Symposium on Concentrated Solar Power and Chemical Energy Technologies*, 2008. [Online]. Available: https://elib.dlr.de/57087/.

[33] J. D. Hertel, V. Martinez-Moll, and R. Pujol-Nadal, "Estimation of the influence of different incidence angle modifier models on the biaxial factorization approach," *Energy Conversion and Management*, vol. 106, pp. 249–259, 2015. DOI: 10.1016/j.enconman.2015.08.082.

[34] F. L. Pedrotti, L. M. Pedrotti, and L. S. Pedrotti, *Introduction to Optics*, 3rd Edition. Cambridge University Press, 2017. DOI: 10.1017/9781108552493.

[35] J. P. Cardoso, A. Mutuberria, C. Marakkos, P. Schoettl, T. Osório, and I. Les, "New functionalities for the Tonatiuh ray-tracing software," in *AIP Conference Proceedings*, vol. 2033, 2018, p. 210 010. DOI: 10.1063/1.5067212.

[36] T. Wendelin, A. Dobos, and A. Lewandowski, "SolTrace: A Ray-Tracing Code for Complex Solar Optical Systems," National Renewable Energy Laboratory (NREL), Golden, CO (United States), Tech. Rep., 2013. DOI: 10.2172/1260924.

[37] Lambda Research Corporation, *TracePro: Optical and Illumination Simulation, Design & Analysis Tool*. [Online]. Available: https://lambdares.com/tracepro (visited on 04/28/2024).

[38] Breault Research Organization, *Advanced Systems Analysis Program (ASAP): Optical Engineering Software for advanced optic systems*. [Online]. Available: https://software.breault.com/asap/ (visited on 04/28/2024).

[39] D. Barnhart, *Optica: optical system design software package for Mathematica*. [Online]. Available: http://www.opticasoftware.com/ (visited on 04/28/2024).

[40] Y. Qiu, Y. L. He, Z. D. Cheng, and K. Wang, "Study on optical and thermal performance of a linear Fresnel solar reflector using molten salt as HTF with MCRT and FVM methods," *Applied Energy*, vol. 146, pp. 162–173, 2015. DOI: 10.1016/j.apenergy.2015.01.135.

[41] S. Benyakhlef, A. Al Mers, O. Merroun, A. Bouatem, N. Boutammachte, S. El Alj, H. Ajdad, Z. Erregueragui, and E. Zemmouri, "Impact of heliostat curvature on optical performance of Linear Fresnel solar concentrators," *Renewable Energy*, vol. 89, pp. 463–474, 2016. DOI: 10.1016/j.renene.2015.12.018.

[42] G. Cardona and R. Pujol-Nadal, "OTSun, a python package for the optical analysis of solar-thermal collectors and photovoltaic cells with arbitrary geometry," *PLOS ONE*, vol. 15, no. 10, F. Li, Ed., e0240735, 2020. DOI: 10.1371/journal.pone.0240735.

[43] M. Fossa, A. Boccalatte, and S. Memme, "Solar Fresnel modelling, geometry enhancement and 3D ray tracing analysis devoted to different energy efficiency definitions and applied to a real facility," *Solar Energy*, vol. 216, pp. 75–89, 2021. DOI: 10.1016/j.solener.2020.12.047.

[44] J. R. Howell, M. P. Mengüç, and R. Siegel, *Thermal radiation heat transfer*. Boca Raton: CRC Press, 2016. DOI: 10.1201/b18835.

[45] G. Morin, J. Dersch, W. Platzer, M. Eck, and A. Häberle, "Comparison of Linear Fresnel and Parabolic Trough Collector power plants," *Solar Energy*, vol. 86, no. 1, pp. 1–12, 2012. DOI: 10.1016/j.solener.2011.06.020.

[46] A. Giostri, M. Binotti, P. Silva, E. Macchi, and G. Manzolini, "Comparison of Two Linear Collectors in Solar Thermal Plants: Parabolic Trough Versus Fresnel," *Journal of Solar Energy Engineering*, vol. 135, no. 1, p. 011 001, 2012. DOI: 10.1115/1.4006792.

[47] H. Schenk, T. Hirsch, J. Fabian Feldhoff, and M. Wittmann, "Energetic Comparison of Linear Fresnel and Parabolic Trough Collector Systems," *Journal of Solar Energy Engineering*, vol. 136, no. 4, pp. 04 101 501–04 101 511, 2014. DOI: 10.1115/1.4027766.

[48] N. Kincaid, G. Mungas, N. Kramer, M. Wagner, and G. Zhu, "An optical performance comparison of three concentrating solar power collector designs in linear Fresnel, parabolic trough, and central receiver," *Applied Energy*, vol. 231, pp. 1109–1121, 2018. DOI: 10.1016/J.APENERGY.2018.09.153.

[49] M. Shokrnia, M. Cagnoli, R. Grena, A. D'Angelo, M. Lanchi, and R. Zanino, "Comparative Techno-Economic Analysis of Parabolic Trough and Linear Fresnel Collectors with Evacuated and Non-Evacuated Receiver Tubes in Different Geographical Regions," *Processes*, vol. 12, no. 11, p. 2376, 2024. DOI: 10.3390/pr12112376.

[50] K.-J. Riffelmann, D. Graf, and P. Nava, "Ultimate Trough: The New Parabolic Trough Collector Generation for Large Scale Solar Thermal Power Plants," in *ASME 2011 5th International Conference on Energy Sustainability, Parts A, B, and C*, ASMEDC, 2011, pp. 789–794. DOI: 10.1115/ES2011-54657.

[51] F. von Reeken, S. Arbes, G. Weinrebe, M. Wöhrbach, and J. Finkbeiner, *PARABOLIC TROUGH CSP TECHNOLOGY: state of the art and market overview*. Brasilia: Projeto Energia Heliotérmica, Ministério da Ciência, Tecnologia e Inovação (MCTI), Deutsche Gesellschaft für Internationale Zusammenarbeit (GIZ), 2014.

[52] D. R. Mills and G. L. Morrison, "Compact linear fresnel reflector solar thermal powerplants," *Solar Energy*, vol. 68, no. 3, pp. 263–283, 2000. DOI: 10.1016/S0038-092X(99)00068-7.

[53] J. Chaves and M. Collares-Pereira, "Etendue-matched two-stage concentrators with multiple receivers," *Solar Energy*, vol. 84, no. 2, pp. 196–207, 2010. DOI: 10.1016/j.solener.2009.10.022.

[54] J. Zhu and Z. Chen, "Optical design of compact linear fresnel reflector systems," *Solar Energy Materials and Solar Cells*, vol. 176, pp. 239–250, 2018. DOI: 10.1016/j.solmat.2017.12.016.

[55] A. Rungasamy, K. Craig, and J. Meyer, "Comparative study of the optical and economic performance of etendue-conserving compact linear Fresnel reflector concepts," *Solar Energy*, vol. 181, pp. 95–107, 2019.

[56] D. Canavarro, J. Chaves, and M. Collares-Pereira, "Simultaneous Multiple Surface method for Linear Fresnel concentrators with tubular receiver," *Solar Energy*, vol. 110, pp. 105–116, 2014. DOI: 10.1016/j.solener.2014.09.002.

[57] A. Vouros, E. Mathioulakis, E. Papanicolaou, and V. Belessiotis, "Performance evaluation of a linear Fresnel collector with catoptric subsets," *Renewable Energy*, vol. 156, pp. 68–83, 2020. DOI: 10.1016/j.renene.2020.04.062.

[58] A. Sánchez-González and J. Gómez-Hernández, "Beam-down linear Fresnel reflector: BDLFR," *Renewable Energy*, vol. 146, pp. 802–815, 2020. DOI: 10.1016/j.renene.2019.07.017.

[59] C. Sammoutos, E. Bellos, A. Kitsopoulou, P. Lykas, E. Vidalis, and C. Tzivanidis, "Optical, thermal and exergy analysis of a beam-down linear Fresnel reflector coupled with a flat plate receiver," *Solar Energy*, vol. 282, p. 112 949, 2024. DOI: 10.1016/j.solener.2024.112949.

[60] J. Cano-Nogueras, J. Muñoz-Antón, and J. M. Martinez-Val, "A New Thermal-Solar Field Configuration: The Rotatory Fresnel Collector or Sundial," *Energies*, vol. 14, no. 14, p. 4139, 2021. DOI: 10.3390/en14144139.

[61] M. Barnetche, L. F. González-Portillo, R. Abbas, M. Ibarra, R. Barbero, and A. Rovira, "Defocus Controller for a Rotatory Fresnel Collector," *SolarPACES Conference Proceedings*, vol. 1, pp. 1–9, 2023. DOI: 10.52825/solarpaces.v1i.733.

[62] S. Mathur, T. Kandpal, and B. Negi, "Optical design and concentration characteristics of linear Fresnel reflector solar concentrators—I. Mirror elements of varying width," *Energy Conversion and Management*, vol. 31, no. 3, pp. 205–219, 1991. DOI: 10.1016/0196-8904(91)90075-T.

[63] S. Mathur, T. Kandpal, and B. Negi, "Optical design and concentration characteristics of linear Fresnel reflector solar concentrators—II. Mirror elements of equal width," *Energy Conversion and Management*, vol. 31, no. 3, pp. 221–232, 1991. DOI: 10.1016/0196-8904(91)90076-U.

[64] J. Nixon and P. Davies, "Cost-exergy optimisation of linear Fresnel reflectors," *Solar Energy*, vol. 86, no. 1, pp. 147–156, 2012. DOI: 10.1016/j.solener.2011.09.024.

[65] M. J. Kochenderfer and T. A. Wheeler, *Algorithms for optimization*. Cambridge: MIT Press, 2019. [Online]. Available: https://algorithmsbook.com/optimization/.

[66] J. R. R. A. Martins and A. Ning, *Engineering Design Optimization*. Cambridge University Press, 2021. DOI: 10.1017/9781108980647.

[67] P. Boito and R. Grena, "Optimization of the geometry of Fresnel linear collectors," *Solar Energy*, vol. 135, pp. 479–486, 2016. DOI: 10.1016/j.solener.2016.05.060.

[68] Z. D. Cheng, X. R. Zhao, Y. L. He, and Y. Qiu, "A novel optical optimization model for linear Fresnel reflector concentrators," *Renewable Energy*, vol. 129, pp. 486–499, 2018. DOI: 10.1016/j.renene.2018.06.019.

[69] H. Ajdad, Y. Filali Baba, A. Al Mers, O. Merroun, A. Bouatem, and N. Boutammachte, "Particle swarm optimization algorithm for optical-geometric optimization of linear fresnel solar concentrators," *Renewable Energy*, vol. 130, pp. 992–1001, 2019. DOI: 10.1016/j.renene.2018.07.001.

[70] J. Ma, C.-L. Wang, Y. Zhou, and R.-D. Wang, "Optimized design of a linear Fresnel collector with a compound parabolic secondary reflector," *Renewable Energy*, vol. 171, pp. 141–148, 2021. DOI: 10.1016/j.renene.2021.02.100.

[71] A. Ahmadpour, A. Dejamkhooy, and H. Shayeghi, "Optimization and modelling of linear Fresnel reflector solar concentrator using various methods based on Monte Carlo Ray–Trace," *Solar Energy*, vol. 245, pp. 67–79, 2022. DOI: 10.1016/j.solener.2022.09.006.

[72] J. Men, X. Zhao, Z. Cheng, Y. Leng, and Y. He, "Study on the annual optical comprehensive performance of linear Fresnel reflector concentrators with an effective multi-objective optimization model," *Solar Energy*, vol. 225, pp. 591–607, 2021. DOI: 10.1016/j.solener.2021.07.051.

[73] R. Abbas, M. Valdés, M. Montes, and J. Martínez-Val, "Design of an innovative linear Fresnel collector by means of optical performance optimization: A comparison with parabolic trough collectors for different latitudes," *Solar Energy*, vol. 153, pp. 459–470, 2017. DOI: 10.1016/j.solener.2017.05.047.

[74] S. Balaji, K. Reddy, and T. Sundararajan, "Optical modelling and performance analysis of a solar LFR receiver system with parabolic and involute secondary reflectors," *Applied Energy*, vol. 179, pp. 1138–1151, 2016. DOI: 10.1016/j.apenergy.2016.07.082.

[75] P. Boito and R. Grena, "Optimal focal length of primary mirrors in Fresnel linear collectors," *Solar Energy*, vol. 155, pp. 1313–1318, 2017. DOI: 10.1016/j.solener.2017.07.079.

[76] G. Zhu, "New adaptive method to optimize the secondary reflector of linear Fresnel collectors," *Solar Energy*, vol. 144, pp. 117–126, 2017. DOI: 10.1016/j.solener.2017.01.005.

[77] A. Vouros, E. Mathioulakis, E. Papanicolaou, and V. Belessiotis, "On the optimal shape of secondary reflectors for linear Fresnel collectors," *Renewable Energy*, vol. 143, pp. 1454–1464, 2019. DOI: 10.1016/j.renene.2019.05.044.

[78] M. Hack, G. Zhu, and T. Wendelin, "Evaluation and comparison of an adaptive method technique for improved performance of linear Fresnel secondary designs," *Applied Energy*, vol. 208, pp. 1441–1451, 2017. DOI: 10.1016/j.apenergy.2017.09.009.

[79] R. Abbas, A. Sebastián, M. Montes, and M. Valdés, "Optical features of linear Fresnel collectors with different secondary reflector technologies," *Applied Energy*, vol. 232, pp. 386–397, 2018. DOI: 10.1016/j.apenergy.2018.09.224.

[80] D. Canavarro, J. Chaves, and M. Collares-Pereira, "New dual asymmetric CEC linear Fresnel concentrator for evacuated tubular receivers," in *AIP Conference Proceedings*, vol. 1850, 2017, p. 040 001. DOI: 10.1063/1.4984397.

[81] L. F. L. Souza, N. Fraidenraich, C. Tiba, and J. M. Gordon, "Linear aplanatic Fresnel reflector for practical high-performance solar concentration," *Solar Energy*, vol. 222, pp. 259–268, 2021. DOI: 10.1016/j.solener.2021.05.002.

[82] J. Chaves, *Introduction to Nonimaging Optics*, 2nd Edition. New York: CRC Press, 2016. DOI: 10.1201/b18785.

Nomenclature

Abbreviations

BLF	Blocking Loss Factor
CLF	Cosine Loss Factor
CLFC	Compact Linear Fresnel Collector
CEC	Compound Elliptical Concentrator
CPC	Compound Parabolic Concentrator
CRS	Central Receiver System
DLF	Defocusing Loss Factor
ELF	End-effect Loss Factor
EM-CLFC	Etendue Match Compact Linear Fresnel Collector
HTF	Heat Transfer Fluid
IAM	Incidence Angle Modifier
LCOE	Levelized Cost of Electricity
LFC	Linear Fresnel Collector
PTC	Parabolic Trough Collector
SLF	Shading Loss Factor

Latin Letters

$\mathbf{F}$	Primary mirrors aim point at the receiver. The tracking point
$\mathbf{F}_1, \mathbf{F}_2$	Edge-points of the primary field
$\mathbf{M}$	Center point of a primary mirror
$\mathbf{S}_1, \mathbf{S}_2$	Edge-points of the receiver/secondary optic

A	Aperture area
A_{abs}	Absorber surface area
A_{gross}	Occupied (land) aperture area
A_{net}	Reflective (net) aperture area
h_s	Secondary optic differential height (from tube to aperture)
I_b	Beam Irradiance
K_L	Longitudinal Incidence Angle Modifier
K_T	Transversal Incidence Angle Modifier
l_e	Lost length due to end-effects

L	Length of the concentrator
n	Number of mirrors in the primary field
q	Flux distribution function over the absorber surface
Q_{abs}	Total absorbed flux
s	Distance (shift) between two neighboring primary mirrors
w	Primary mirror width
W_p	Total width of the primary field
W_s	Aperture width of the secondary optic
z_s	Shape function of the secondary optic

$\vec{I}_x, \vec{I}_y, \vec{I}_z$	Direction vectors of an xyz right-handed coordinate system
$\vec{n}$	Normal vector to the mirror surface at the center point
$\vec{S}$	Incident sunlight direction vector
$\vec{S}_L$	Projection of $\vec{S}$ in the longitudinal plane
$\vec{S}_T$	Projection of $\vec{S}$ in the transversal plane
$\vec{v}_f$	Primary mirror focusing vector: $\vec{v}_f = \mathbf{F} - \mathbf{M}$
$\hat{x}$	Decision vector. Defines a geometric configuration

Greek Letters

η_{opt}	Optical efficiency
η_{opt0}	Optical efficiency at normal incidence
λ	Primary mirror angular position
θ_L	Longitudinal incidence angle
θ_{LS}	Longitudinal-solar incidence angle
θ_T	Transversal incidence angle
κ	Curvature profile of primary mirrors
τ	Primary mirror tracking angle
γ	Intercept factor
Π	Concatenation of surfaces optical properties

Indices

i	General counting index

Chapter 3

An optical method[†]

Abstract

Ray-tracing is the main method used to compute the optical analysis problem due to its capability to precisely model even the most complex optical system, however, it can lead to convergence problems in optimization studies. This chapter presents an analytical method for the case of linear Fresnel collectors with a flat receiver. To advance the state of the art, it develops a bi-axial approach based on a vector analysis, that coupled with a linear integration of the effective source yields the flux intercepted by the receiver and then the concentrator efficiency. Study cases were elaborated to evaluate how the proposed method approximates results of ray-tracing simulations (numerical experiments) carried out in SolTrace, considering two linear Fresnel geometries, five effective sources, and six different locations with latitudes up to almost 40°. The validation results indicate that analytical and ray-tracing do agree very well: maximum absolute deviations are seen for incidence angles higher than 80°, which can yield a high root mean square error when averaging it for the whole incidence domain. Such averaged absolute errors ranged between 0.0004 and 0.0143 for the analyzed cases, however, the effect on annual collected energy is reduced since high incidences are usually associated with low values of irradiance. The annual averaged efficiency calculations indicate errors up to 2.6% between analytical and ray-tracing computations, which occur for high latitude locations. For these reasons, the linear integration stands as a reasonable approximation to compute the flux intercepted by the receiver, particularly for effective sources with a lower size and that can be fairly approximated by a Gaussian distribution.

Keywords: Linear Fresnel collector, Optical analysis, Analytical method.

[†]A. V. Santos, D. Canavarro, P. Horta, and M. Collares-Pereira, "An analytical method for the optical analysis of Linear Fresnel Reflectors with a flat receiver," Solar Energy, vol. 227, pp. 203–216, 2021. https://doi.org/10.1016/j.solener.2021.08.085.

3.1 Introduction

The optical analysis of Linear Fresnel Collectors (LFCs) deals with determining the absorbed flux at the receiver [1]. Consequently, this problem involves computing the optical efficiency as function of the concentrator geometry, considering particular conditions of incidence, sunshape, and optical errors. Ray-tracing is the main method, however, the stochastic nature of these simulations holds inherent fluctuations [2] that coupled to the time-consuming computations [3–6] can lead to convergence problems in optimization studies.

The analytical approach is an alternative to ray-tracing. It is based on computing the fraction of the concentrator aperture effectively used to collect the incoming solar radiation. As described in Section 2.2, the main optical losses in LFCs are well known, and the literature includes a considerable number of models for them [7–12]. These models are significantly faster than ray-tracing since losses are computed through function evaluations. However, they lack generality to accommodate different geometries, incidence angles, sunshape, and optical errors, as it is required for a precise computation of the optical performance.

Zhu [13] presented a vector-based analysis suitable for both curved and flat primary mirrors, but not including end-losses nor receiver shading. Considering parabolic troughs, Bendt et al. [14] convolve sunshape and optical errors functions to define an effective source, and use a linear integration to determine the fraction of flux intercepted by the receiver. However, Bendt's approach considers only a transversal plane analysis, with longitudinal effects being accounted for by modifying the size of the source as function of the incidence angle. Overall, these methods offer a starting point to overcome the problems of previous models.

As usual in LFCs, the receiver includes a secondary optic to enhance the performance of the concentrator, which adds complex optical phenomena difficult to model. On the other hand, the aperture of a secondary can be modeled as a flat receiver, and computing the flux intercepted by such flat target is significantly easier. Indeed, evidence in the literature suggest that the fraction of rays entering the aperture of some types of secondary optic that hits the absorber remains constant as θ_T and θ_L vary [10, 15–17], meaning that the optical efficiency of the secondary optic does not vary with incidence angle.

This chapter then develops an analytical optical method for linear Fresnel collectors with a flat receiver. It uses a bi-axial development of a vector-based analysis and a linear integration of an effective source to determine the optical efficiency as function of the concentrator geometry, incidence direction, sunshape, and optical errors. The method is then validated by confronting its results against the ones from a ray-tracing tool for a set of different conditions, comparing absolute values of efficiency and annual energetic calculations for a set of locations.

3.2 Vector-based analysis

Consider an xyz Local Coordinate System (LCS), whose unit vectors are $\vec{I}_x$, $\vec{I}_y$, and $\vec{I}_z$, as given by Equation A.1. The linear Fresnel geometry is defined by a transversal plane (a zx plane) extruded over the longitudinal direction (the y-axis) a length L.

The vector analysis starts by considering $y = 0$ as the reference plane so that a point $\mathbf{P}$ in such a plane is of the kind $\mathbf{P} = \{p_x, 0, p_z\}$, as depicted in Figure 3.1. In this figure, the incident sunlight is represented by $\vec{S}_T$, whose direction is given by θ_T, the transversal incidence angle; $\vec{S}_T$ is reflected as $\vec{v}_{n,T}$, where $\vec{n}_s$ is the normal to the mirror surface at $\mathbf{P}$.

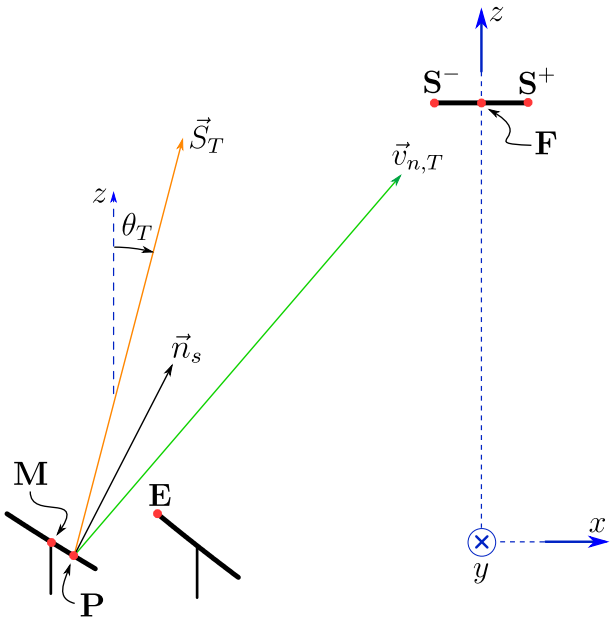

Figure 3.1: Reference transversal plane ($y = 0$). It shows the reflection of an incident ray at a generic point **P** at a mirror surface, so that $\vec{S}_T$ is reflected as $\vec{v}_{n,T}$, where $\vec{n}_s$ is the normal to the mirror surface.

Figure 3.1 also shows other useful geometric elements: $\mathbf{S}^+$ and $\mathbf{S}^-$ stands for the edges of the flat receiver; **M** and **F** represent the mirror center point and the receiver aim point, respectively, used for the tracking procedure detailed in Subsection 2.1.4; **E** stands for the edge-point of the neighboring mirror, essential to shading and blocking computations. In Figure 3.1, the edge-points of neighboring mirrors for shading and blocking are the same but hereafter they are denominated as $\mathbf{E}_{s,T}$ and $\mathbf{E}_{b,T}$, respectively, for the sake of generality.

In general, the sunlight incidence direction, $\vec{S}$, is a function of both transversal and longitudinal incidence angles, θ_T and θ_L, respectively (refer to Equation 2.1). The reflection of $\vec{S}$ at **P** is $\vec{v}_n$, and it is given by:

$$\vec{v}_n = \text{reft}(\vec{S}, \vec{n}_s), \tag{3.1}$$

where reft is a reflection function given by Equation A.5, and $\vec{n}_s$ is the normal to the mirror surface at **P**. For this case, Figure 3.2 illustrates how the incident ray $\vec{S}$ is reflected and that the corresponding reflected ray, $\vec{v}_n$, has a longitudinal component.

Following Zhu's [13] definition[1], the incidence plane, π_i, has a normal vector, $\vec{n}_i$, given by:

$$\vec{n}_i = \frac{\vec{S} \times \vec{I}_x}{|\vec{S} \times \vec{I}_x|}, \tag{3.2}$$

where $\vec{I}_x$ is the unit vector representing the x-axis of the coordinate system attached to the concentrator aperture, as defined in Equation A.1. Then, the reflection plane, here represented by π_r, has a normal vector, $\vec{n}_r$, that is given by:

$$\vec{n}_r = \text{reft}(\vec{n}_i, \vec{n}_s). \tag{3.3}$$

As Figure 3.2 shows, the reflection plane intercepts the receiver at points $\mathbf{T}^+$ and $\mathbf{T}^-$ and

[1] Feldhoff [18] considers the longitudinal axis to construct the incidence plane.

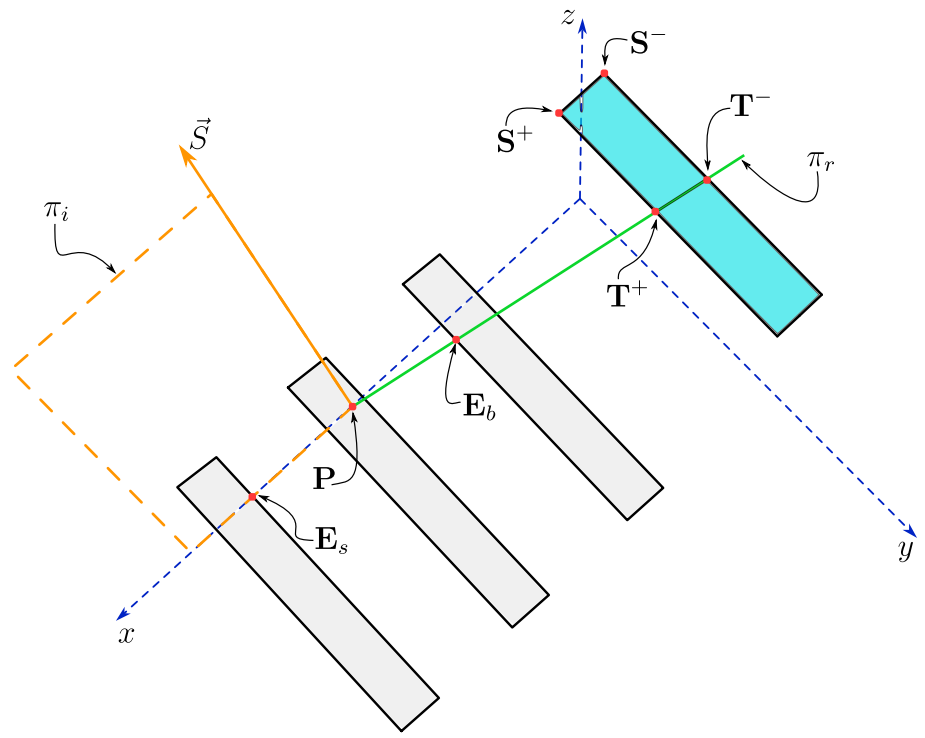

Figure 3.2: Top view of a general incidence analysis. It shows the incidence and reflection planes, π_i and π_r, respectively, and the interception of these planes in the receiver and neighboring mirrors.

defines the limiting vectors $\vec{v}_l^+$ and $\vec{v}_l^-$, respectively, as:

$$\begin{aligned} \mathbf{T}^+ &= \text{islp}(\mathbf{S}^+, \vec{I}_y, \mathbf{P}, \vec{n}_r) \rightarrow \vec{v}_l^+ = \mathbf{T}^+ - \mathbf{P}, \\ \mathbf{T}^- &= \text{islp}(\mathbf{S}^-, \vec{I}_y, \mathbf{P}, \vec{n}_r) \rightarrow \vec{v}_l^- = \mathbf{T}^- - \mathbf{P}, \end{aligned} \tag{3.4}$$

where islp is a function that computes the interception between a straight line and a plane, as defined in Equation A.6. The limiting vectors are used to compute the amount of flux reflected by the primary mirrors that is actually intercepted by the receiver.

Regarding the shading and blocking from the neighboring mirrors, edge-points $\mathbf{E}_s$ and $\mathbf{E}_b$ are the interception of incidence and reflection planes with the neighboring mirrors. They define the neighbor shading and blocking vectors, $\vec{v}_{ms}$ and $\vec{v}_{mb}$, respectively, as given by Equation 3.5.

$$\begin{aligned} \mathbf{E}_s &= \text{islp}(\mathbf{E}_{s,T}, \vec{I}_y, \mathbf{P}, \vec{n}_i) \rightarrow \vec{v}_{ms} = \mathbf{E}_s - \mathbf{P} \\ \mathbf{E}_b &= \text{islp}(\mathbf{E}_{b,T}, \vec{I}_y, \mathbf{P}, \vec{n}_r) \rightarrow \vec{v}_{mb} = \mathbf{E}_b - \mathbf{P} \end{aligned} \tag{3.5}$$

Lastly, the receiver can also cast a shade on the primary field. For this computation, the receiver shading vectors, $\vec{v}_{rs}^+$ and $\vec{v}_{rs}^-$, are calculated as shown in Equation 3.6, based on the receiver edge-points $\mathbf{S}^+$ and $\mathbf{S}^-$, respectively, and the incidence plane π_i.

$$\begin{aligned} \mathbf{R}^+ &= \text{islp}(\mathbf{S}^+, \vec{I}_y, \mathbf{P}, \vec{n}_i) \rightarrow \vec{v}_{rs}^+ = \mathbf{R}^+ - \mathbf{P} \\ \mathbf{R}^- &= \text{islp}(\mathbf{S}^-, \vec{I}_y, \mathbf{P}, \vec{n}_i) \rightarrow \vec{v}_{rs}^- = \mathbf{R}^- - \mathbf{P} \end{aligned} \tag{3.6}$$

In conclusion, the vector analysis presented in this section aims to define the limiting vectors, $\vec{v}_l^+$ and $\vec{v}_l^-$, the neighboring vectors, $\vec{v}_{ms}$ and $\vec{v}_{mb}$, and the receiver shading vectors, $\vec{v}_{rs}^+$ and $\vec{v}_{rs}^-$. Their computations are based on the definition of the geometric elements in the

reference transversal plane, and a general incidence direction function of both transversal and longitudinal incidence angles, θ_T and θ_L, respectively.

3.3 Beam flux analysis and local intercept factor

Direct normal solar irradiance is distributed over the radial distance from its incidence direction – the sunshape profile. Furthermore, the concentrator is imperfect: reflection, tracking, and contour of real elements cause further angular deviations from what is ideally expected – the optical errors. Finally, sunshape and optical errors are convoluted to produce an effective source: a broadened profile that represents all deviations [1]. Thus, sunlight can be modeled as a beam instead of a ray. The beam is defined by a main direction and an angular profile that rules the flux distribution on a plane perpendicular to such direction. All these concepts are detailed in Section B.2, Appendix B.

Therefore, for a generic point **P** in a mirror surface the incident beam is defined by $\vec{S}$, and the plane perpendicular to it is called sun plane. The reflected beam is defined by $\vec{v}_n$, which defines the image plane. Figure 3.3 shows how the vectors defined in the previous section lie regarding $\vec{S}$ and $\vec{v}_n$ in the incidence and reflection planes, respectively. The angles defined in this figure are important to quantify the amount of flux within a particular interval. For example, the angular interval between $\left[\theta_l^+, \theta_l^-\right]$ rules the amount of the reflected beam that is intercepted by the receiver – see Figure 3.3b –, a value that is defined by the probability of ray within the incident beam after reflection has its direction between the angular range defined by point **P** acceptance angles, θ_l^+ and θ_l^-.

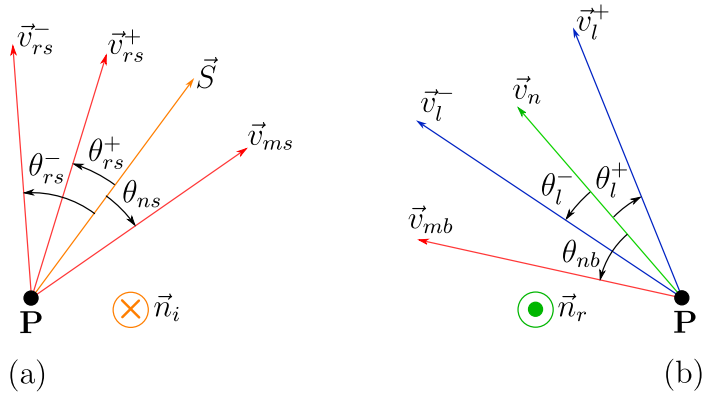

Figure 3.3: Incidence (a) and reflection (b) plane views. The angles in this figure are calculated based on the angpn function defined in Equation A.7. For example, $\theta_{ns} = \text{angpn}(\vec{S}, \vec{v}_{ms}, \vec{n}_i)$ and $\theta_l^- = \text{angpn}(\vec{v}_n, \vec{v}_l^-, \vec{n}_r)$, where $\vec{n}_i$ points into the paper sheet and $\vec{n}_r$ points out of the paper sheet.

Due to the linear symmetry of the concentrator, one can use the linear integration presented by Bendt et al. [14], detailed in Subsection B.2.5, to calculate the fraction of the flux that lies between an angular interval such as $\left[\theta_l^+, \theta_l^-\right]$. For this matter, the definition if an angle is positive or negative concerning the beam main direction is a key issue. Thus, angles in Figure 3.3 must be calculated as exemplified bellow:

$$\begin{aligned} \theta_l^+ &= \text{angpn}(\vec{v}_n, \vec{v}_l^+, \vec{n}_r), \\ \theta_l^- &= \text{angpn}(\vec{v}_n, \vec{v}_l^-, \vec{n}_r), \end{aligned} \tag{3.7}$$

where $\text{angpn}(\vec{u}, \vec{v}, \vec{n})$ is a function that calculates the angle between vectors $\vec{u}$ and $\vec{v}$, in the range $[-\pi, \pi]$, considering if $\vec{v}$ is on a positive (counter-clockwise) or negative (clockwise)

rotation around $\vec{n}$ with respect to $\vec{u}$, for $\vec{u}$ and $\vec{v}$ defined in a plane given by a normal vector $\vec{n}$, as shown in Equation A.7. Therefore, the angular interval corresponding to receiver shading is $[\theta_{rs}^{+}, \theta_{rs}^{-}]$, and for neighbor shading and blocking are $[\theta_{ns}, \pi]$ and $[\theta_{nb}, \pi]$, respectively. Of course, these intervals might intersect and, more importantly, overlap the one corresponding to the receiver flux: $\left[\theta_{l}^{+}, \theta_{l}^{-}\right]$. Then, the proper arithmetic of intervals should be done to ensure a due accounting of the optical losses, following the preference order: receiver shading, neighbor shading, and neighbor blocking – a shaded flux cannot be reflected as a blocked flux cannot be intercepted by the receiver.

The surface point **P** can be interpreted as the center of an elementary segment of area of a mirror, which reflects sunlight towards the receiver. Furthermore, due to cosine effect only a fraction of this surface is effectively used, as ruled by the incidence angle θ_i given by Equation 3.8.

$$\theta_i = \text{ang}(\vec{S}, \vec{n}_s) \tag{3.8}$$

Then, considering B as the linear cumulative density function of the effective source (refer to Subsection B.2.5) so that $\int_{-\infty}^{\infty} B(\theta)\mathrm{d}\theta = 1$, the fraction of the incident beam intercepted by the receiver is defined as the local intercept factor, γ_p, is given by Equation 3.9.

$$\gamma_p = \cos\theta_i \int_{\theta_l^{+}}^{\theta_l^{-}} B(\theta)\mathrm{d}\theta \tag{3.9}$$

In this sense, this modeling assumes that θ_l^{+} and θ_l^{-} do not vary along the small surface segment represented by **P**.

3.4 From local to concentrator efficiency

γ_p represents the fraction flux incident at an elementary segment of the mirror surface that is actually intercepted by the receiver. Indeed, one can integrate this local factor and yield an averaged one for the whole mirror, as presented in Equation 3.10:

$$\gamma_m = \frac{\int_S \gamma_p(x, y)\,\mathrm{d}x\,\mathrm{d}y}{w \cdot L}, \tag{3.10}$$

where S stands for an integration over the mirror surface, x and y represent the coordinates of **P** on the mirror surface, whilst the z-coordinate of **P** is a function of x defined by z_s, the shape function of the mirror.

Equation 3.10 is a general formulation that considers γ_p varying in both transversal and longitudinal axes of the mirror. However, a reasonable simplification is to consider that this local factor does not vary in the longitudinal axis so that $\gamma_p(x, y) = \gamma_p(x)$. Then, the integration is now over longitudinal stripes, as illustrated (in blue) in Figure 3.4.

Moreover, Figure 3.4a also illustrate another important issue: the case where a fraction of the mirror length is not subject to shading from the neighboring mirror due to the longitudinal component of the incident sunlight. Of course, the same phenomenon occur for the shading from the receiver, so that a fraction of the length is not subjected to this optical loss.

In this sense, the longitudinal strip representing **P** can be divided into three sections, as in Figure 3.4b. One has the length l_{rs} and refers to the fraction not shaded by the receiver, so that:

$$l_{rs} = \frac{|\vec{I}_y \cdot \vec{v}_{rs}^{+} + \vec{I}_y \cdot \vec{v}_{rs}^{-}|}{2L}, \tag{3.11}$$

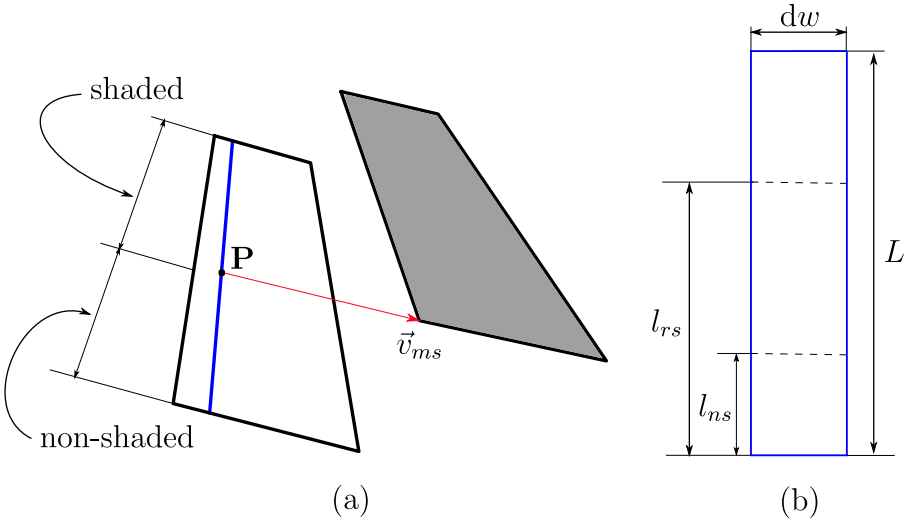

Figure 3.4: Integration of the local intercept factor as longitudinal stripes along **P**. It also shows (a) the longitudinal effect on the neighbor shading and (b) the non-shaded segments that represent fractions of the total length of the primary mirror. Thus, l_{rs} and l_{ns} represent the fraction of the total length, L, that are not subjected to receiver and neighboring shading, respectively.

where $\vec{v}_{rs}^{+}$ and $\vec{v}_{rs}^{-}$ are the receiver shading vectors, and L stands for the total length of the primary mirror. A second longitudinal section is defined by l_{ns} in Figure 3.4b, and refers to the fraction not shaded by the neighboring mirror, so that:

$$l_{ns} = \frac{|\vec{I}_y \cdot \vec{v}_{ms}|}{L}, \tag{3.12}$$

where $\vec{v}_{ms}$ is the neighbor shading vector. Then, the remaining fraction of the length is then subjected to both receiver and neighboring shading.

Furthermore, the fact that mirrors have a finite length implies that some flux is lost because it would require a longer receiver to collect it, defining end-losses. Then, the fraction of the length characterizing end-losses, l_e, is determined by the limiting vectors, $\vec{v}_l^{-}$ and $\vec{v}_l^{+}$, as given by Equation 3.13. Of course, end-losses only occur when there is some energy to be collected.

$$l_e = \frac{|\vec{I}_y \cdot \vec{v}_l^{+} + \vec{I}_y \cdot \vec{v}_l^{-}|}{2L} \tag{3.13}$$

The primary field is composed of a finite number of primary mirrors, as represented by n. Then, one can, finally, average the mirror intercept factor, γ_m, to yield a value for whole linear Fresnel collector, as given by Equation 3.14, where w stands for the mirror width, and k is an index to range in the whole primary field.

$$\gamma = \frac{\sum_{k=1}^{n} \gamma_m^k \cdot w^k}{\sum_{k=1}^{n} w^k} \tag{3.14}$$

Moreover, a fraction of the incident flux is lost due to the properties of the surfaces and materials. Then, the optical efficiency, η, is given by:

$$\eta = \rho\alpha\gamma, \tag{3.15}$$

where ρ represents the reflectivity of the primary mirrors, and α is the absorber absorptivity. For this case of a flat receiver, sunlight only interacts with each surface (primaries and receiver) once. For convenience, in this chapter all computations consider both equals to 1.

3.5 Validation approach

3.5.1 Overview

The proposed analytical method is a simpler and faster approach mainly based on function evaluations. Nevertheless, the presented models should be validated to evaluate how they can approximate the results of ray-tracing simulations (numerical experiments). For this matter, the analytical method is implemented in a Python code based on Numpy [19] and Numba [20] libraries. The first is used to represent point and vectors as arrays and to perform vector calculations, whilst the second provides a just-in-time compilation that speed-up the code. Ray-tracing simulations are carried out in SolTrace [21], a validated open-source tool widely used for the analysis of solar concentrating systems.

The validation of the analytical method is based on the comparison of its results against the ones from SolTrace, both considering the same optical system. In this sense, an optical system is defined by a concentrator geometry, a sunshape profile, and optical errors settings.

3.5.2 Optical systems

For the analysis presented in this chapter, the linear Fresnel geometries are based on the model shown in Figure 2.3 and uses the same nomenclature. That is, n denotes the number of primary mirrors, w is the mirror width, and s stands for the shift between neighboring mirrors. Here, primary fields have a uniform configurations regarding w and s, comprising different designs in order to verify the method capabilities of reproducing ray-tracing results under distinct geometrical scenarios. These geometries are defined in in Table 3.1, where R stands for the curvature radius design of the primary mirrors, where cylindrical and flat mirrors are considered in uniform and non-uniform configurations. In this case, θ_d represents the design position of Rabl's design [1] (refer to Section 4.2.2).

Table 3.1: Evaluated Linear Fresnel Collector (LFC) geometries. These are base cases that consider with a length, L, of 30.0 m.

Geometry	n [-]	w [m]	s [m]	R	H_R [m]	W_s [m]
LFC 1	16	0.75	1.054	$\theta_d = 0°$	7.20	0.34
LFC 2	11	0.25	0.275	Flat	3.13	0.60

The flat receiver is positioned an height H_R above the primary field, and has a width given by W_s. As mentioned before, such a flat target is interpreted as the aperture of a secondary optic. Therefore, $H = H_R$ and the tracking point $\mathbf{F}$ is then the receiver mid-point (refer to Figures 2.3 and 2.4).

The convolution of a sunshape and optical errors constitute an Effective Source (ES), as described in Subsection B.2.4. The validation procedure in this chapter considers different sources, as depicted in Table 3.2. The purpose is to show for which conditions the analytical

method fairly reproduces ray-tracing results and for which it does not, particularly since the linear integration is just an approximation of the intercepted flux.

Table 3.2: Effective sources considered in the optical evaluation.

Source	Sunshape	Optical errors	δ_{es}
ES1	None	None	0.0 mrad
ES2	$\Delta_{sun} = 4.65$ mrad	None	3.29 mrad
ES3	$\Delta_{sun} = 4.65$ mrad	$\sigma_o = 5.0$ mrad	7.80 mrad
ES4	$\sigma_{sun} = 2.80$ mrad	$\sigma_o = 5.0$ mrad	8.10 mrad
ES5	CSR = 0.025	$\sigma_o = 5.0$ mrad	8.14 mrad

In Table 3.2, Δ_{sun} stands for the half-width of a pillbox sunshape, σ_{sun} is the standard deviation of a Gaussian profile, and CSR represents the circumsolar ratio of a Buie [22] sunshape. Optical errors are modeled with a Gaussian distribution whose standard deviation is σ_o. Moreover, ES1 refers to a collimated sunlight model, here represented by a Gaussian distribution of very low standard deviation ($\ll 1.0$ mrad).

3.5.3 Evaluation metrics

Here, the main comparison metric is given by the optical efficiency, so that the any deviation is measured as $\Delta\eta$, so that:

$$\Delta\eta = \eta^{an} - \eta^{rt}, \tag{3.16}$$

where the superscripts an and rt stands for results from the analytical method and ray-tracing simulations, respectively. Thus, η^{an} is then given by Equation 3.15, whilst the efficiency calculated from SolTrace simulations, η^{rt}, is defined by Equation 3.17,

$$\eta^{rt} = \frac{p_{ray} \cdot N_{rays}}{I_b \sum_{k=1}^{n} w^k \cdot L}, \tag{3.17}$$

where N_{rays} and p_{ray} are number of absorbed rays and the power carried by each ray, respectively, outputs from the simulations, and $I_b = 1.0\,\mathrm{kW/m^2}$.

Of course, η has a directional nature, as it changes with the incidence direction given by θ_T and θ_L. Therefore, it is reasonable to assume that $\Delta\eta$ also varies with θ_T and θ_L. To encompass symmetric and non-symmetric primary fields regarding the aim-point $\mathbf{F}$, $\theta_T \in [-90°, +90°]$, $\theta_L \in [0, +90°]$, and these domains are discretized in steps of 5°. Moreover, the analysis presented in this chapter considers that if $|\theta_T| = 90°$ or $|\theta_L| = 90°$, $\eta = 0$.

As defined by Equation 3.16, $\Delta\eta$ can assume positive and negative values. Then, one can use the Root Mean Square Error (RMSE), δ_η, as a metric for the overall deviation between analytical and ray-tracing results for a particular optical system. Considering the incidence domain divided into N points, δ_η is then defined as shown in Equation 3.18.

$$\delta_\eta = \sqrt{\frac{1}{N} \sum_{j=1}^{N} \left(\eta_j^{an} - \eta_j^{rt}\right)^2} \tag{3.18}$$

δ_η is then an averaged value that considers different incidence directions with the same weight. It well-known on the other hand that lower incidences are associated with lower

values of irradiance, which have smaller contributions for the overall collected energy. In this sense, averaged annual efficiency, $\bar{\eta}$, can be defined as shown in Equation 3.19:

$$\bar{\eta} = \frac{\sum_{h=1}^{8760} \eta(\theta_T^h, \theta_L^h) I_b^h}{\sum_{h=1}^{8760} I_b^h}, \tag{3.19}$$

where h is an index to range for each 8760 hours of the year. Then, one can also evaluate the difference between analytical and ray-tracing results by the relative variation of annual efficiency, $\Delta\bar{\eta}$, as defined by Equation 3.20.

$$\Delta\bar{\eta} = \frac{\bar{\eta}^{an} - \bar{\eta}^{rt}}{\bar{\eta}^{rt}} \tag{3.20}$$

For the purpose of computations involving $\Delta\bar{\eta}$, the locations shown in Table 3.3 where considered. Data of solar position were calculated based on the algorithm proposed by Reda and Andreas [23], and converted to θ_T and θ_L as defined in Section B.1. Moreover, typical meteorological year data regarding beam irradiance was taken from the PVGIS application program interface of the pvlib library [24].

Table 3.3: Main data of the analyzed locations for energetic calculations.

Location	Latitude	Longitude
Lodwar (Kenya)	3.12°	35.60°
Denbel (Ethiopia)	9.85°	42.78°
Najran (Saudi Arabia)	17.57°	44.23°
Aswan (Egypt)	24.1°	32.9°
Quarzazate (Morocco)	31.01°	-6.86°
Evora (Portugal)	38.5°	-8.0°

3.5.4 Convergence analysis

The mathematical model presented in Section 3.4 is based on integrating the local intercept factor over a continuous domain. However, a simpler approach is to discretize it, dividing the mirror width into a finite number of points, making it more suitable for numerical evaluation and implementation. Then, Equation 3.10 becomes a discrete summation instead of a continuous one, so that:

$$\gamma_m = \frac{1}{N_p} \sum_{j=1}^{N_p} \gamma_p, \tag{3.21}$$

where N_p is the number of surface points which have the same projected aperture. Thus, a first convergence analysis aims to determine a value of N_p that does not affect η^{an}.

Results of η^{an} as function of N_p are shown in Figure 3.5 for two pairs of incidence angles as given by $\{\theta_T, \theta_L\}$: (a) {0°,0°} and (b) {85°,85°}, considering geometry LFC 1 and source ES3, for $11 \leq N_p \leq 701$. As can be seen, results are not strongly dependent on N_p, and rapidly converge so that for $N_p \geq 300$, analytical results are in a quite steady region. Therefore, a density of 400 points per meter of mirror width (300/0.75 m) is hereafter used for all analytical computations.

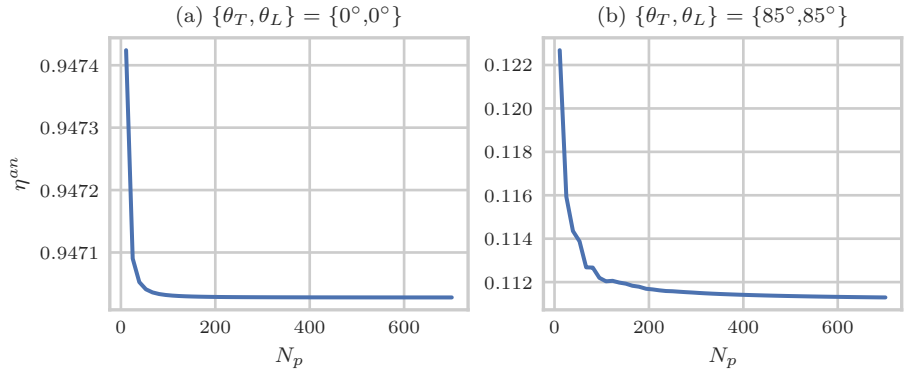

Figure 3.5: Convergence analysis of the domain discretization for the analytical method computations. It shows how the analytical results of otpical efficiency vary in terms of the number of discrete points to discretize the mirror width, for two incidence directions: (a) {0°,0°} and (b) {85°,85°}, considering geometry LFC 1 and source ES3.

Ray-tracing is based on a stochastic process that simulates the interaction of rays with surface and materials, so that the accuracy of results depends on the number of simulated rays. Instead of rays, SolTrace does work with a desired number of ray intersections with the geometrical elements of the optical system. Thus, the ray-tracing convergence analysis aims to determine the number of ray intersections to be traced so that results are within a reasonable narrow interval.

Figure 3.6 present results of the convergence analysis of traced rays for two pairs of incidence angles given by $\{\theta_T, \theta_L\}$: (a) {0°, 0°} and (b) {85°,85°}, considering geometry LFC 1 and source ES3. It shows violin plots of the distribution of values of η^{rt} obtained from 100 simulations for different quantities of ray intersections – the width of the violin plots indicates the density of data points, with wider sections showing more frequent occurrences of those values, the horizontal bars in the middle represent the mean of the values for each set of ray intersections, and vertical lines that represent the distance between maximum and minimum values.

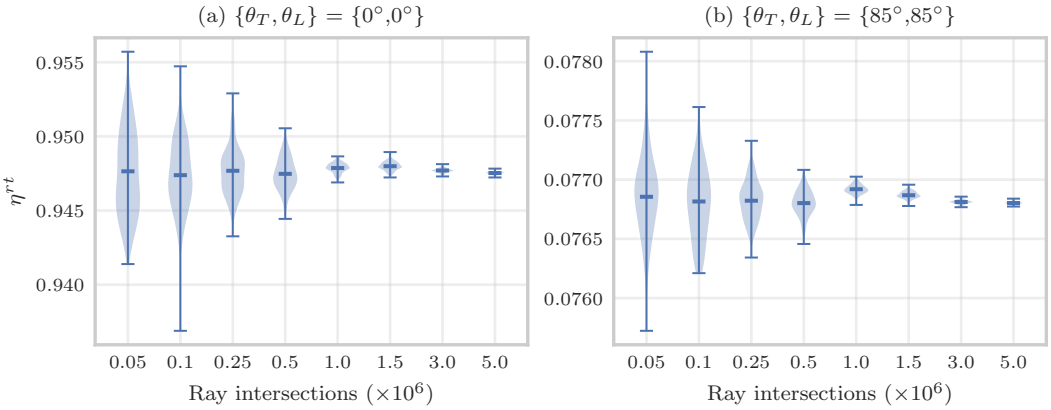

Figure 3.6: Convergence analysis of traced rays. It shows how the ray-tracing results of optical efficiency vary in terms of the number of ray intersections in SolTrace for two incidence directions: (a) {0°,0°} and (b) {85°,85°}, considering geometry LFC 1 and source ES3. A total of 100 simulations were carried out for each value of desired intersections, considering pseudo random computation using the current clock time.

As can be seen in Figure 3.6, the spread of the distributions narrows as the number of ray intersections increases, and ray-tracing becomes more stable and less variable with higher

computational effort, particularly for more than 1.0×10^6 ray intersections. Therefore, a density of 2517 ray intersections per square meter of gross aperture area ($1.25 \times 10^6 / 496.8\,\mathrm{m}^2$) is hereafter used in all ray-tracing simulations. Moreover, a minimum of 2.0×10^5 ray intersections is also considered to avoid simulations with few rays, and all simulations concerning the validation have a fixed seed for pseudo random computations to ensure replication.

3.6 Results and discussion

The analytical method validation is based on the comparison of its results to SolTrace simulations under different incidence conditions and optical systems. For this mater, considering a particular optical system, the error, $\Delta\eta$, is then given by the difference between analytical and ray-tracing results of optical efficiency for a particular incidence, as defined in Equation 3.16. Moreover, the Root Mean Square Error (RMSE), δ_η, as defined in Equation 3.18, provides an averaged error value for the whole range of incidences.

In this context, initial validation results presented in Figure 3.7 consider optical systems defined by geometry LFC 1 (refer to Table 3.1) and sources ES1 and ES5 (refer to Table 3.2). It shows $\Delta\eta$ as functions of both θ_T and θ_L. As it is evident from the plots, error values are quite symmetric, as expected from a symmetric geometry such as LFC 1; $\Delta\eta$ can assume positive and negative values, and is generally low across most incidence angles, but peak when both θ_T and θ_L exceed 80°. This trend is more pronounced in Figure 3.7b (LFC 1 and ES5), where the highest $\Delta\eta$ values are observed. In contrast, Figure 3.7a (LFC 1 and ES1) shows a more confined region of higher error values, suggesting that the analytical method is less sensitive to the ES1 source.

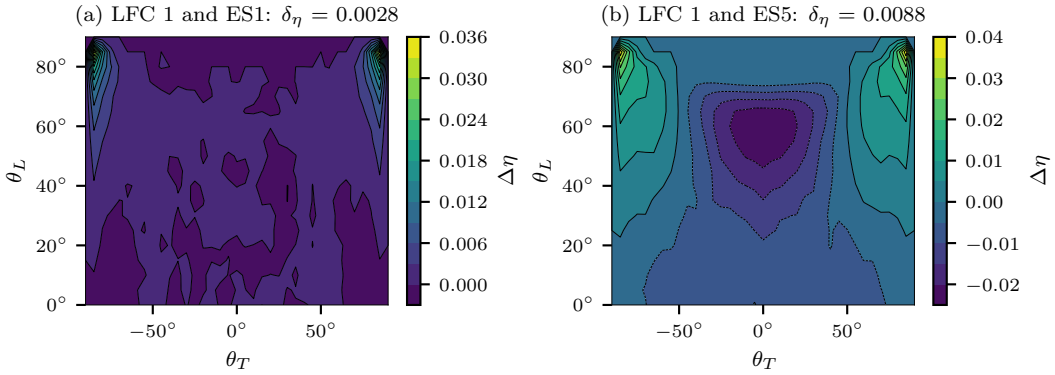

Figure 3.7: Analytical method error for the geometry LFC 1 and Effective Sources (ESs) (a) ES1 and (b) ES5. It shows how $\Delta\eta$ vary as function of both θ_T and θ_L for different source conditions.

Furthermore, results in Figure 3.7 reveal that $\Delta\eta$ increases with the size of the source, as reflected in the comparison of Figures 3.7a and 3.7b, where the broader source results in higher absolute values of $\Delta\eta$, and a higher value of δ_η: 0.0088 for ES5 compared to 0.0028 for ES1. The higher δ_η value for ES5 highlights the greater deviation of the analytical method from the expected results when larger sources are involved.

Indeed, Figure 3.8 shows that δ_η (represented by the blue curve) increases as the source RMS width grows. It also provides a factorized breakdown of transversal efficiency ($\theta_L = 0$), shown by δ_{η_T} (the yellow curve), and longitudinal efficiency ($\theta_T = 0$), represented by δ_{η_L} (the green curve). This factorized result shows that the increase in δ_η is primarily driven by longitudinal effects, as δ_{η_L} exhibits a significantly larger error than δ_{η_T}. Moreover, this

figure suggests that factors beyond source size contribute to a reduction in the accuracy of the analytical method since an increase in δ_η is observed between ES4 and ES5 despite a minimal increase in source size (refer to Table 3.2).

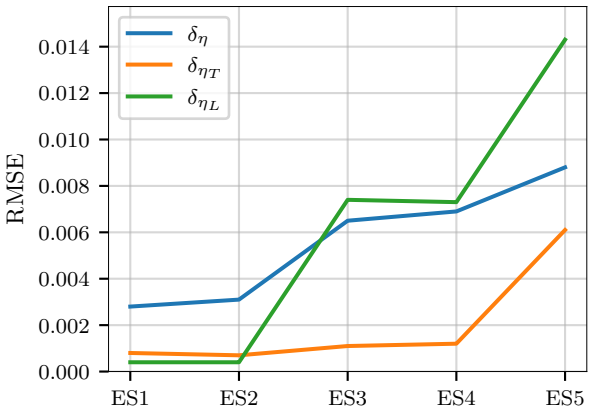

Figure 3.8: Root Mean Square Error (RMSE) of the analytical method by Effective Source (ES) for the geometry LFC 1. It shows how the RMSE values for differences ESs, considering a bi-axial, represented by δ_η, and a factorized approach, as given by transversal and longitudinal efficiencies, δ_{η_T} and δ_{η_L}, respectively.

As described in Section 3.3, the calculation of the local intercept factor, γ_p, is done by a linear integration of the effective source distribution. Of course, this approach is an approximation and has limitations. The first issue is in the spot produced in the receiver. The extension of the solar aureole in the image plane is fairly defined by a circle, which supports the radially symmetric distribution assumption. Since the direction of the reflected solar beam is not always perpendicular to the receiver plane, the projection of the solar aureole onto the receiver is not a circle but an ellipse, as illustrated in Figure 3.9, and the radial symmetry assumption fails – for example, the Gaussian optical error should be better described by an elliptical distribution instead of a circular one [25, 26].

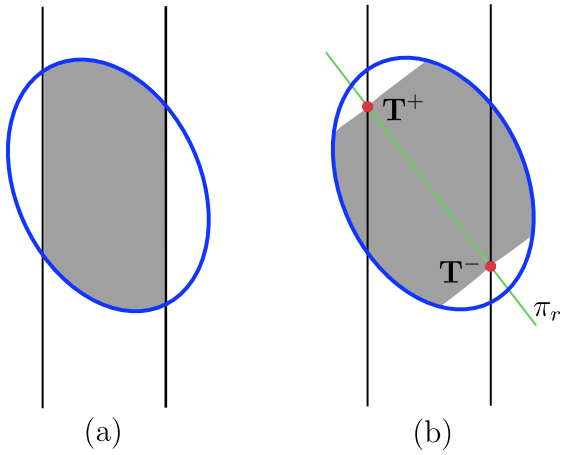

Figure 3.9: The flux intercepted by the receiver in the local intercept factor calculation. The linear integration of the effective source approximates the actual intercepted flux and introduces an error. The projection of the image plane onto the receiver is not a circle but an ellipse, and (a) the actual intercepted flux is only approximated (b) the linear integration of the effective source probability density function (the proportions are not real, and are intentionally oversized for clarity).

For these reasons, the linear integration, Figure 3.9b, only approximates the actual intercepted flux, Figure 3.9a. Of course, this approximation fails as incidence angles gets

higher, particularly the longitudinal one, as shown in Figure 3.7, thus reducing the analytical method accuracy to reproduce ray-tracing results. Moreover, the procedure described in Section 3.3 considers a Gaussian approximation for the linear cumulative density function (refer to Subsection B.2.5), since the convolution of a Buie sunshape with Gaussian errors yields an effective source whose probability density function is not easily described by an analytical function, implying that the method's accuracy decreases as the complexity of the source distribution increases.

As a matter of comparison, the ray-tracing code developed by Cardona and Pujol-Nadal [27] was validated against Tonatiuh [28], considering a Buie's sunshape model with a circumsolar ratio of 0.05. Their results presented an RMSE of 0.0020 and 0.0013 for transversal and longitudinal efficiencies, δ_{η_T} and δ_{η_L}, respectively, although the authors have not considered incidences for which θ_T or θ_L are greater than 80°. These values are considerable lower than the ones presented in Figure 3.8 for the corresponding Effective Source (ES).

The previous results show that higher deviations, as given by $\Delta\eta$, occur at high incidence angles. These angles are associated with lower irradiance values, meaning that the corresponding energy is, for any practical purpose, very small. As a results, the error in energy collection calculations based on the analytical method is effectively diluted. To assess this matter, annual averaged efficiency calculations were done considering both factorized and bi-axial models, as defined in Equation 3.19. Figure 3.10 shows these results, as given by Equation 3.20, for geometry LFC 1 and source ES5, considering North-South (NS) and East-West (EW) mountings for locations presented in Table 3.3.

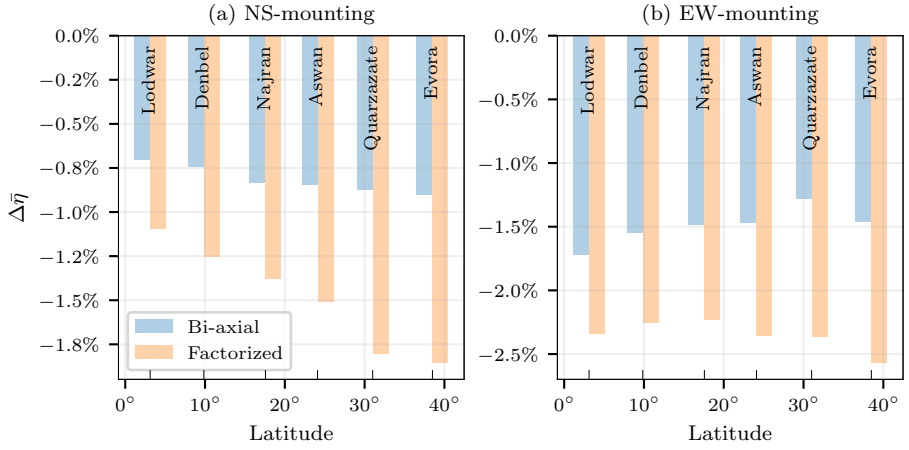

Figure 3.10: Analytical method error on the annual averaged efficiency, as given by Equation 3.20. It considers geometry LFC 1 and the effective source ES5 for a wide range of latitude, as given by the different locations.

Figure 3.10 shows that values of $\Delta\bar{\eta}$ increase with the location latitude. This is caused by more longitudinal effects related to high incidence angles that are more frequent in high latitude locations. It also shows that the factorized model shows higher differences between analytical and ray-tracing calculations, as expected from the data in Figure 3.8 since the factorized error is significantly higher than the bi-axial due to the longitudinal contributions (see Figure 3.8). Moreover, for this case of LFC 1 and ES5, the analytical method underestimate the averaged annual efficiency for all analyzed locations for both NS and EW orientations. On the other hand, errors for the factorized method are mostly below -2.5%, while bi-axial calculations present errors below -1.7%, as shown in Figure 3.10b.

Considering a different linear Fresnel geometry, the LFC 2 in Table 3.1, Figure 3.11 shows the results of $\Delta\bar{\eta}$ for locations presented in Table 3.3, considering the source ES5. As can

be seen, annual energy computation errors are now lower than 0.65% – indeed, very low values. These results indicate that for lower values of mirror width and receiver height (the concentrator length is the same) errors are quite reduced. For this geometry, the factorized approach yields a lower error than the bi-axial model, in contrast to the data in Figure 3.10.

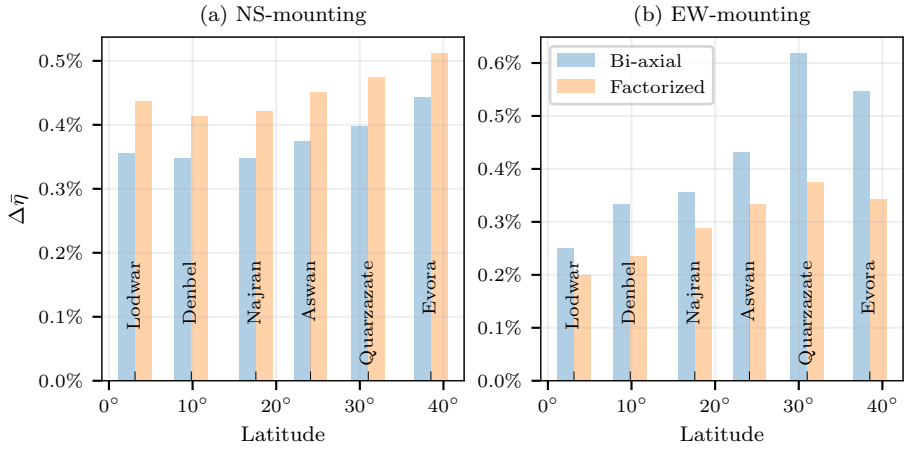

Figure 3.11: Analytical method error on the annual averaged efficiency, as given by Equation 3.20. It considers geometry LFC 2 and the effective source ES5 for a wide range of latitude, as given by the different locations.

Concerning the computational time, the bi-axial optical analysis evaluates the concentrator efficiency for 703 different incidences and takes approximately 25 seconds for the analytical method, while ray-tracing simulations takes 4.1 hours – the Numba module [20] provides a just-in-time compilation that improves the code speed and yields a quite fast computation.

3.7 Conclusions

This chapter presents an analytical optical method for the efficiency computation of linear Fresnel collectors with a flat receiver. The developed method has a bi-axial development based on a vector analysis using a linear integration of the effective source probability density function. Its results were compared to ray-tracing simulations performed in SolTrace. Overall, the Root Mean Square Error, δ_η, and the error in the annual averaged efficiency, $\Delta\bar{\eta}$, were the two main comparison parameters through bi-axial and factorized approaches.

The ensuing results indicate that analytical and ray-tracing do agree very well. Generally, higher values of δ_η were observed for $\theta_L \geq 80°$, and increasing with the Root Mean Square (RMS) width and complexity (convolution of different distributions) of the effective source. Considering the analyzed optical systems, the maximum value of δ_η observed for the bi-axial model was 0.0088, while for transversal and longitudinal (factorized) models were 0.0061 and 0.0143, respectively. These values are considerably higher than those found by Cardona and Pujol-Nadal [27] for the validation of their ray-tracing tool, although they did not included angles higher than 80°, which are considered in the analysis presented in this chapter. On the other hand, despite worst cases of δ_η can be relatively high, maximum values of $\Delta\bar{\eta}$ were lower than 2.6% since high incidence angles are usually associated with low values of irradiance, reducing the impact on the energetic computations on a yearly basis.

For this matter, the linear integration stands as a reasonable approximation to compute the flux intercepted by the receiver, particularly for effective sources with a lower size and that can be fairly approximated by a Gaussian distribution – findings that highlight the

importance of source characteristics in the error analysis of optical systems and suggest that additional considerations may be required for optical systems utilizing larger or more complex sources.

Finally, the considerable faster computation of the analytical method compared to the time-consuming ray-tracing simulations carried out in SolTrace allows it to be used in optimization routines of further studies related to the design of linear Fresnel collectors.

References

[1] A. Rabl, *Active Solar Collectors and Their Applications*. New York: Oxford University Press, 1985. [Online]. Available: https://shorturl.at/oGLX6.

[2] P. Boito and R. Grena, "Optimization of the geometry of Fresnel linear collectors," *Solar Energy*, vol. 135, pp. 479–486, 2016. DOI: 10.1016/j.solener.2016.05.060.

[3] R. Abbas, M. Valdés, M. Montes, and J. Martínez-Val, "Design of an innovative linear Fresnel collector by means of optical performance optimization: A comparison with parabolic trough collectors for different latitudes," *Solar Energy*, vol. 153, pp. 459–470, 2017. DOI: 10.1016/j.solener.2017.05.047.

[4] H. Ajdad, Y. Filali Baba, A. Al Mers, O. Merroun, A. Bouatem, and N. Boutammachte, "Particle swarm optimization algorithm for optical-geometric optimization of linear fresnel solar concentrators," *Renewable Energy*, vol. 130, pp. 992–1001, 2019. DOI: 10.1016/j.renene.2018.07.001.

[5] Z. D. Cheng, X. R. Zhao, Y. L. He, and Y. Qiu, "A novel optical optimization model for linear Fresnel reflector concentrators," *Renewable Energy*, vol. 129, pp. 486–499, 2018. DOI: 10.1016/j.renene.2018.06.019.

[6] J. Men, X. Zhao, Z. Cheng, Y. Leng, and Y. He, "Study on the annual optical comprehensive performance of linear Fresnel reflector concentrators with an effective multi-objective optimization model," *Solar Energy*, vol. 225, pp. 591–607, 2021. DOI: 10.1016/j.solener.2021.07.051.

[7] R. Abbas, M. J. Montes, M. Piera, and J. M. Martínez-Val, "Solar radiation concentration features in Linear Fresnel Reflector arrays," *Energy Conversion and Management*, vol. 54, no. 1, pp. 133–144, 2012. DOI: 10.1016/j.enconman.2011.10.010.

[8] A. Heimsath, G. Bern, D. van Rooyen, and P. Nitz, "Quantifying Optical Loss Factors of Small Linear Concentrating Collectors for Process Heat Application," *Energy Procedia*, vol. 48, pp. 77–86, 2014. DOI: 10.1016/j.egypro.2014.02.010.

[9] M. Hongn, S. F. Larsen, M. Gea, and M. Altamirano, "Least square based method for the estimation of the optical end loss of linear Fresnel concentrators," *Solar Energy*, vol. 111, pp. 264–276, 2015. DOI: 10.1016/j.solener.2014.10.042.

[10] V. Sharma, J. K. Nayak, and S. B. Kedare, "Effects of shading and blocking in linear Fresnel reflector field," *Solar Energy*, vol. 113, pp. 114–138, 2015. DOI: 10.1016/j.solener.2014.12.026.

[11] E. Bellos and C. Tzivanidis, "Development of analytical expressions for the incident angle modifiers of a linear Fresnel reflector," *Solar Energy*, vol. 173, pp. 769–779, 2018. DOI: 10.1016/j.solener.2018.08.019.

[12] M. Yang, Y. Zhu, and R. A. Taylor, "End losses minimization of linear Fresnel reflectors with a simple, two-axis mechanical tracking system," *Energy Conversion and Management*, vol. 161, pp. 284–293, 2018. DOI: 10.1016/j.enconman.2018.01.082.

[13] G. Zhu, "Development of an analytical optical method for linear Fresnel collectors," *Solar Energy*, vol. 94, pp. 240–252, 2013. DOI: 10.1016/j.solener.2013.05.003.

[14] P. Bendt, A. Rabl, H. W. Gaul, and K. A. Reed, "Optical analysis and optimization of line focus solar collectors," National Renewable Energy Laboratory (NREL), Golden, CO (United States), Tech. Rep., 1979, p. 75. DOI: 10.2172/5746400.

[15] G. Zhu, "New adaptive method to optimize the secondary reflector of linear Fresnel collectors," *Solar Energy*, vol. 144, pp. 117–126, 2017. DOI: 10.1016/j.solener.2017.01.005.

[16] M. Hack, G. Zhu, and T. Wendelin, "Evaluation and comparison of an adaptive method technique for improved performance of linear Fresnel secondary designs," *Applied Energy*, vol. 208, pp. 1441–1451, 2017. DOI: 10.1016/j.apenergy.2017.09.009.

[17] A. Vouros, E. Mathioulakis, E. Papanicolaou, and V. Belessiotis, "On the optimal shape of secondary reflectors for linear Fresnel collectors," *Renewable Energy*, vol. 143, pp. 1454–1464, 2019. DOI: 10.1016/j.renene.2019.05.044.

[18] J. F. Feldhoff, "Linear Fresnel Collectors: A Technology Overview," in *SFERA Summer School*, Almeria, 2012, pp. 1–30. [Online]. Available: http://www.redrok.com/Fabian_Feldhoff_Linear_Fresnel.pdf.

[19] C. R. Harris, K. J. Millman, S. J. van der Walt, R. Gommers, P. Virtanen, D. Cournapeau, E. Wieser, J. Taylor, S. Berg, N. J. Smith, R. Kern, M. Picus, S. Hoyer, M. H. van Kerkwijk, M. Brett, A. Haldane, J. F. del Río, M. Wiebe, P. Peterson, P. Gérard-Marchant, K. Sheppard, T. Reddy, W. Weckesser, H. Abbasi, C. Gohlke, and T. E. Oliphant, "Array programming with NumPy," *Nature*, vol. 585, no. 7825, pp. 357–362, 2020. DOI: 10.1038/s41586-020-2649-2.

[20] S. K. Lam, A. Pitrou, and S. Seibert, "Numba," in *Proceedings of the Second Workshop on the LLVM Compiler Infrastructure in HPC*, vol. 2015-Janua, New York, NY, USA: ACM, 2015, pp. 1–6. DOI: 10.1145/2833157.2833162.

[21] T. Wendelin, A. Dobos, and A. Lewandowski, "SolTrace: A Ray-Tracing Code for Complex Solar Optical Systems," National Renewable Energy Laboratory (NREL), Golden, CO (United States), Tech. Rep., 2013. DOI: 10.2172/1260924.

[22] D. Buie, A. Monger, and C. Dey, "Sunshape distributions for terrestrial solar simulations," *Solar Energy*, vol. 74, no. 2, pp. 113–122, 2003. DOI: 10.1016/S0038-092X(03)00125-7.

[23] I. Reda and A. Andreas, "Solar position algorithm for solar radiation applications," *Solar Energy*, vol. 76, no. 5, pp. 577–589, 2004. DOI: 10.1016/j.solener.2003.12.003.

[24] W. F. Holmgren, C. W. Hansen, and M. A. Mikofski, "Pvlib python: A python package for modeling solar energy systems," *Journal of Open Source Software*, vol. 3, no. 29, p. 884, 2018. DOI: 10.21105/joss.00884.

[25] G. Johnston, "On the Analysis of Surface Error Distributions on Concentrated Solar Collectors," *Journal of Solar Energy Engineering*, vol. 117, no. 4, pp. 294–296, 1995. DOI: 10.1115/1.2847843.

[26] C. N. Vittitoe and F. Biggs, "Six-gaussian representation of the angular-brightness distribution for solar radiation," *Solar Energy*, vol. 27, no. 6, pp. 469–490, 1981. DOI: 10.1016/0038-092X(81)90043-8.

[27] G. Cardona and R. Pujol-Nadal, "OTSun, a python package for the optical analysis of solar-thermal collectors and photovoltaic cells with arbitrary geometry," *PLOS ONE*, vol. 15, no. 10, F. Li, Ed., e0240735, 2020. DOI: 10.1371/journal.pone.0240735.

[28] J. P. Cardoso, A. Mutuberria, C. Marakkos, P. Schoettl, T. Osório, and I. Les, "New functionalities for the Tonatiuh ray-tracing software," in *AIP Conference Proceedings*, vol. 2033, 2018, p. 210 010. DOI: 10.1063/1.5067212.

Nomenclature

Abbreviations

CSR	Circumsolar Ratio
ES	Effective Source
IAM	Incidence Angle Modifier
LCS	Local Coordinate System
LFC	Linear Fresnel Collector
RMSE	Root Mean Square Error

Latin Letters

$\mathbf{E}_b$	Neighbor blocking edge point
$\mathbf{E}_s$	Neighbor shading edge point
$\mathbf{F}$	Primary mirrors aim point at the receiver. The tracking point
$\mathbf{P}$	A generic point in a primary mirror surface
$\mathbf{M}$	The center point of a primary mirror
$\mathbf{R}^+, \mathbf{R}^-$	Receiver shading edge points
$\mathbf{S}^+, \mathbf{S}^-$	Receiver edge points in the reference plane
$\mathbf{T}^+, \mathbf{T}^-$	Intercepted flux edge points
B	Linear cumulative density function of the effective source
w	Primary mirror width
N_p	Number of points used to discretize the mirror width domain
N^a_{rays}	Number of absorbed rays
p_{ray}	Power carried by a ray
z_s	Shape function of a primary mirror
$\vec{I}_x, \vec{I}_y, \vec{I}_z$	Direction vectors of an xyz right-handed coordinate system
$\vec{n}_i$	Normal vector to the incidence plane
$\vec{n}_s$	Normal vector to the primary mirror surface
$\vec{n}_r$	Normal vector to the reflection plane
$\vec{v}_l^+, \vec{v}_l^-$	Limiting vectors
$\vec{v}_{ms}$	Neighboring shading vector
$\vec{v}_{mb}$	Neighboring blocking vector
$\vec{v}_n$	Reflected ray direction vector
$\vec{v}_{n,T}$	Projection of $\vec{v}_n$ in the transversal plane
$\vec{v}_{rs}^+, \vec{v}_{rs}^-$	Receiver shading vectors
$\vec{S}$	Incidence ray direction vector
$\vec{S}_T$	Projection of $\vec{S}$ in the transversal plane

Greek Letters

θ_d	Design position for the curvature radius design
θ_l^+, θ_l^-	Acceptance angles in which **P** sees the receiver in the reflection plane
θ_{nb}	Neighbor blocking angle
θ_{ns}	Neighbor shading angle
θ_{rs}^+, θ_{rs}^-	Receiver shading angles
θ_L	Longitudinal incidence angle
θ_T	Transversal incidence angle
δ_{es}	RMS width of the effective source distribution
δ_{sun}	RMS width of the sunshape distribution
δ_o	RMS width of the overall optical error distribution
δ_η	RMSE between analytical and ray-tracing results of η
$\Delta\eta$	Error between analytical and ray-tracing results of η
$\Delta\bar{\eta}$	Relative error between analytical and ray-tracing results of $\bar{\eta}$
γ	Concentrator intercept factor
γ_m	Mirror intercept factor
γ_p	Local intercept factor at point **P** on the mirror surface
η	Concentrator optical efficiency
η_T	Transversal optical efficiency
η_L	Longitudinal optical efficiency
π_i	The incidence plane
π_r	The reflection plane

Indices

h	Hour index
k	General counting index

Superscripts

an	Results from the analytical method
rt	Results from ray-tracing simulations

Chapter 4

On the shape of the primary mirrors[†]

Abstract

One key aspect of the curvature design of linear Fresnel primary mirrors is the selection of a bent shape: parabolic or cylindrical. This chapter introduces a new and general approach to comparing both shapes, based on the root mean square measure of local slope deviations as an overall metric to represent how much a cylindrical mirror deviates from a parabolic one. The ensuing results demonstrate the influence of design parameters and indicate that, for reasonable geometric configurations found in current commercial linear Fresnel collectors, the maximum values of overall slope deviations are below 0.7 mrad – more than ten times smaller than the optical errors in state-of-the-art mirror panels. Moreover, the main hypothesis is that parabolic and cylindrical primary mirrors perform similarly when the root mean square slope deviation is low or negligible compared to other sources of beam spread that compose the effective source (e.g., sunshape, specular error, contour error, tracking error). To validate this hypothesis, literature data on reported cases of equivalence were analyzed in terms of worst-case scenarios of the proposed metric, and the results of this analysis corroborate the hypothesis.

Keywords: Linear Fresnel collector, Geometric design, Primary mirrors shape.

[†]A. V. Santos, D. Canavarro, P. Horta, and M. Collares-Pereira, "On the comparison of parabolical and cylindrical primary mirrors for linear Fresnel solar concentrators," Renewable Energy, vol. 218, p. 119 380,2023. https://doi.org/10.1016/j.renene.2023.119380.

4.1 Introduction

The curvature design of linear Fresnel primary mirrors involves selecting both the shape and the curvature value. The available shapes are flat, parabolic, and cylindrical. Since flat mirrors lack focusing capability, the curved mirrors (parabolic or cylindrical) achieve better concentration and energy collection under the same conditions [1–3]. Therefore, the design process focuses on choosing a bent shape and determining the appropriate curvature. This chapter analyzes the selection of a bent shape.

The literature includes studies that compare parabolic and cylindrical primary fields, although this comparison is not the main focus of these works. Abbas et al. [4] and Balaji et al. [5] compared receiver flux maps, while Qiu et al. [6], Boito and Grena [7], Cheng et al. [8], and Men et al. [9] used optical efficiency-based comparison metrics. Abbas and Martínez-Val [10] analyzed the maximum deflection of reflected rays at the receiver due to differences in local extrinsic curvature between the two shapes under identical design conditions. The results from these works indicate that parabolic and cylindrical primary mirrors can achieve similar performance, although the underlying reasons and the specific conditions under which this equivalence holds remain not fully exploited. Some studies only identified this equivalence after conducting performance computations [4–8]. Abbas and Martínez-Val [10] provided an equivalence assessment based on a local measure, which, while informative, does not offer an overall metric for the entire mirror. Furthermore, these studies do not account for a broad range of design conditions in their comparison.

Despite these particular results, there is still no general approach for this comparison before performance computations – a methodological gap – explaining why both shapes can yield the same performance and up to which conditions it stands. Thus, this chapter introduces a geometric approach to address this comparison, guided by two research questions:

- Why can both shapes yield the same performance?
- Under which conditions does this equivalence stand?

Considering the potential impact on manufacturing costs since cylindrical mirrors are simpler and cheaper to produce [11], these questions are relevant for developing cost-effective materials and manufacturing methods without compromising performance, ultimately enabling more competitive designs.

To explore these questions, the chapter first outlines the design of parabolic and cylindrical mirrors, deriving the geometric parameters involved in the procedures. It defines the root mean square (RMS) measure of the local slope deviation as the geometric comparison metric, which represents the overall deviation between the two shapes. Next, the RMS measure is analyzed under worst-case scenarios to assess how design parameters influence it. Lastly, existing literature on equivalence is evaluated using this proposed comparison metric to test the hypothesis that parabolic and cylindrical primary mirrors perform similarly when the RMS slope deviation is low or negligible compared to other sources of beam spread, such as sunshape, specular error, and contour error.

4.2 Models

Parabolic and cylindrical mirror designs assume collimated sunlight and perfect specular reflection, disregarding optical errors. At the design position (a specific transversal incidence

angle), the mirror directs all incident sunlight to the receiver's aim point. These procedures incorporate the geometric parameters related to the tracking procedure described in Subsection 2.1.4 and illustrated in Figure 2.4. Consequently, the same nomenclature is adopted throughout this chapter. The next two subsections present the curvature design formulations for parabolic [12] and cylindrical [13] primary mirrors.

4.2.1 Parabolic mirrors design

A parabolic surface can perfectly reflect all rays parallel to its optical axis onto its focus. Whereas the first approach to the design of a parabolic primary field stands for breaking one wide parabola into several segments, aligning the segments horizontally, and letting them individually track the sun, a better design is achieved when each mirror is a specific segment of a particular parabola [12], as shown in Figure 4.1.

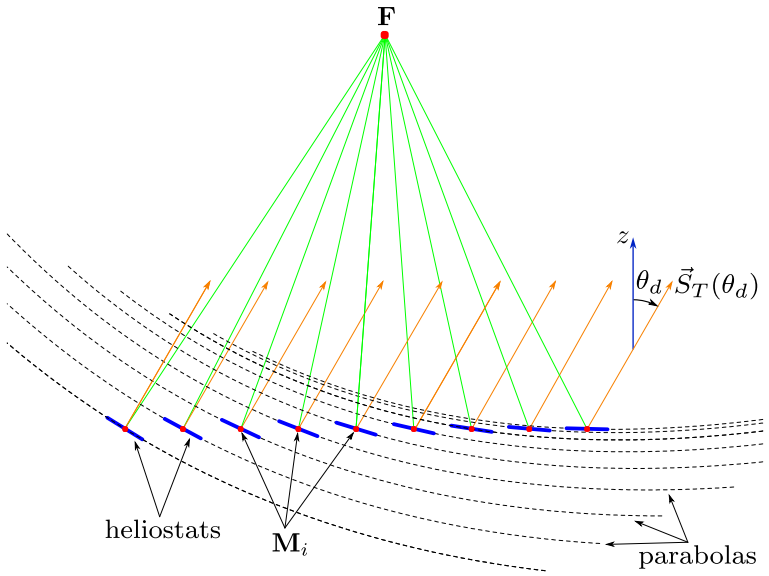

Figure 4.1: The design of parabolic primaries: each mirror is a specific segment of a particular parabola, whose optical axis is aligned with the incidence direction in the transversal plane for the design position, θ_d. Adapted from Häberle [12].

The design approach illustrated in Figure 4.1 shows that parabolas' optical axes are aligned with the sunlight incidence direction in the transversal plane, $\vec{S}_T$, for the design position, θ_d, a particular transversal angle. A closer look shows that mirrors are segments of tilted parabolas whose axes deviate from the vertical at an angle θ_d, as depicted in Figure 4.2a.

A tilted parabola has a complicated equation, so that the definition of mirror contour is challenging. On the other hand, as shown in Figure 4.2a, an uv coordinate system aligned with the parabola optical axis can be defined in addition to the standard zx reference frame. In this tilted frame, the mirror is a segment of a vertical parabola, as shown in Figure 4.2b, which has a well-known straightforward equation in the rotated coordinates system: $v(u) = u^2/4f_m$, where f_m is the parabola focal length.

A generic point in the tilted coordinate system, ${}^{uv}\mathbf{P}$, is mapped in the fixed coordinates system as ${}^{zx}\mathbf{P}$ by the below equation:

$$ {}^{zx}\mathbf{P} = {}^{zx}\mathbf{V} + R_y(\theta_d) \cdot {}^{uv}\mathbf{P}, \tag{4.1} $$

where R_y is a rotation matrix function as defined in Equation A.4, and ${}^{zx}\mathbf{V}$ is the origin

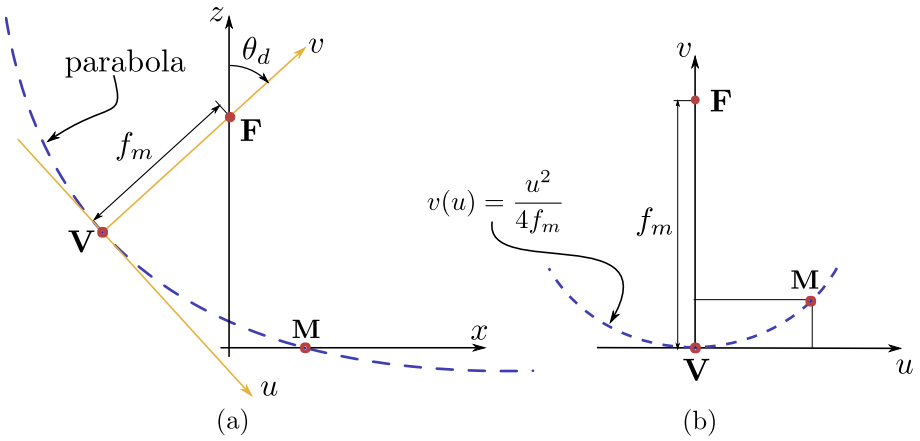

Figure 4.2: The design of a parabolic primary mirror. When viewed from (a) the conventional zx coordinate system, the mirrors comprises a segment of a tilted parabola. However, (b) a more convenient and tilted uv coordinate system can be defined, so that the mirror comprises a segment of a vertical parabola, which has a straightforward equation.

of the uv coordinate system represented in the zx coordinate system, i.e., the vertex of the tilted parabola represented in the zx system. The inverse mapping can be easily computed by inverting this equation as well[1].

Figure 4.3 details the parabolic surface in the uv coordinate system. Of course, the primary mirror only comprises a segment of it, whose width is w. The tangent line t at the mirror center has a local slope given by ξ, and the edges of the parabolic primary are defined by points $\mathbf{E}_1$ and $\mathbf{E}_2$ – these points are determined by the interception between straight lines s_1 and s_2 with the parabolic surface. Then, Equation 4.1 is used to transform the contour of the parabolic primary mirror to the fixed zx coordinate system.

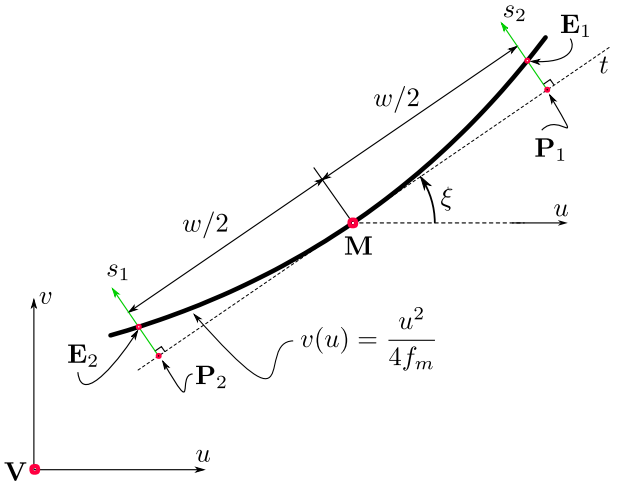

Figure 4.3: The design of parabolic primary mirror in the uv coordinates system. In this tilted reference frame, the parabolic surface has a simple equation, $v(u) = u^2/4f_m$, and the mirror only comprises a section of it, whose width is w. The tangent line t at the mirror center has a local slope given by ξ, and the interception between straight lines s_1 and s_2 with the parabolic surface define the edge-points $\mathbf{E}_1$ and $\mathbf{E}_2$ of the mirror.

[1]Here, it is important to highlight that points in the zx and uv coordinate systems are of the kind $\{p_x, 0, p_z\}$ and $\{p_u, 0, p_v\}$, respectively.

The *specific reference* defined by Abbas and Martínez-Val [14] considers a design where the transversal incidence direction $\vec{S}_T(\theta_d)$ aligns with the focusing vector $\vec{v}_f$, i.e., $\theta_d = \lambda$. In this case, $f_m = f = |\vec{v}_f| = [\mathbf{F}, \mathbf{M}]$, the parabolic surface is defined by $v(u) = u^2/4f$, the vertex is at $\mathbf{M}$, and the mirror comprises the interval in which $u \in [-w/2, w/2]$. More simply, this design is analogous to one obtained from the central symmetrical section of vertical parabola whose focal length is f, vertex is at $\mathbf{M}$, and width is w. The design of a parabolical primary by a vertical parabola is a common approach taken in many studies [3, 6, 15, 16].

The *sun reference* is when the design position for all primaries is the typical sun position: a weighted average of positions in the transversal plane for the year. The typical position for an NS-oriented field is the normal incidence (*zenithal reference*), i.e., $\theta_d = 0$ [14].

4.2.2 Cylindrical mirrors design

A cylindrical surface has a well-known focusing ability based on the relation between the mirror curvature radius, R, and width, w: $R \gg w$. Considering it, Rabl [13] presented a general analysis to determine the value of R such that a mirror whose center point is located at $\mathbf{M}$ focuses all incoming collimated sunlight with a particular transversal incidence, $\vec{S}_T(\theta_d)$, at the desired focus $\mathbf{F}$. Figure 4.4 illustrates this situation.

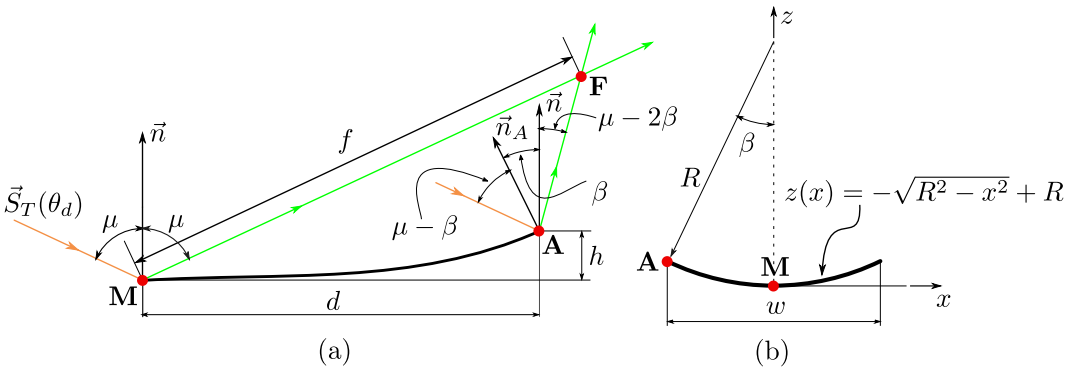

Figure 4.4: The design of a cylindrical primary mirror. (a) Focusing analysis and geometric relations on focusing incident rays at the desired aim point – adapted from Rabl [13]. (b) Geometric elements of a cylindrical (circular) mirror at a horizontal position ($\tau = 0$).

For the condition of $R \gg w$, it is straightforward that $h \approx 0$. Thus, from Figure 4.4, one can derive the following relation:

$$\frac{d}{\sin(2\beta)} = \frac{f}{\cos(\mu - 2\beta)}, \tag{4.2}$$

and since $\sin\beta \approx \beta \approx d/R$ and $\cos(\mu - 2\beta) \approx \cos\mu$, this previous equation can be simplified to give an explicit function for R, as shown in Equation 4.3, where μ relates to θ_d and λ as given by Equation 2.10.

$$R = \frac{2f}{\cos\mu} \tag{4.3}$$

One can derive from Equation 4.3 that for the case when $\theta_d = \lambda$ (specific reference design), $R = 2f$, precisely the equation proposed by Abbas et al. [4] and used by Pulido-Iparraguirre et al. [17]. For the case when $\theta_d = 0$ (zenithal reference), $R = 2f/\cos(\lambda/2)$, an expression used by other authors [18, 19] to design cylindrical mirrors.

4.2.3 Slope deviation as the comparison metric

Equation 4.3 considers approximations that are outcomes of the condition that $R \gg w$. Of course, these approximations lead to cylindrical mirrors not perfectly focusing all sunlight at **F**, as happens in parabolic mirrors. Thus, the cylindrical mirror surface diverges from the parabolic one designed with the same conditions of θ_d, λ, w, and H (see Figure 2.4).

For this reason, the parabolic surface is here considered as the desired one, and the local slope deviation, $\Delta\xi$, measures how much the cylindrical mirror deviates from this ideal shape. Equation 4.4 defines the mathematical model used for $\Delta\xi$, where $z_c(x)$ and $z_p(x)$ represent the shape functions of the cylindrical and parabolic mirrors, respectively.

$$\Delta\xi(x) = \tan^{-1}\left(\frac{\mathrm{d}z_c(x)}{\mathrm{d}x}\right) - \tan^{-1}\left(\frac{\mathrm{d}z_p(x)}{\mathrm{d}x}\right) \tag{4.4}$$

Based on this local deviation metric, the RMS measure, δ_ξ, is defined in Equation 4.5, where w is the mirror width. Meiser et al. [20] have used a RMS measure to analyze how much parabolic trough panels deviate from the desired theoretical shape. In a similar way, δ_ξ is an overall metric to represent how much the cylindrical mirror deviates from the desired parabolic shape.

$$\delta_\xi = \sqrt{\frac{1}{w}\int_{-w/2}^{+w/2} \Delta\xi(x)^2 \mathrm{d}x} \tag{4.5}$$

The advantage of using δ_ξ as the deviation metric is that it can be directly compared to other sources of beam spread. Considering the concept of an effective source as the convolution of a sunshape and optical errors [13] (refer to Subsection B.2.4), the use of cylindrical mirrors would add a new source of error due to its deviation from the (ideal) parabolic shape. In short, this proposition is shown in Equation 4.6 by the δ_ξ term, where δ_{es}, δ_{sun}, and δ_{opt} are the RMS widths of the effective source, sunshape, and optical errors, respectively. Moreover, δ_ξ is multiplied by a factor of 2 since a slope deviation of $\Delta\xi$ causes a deflection of $2\Delta\xi$ in reflected rays (refer to Figure B.7).

$$\delta_{es}^2 = \delta_{sun}^2 + \delta_{opt}^2 + 4\delta_\xi^2 \tag{4.6}$$

A reasonable hypothesis derived from Equation 4.6 is that cylindrical and parabolic primary mirrors perform similarly when δ_ξ is low or negligible regarding the other sources of beam spread. Thus, the comparison through δ_ξ is carried out before performance computations and does not depends on parameters such as receiver size, position, and orientation, among others – they are the same for both cases. The deviation as given by δ_ξ depends only on the design parameters that influence it: w/H, θ_d and λ.

Now that design models and a deviation metric to compare parabolic and cylindrical mirrors are defined, the influence of w/H, θ_d and λ on δ_ξ can be examined to identify worst-case scenarios and the resulting deviations. Additionally, the previously stated hypothesis can be evaluated. These topics are the scope of the next section, which begins with a validation analysis of the models implemented in Python, based on NumPy [21] and SciPy [22].

4.3 Results and discussion

4.3.1 Models validation

Figure 4.5 shows an example of primary mirrors designed with the implemented models for $w/H = 0.3$, $\theta_d = -50°$, and $\lambda = 20°$. It presents (a) the mirror contour, and (b) the local slope deviation. These results show that the parabolic mirror comprises a non-symmetric segment, contrary to the cylindrical one, as shown in Figure 4.5a. As expected, deviations increase from the center to the edges of the mirror, as shown in Figure 4.5b, comprising a RMS value of 2.1 mrad.

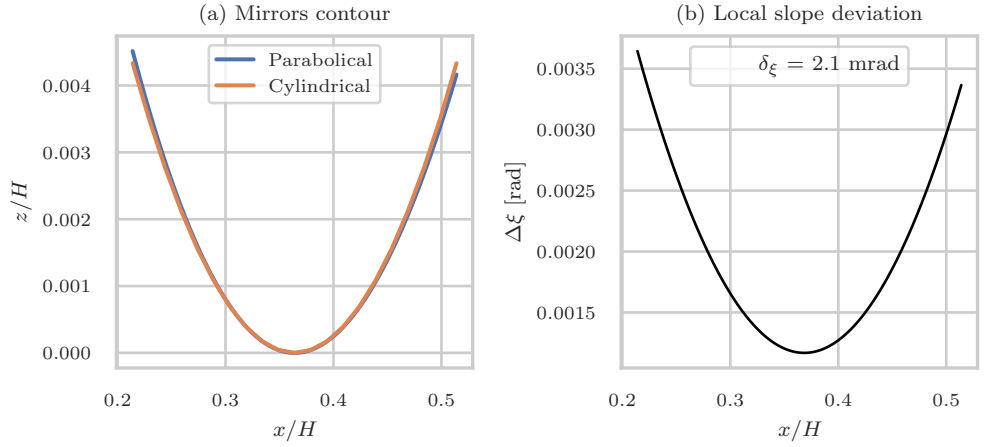

Figure 4.5: Example of designed primary mirrors based on the implemented mathematical models for $w/H = 0.3$, $\theta_d = -50°$, and $\lambda = 20°$. It presents (a) the mirror contour, and (b) the local slope deviation, whose RMS value is 2.1 mrad.

As a matter of comparison, Abbas and Martínez-Val [14] argue that the state-of-the-art standard deviation for overall Gaussian optical errors in solar energy applications is 5.0 mrad. This corresponds to a root mean square (RMS) width of $5\sqrt{2}$, or $\delta_{opt} = 7.1$ mrad. Figure 4.5 shows that even in a case where the surface contours of parabolic and cylindrical mirrors nearly coincide (Figure 4.5a), an RMS slope deviation of 2.1 mrad is observed — a substantial value that may not even represent the worst-case scenario in design conditions.

4.3.2 Worst-case scenarios of slope deviation

The analysis of how the root mean square slope deviation, δ_ξ, varies with design parameters reveals the worst-case scenarios for the deviation between parabolic and cylindrical mirrors. That is, the conditions that result in the highest values of δ_ξ. Accordingly, Figure 4.6 presents δ_ξ as a function of λ and θ_d for two different cases of w/H.

Both cases in Figure 4.6 exhibit the same overall trend, differing only in the magnitude of δ_ξ. These results also indicate that as w/H increases, slope deviations get higher in the whole domain of λ and θ_d, with the maximum values, $\delta_{\xi,max}$, occurring near $\lambda = 0$, positions corresponding to the shortest focusing distances, where $f/H = \cos\lambda$ (refer to Figure 2.4). Since R is proportional to $2f$, as defined in Equation 4.3, the ratio w/R reaches its highest values around $\lambda = 0$. In this region, the approximation $\sin\beta \approx \beta$ fails and δ_ξ increases. Furthermore, the higher values of δ_ξ in Figure 4.6 also correspond to conditions far from the specific reference design – represented by the red line. From Figure 2.4, it follows that

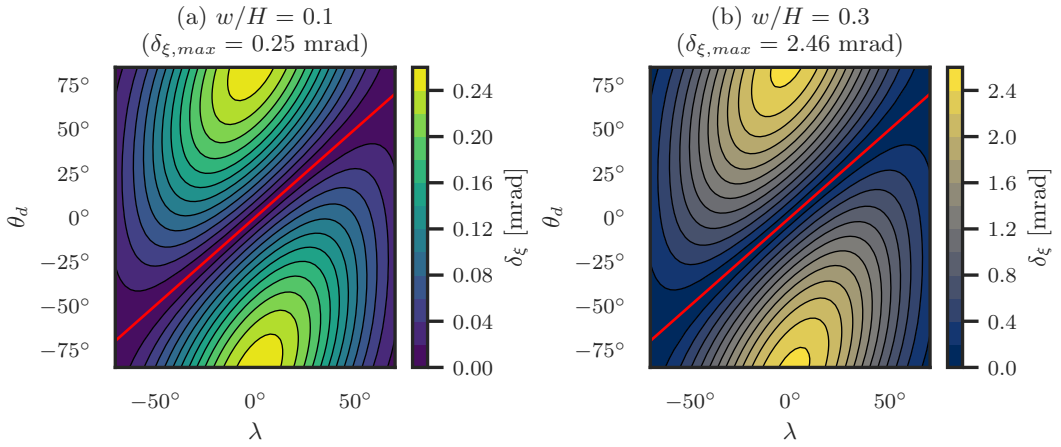

Figure 4.6: Root mean square slope deviation as a function of λ and θ_d: $\delta_\xi(\lambda, \theta_d)$. Mirrors were designed for (a) $w/H = 0.1$; (b) $w/H = 0.3$. The red line represents the specific reference design: $\theta_d = \lambda$.

$\mu = (\theta_d - \lambda)/2$. For the specific reference design, where $\theta_d = \lambda$, it leads to $\mu = 0$. Therefore, as conditions get out of the specific reference design, the approximation $\cos(\mu - 2\beta) \approx \cos\mu$, introduced in Subsection 4.2.2, also breaks down, leading to an increase in δ_ξ.

Thus, Figure 4.6 suggest that a specific reference design yield the lowest values of δ_ξ, while the central mirror ($\lambda = 0$) in the zenithal reference case ($\theta_d = 0$) exhibits the highest deviations — corroborating the findings of a previous study [10].

In this context, Figure 4.7 presents the maximum RMS slope deviation, $\delta_{\xi,max}$, across the entire design domain of λ and θ_d, as a function of w/H. This figure shows that deviations can reach values as high as 7.0 mrad. However, such a scenario ($w/H = 0.5$) is unrealistic for linear Fresnel concentrators – for example, if $H = 8.0$ m, then $w = 4.0$ m.

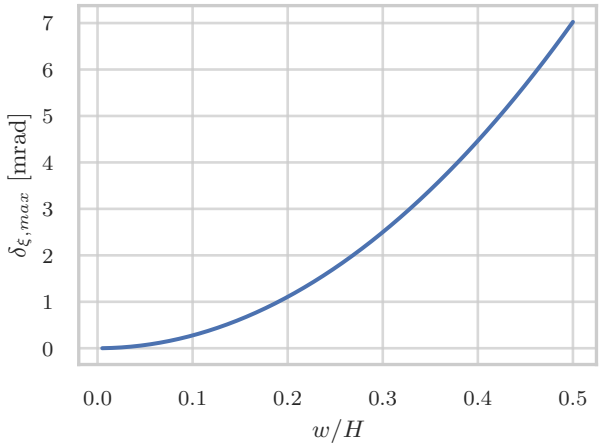

Figure 4.7: Maximum root mean square slope deviation as a function of the ratio between mirror width and receiver height: $\delta_{\xi,max}(w/H)$. It considers the maximum δ_ξ across the entire design domain of λ and θ_d: $-70° \leq \lambda \leq +70°$ and $-85° \leq \theta_d \leq +85°$.

On the other hand, realistic design conditions based on reported values in the literature – such as $w/H < 0.2$ [7, 10] – lead to significantly lower deviations, due to the non-linear relationship between $\delta_{\xi,max}$ and w/H shown in Figure 4.7. As further evidence, Table 4.1 presents the maximum deviations associated with the geometric characteristics of commer-

cial LFC technologies. The table shows that maximum RMS deviations remain below 0.7 mrad — more than ten times lower than typical values of overall Gaussian optical errors (δ_{opt} = 7.1 mrad [14]).

Table 4.1: Maximum RMS slope deviation, $\delta_{\xi,max}$, for geometries of commercial linear Fresnel technologies. It considers the maximum deviation in the domain of λ and θ_d.

LFC technologies	w/H	$\delta_{\xi,max}$ [mrad]
Novatec [23]	0.095	0.25
Industrial Solar [23]	0.125	0.43
SunCNIM [23]	0.111	0.34
Areva [23]	0.081	0.18
Soltigua [23, 24]	0.156	0.67

δ_ξ represents an overall measure of how much the cylindrical mirror deviates from the parabolic one. Accordingly, a reasonable hypothesis is that both mirrors are indistinguishable — at least from the receiver's point of view – when δ_ξ is very small ($\delta_\xi \ll 1$) or negligible regarding the other error sources ($\delta_\xi \ll \delta_{es}$). Under these conditions, both configurations would be expected to perform similarly.

The literature includes a substantial number of studies in which primary fields based on both mirror shapes exhibit equivalent performance. These cases can be assessed by examining worst-case scenarios for δ_ξ, in order to validate the proposed equivalence hypothesis.

4.3.3 Evidence of equivalence in the literature

As previously mentioned, some studies found that parabolical and cylindrical primary fields can yield the same flux maps [4, 5] and optical efficiency [6, 8, 16].

These works consider different design conditions, but the most straightforward are those presented by Qiu et al. [6] and Cheng et al. [8]. In these cases, the parabolic mirrors are defined as symmetric vertical parabolas, as illustrated in Figure 4.2b, and are defined by a focal length, f_m, and a width, w. Cylindrical mirror design considers a curvature radius, R, instead of the focal length, as illustrated in Figure 4.4. Table 4.2 shows the values of w, f_m, and R used in these studies (and ensuing results).

Table 4.2: Geometric parameters of parabolical and cylindrical primary mirrors considered by Qiu et al. [6] and Cheng et al. [8].

Reference	w [m]	f_m [m]	R [m]
Qiu et al. [6]	0.6	10.6	21.7
Cheng et al. [8]	0.25	12.33	24.75

Figure 4.8 presents slope deviation profiles of the parabolical and cylindrical primaries as designed by Qiu et al. [6] and Cheng et al. [8]. As can be seen, the local slope deviations are very low. Indeed, values of δ_ξ are 0.19 and 0.01 mrad for Qiu and Cheng's cases, respectively. These are negligible values compared to the 7.8 mrad RMS width of the effective source considered in those works: $\delta_{es}/\delta_\xi > 41$ and $\delta_{es}/\delta_\xi > 780$, respectively.

Other studies [4, 5, 7] found this equivalence for different conditions but all of them can be summarized by an analysis concerning the specific reference design: $\theta_d = \lambda$. In this case,

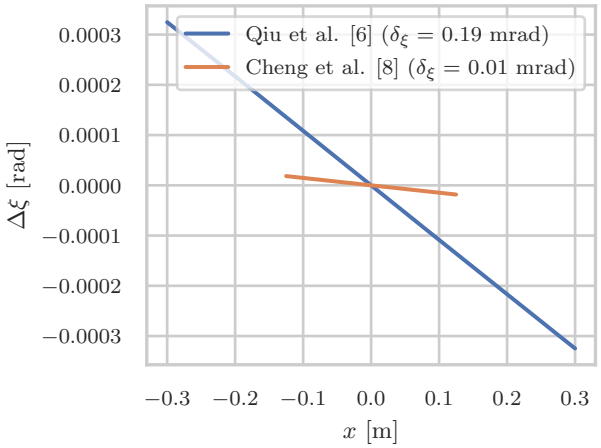

Figure 4.8: Slope deviation of parabolical and cylindrical primary mirrors along mirrors width. It considers the mirrors designed by Qiu et al. [6] and Cheng et al. [8].

the parabolic mirror comprises the central section of a vertical parabola whose focal length is f, and the cylindrical mirror radius is $R = 2f$ (see Figure 2.4). Then, the RMS slope deviation, δ_ξ, can be directly calculated as shown in Equation 4.7.

$$\delta_\xi = \sqrt{\frac{1}{w}\int_{-w/2}^{+w/2}\left[\tan^{-1}\left(\frac{x}{\sqrt{R^2-x^2}}\right) - \tan^{-1}\left(\frac{x}{2f}\right)\right]^2 \mathrm{d}x} \tag{4.7}$$

In the specific reference design, the worst-case scenario is when $\lambda = 0$, and thus $f = H$ and $R = 2H$. Then, one can solve Equation 4.7 to express δ_ξ as function of the ratio w/H. These results are shown in Figure 4.9, where the points corresponding to the width to height ratios from Abbas et al. [4], Balaji et al. [5], and Boito and Grena [7] are highlighted.

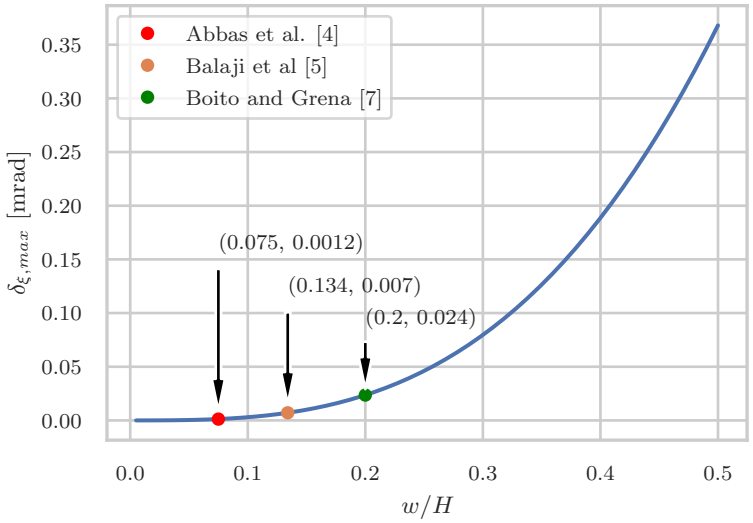

Figure 4.9: Maximum root mean square slope deviation as a function of the ratio between mirror width and receiver height: $\delta_{\xi,max}(w/H)$. It considers the worst condition of a specific reference: $\lambda = 0$, so $f_m = H$ and $R = 2f_m$. It is a case analogous to the comparison of a vertical parabola and a circle when $R = 2f_m$. This figure also shows the maximum values of δ_ξ for the width-height ratio of previous studies [4, 5, 7].

Figure 4.9 shows that, even under unrealistic conditions, the maximum deviation values for a specific reference design remain quite low—reaching up to 0.36 mrad for $w/H = 0.5$.

Abbas et al. [4] consider a w/H ratio of 0.075, which corresponds to a maximum deviation of just 0.0012 mrad – a negligible value that explains why equivalence was observed even under a collimated sunlight model with no optical errors (i.e., $\delta_{es} = 0$). Similarly, Balaji et al. [5] use a w/H ratio of 0.134, resulting in a $\delta_{\xi,max}$ of 0.007 mrad – 471 times smaller than the 3.3 mrad size of the effective source they considered. Boito and Grena [7] explore w/H values up to 0.2, corresponding to a maximum deviation of 0.024 mrad, which is 130 times smaller than their assumed RMS effective source width of 3.2 mrad.

In conclusion, the results from the literature cases, when interpreted in terms of $\delta_{\xi,max}$, support the previously established hypothesis: for negligible values of δ_ξ the two mirror types are indistinguishable from the receiver's perspective and therefore exhibit similar performance.

4.3.4 Further discussion

The mathematical models presented in this chapter show that despite δ_ξ can achieve high values, realistic geometric conditions as of commercial linear Fresnel technologies restrict maximum deviations up to 0.67 mrad, as shown in Table 4.1. Furthermore, Figure 4.10a shows that maximum deviations can be significantly reduced if further design constraints such as zenithal and specific references (orange and green lines, respectively) are imposed.

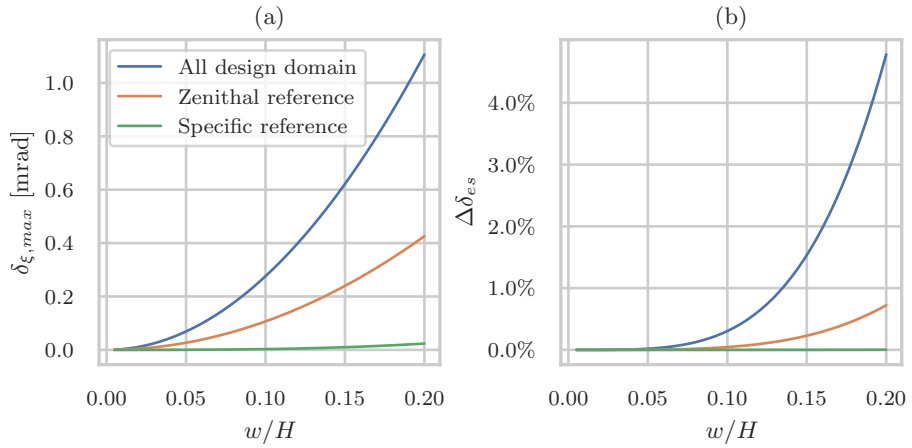

Figure 4.10: (a) Maximum root mean square slope deviation as a function of the ratio between mirror width and receiver height: $\delta_{\xi,max}(w/H)$. (b) Effective source percentage increase due to the deviation: $\Delta\delta_{es} = \sqrt{1 + (2\delta_\xi/\delta_{es})^2} - 1$, considering $\delta_{es} = 8.4$ mrad. It presents worst-case scenario values for different design conditions: (1) the whole domain of θ_d and λ; (2) the zenithal reference ($\theta_d = 0$); and (3) the specific reference ($\theta_d = \lambda$).

In the same context, it is also straightforward to assess the impact of $\delta_{\xi,max}$ in the spread of an effective source. Considering a base case consisting of Buie's sunshape [25] with a circumsolar ratio of 5% and a 5.0 mrad standard deviation for the overall Gaussian error ($\delta_{es} = 8.4$ mrad), Figure 4.10b illustrates the resulting increase in the effective source – denoted here by $\Delta\delta_{es}$ – as a function of w/H. As shown, $\Delta\delta_{es}$ remains relatively low: up to 3.5% for a case considering the full design domain (blue line); under the sun reference design (orange line), the increase is less than 1%; and for the specific reference design (green line), it is practically zero for $w/H \leq 0.2$. Although these increases are small, they depend on the size of the base source – 8.4 mrad in the case shown in Figure 4.10b.

Furthermore, two additional considerations add further substance to the limited effect of $\Delta\delta_{es}$ on performance. First, the values in Figure 4.10 represent only the worst-case deviations. Since primary mirrors are discretely distributed across the field, not all will experience

maximum slope deviations – in fact, the average deviation is expected to be lower. Second, in solar thermal applications, the receiver has a finite size that introduces tolerance to optical errors, thereby mitigating the impact of such deviations. This tolerance is typically defined by the concentrator acceptance angle. Both of these factors are case-specific and cannot be evaluated quantitatively in general terms; they depend on the mirror distribution and the actual acceptance angle value. Nevertheless, Figure 4.10 remains a valuable tool for estimating maximum deviations and for assessing the equivalence between parabolic and cylindrical primary mirrors prior to performance simulations.

4.4 Conclusions

In this chapter, the Root Mean Square (RMS) measure of the local slope deviation was used as a geometric parameter to compare parabolic and cylindrical primary mirrors, quantifying how much a cylindrical mirror deviates from the ideal parabolic shape. The core hypothesis was that both mirror types are equivalent – at least from the receiver perspective – when RMS values are low or negligible compared to other sources of beam spread, such as sunshape and optical errors.

The results show that slope deviations can be significant, but only under design conditions that are unrealistic for linear Fresnel concentrators. In contrast, more reasonable design configurations substantially reduce the maximum deviations – reaching values ten times lower than those of state-of-the-art overall optical error measures. Additionally, design constraints such as zenithal or specific reference configurations can further reduce these deviations, with values falling below 0.5 mrad for a width-to-height ratio of 0.2.

Moreover, equivalence cases reported in the literature corroborate the proposed hypothesis: when slope deviation is negligible, the two mirror types appear indistinguishable from the receiver perspective and consequently deliver similar optical performance. Thus, using cylindrical mirrors instead of parabolic ones is a sound choice. Their specification is relatively straightforward, relying solely on the radius of curvature. In practice, cylindrical mirrors are simpler and more cost-effective to manufacture [11], enabling the use of cheaper materials and production methods without compromising performance – an essential factor for developing economically viable solutions.

The findings presented in this chapter contribute to fill a methodological gap, providing a means to compare curved primary mirrors prior to detailed performance simulations. Furthermore, since equivalence between parabolic and cylindrical mirrors holds across a broad range of design conditions relevant to linear Fresnel technology, it is reasonable to exclude parabolic mirrors from consideration. This simplification reduces the number of decision variables and streamlines the overall design process for linear Fresnel systems.

References

[1] D. Feuermann and J. M. Gordon, "Analysis of a Two-Stage Linear Fresnel Reflector Solar Concentrator," *Journal of Solar Energy Engineering*, vol. 113, no. 4, pp. 272–279, 1991. DOI: 10.1115/1.2929973.

[2] R. Abbas, J. Muñoz-Antón, M. Valdés, and J. Martínez-Val, "High concentration linear Fresnel reflectors," *Energy Conversion and Management*, vol. 72, pp. 60–68, 2013. DOI: 10.1016/j.enconman.2013.01.039.

[3] S. Benyakhlef, A. Al Mers, O. Merroun, A. Bouatem, N. Boutammachte, S. El Alj, H. Ajdad, Z. Erregueragui, and E. Zemmouri, "Impact of heliostat curvature on optical performance of Linear Fresnel solar concentrators," *Renewable Energy*, vol. 89, pp. 463–474, 2016. DOI: 10.1016/j.renene.2015.12.018.

[4] R. Abbas, M. J. Montes, M. Piera, and J. M. Martínez-Val, "Solar radiation concentration features in Linear Fresnel Reflector arrays," *Energy Conversion and Management*, vol. 54, no. 1, pp. 133–144, 2012. DOI: 10.1016/j.enconman.2011.10.010.

[5] S. Balaji, K. Reddy, and T. Sundararajan, "Optical modelling and performance analysis of a solar LFR receiver system with parabolic and involute secondary reflectors," *Applied Energy*, vol. 179, pp. 1138–1151, 2016. DOI: 10.1016/j.apenergy.2016.07.082.

[6] Y. Qiu, Y. L. He, Z. D. Cheng, and K. Wang, "Study on optical and thermal performance of a linear Fresnel solar reflector using molten salt as HTF with MCRT and FVM methods," *Applied Energy*, vol. 146, pp. 162–173, 2015. DOI: 10.1016/j.apenergy.2015.01.135.

[7] P. Boito and R. Grena, "Optimal focal length of primary mirrors in Fresnel linear collectors," *Solar Energy*, vol. 155, pp. 1313–1318, 2017. DOI: 10.1016/j.solener.2017.07.079.

[8] Z. D. Cheng, X. R. Zhao, Y. L. He, and Y. Qiu, "A novel optical optimization model for linear Fresnel reflector concentrators," *Renewable Energy*, vol. 129, pp. 486–499, 2018. DOI: 10.1016/j.renene.2018.06.019.

[9] J. Men, X. Zhao, Z. Cheng, Y. Leng, and Y. He, "Study on the annual optical comprehensive performance of linear Fresnel reflector concentrators with an effective multi-objective optimization model," *Solar Energy*, vol. 225, pp. 591–607, 2021. DOI: 10.1016/j.solener.2021.07.051.

[10] R. Abbas and J. Martínez-Val, "A comprehensive optical characterization of linear Fresnel collectors by means of an analytic study," *Applied Energy*, vol. 185, pp. 1136–1151, 2017. DOI: 10.1016/j.apenergy.2016.01.065.

[11] D. Pulido-Iparraguirre, L. Valenzuela, J. Fernández-Reche, J. Galindo, and J. Rodríguez, "Design, Manufacturing and Characterization of Linear Fresnel Reflector's Facets," *Energies*, vol. 12, no. 14, p. 2795, 2019. DOI: 10.3390/en12142795.

[12] A. Häberle, "Linear Fresnel Collectors," in *Solar Energy*, C. Richter, D. Lincot, and C. A. Gueymard, Eds., Springer New York, 2013, pp. 72–78. DOI: 10.1007/978-1-4614-5806-7_679.

[13] A. Rabl, *Active Solar Collectors and Their Applications*. New York: Oxford University Press, 1985. [Online]. Available: https://shorturl.at/oGLX6.

[14] R. Abbas and J. Martínez-Val, "Analytic optical design of linear Fresnel collectors with variable widths and shifts of mirrors," *Renewable Energy*, vol. 75, pp. 81–92, 2015. DOI: 10.1016/j.renene.2014.09.029.

[15] M. Moghimi, K. Craig, and J. Meyer, "Simulation-based optimisation of a linear Fresnel collector mirror field and receiver for optical, thermal and economic performance," *Solar Energy*, vol. 153, pp. 655–678, 2017. DOI: 10.1016/J.SOLENER.2017.06.001.

[16] H. Ajdad, Y. Filali Baba, A. Al Mers, O. Merroun, A. Bouatem, and N. Boutammachte, "Particle swarm optimization algorithm for optical-geometric optimization of linear fresnel solar concentrators," *Renewable Energy*, vol. 130, pp. 992–1001, 2019. DOI: 10.1016/j.renene.2018.07.001.

[17] D. Pulido-Iparraguirre, L. Valenzuela, J.-J. Serrano-Aguilera, and A. Fernández-García, "Optimized design of a Linear Fresnel reflector for solar process heat applications," *Renewable Energy*, vol. 131, pp. 1089–1106, 2019. DOI: 10.1016/j.renene.2018.08.018.

[18] J. Facão and A. C. Oliveira, "Numerical simulation of a trapezoidal cavity receiver for a linear Fresnel solar collector concentrator," *Renewable Energy*, vol. 36, no. 1, pp. 90–96, 2011. DOI: 10.1016/j.renene.2010.06.003.

[19] J. Ma, C.-L. Wang, Y. Zhou, and R.-D. Wang, "Optimized design of a linear Fresnel collector with a compound parabolic secondary reflector," *Renewable Energy*, vol. 171, pp. 141–148, 2021. DOI: 10.1016/j.renene.2021.02.100.

[20] S. Meiser, E. Lüpfert, B. Schiricke, and R. Pitz-Paal, "Analysis of Parabolic Trough Concentrator Mirror Shape Accuracy in different Measurement Setups," *Energy Procedia*, vol. 49, pp. 2135–2144, 2014. DOI: 10.1016/j.egypro.2014.03.226.

[21] C. R. Harris, K. J. Millman, S. J. van der Walt, R. Gommers, P. Virtanen, D. Cournapeau, E. Wieser, J. Taylor, S. Berg, N. J. Smith, R. Kern, M. Picus, S. Hoyer, M. H. van Kerkwijk, M. Brett, A. Haldane, J. F. del Río, M. Wiebe, P. Peterson, P. Gérard-Marchant, K. Sheppard, T. Reddy, W. Weckesser, H. Abbasi, C. Gohlke, and T. E. Oliphant, "Array programming with NumPy," *Nature*, vol. 585, no. 7825, pp. 357–362, 2020. DOI: 10.1038/s41586-020-2649-2.

[22] P. Virtanen, R. Gommers, T. E. Oliphant, M. Haberland, T. Reddy, D. Cournapeau, E. Burovski, P. Peterson, W. Weckesser, J. Bright, S. J. van der Walt, M. Brett, J. Wilson, K. J. Millman, N. Mayorov, A. R. J. Nelson, E. Jones, R. Kern, E. Larson, C. J. Carey, I. Polat, Y. Feng, E. W. Moore, J. VanderPlas, D. Laxalde, J. Perktold, R. Cimrman, I. Henriksen, E. A. Quintero, C. R. Harris, A. M. Archibald, A. H. Ribeiro, F. Pedregosa, and P. van Mulbregt, "SciPy 1.0: fundamental algorithms for scientific computing in Python," *Nature Methods*, vol. 17, no. 3, pp. 261–272, 2020. DOI: 10.1038/s41592-019-0686-2.

[23] A. Häberle, S. Scherer, M. Berger, and J. Farian, *FRESNEL CSP TECHNOLOGY: state of the art and market overview*. Brasilia: Projeto Energia Heliotérmica, Ministério da Ciência, Tecnologia e Inovação (MCTI-BRASIL), Deutsche Gesellschaft für Internationale Zusammenarbeit (GIZ), Projects in Solar Energy (PSE AG), 2014. [Online]. Available: https://shorturl.at/knyA6.

[24] M. Cagnoli, D. Mazzei, M. Procopio, V. Russo, L. Savoldi, and R. Zanino, "Analysis of the performance of linear Fresnel collectors: Encapsulated vs. evacuated tubes," *Solar Energy*, vol. 164, pp. 119–138, 2018. DOI: 10.1016/j.solener.2018.02.037.

[25] D. Buie, A. Monger, and C. Dey, "Sunshape distributions for terrestrial solar simulations," *Solar Energy*, vol. 74, no. 2, pp. 113–122, 2003. DOI: 10.1016/S0038-092X(03)00125-7.

Nomenclature

Abbreviations

RMS	Root Mean Square

Latin Letters

[**A**,**B**]	The Euclidean distance between points **A** and **B**
F	The aim point at the receiver. The tracking point of a primary mirror

$\mathbf{M}$	The center point of a primary mirror
f	Focusing distance of a primary mirror: $f = [\mathbf{F},\mathbf{M}]$
f_m	Focal length of a parabolical primary mirror
H	Tracking point height above the primary
w	Primary mirror width
R	Curvature radius of a cylindrical primary mirror
z_p	Shape function of a parabolical primary mirror
z_c	Shape function of a cylindrical primary mirror
$\vec{v}_f$	Primary mirror focusing vector: $\vec{v}_f = \mathbf{F} - \mathbf{M}$
$\vec{S}_T$	Projection of the incidence sunlight direction in the transversal plane

Greek Letters

λ	Primary mirror angular position
θ_T	Transversal incidence angle
θ_d	Curvature design position. A transversal incidence angle
δ_{es}	RMS width of the effective source distribution
δ_{sun}	RMS width of the sunshape distribution
δ_{opt}	RMS width of the overall optical error distribution
ξ	Local surface slope
$\Delta\xi$	Slope deviation
δ_ξ	RMS slope deviation
$\delta_{\xi,max}$	Maximum RMS slope deviation
τ	Primary mirror tracking angle

Chapter 5

On the radius of the primary mirrors[†]

Abstract

The curvature radius design of linear Fresnel primary mirrors relates to two possible configurations: non-uniform, where each mirror has a particular radius value, and uniform, where all mirrors have the same value. Different non-uniform designs have been proposed but never compared to understand their differences or whether these differences exist. Moreover, it is unclear how much performance loss would result from using a simpler uniform curvature design, particularly concerning the tolerance to optical errors. This study aims to fill these gaps by comparing the annual average optical efficiency and acceptance angle of different curvature radius design propositions for two study cases. The results reveal that the sun reference is the fair option among the non-uniform designs since it offers annual efficiency with deviations less than 0.4% to the maximum but also shows a higher tolerance to optical errors, outperforming other options in terms of acceptance angle. In contrast, uniform curvature designs, while simpler in terms of manufacturing, operation, and maintenance, exhibit lower overall optical performance. Compared to the optimum non-uniform design, the best uniform configuration shows a reduction in annual efficiency by up to 1.9% and a higher drop in acceptance by up to 15%. Notably, these optimum designs (uniform and non-uniform) allow for a simplified determination of mirror radii without needing time-intensive performance evaluations such as ray-tracing.

Keywords: Linear Fresnel collector, Geometric design, Primary mirrors radius.

[†]A. V. Santos, D. Canavarro, P. Horta, and M. Collares-Pereira, "Assessment of the optimal curvature radius of linear Fresnel primary mirrors", Solar Energy, vol. 270, p. 112 376, 2024. https://doi.org/10.1016/j.solener.2024.112376.

5.1 Introduction

The design of linear Fresnel primary mirrors involves selecting a curved profile (typically parabolic or cylindrical) and determining an appropriate curvature value. Chapter 4 dealt with the shape selection and demonstrated that parabolic and cylindrical shapes are indistinguishable from the receiver perspective. Consequently, this chapter focuses exclusively on determining the appropriate curvature value.

For this task, the analysis considers the case of cylindrical mirrors due to their greater potential for reducing manufacturing costs and since their geometry is defined solely by the radius of curvature. Two primary field configurations are possible: uniform (all mirrors share the same curvature radius) and non-uniform (each mirror has its own specific radius). The corresponding literature involves two approaches: analytical and optimization studies. Many works have been published, different designs for the non-uniform curvature case have been proposed, and the optimum uniform design was also addressed. Nevertheless, it is possible to identify issues that need further discussion.

Different non-uniform design propositions were never confronted to understand their differences in energy yield (or whether they exist). Boito and Grena's [1, 2] results of optimum curvature were not compared with the sun and specific reference designs proposed by Abbas and Martínez-Val [3, 4]. It is also unknown whether a different design position other than those two gives the true optimum. Furthermore, some designs neglect optical losses as influencing factors, which might not be accurate. In this sense, the following research questions are then proposed to address these open subjects:

- can a design position better than specific and sun references be achieved?
- is the annual optical efficiency of the optimum design position the same as the one obtained by an optimum search algorithm where curvatures are variables to maximize the annual efficiency?
- are these results following the yield of Boito and Grena's design?

The uniform curvature configuration was addressed by parametric analysis [5–7], gradient-based methods [1, 2], and computational intelligence approaches [8, 9]. These studies were fruitful in their particular cases, but only Pulido-Iparraguirre et al. [7] presented a design tool – the curvature radius of the farthest heliostat with a specific reference – to be used by others in designing a primary field. Nevertheless, Moghimi et al. [6] found an optimum value with a higher curvature radius than the one resulting from this design tool. Moreover, some studies [1, 6] found that an optimum uniform curvature configuration has a slightly lower performance than a non-uniform design. This result might be due to a comparison to a non-uniform configuration that is not the true optimum. In this sense, the performance reduction of the uniform design needs further discussion, not only from the energetic (optical efficiency) point of view but also from the differences in the tolerance to optical errors, i.e., the acceptance angles. For this matter, the following research questions are then proposed:

- is the slight performance drop a feature of optimum uniform designs?
- does Iparraguirre's design tool for the uniform curvature approximate the optimum performance?

To address all established research questions, the remainder of this chapter begins with a detailed methodological outline, describing design approaches, optical method, comparison metrics, and relevant boundary conditions. Subsequently, results and discussions are

presented, first for non-uniform designs and then for the uniform configuration. Finally, conclusions are drawn, highlighting key insights and practical recommendations based on the comparative analyses.

5.2 Materials and methods

5.2.1 Overview

The design of the curvature radius of linear Fresnel primary mirrors follows two major distinct paths: each mirror is designed independently, resulting in a non-uniform curvature configuration (i.e., each mirror has a particular curvature value), or a uniform configuration is considered, where all mirrors have the same curvature value. Whereas the first path finds an optimization procedure by a univariate parametric analysis of the curvature radius of each primary mirror on the concentrator annual optical efficiency – the NUN-OR –, the later path presents as the optimization routine a univariate parametric analysis of a single value of curvature radius on the annual optical efficiency – the UN-OR.

This chapter presents an assessment of both uniform and non-uniform curvature designs by comparing Rabl's general analysis [10], specific and sun reference approaches [3], Boito and Grena's (BG) design [2], the non-uniform optimization routine (NUN-OR), and the uniform optimization routine (UN-OR). These designs are applied to two base geometries defined in Subsection 5.2.4 and are evaluated optically as detailed in Subsection 5.2.5. The assessment considers two annual performance metrics: optical efficiency and acceptance half-angle. The next two subsections provide detailed descriptions of Rabl's and Boito and Grena's designs.

5.2.2 Rabl's design

Rabl [10] presented a general analysis to determine the curvature radius R of a cylindrical mirror so that all incident (collimated) sunlight at its aperture is reflected in a desired aim-point for the design position, θ_d, a particular transversal incidence angle. Equation 5.1 define the value of R as function of f, the distance between mirror center point and the aim at the receiver, where $\mu = (\theta_d - \lambda)/2$, and λ is the mirror angular position as given by Equation 2.9 and illustrated in Figure 2.4.

$$R = \frac{2f}{\cos \mu} \tag{5.1}$$

Therefore, R varies with θ_d, and so the concentrator performance. The specific and sun references were defined by Abbas and Martínez-Val [3] and stated as the two main design positions. Their corresponding procedures were already detailed in Subsection 4.2.2 and are not repeated here for the sake of conciseness.

5.2.3 Boito and Grena's design

Boito and Grena [2] computed the curvature radius of a single heliostat (without its neighbors) that gives the maximum annual optical efficiency for a wide range of positions, $0° \leq \lambda \leq 63.4°$, and locations given by different latitudes, $0° \leq \phi \leq 60.0°$, considering a 4.56 mrad half-width pillbox sunshape without optical errors. Then, results were fitted to present the optimum radius R as a function, Equation 5.2, of the local latitude, ϕ, and the

mirror relative position to its tracking point at the receiver, i.e., parameters m and H in Figure 2.4. Computing a single primary mirror without its neighbor neglects shading and blocking losses.

$$R = 2H \left[a_\phi + b_\phi \left(\frac{|m|}{H} \right)^{1.6} \right] \tag{5.2}$$

In Equation 5.2, a_ϕ and b_ϕ are fitting coefficients, functions of the local latitude, ϕ (in radians), as given by Equation 5.3.

$$\begin{aligned} a_\phi &= 1.0628 + 0.0467\phi^2 \\ b_\phi &= 0.7448 + 0.1394\phi^2 \end{aligned} \tag{5.3}$$

5.2.4 Geometric configurations

The evaluation of the different curvature designs involves the analysis of two study cases based on the model presented in Figure 2.3, but with uniform width ($w_i = w$) and uniform displacement between two neighbor mirrors ($s_i = s$), as shown in Table 5.1. For the sake of this assessment, the absorber is flat, horizontal, centered regarding the primary field, and stands for the aperture of the secondary optic, so that here $H_R = H$. The aim-point of the primary mirrors is the midpoint of the flat receiver, whose width is given by W_s.

Table 5.1: Geometric configurations of the analyzed Linear Fresnel Collectors (LFCs). A length in the longitudinal direction of 120 m was also considered.

Geometry	n [-]	s [m]	w [m]	H_R [m]	W_s [m]	FF [-]
LFC 1	16	1.054	0.75	7.9	0.34	0.725
LFC 2	20	0.832	0.75	7.9	0.34	0.906

In Table 5.1, FF stands for the primary field filling factor, a packing measure, defined as the ratio between net and gross aperture when all mirrors are at the horizontal position. A higher filling factor means a denser primary field; that is, a higher number of mirrors for the same field width. It also implies higher shading and blocking losses [11].

5.2.5 Optical evaluation

The optical analysis measures the concentrator optical efficiency for a given incidence direction. The calculation used in this chapter considers the analytical method developed in Chapter 3. However, here, end-losses are not computed since the curvature radius of the (linear) primary mirrors does not affect the longitudinal behavior of the concentrator.

The annual optical efficiency, $\bar{\eta}$, is defined as the ratio between absorbed and available energy. It is calculated based on McIntire's factorization [12], and is given by:

$$\bar{\eta} = \frac{\sum_{h=1}^{8760} \eta_T(\theta_T^h)\eta_L(\theta_{LS}^h) I_b^h}{\eta_0 \sum_{h=1}^{8760} I_b^h}, \tag{5.4}$$

where η_T and η_L are the transversal and longitudinal instantaneous optical efficiencies, respectively. Bernhard's approach [13] with the longitudinal-solar angle, θ_{LS}, is used to

approximate the bi-axial efficiency from the factorized model [14, 15], and primary mirrors reflectivity and receiver absorptivity as with ideal properties (i.e., equal to 1). Moreover, I_b represents the beam irradiance (or Direct Normal Irradiance (DNI)); θ_T and θ_{LS} are the transversal and longitudinal-solar incidence angles, respectively; η_0 is the optical efficiency at normal incidence, and h represents an index that ranges within all 8760 hours of the year.

The sun reference [3] is the weighted average of positions in the transversal plane for the whole year, as given by Equation 5.5.

$$\bar{\theta}_T = \frac{\sum_{h=1}^{8760} \theta_T^h I_b^h}{\sum_{h=1}^{8760} I_b^h} \tag{5.5}$$

The other optical metric used in this work is the acceptance half-angle: θ_a. It is based on the off-axis incidences for which the concentrator collects 90% of its on-axis power, in both clockwise, θ_a^+ , and counter-clockwise, θ_a^-, directions, where $2\theta_a = \theta_a^+ - \theta_a^-$. This definition is usually used for concentrators in which the transmission-acceptance curve does not have the ideal pillbox profile (as in the compound parabolic concentrator) [16, 17].

In this chapter, acceptance angle computations are based on efficiencies for off-axis incidences of a particular transversal incidence θ_T (with $\theta_L = 0$). The primaries are tilted at the correspondent tracking position for θ_T, and no further tracking is done for the off-axis incidences. Considering this definition and incidence dependent optical effects, the acceptance half-angle θ_a depends on θ_T. The annual average acceptance half-angle, $\bar{\theta}_a$, is then defined as a weighted measure based on the annual distribution of incidences in the transversal plane and the correspondent flux at the receiver, according to Equation 5.6.

$$\bar{\theta}_a = \frac{\sum_{h=1}^{8760} \theta_a(\theta_T^h)\eta_T(\theta_T^h)I_b^h}{\sum_{h=1}^{8760} \eta_T(\theta_T^h)I_b^h} \tag{5.6}$$

The evaluations of $\bar{\eta}$ and $\bar{\theta}_a$ involve hourly data from typical meteorological year regarding beam irradiance from the PVGIS application program interface of the pvlib library [18]. Solar position is then calculated based on the algorithm proposed by Reda and Andreas [19], and converted to θ_T and θ_{LS} for two types of field orientations: North-South (NS) and East-West (EW) mountings, as defined in Section B.1. These computations considers two locations, Evora (Portugal) and Aswan (Egypt), whose data are summarized in Table 5.2.

Table 5.2: Main data of the two simulated locations.

Location	Latitude	Longitude	Annual sum of DNI
Evora	38.5°	-8.0°	1994.8 kWh $\cdot$ m^{-2} $\cdot$ yr^{-1}
Aswan	24.1°	32.9°	2784.1 kWh $\cdot$ m^{-2} $\cdot$ yr^{-1}

Moreover, these optical evaluations consider the two Effective Sources (ESs) shown in Table 5.3, where Δ_{sun} and σ_{sun} stands for the half-width and standard deviation of pillbox and Gaussian sunshape profiles, respectively; σ_{opt} represents the standard deviation of a Gaussian overall error, and δ_{es} stands for the source Root Mean Square (RMS) width (refer to Subsection B.2.4).

Table 5.3: Effective sources considered in the optical evaluation.

Source	Sunshape	Optical errors	δ_{es}
ES1	Pillbox: $\Delta_{sun} = 4.65$ mrad	None	3.3 mrad
ES2	Gaussian: $\sigma_{sun} = 2.8$ mrad	Gaussian: $\sigma_{opt} = 5.0$ mrad	8.10 mrad

5.3 Results and discussion

5.3.1 Non-uniform designs

Among the non-uniform design propositions, which one yields the highest annual optical efficiency? Figure 5.1 shows results for Evora (refer to Table 5.2), with North-South (NS) and East-West (EW) orientations and the two effective sources (ESs) shown in Table 5.3. It indicates that the sun reference is a better design than the specific reference – as already observed by Abbas and Martínez-Val [3]. The optimum design position, θ_d^*, yields an annual efficiency, $\bar{\eta}^* = \bar{\eta}(\theta_d^*)$, very close to the sun reference design. Boito and Grena's (BG) design only yields a higher efficiency than $\bar{\eta}^*$ at the particular conditions it was developed: NS-mounting and a (≈ 4.65 mrad half-width) pillbox sunshape without optical errors, as shown in Figure 5.1a. Finally, the NUN-OR design yields the highest annual efficiency, as expected.

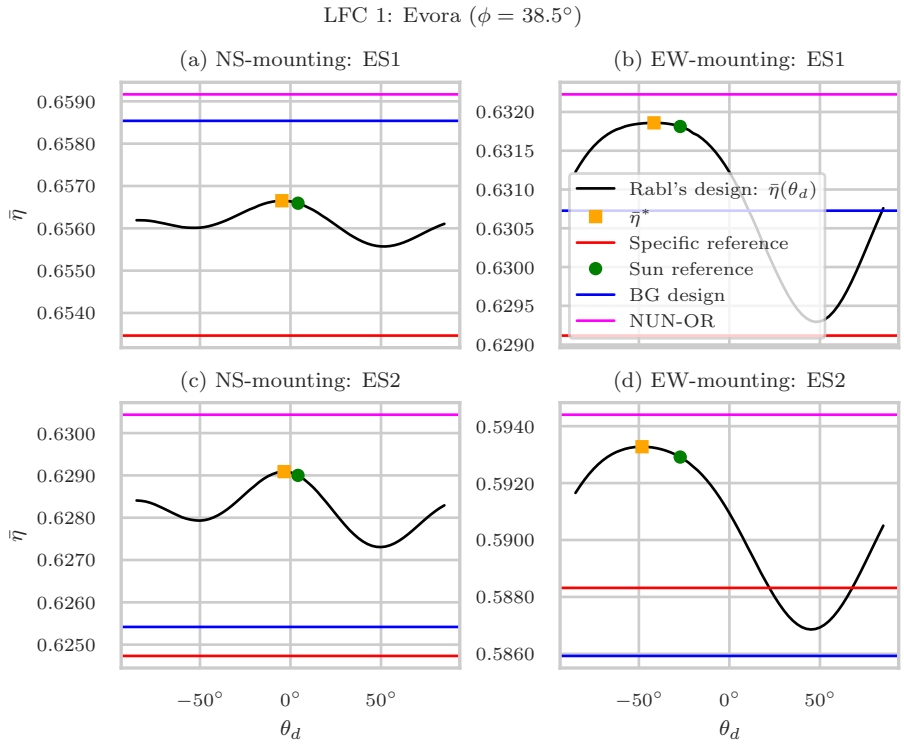

Figure 5.1: Annual optical efficiency results of non-uniform curvature radius designs for Evora (refer to Table 5.2). It considers the geometry LFC 1 shown in Table 5.1, both effective sources presented in Table 5.3, and shows a comparison for (a) NS-mounting and ES1, (b) EW-mounting and ES1, (c) NS-mounting and ES2, (d) EW-mounting and ES2. As shown, Rabl's design is a function of θ_d, the design position. θ_d^* is the optimum design position, so that $\bar{\eta}^* = \bar{\eta}(\theta_d^*)$. θ_d^* and sun reference hold particular values of θ_d, and are represented by an yellow square and a green dot, respectively. Specific reference, BG and NUN-OR designs are not dependent on θ_d and are represented by horizontal lines.

In general, results in Figure 5.1 also show that the design position of a sun reference for NS-mounting is practically 0°(the zenithal reference), but it substantially changes for the EW cases; NS-mounting yields higher annual efficiency than the EW cases and is less sensitive to variations in the design position concerning Rabl's design.

Although the NUN-OR design yields the highest efficiency, the differences to other non-uniform designs are not that high. Indeed, Figure 5.2 details the relative difference in annual optical efficiency of non-uniform designs regarding the NUN-OR, considering the values in Figure 5.1. It shows that deviations are lower than 0.9% and 1.5% for NS and EW cases, respectively, for Evora. Moreover, sun reference and optimum design position are analogous since both cases yield virtually the same efficiency; deviations of sun reference regarding the NUN-OR are lower than 0.4% – see Figure 5.2a – and are even lower for the case of ES2 (a more realistic model) – see Figure 5.2b; an EW-mounting is more sensitive to curvature radius design, as deviations increase from a simple modeling (ES1) to more realistic conditions of sunshape and optical errors (ES2); BG design also declines with ES2.

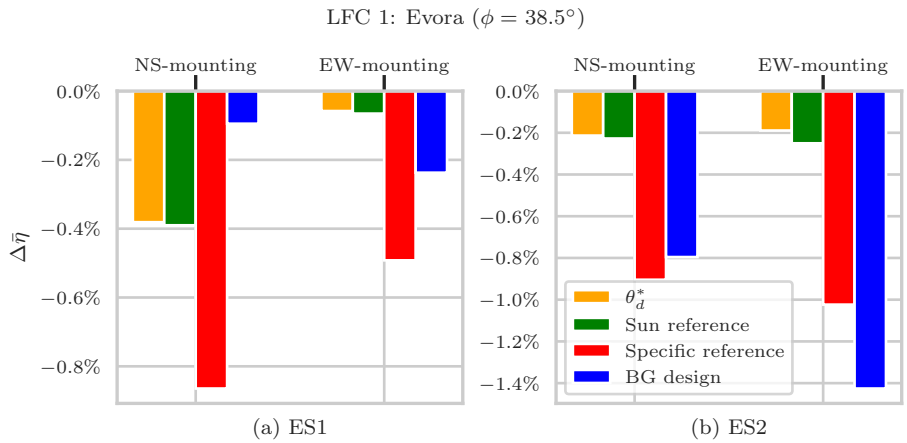

Figure 5.2: Percentual variation of annual optical efficiency for different non-uniform curvature radius designs regarding the NUN-OR. It shows deviations for efficiency values of Fig. 3: the case of geometry LFC 1 and for Evora for both sources shown in Table 5.3.

Considering now a different location, Figure 5.3 shows results for Aswan. It is clear the same trend observed before: sun reference yields higher values of efficiency than specific reference and is virtually the optimum design position; BG design only gives higher efficiency than the sun reference for certain conditions; the NUN-OR yields the highest value in all cases.

Regarding non-uniform curvature designs, considering the results in Figures 5.2 and 5.3, it is possible to state that the sun reference is virtually the best design position. It also yields an annual optical efficiency very close to the true optimum value – the results show reductions lower than 0.4%. Furthermore, Boito and Grena's design only yields an efficiency value closer to the true optimum in the conditions that it was developed (an NS-mounting and a 4.65 mrad half-width pillbox sunshape) – a quite simple model of an effective source.

Another aspect is that Rabl's and BG's propositions neglect shading and blocking as influencing factors. In other words, primary mirrors are designed independently, without accounting for adjacent mirrors. A first look in the results depicted in Figures 5.2a and 5.3a would suggest that these losses may indeed be neglected, as the BG design closely approaches the true optimum. However, this conclusion can be further analyzed through a reasonable hypothesis: if shading and blocking losses significantly impact curvature design, the deviation of Rabl's and BG's designs from the true optimum would be more pronounced in a primary field geometry characterized by higher shading and blocking losses.

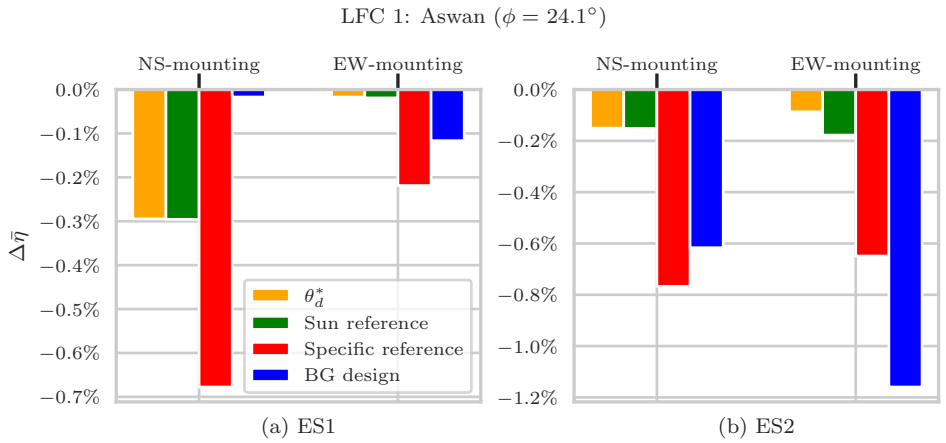

Figure 5.3: Percentual variation of annual optical efficiency for different non-uniform curvature radius designs regarding the NUN-OR. It shows the case of geometry LFC 1 and for Aswan for both sources shown in Table 5.3.

In this context, Figure 5.4 shows deviations of annual optical efficiency regarding the NUN-OR (true optimum) of the LFC 2 geometry for Aswan – Montes et al. [11] showed that a higher filling factor increases shading and blocking losses (refer to Table 5.1). This figure indicates that the differences among the non-uniform designs did not increase. The deviation between the higher and lowest values of $\bar{\eta}$ remain quite low: maximum deviation is still lower than 0.9%. Therefore, shading and blocking can be neglected in this regard, and Rabl and BG designs do not fall by increasing the filling factor of the primary field.

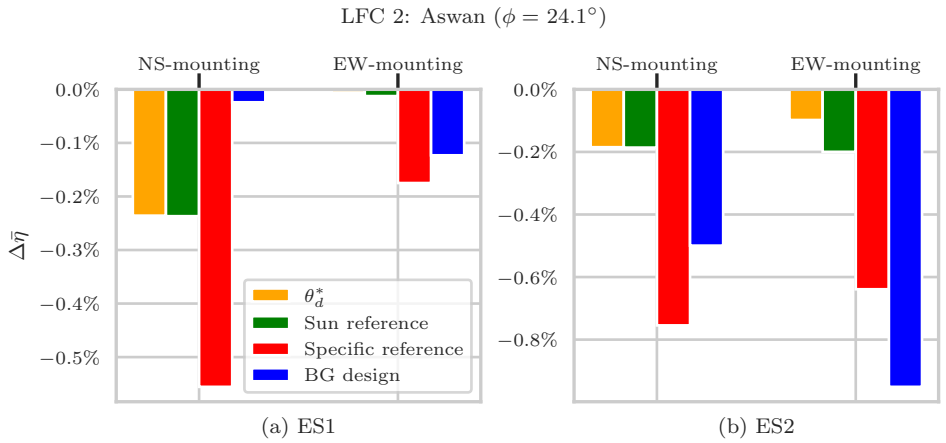

Figure 5.4: Percentual variation of annual optical efficiency for different non-uniform curvature radius designs regarding the NUN-OR. It shows the case of geometry LFC 2 and for Aswan for both sources shown in Table 5.3.

The above results show that non-uniform curvature designs slightly differ in terms of annual optical efficiency. On the other hand, they can also be evaluated by the acceptance angle – a measure of the optic tolerance to optical errors, so that a higher acceptance means that the concentrator can be manufactured with cheaper materials and methods, which implies cost reduction without efficiency drops.

Figure 5.5 shows the values of the acceptance half-angle, θ_a, as a function of the curvature designs and the transversal incidence angle, θ_T, for Evora, considering LFC 1 and both effective sources presented in Table 5.3. As can be seen, regardless of the curvature design,

the acceptance half-angle varies with the transversal incidence angle θ_T, and that deviations among them are higher than those for the annual optical efficiency.

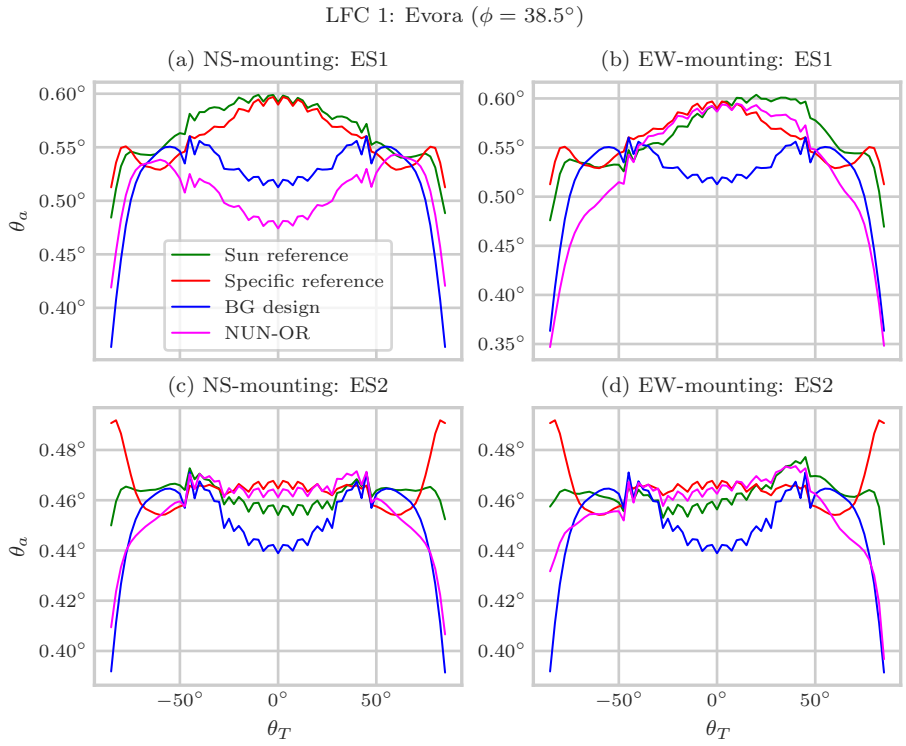

Figure 5.5: Acceptance half-angle as a function of the transversal incidence angle, considering Evora as the location and the LFC 1 geometry. The picture presents a comparison of all non-uniform designs for (a) NS-mounting and ES1, (b) EW-mounting and ES1, (c) NS-mounting and ES2, and (d) EW-mounting and ES2.

Considering the simple effective source model represented by ES1, it is clear that specific and sun references outperforms all other designs for a NS-mounting, as shown in Figure 5.5a; for the EW-mounting, the NUN-OR design come closer and now the BG design clearly presents the worse performance among the non-uniform designs, as shown in Figure 5.5b.

On the other hand, these results changes for the case of ES2, a more realist source model. As shown in Figures 5.5c and 5.5d, the difference among the designs are diluted for both NS and EW cases – for example, no significantly differences between sun and specific references are now seen; the profiles are now more constant and have a lower variation with θ_T; the BG design clearly presents the worse performance among the non-uniform designs for a wide range of incidences. Furthermore, it is clear that sun reference design for an East-West case produces a non-symmetric primary field, as highlighted in the corresponding profiles shown in Figures 5.5b and 5.5d.

Nevertheless, it is possible to present a direct comparison of these non-uniform curvature designs by the averaged acceptance value, $\bar{\theta}_a$, defined in Equation 5.6. These results are presented in Figure 5.6, for Evora, and considering the geometry LFC 1. In general, the BG design has the worst performance; differences among the designs are more significant than in the case of efficiency: up to 13.8%, as shown in Figure 5.6b, but are only up to 2.2% in the case of a more realist source model, as shown in Figure 5.6d. Moreover, sun and specific references yield the higher values of average acceptance in all cases shown in Figure 5.6.

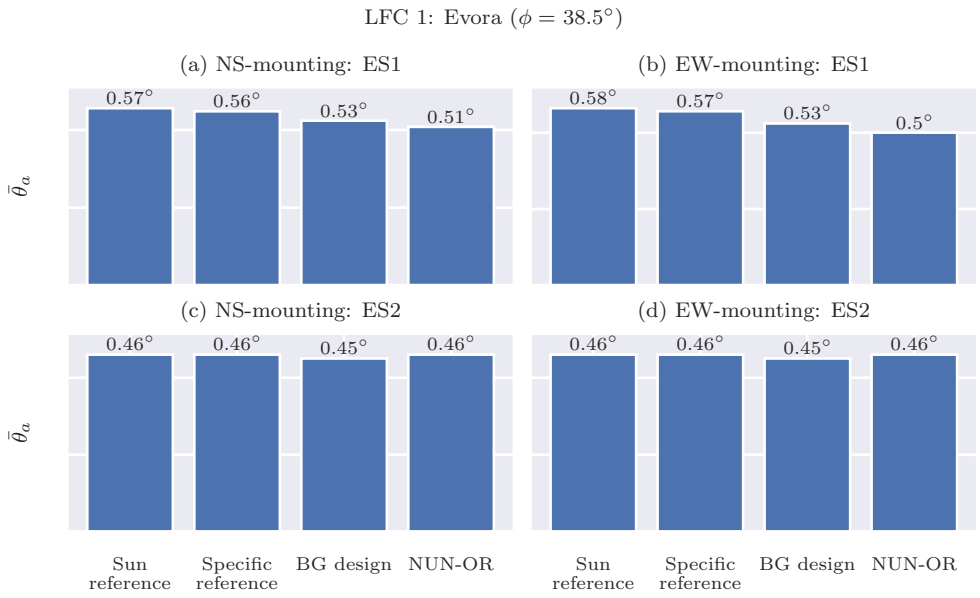

Figure 5.6: Annual average acceptance half-angle for (a) NS-mounting and ES1, (b) EW-mounting and ES1, (c) NS-mounting and ES2, and (d) EW-mounting and ES2. It presents a comparison of non-uniform designs, considering Evora and the LFC 1 geometry.

5.3.2 Uniform design

The uniform curvature configuration considers a single value of curvature radius for whole the primary field. The optimum radius can be determined by a univariate parametric analysis on the annual optical efficiency of the concentrator, an optimization procedure here denominated as the UN-OR design.

Figure 5.7 compares the annual averaged optical efficiency by presenting the relative differences between the annual efficiencies of the UN-OR and sun-reference designs, both relative to the NUN-OR. It is evident that the UN-OR consistently exhibits a lower efficiency than the NUN-OR design (always negative values), with deviation values in the same order of magnitude as worst case of non-uniform designs: up to 1.8%, as shown in Figure 5.7b. Furthermore, the results indicate that EW-mountings are more sensitive to the uniform radius design, showing greater deviations than NS cases across all effective sources and locations. Additionally, Figures 5.7b and 5.7d highlight that incorporating a more realistic modeling of sunshape and optical errors leads to higher deviations of the UN-OR regarding the NUN-OR.

Figure 5.7 also shows that the UN-OR can even surpass the sun reference design (a non-uniform design), but it only occurs for NS-mounting and a simple model of effective source (ES1) – see Figures 5.7a and 5.7c. In the case of a more realistic source model (ES2), the sun reference always outperforms the UN-OR design – see Figures 5.7b and 5.7d. While similar results were obtained for the LFC 2 geometry, they are omitted here for conciseness.

The outcomes in Figure 5.7 follow the findings of previous studies concerning the performance reduction of the optimum uniform configurations over non-uniform designs. Moghimi et al. [6] found a reduction of 3.4% when compared to the specific reference design but for a daily efficiency metric, and Boito and Grena [1] found a reduction of 2.7% but in an objective function that incorporates cost considerations. Thus, the minor decrease in annual optical efficiency when compared to the non-uniform optimum characterizes a distinctive attribute of the optimum uniform design.

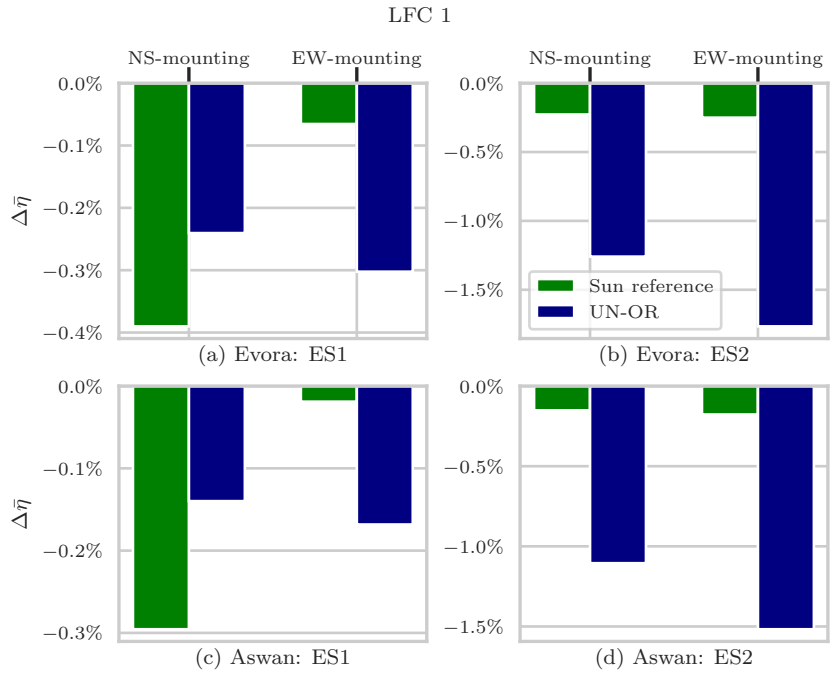

Figure 5.7: Percentual variation of annual optical efficiencies for sun reference and UN-OR designs regarding the NUN-OR, considering the LFC 1 geometry shown in Table 5.1. It shows deviations for the case of geometry LFC 1 and for Evora and Aswan for both sources shown in Table 5.3.

Concerning acceptance results, Figure 5.8 presents a comparison of annual average half-acceptance among three designs: sun reference, NUN-OR, and the UN-OR. As in the case of the optical efficiency, the UN-OR design presents the lowest performance, but now the differences are higher: up to 15%, as shown in Figure 5.8a, i.e., the simpler source model (ES1). On the other hand, for ES2 these deviations are lower: 4.3% for NS and 6.5% for EW-mounting, as shown in Figures 5.8c and 5.8d, respectively. In this sense, these results indicates that the EW-mounting is more sensitive to the uniform curvature radius concerning the concentrator tolerance to optical errors.

These uniform curvature design results mean that a single curvature radius for the whole primary field would imply a more significant drop in the tolerance to optical errors (acceptance half-angle) than in the efficiency. Similar results were obtained for Aswan, and also for the LFC 2 geometry – they are omitted here for conciseness.

Non-uniform designs such as specific and sun references, as well as the BG design, are characterized by simple equations, as detailed in Section 5.2. However, the literature concerning the uniform design still lacks a tool to guide the calculation of an optimum value for the whole primary field.

Currently, the sole suggestion is the one by Pulido-Iparraguirre et al. [7]: to adopt a uniform radius equivalent to that of the farthest mirror based on a specific reference design, which entails setting the curvature radius as twice the distance from the farthest mirror to the aim-point at the receiver. However, Moghimi et al. [6] achieved an optimal radius with a different value that of this design tool; a further analysis on Pulido-Iparraguirre's work shows that only a short interval of radiuses was tested, and that the best value lies in the upper edge of the interval. These two facts suggest that a further analysis should be done regarding this subject.

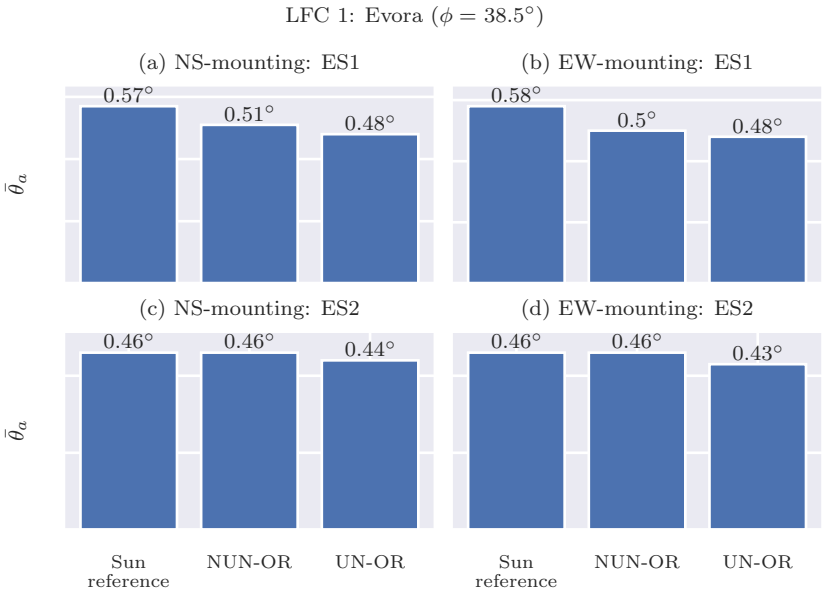

Figure 5.8: Comparison of annual average acceptance half-angle for (a) NS-mounting and ES1, (b) EW-mounting and ES1, (c) NS-mounting and ES2, and (d) EW-mounting and ES2. It considers Evora and the LFC 1 geometry to compare sun reference, optimum non-uniform (NUN-OR) and optimum uniform (UN-OR) designs

In this sense, Figure 5.9 depicts the data from the UN-OR design for the LFC 1, considering Evora. It shows how the concentrator annual efficiency varies as function of the uniform curvature radius of the primary field (the blue solid line), as well as the radius interval defined by a specific reference design for the closest and farthest mirrors (red dashed lines).

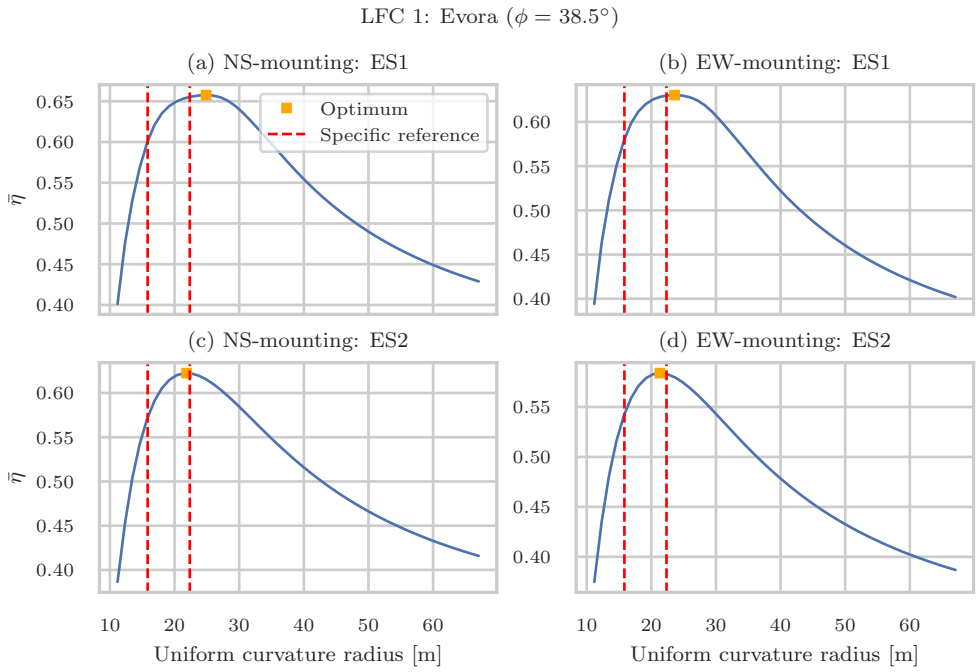

Figure 5.9: Parametric analysis of the uniform curvature radius on the annual optical efficiency. It considers the case of geometry LFC 1 for Evora.

Figure 5.9 shows that the radius that yields the highest efficiency (yellow square) is not

exactly the one of the farthest mirror at a specific reference design but is close to it. Indeed, the optimum uniform radius can be lower (Figures 5.9c and 5.9d) or higher (Figures 5.9a and 5.9b) than this reference value, depending on the effective source model. Nevertheless, adopting the uniform radius as the one derived from the farthest mirror using the specific reference design would lead to only a marginal reduction in annual optical efficiency compared to the optimal solution, amounting to a mere 0.15% – as illustrated in Fig. 12d. Comparable outcomes were obtained for Aswan and the LFC 2 geometry; however, for conciseness, these results are not presented here. Thus, this design approach seem as a reasonable proposition.

5.4 Conclusions

Regarding the non-uniform curvature design, the sun reference is a very reasonable choice. It is virtually the best design position, yields practically the highest annual optical efficiency (deviations are lower than 0.4% to the maximum value), and has an obvious advantage in terms of tolerance to optical errors (acceptance angle) to the other design options. Moreover, mirrors radiuses are defined by a simple equation and does not involve performance evaluations that could be very time-consuming: e.g., if ray-tracing is the optical method.

Another curvature design option is when all mirrors have the same radius – the uniform configuration. The results on this case indicate that the optimum uniform configuration has a lower overall optical performance compared to the optimum non-uniform design, with values of annual efficiency reduced by up to 1.9% and drops of tolerance to errors one order of magnitude higher, up to 15%. Moreover, the use of a uniform radius value as twice the distance of the farthest mirror to the aim-point at the receiver is a very reasonable design tool since it is very close to the actual optimum radius and yields an efficiency only 0.2% lower than the optimum uniform case.

In general, this chapter presents results that contribute to fill an empirical gap by comparing different propositions of curvature radius designs. Furthermore, it also give important insights on the influence of these different designs on the concentrator tolerance to optical errors, a novel result to be added to the literature on the design of linear Fresnel collectors.

References

[1] P. Boito and R. Grena, "Optimization of the geometry of Fresnel linear collectors," *Solar Energy*, vol. 135, pp. 479–486, 2016. DOI: 10.1016/j.solener.2016.05.060.

[2] P. Boito and R. Grena, "Optimal focal length of primary mirrors in Fresnel linear collectors," *Solar Energy*, vol. 155, pp. 1313–1318, 2017. DOI: 10.1016/j.solener.2017.07.079.

[3] R. Abbas and J. Martínez-Val, "Analytic optical design of linear Fresnel collectors with variable widths and shifts of mirrors," *Renewable Energy*, vol. 75, pp. 81–92, 2015. DOI: 10.1016/j.renene.2014.09.029.

[4] R. Abbas and J. Martínez-Val, "A comprehensive optical characterization of linear Fresnel collectors by means of an analytic study," *Applied Energy*, vol. 185, pp. 1136–1151, 2017. DOI: 10.1016/j.apenergy.2016.01.065.

[5] Y. Qiu, Y. L. He, Z. D. Cheng, and K. Wang, "Study on optical and thermal performance of a linear Fresnel solar reflector using molten salt as HTF with MCRT and FVM methods," *Applied Energy*, vol. 146, pp. 162–173, 2015. DOI: 10.1016/j.apenergy.2015.01.135.

[6] M. Moghimi, K. Craig, and J. Meyer, "Simulation-based optimisation of a linear Fresnel collector mirror field and receiver for optical, thermal and economic performance," *Solar Energy*, vol. 153, pp. 655–678, 2017. DOI: 10.1016/J.SOLENER.2017.06.001.

[7] D. Pulido-Iparraguirre, L. Valenzuela, J.-J. Serrano-Aguilera, and A. Fernández-García, "Optimized design of a Linear Fresnel reflector for solar process heat applications," *Renewable Energy*, vol. 131, pp. 1089–1106, 2019. DOI: 10.1016/j.renene.2018.08.018.

[8] Z. D. Cheng, X. R. Zhao, Y. L. He, and Y. Qiu, "A novel optical optimization model for linear Fresnel reflector concentrators," *Renewable Energy*, vol. 129, pp. 486–499, 2018. DOI: 10.1016/j.renene.2018.06.019.

[9] H. Ajdad, Y. Filali Baba, A. Al Mers, O. Merroun, A. Bouatem, and N. Boutammachte, "Particle swarm optimization algorithm for optical-geometric optimization of linear fresnel solar concentrators," *Renewable Energy*, vol. 130, pp. 992–1001, 2019. DOI: 10.1016/j.renene.2018.07.001.

[10] A. Rabl, *Active Solar Collectors and Their Applications*. New York: Oxford University Press, 1985. [Online]. Available: https://shorturl.at/oGLX6.

[11] M. J. Montes, C. Rubbia, R. Abbas, and J. M. Martínez-Val, "A comparative analysis of configurations of linear Fresnel collectors for concentrating solar power," *Energy*, vol. 73, pp. 192–203, 2014. DOI: 10.1016/j.energy.2014.06.010.

[12] W. R. McIntire, "Factored approximations for biaxial incident angle modifiers," *Solar Energy*, vol. 29, no. 4, pp. 315–322, 1982. DOI: 10.1016/0038-092X(82)90246-8.

[13] R. Bernhard, S. Hein, J. LaLaing, M. Eck, M. Eickhoff, M. Pfaender, G. Morin, and A. Häberle, "Linear Fresnel collector demonstration on the PSA Part II - Commissioning and first performance tests," in *14th International Symposium on Concentrated Solar Power and Chemical Energy Technologies*, 2008. [Online]. Available: https://elib.dlr.de/57087/.

[14] J. D. Hertel, V. Martinez-Moll, and R. Pujol-Nadal, "Estimation of the influence of different incidence angle modifier models on the biaxial factorization approach," *Energy Conversion and Management*, vol. 106, pp. 249–259, 2015. DOI: 10.1016/j.enconman.2015.08.082.

[15] P. Horta and T. Osório, "Optical Characterization Parameters for Line-focusing Solar Concentrators: Measurement Procedures and Extended Simulation Results," *Energy Procedia*, vol. 49, pp. 98–108, 2014. DOI: 10.1016/j.egypro.2014.03.011.

[16] D. Canavarro, J. Chaves, and M. Collares-Pereira, "Simultaneous Multiple Surface method for Linear Fresnel concentrators with tubular receiver," *Solar Energy*, vol. 110, pp. 105–116, 2014. DOI: 10.1016/j.solener.2014.09.002.

[17] J. Chaves, *Introduction to Nonimaging Optics*, 2nd Edition. New York: CRC Press, 2016. DOI: 10.1201/b18785.

[18] W. F. Holmgren, C. W. Hansen, and M. A. Mikofski, "Pvlib python: A python package for modeling solar energy systems," *Journal of Open Source Software*, vol. 3, no. 29, p. 884, 2018. DOI: 10.21105/joss.00884.

[19] I. Reda and A. Andreas, "Solar position algorithm for solar radiation applications," *Solar Energy*, vol. 76, no. 5, pp. 577–589, 2004. DOI: 10.1016/j.solener.2003.12.003.

Nomenclature

Abbreviations

BG	Boito and Grena's curvature radius design
DNI	Direct Normal Irradiance
ES	Effective Source
EW	East-West
LFC	Linear Fresnel Collector
NS	North-South
NUN-OR	Non-uniform curvature radius Optimization Routine
RMS	Root Mean Square
UN-OR	Uniform curvature radius Optimization Routine

Latin Letters

H	Tracking point height above the primary field
H_R	Receiver height above the primary field
I_b	Beam Irradiance. Direct Normal Irradiance (DNI)
m	Horizontal coordinate of a primary mirror center point
w	Primary mirror width
R	Curvature radius of a primary mirror
FF	Filling factor of a primary field

Greek Letters

λ	Primary mirror angular position
$\bar{\eta}$	Annual averaged optical efficiency
η_T	Transversal optical efficiency
η_L	Longitudinal optical efficiency
η_0	Optical efficiency at normal incidence
ϕ	Local latitude
θ_a	Acceptance half-angle
$\bar{\theta}_a$	Annual averaged acceptance half-angle
θ_d	Curvature radius design position. A transversal incidence angle
θ_d^*	Optimum design position
θ_L	Longitudinal incidence angle
θ_{LS}	Longitudinal-solar incidence angle
θ_T	Transversal incidence angle
$\bar{\theta}_T$	Sun reference design position
δ_{es}	RMS width of the effective source distribution
Δ_{sun}	Half-width of a Pillbox sunshape distribution

σ_{opt}	Standard deviation of an overall error Gaussian distribution
σ_{sun}	Standard deviation of a Gaussian sunshape distribution

Indices

h	Hour index

Chapter 6

On secondary optics[†]

Abstract

The Compound Parabolic Concentrator (CPC) is a winner secondary optic in comparison studies and under assessments including efficiency and flux uniformity, although never compared to the Compound Elliptical Concentrator (CEC) and a recently proposed aplanatic design. Moreover, CPC optimum geometries resulting from stochastic optimization needs to be confronted to the theoretical edge-ray designs to better evaluate the necessity of including it in the optimization routine. The developed results indicate that when the efficiency is the solely optimization objective, CPC optimum geometry highly diverge from the edge-ray design, presenting a better efficiency but far lower performance in terms of flux uniformity and acceptance. In a two-objective problem involving efficiency and flux uniformity, optimum geometries for the CPC are now closer to the edge-ray design, particularly if the later considers the same gap size. Indeed, the gap size emerges as an important decision variable in the secondary optic design to play with the trade-off between the optical efficiency, flux uniformity, and acceptance. The comparison results between CPC and CEC edge-ray designs shows that both optics relate to a trade-off between optical efficiency and acceptance – the CPC presents a higher acceptance, the CEC has higher efficiency, whilst results of flux uniformity are practically the same. Regarding the aplanatic design, it poorly performs in terms of acceptance compared to CPC and CEC edge-ray designs, although outperform both in flux uniformity, and is outperformed by the CEC in terms of efficiency.

Keywords: Linear Fresnel collector, Secondary optics design, Optical analysis.

[†]A. Santos, D. Canavarro, C. A. Arancibia-Bulnes, P. Horta, and M. Collares-Pereira, "A comparison of secondary optic designs for linear Fresnel collectors with a single tubular absorber," Solar Energy, vol. 282,p. 112 936, 2024. https://doi.org/10.1016/j.solener.2024.112936.

6.1 Introduction

The secondary optic has a key role to enhance the overall performance of Linear Fresnel Collectors (LFCs) [1–3]. For high-temperature applications such as solar thermal electricity (> 400 ^{o}C) [4, 5], an evacuated tube [6] is the main absorber due to its rather low thermal losses [7, 8]. Thus, this chapter considers the design of secondary optics for LFCs with a single absorber tube, which could be encapsulated by a concentric (evacuated) glass cover.

In this context, the literature comprises several propositions [1, 3, 9–18] but only a few comparison studies [3, 19, 20]. The results from these works indicate the Compound Parabolic Concentrator (CPC) [21] as the best secondary optic, whether in optical efficiency or flux homogeneity. Following the model presented by Oommen and Jayaraman [22], other works [23, 24] have determined stochastic optimized CPC geometries by using computational intelligence algorithms, which does not necessarily obey the edge-ray principle [21, 25]. On the other hand, not using this principle implies adding more decision variables to the linear Fresnel collector design problem. Furthermore, the recently proposed Aplanatic Optic Concentrator (AOC) [16] and the Compound Elliptical Concentrator (CEC) [13] are two secondary optic designs never compared to the CPC optic.

Although optical efficiency is an important performance metric, low circumferential flux homogeneity poses a significant issue in real-world operation, as it can lead to the failure of evacuated tubes by compromising the vacuum seal and increasing thermal losses, or lead to undesired flow regimes in two-phase flows as those occurring in direct steam generation. Previous studies have indicated a trade-off between efficiency and flux uniformity [3, 20, 24]. However, these comparative studies [3, 19, 20] did not include acceptance results – a key metric for evaluating the impact of different secondary optics on a concentrator tolerance to optical errors [25].

Considering the above discussion, the following research questions are proposed to be addressed in this chapter:

- how far are CPC and CEC edge-ray secondaries to the optimized CPC cases reported in the literature?
- how far are CPC and CEC edge-ray secondaries to the AOC?

To address these questions, the remainder of this chapter is structured as follows. It begins by detailing the geometric models and describing non-imaging and aplanatic designs. Next, the ray-tracing framework used to evaluate these optical systems is outlined, along with the definition of the performance metrics of efficiency, circumferential flux uniformity, and tolerance to errors. The results are then presented, starting with a comparison between optimized and edge-ray non-imaging optical designs, followed by an analysis regarding the aplanatic optics, and a discussion concerning optical and position errors. Finally, conclusions are drawn based on the results and analysis presented.

6.2 Analyzed secondary optics

6.2.1 Geometric model

The geometric model considered in this chapter follows the one presented in Figure 2.3 (refer to Section 2.1). However, here the distance between two consecutive centers (the shift) is

represented by d. Thus, accordingly, w stands for the mirror width, H_R for the absorber tube (receiver center) height, R for the curvature radius of the primary mirrors, and n represents the number of mirrors in the primary field. Moreover, r_a stands for the absorber tube radius, and r_{go} for the outer cover radius, when it is the case.

6.2.2 Non-imaging optic designs

Non-Imaging Optics (NIO) designs have been widely used as the secondary optic of linear Fresnel collectors [1, 10, 13]. In general, the design is based on the edge-ray principle, which states that if rays from the edges of the source (the primary field) are reflected onto the edges of the receiver (the absorber tube), all other in between rays will also reach the receiver [21].

Figure 6.1 illustrates the edge-ray design of Compound Parabolic Concentrator (CPC) and Compound Elliptical Concentrator (CEC) as secondary optics for a Linear Fresnel Collector (LFC) with a single absorber tube. Fundamentally, these optics are defined by the edge-rays (green lines) from the primary edges, $\mathbf{F}_1$ and $\mathbf{F}_2$, to the absorber edges, the tangent points $\mathbf{T}_1$ and $\mathbf{T}_2$, as shown Figure 6.1a. As shown in Figure 6.1b, an edge-ray secondary optic is composed of involute and conic sections. A macro focal parabola is the conic of a CPC secondary, whilst a macro focal ellipse is the conic of a CEC optic.

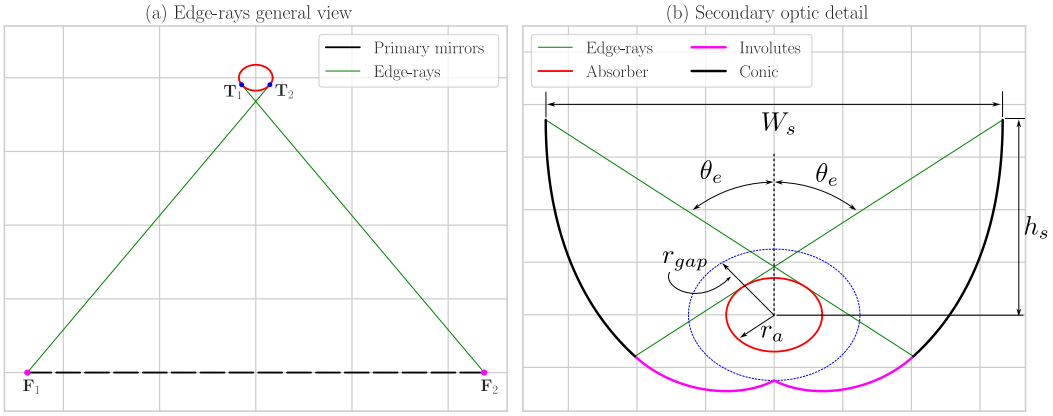

Figure 6.1: Non-Imaging Optics (NIO) designs as the secondary optic of a Linear Fresnel Collector (LFC) with a tubular absorber. It shows (a) the edge-ray principle: rays from the edges of the primary field, $\mathbf{F}_1$ and $\mathbf{F}_2$, to the edges of the absorber tube, the tangent points $\mathbf{T}_1$ and $\mathbf{T}_2$; (b) details of NIO secondaries: a macro focal parabola is the conic of a CPC secondary, whilst a macro focal ellipse is the conic of a CEC optic.

The CPC design is fully defined by the absorber tube radius, r_a, the gap size, r_{gap}, and the angular aperture defined by the edge-rays, θ_e, which corresponds to the acceptance half-angle, θ_a. In this configuration, the secondary mirror reflects, tangentially to the receiver, all rays that are parallel to the defined edge rays – that is, the primary field is modeled as an infinitely large source at an infinite distance. In contrast, the CEC optic is defined by r_a, r_{gap}, and the edge-points of the primary field, $\mathbf{F}_1$ and $\mathbf{F}_2$. It models the primary as a finite source at a finite distance, and all rays leaving $\mathbf{F}_1$ and $\mathbf{F}_2$ are reflected tangentially to the absorber [25]. For the sake of clarity and conciseness, the equations for the involutes and corresponding conics of the CPC and CEC optics are not presented here. However, these equations, along with the complete design procedure, are detailed by Chaves [25].

Figure 6.1b shows an important geometric parameter: r_{gap}, the gap size (or gap radius). In theory, both CPC and CEC optics can be designed to touch the tube, i.e., $r_{gap} = 0$. However,

to avoid thermal short-circuits (the absorber heats up) and due to practical conditions of an absorber with a glass cover, a gap is imposed between the secondary optic and the tube: $r_{gap} \geq r_{go} > r_a$, where r_{go} represents the glass outer cover radius. Alternatively, one can define $\Delta r_g = r_{gap} - r_{go}$ to rule the gap size. Of course, higher gaps mean more optical losses, so that a simple choice is to consider the lowest possible value: $\Delta r_g = 0$.

Oommen and Jayaraman [22] presented a set of simple equations for the CPC optic, which are functions of r_a, r_{gap}, and the acceptance half-angle, θ_a. This model was not presented as a secondary optic design for an LFC, although many studies have used it with this purpose [18–20, 23, 24, 26–28]. In this sense, Oommen's model was used considering θ_a, r_{gap}, and a third parameter, the maximum opening angle, hereafter referred to as θ_{max}, as decision variables to be optimized [23, 24]. That is, this design does not necessarily follow the edge-rays principle since the selected value of θ_a may differ from that of θ_e, with θ_{max} representing a measure for the truncation of the CPC optic. In a non-truncated case (full open optic), $\theta_a + \theta_{max} = 270°$.

Figure 6.2 presents a validation of the implemented models for these non-imaging optic designs. Figure 6.2a reproduces the geometry reported by Qiu et al. [28] based on Oommen's model: $r_a = 0.035$ m, $H_R = 8.0$ m, $r_{gap} = 0.0625$ m, $\theta_a = 56°$, and $\theta_{max} = 193.09°$ (3.37 rad). As can be seen, the implemented functions yield a secondary optic whose aperture width is $W_s = 0.295$ m and displaced $h_s = 0.07$ m from the tube center. These results match the reported data. Furthermore, Figure 6.2b shows a comparison of Chaves' [25] and Oommen's models [22] for the same design conditions: $r_a = 0.035$ m, $r_{gap} = 0.0625$ m, $\theta_a = \theta_e = 60°$, and a full opened optic, i.e., $\theta_a + \theta_{max} = 270°$ ($3\pi/2$). As seen, both models yield the same contour.

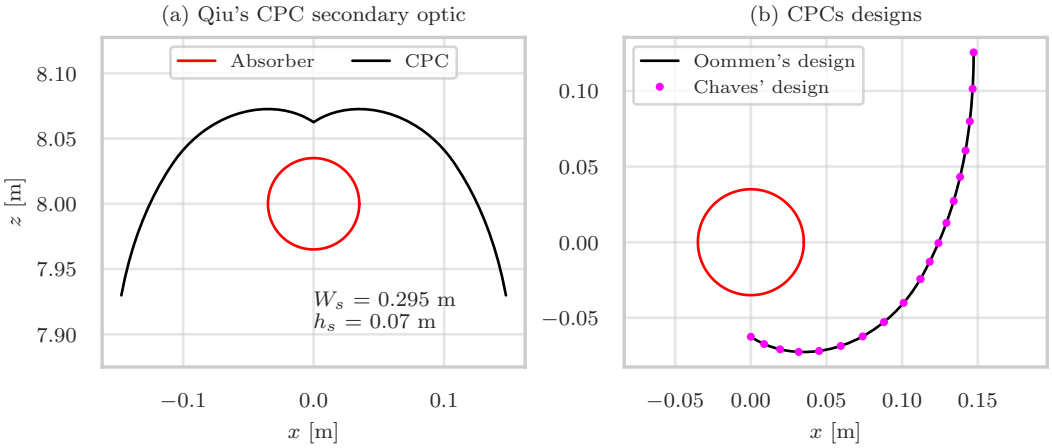

Figure 6.2: Validation analysis regarding implemented models for non-imaging optic designs. Figure (a) reproduces the CPC geometry reported by Qiu et al. [28] based on the model by Oommen and Jayaraman [22] – it yields an aperture width of 0.295 m and located 7.93 m above the primary field. Figure (b) compares the CPC designs presented by Chaves [25] and Oommen and Jayaraman [22].

6.2.3 Aplanatic linear Fresnel design

Gomes et al. [29] have analyzed a range of linear aplanatic design parameters (s, k, NA) that yield highest intercept factor (efficiency). Then, Souza et al. [16] extended this previous analysis to propose an aplanatic linear Fresnel design with high concentration and high optical efficiency: the authors found that the optimum aplanatic decision variables are

$\{s, k, \text{NA}\} = \{-2.25, -0.1, 1.0\}$, considering an absorber tube of $r_a = 0.012$ m, and primary aplanatic optic with a total aperture of $W_a = 1.9925$ m. Figure 6.3a illustrates these aplanatic optics, as well as the linear Fresnel derived from them.

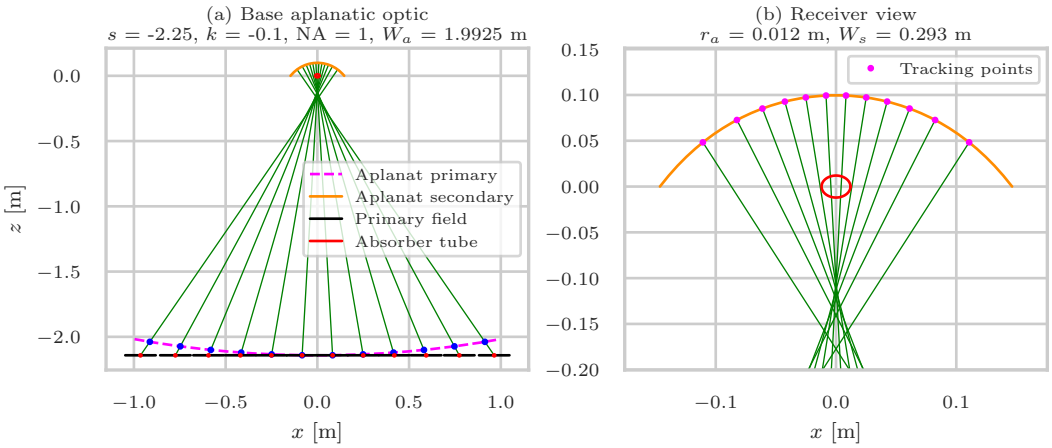

Figure 6.3: The aplanatic linear Fresnel concentrator by Souza et al. [16]. Figure (a) shows primary and secondary aplanatics for $\{s, k, \text{NA}\} = \{-2.25, -0.1, 1.0\}$, and a primary width $W_a = 1.9925$ m, as well as the horizontal primary field constructed from the aplanatic optics – the width of the primary field is larger than the value of the aplanatic primary. Figure (b) shows a close look at the receiver and illustrates the tracking points of the primary mirrors.

The determination of the linear Fresnel primary field from these primary and secondary aplanatic optics is as follows. First, the aplanatic primary is divided into twelve equal-width segments at the aperture plane. The center of each segment (depicted as blue dots in Figure 6.3a) corresponds to a point in the aplanatic secondary, as defined by the aplanatic equations [29]. Next, center of each segment is projected onto a horizontal plane while maintaining the direction of the line connecting them to their corresponding point in the aplanatic secondary – these points in the secondary serve as the tracking points for the primary mirrors, as illustrated in Figure 6.3b. The green lines connect the center of the primary mirrors to the corresponding tracking points at the aplanatic secondary optic. Although the primary mirrors are very close in Figure 6.3a, a verification was done: the distance between two neighboring mirrors is enough for them not to collide in their tracking procedure. Finally, the curvature radius of each primary is defined by a zenithal reference design [30], which assumes normal incidence as the design position.

This process of constructing a segmented and horizontal linear Fresnel primary field from a continuous aplanatic primary optic yields a uniform configuration in terms of width (meaning all primaries have the same width) but a non-uniform configuration in terms of curvature radius and distance between neighboring mirrors (each primary having its specific values).

6.3 Materials and methods

6.3.1 Overview

Ray-tracing is the most appropriate optical method for evaluating LFCs with a secondary optic since it can account for the complex optical phenomena (multiple reflections and transmission, as well as total internal reflection) that might occur in the receiver. In this

chapter, ray-tracing simulations are carried out with SolTrace [31], and a Python library is used for automating script writing [32].

A transversal plane (bi-dimensional) model is considered. That is, the longitudinal effects are neglected, and a range of transversal incidence angles, θ_T, is considered in the optical characterization. In this sense, $\theta_T \in [0°, 85°]$ since only symmetric cases are addressed. This optical characterization determines three performance metrics as functions of θ_T: optical efficiency, flux uniformity, and acceptance. The first one gives the conversion rate of incident sunlight into absorbed flux; the second represents an issue in real operation since low uniformity can cause the failure of evacuated tubes, damaging the vacuum seal and leading to higher thermal losses. The acceptance gives a metric of the concentrator tolerance to optical errors such as tracking and misalignment, an important factor in long-term energy collection, operation, and maintenance.

Moreover, annual average values of these metrics are calculated based on hourly data of a Typical Meteorological Year (TMY) taken from the PVGIS Application Program Interface [33]. For each one of the 8760 hours of the year, sun azimuth and zenith are calculated by a solar position algorithm [34] and then converted to transversal and longitudinal incidence angles, θ_T and θ_L, respectively, considering North-South (NS) and East-West (EW) orientations for the concentrator.

6.3.2 Evaluation metrics

The optical efficiency, η, is defined as shown in Equation 6.1, where Q_{abs} is the flux absorbed in the receiver, defined as the product between the number of absorbed rays, N^a_{rays}, and the power carried by each ray, q_{ray}, outputs of a ray-tracing simulation; I_b is the Direct Normal Irradiance (DNI), here always considered as 1000 W/m^2, and A_{net} is the mirror aperture area (the sum of the product between mirror width, w, and length, L, where n stands for the number of mirrors in the primary field).

$$\eta = \frac{Q_{abs}}{I_b \cdot A_{net}} = \frac{q_{ray} \cdot N^a_{rays}}{I_b \cdot \sum_{i=1}^{n} w \cdot L} \tag{6.1}$$

Of course, η is a function of θ_T and one can write $\eta = \eta(\theta_T)$. Thus, an annual averaged value of efficiency, $\bar{\eta}$, is defined in Equation 6.2, where h is an index that ranges for each of the 8760 hours of the year.

$$\bar{\eta} = \frac{\sum_{h=1}^{8760} \eta(\theta_T^h) I_b^h}{\sum_{h=1}^{8760} I_b^h}, \tag{6.2}$$

The circumferential flux uniformity is measured by the non-uniformity index, represented by δ, as defined in Equation 6.3: higher values of δ_q mean lower flux uniformity, and vice-versa.

$$\delta_q = \frac{\sigma_q}{\mu_q} \tag{6.3}$$

In Equation 6.3, μ_q is the average flux density in the absorber, as given by Equation 6.4: the ratio of the absorbed flux, Q_{abs} and absorber area, A_{abs}.

$$\mu_q = \frac{Q_{abs}}{A_{abs}} \tag{6.4}$$

Then, σ_q represents the standard deviation of the circumferential flux distribution. In SolTrace, the circumferential width of the absorber tube is divided into bins, here represented by N_{bins}, and σ_q is calculated by a discrete approach, as given by Equation 6.5, where q_i represents the flux density in a circumferential bin of index i.

$$\sigma_q = \sqrt{\frac{1}{N_{bins}} \sum_{i=1}^{N_{bins}} (q_i - \mu_q)^2} \tag{6.5}$$

For the analysis presented in this chapter, $N_{bins} = 150$ for all simulations. In fact, q_i represents the average of the longitudinal bins, so that:

$$q_i = \frac{1}{N_{y-bins}} \sum_{j=1}^{N_{y-bins}} q_{ij}, \tag{6.6}$$

where y refers to the direction of the longitudinal width of the absorber tube (divided in N_{y-bins}), and q_{ij} is the flux intensity in a bin of index ij. For the analysis presented in this chapter, $N_{y-bins} = 150$ for all simulations.

Of course, δ_q is a functions of θ_T and one can write $\delta_q = \delta_q(\theta_T)$. Thus, an annual averaged value of non-uniformity index, $\bar{\delta}_q$, is defined in Equation 6.7, where h is an index that ranges for each of the 8760 hours of the year.

$$\bar{\delta}_q = \frac{\sum_{h=1}^{8760} \delta_q(\theta_T^h) I_b^h}{\sum_{h=1}^{8760} I_b^h} \tag{6.7}$$

The acceptance of a Linear Fresnel Collector (LFC), as in non-ideal concentrators, is not based on geometric relations but on ray-tracing analysis since the transmission-acceptance curve does not follow the step-shaped function of ideal concentrators [25].

Thus, the acceptance half-angle of the concentrator, β, is calculated based on the off-axis incidence, here denominated by ψ, for which the concentrator collects 90% of the on-axis flux [25]. Hence, the primary field is positioned for a particular transversal incidence θ_T, and then the absorbed flux is calculated for off-axis incidences ($\theta_T \pm \psi$) but without further tracking, as illustrated in Figure 6.4a.

The off-axis incidences for which the absorbed flux is 90% of the on-axis flux ($\psi = 0$) are ψ^+ and ψ^-, as shown in Figure 6.4b. Therefore, β is calculated as given by Equation 6.8.

$$\beta = \frac{\psi^+ - \psi^-}{2} \tag{6.8}$$

Of course, β is a function of θ_T and one can write $\beta = \beta(\theta_T)$. Thus, an annual averaged value of acceptance, $\bar{\beta}$, is defined in Equation 6.9, where h is an index that ranges for each of the 8760 hours of the year.

$$\bar{\beta} = \frac{\sum_{h=1}^{8760} \beta(\theta_T^h) I_b^h}{\sum_{h=1}^{8760} I_b^h} \tag{6.9}$$

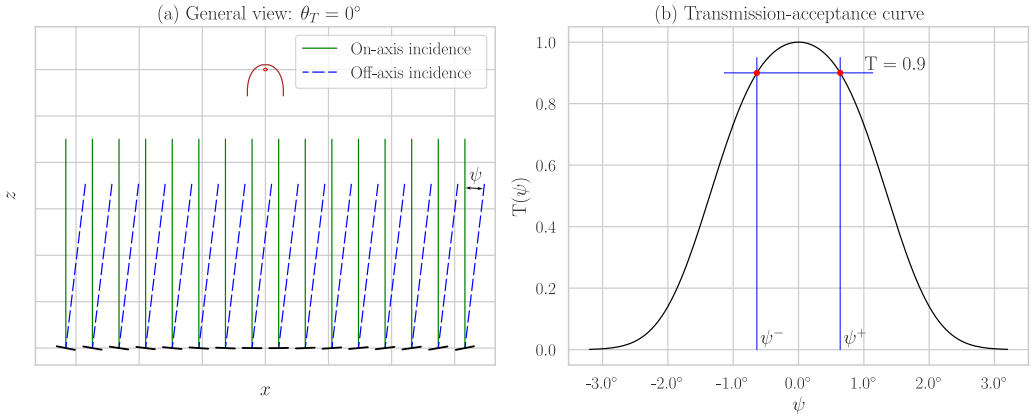

Figure 6.4: Acceptance analysis for a Linear Fresnel Collector (LFC). Figure (a) illustrates the primary field positioned for a particular transversal incidence (here, $\theta_T = 0$, as well as the on-axis (green lines) and off-axis rays (dashed blue lines) for that position. Figure (b) shows the transmission-acceptance curve, i.e., how the normalized flux, T, varies with ψ, the off-axis incidence – the positive and negative off-axis incidences for which $T(\psi) = 0.9$ are ψ^+ and ψ^-, respectively.

6.3.3 Convergence of traced rays

The convergence analysis aims to determine the number of ray intersections to be traced to achieve convergence of the flux distributions. Thus, it was defined an LFC geometry with 132.8 m^2 of aperture area (16.56 m $\times$ 8.0 m) and a CEC secondary optic, as in Table 6.1.

Table 6.1: Linear Fresnel geometry used in the convergence study. The primary field has a uniform width and shift, but a non-uniform curvature design (zenithal reference). The receiver comprises a SHOTT like evacuated tube, a CEC secondary optic, and glass cover thickness of 0.003 m.

n	W_p	w	d	R	r_a	r_{go}	r_{gap}	H_R
16	16.56	0.75	1.054	var*	0.035	0.0625	0.0625	7.2

Furthermore, this convergence analysis considers the settings presented in Table 6.2, where Δ_{sun} stands for the half-width of a pillbox sunshape. ρ_p and ρ_s refers to the reflectivity of primary and secondary optics, respectively. α and τ refers to the absorption of transmission coefficients of the absorber tube and glass cover, respectively. σ_c and σ_s refers to the standard deviation of Gaussian profiles of the contour and specular errors, respectively.

Table 6.2: Optical settings considered in the convergence analysis of traced rays.

ρ_p	ρ_s	α	τ	Δ_{sun}	σ_c	σ_s
0.95	0.95	0.96	0.98	4.65	2.0	3.0

Figure 6.5 presents the results regarding the converge analysis of traced rays. It shows violin plots of the optical efficiency and circumferential uniformity index results of 50 simulations for different values of ray intersections – the width of violin plots indicates the density of data points, with wider sections showing more frequent occurrences of those values, the horizontal bars in the middle represent the mean for each set of ray intersections, and vertical lines that represent the distance between maximum and minimum values. As can be seen, the

mean results converge very well for a number of intersections greater than 1.0×10^6, and the the dispersion remains quite constant beyond this value.

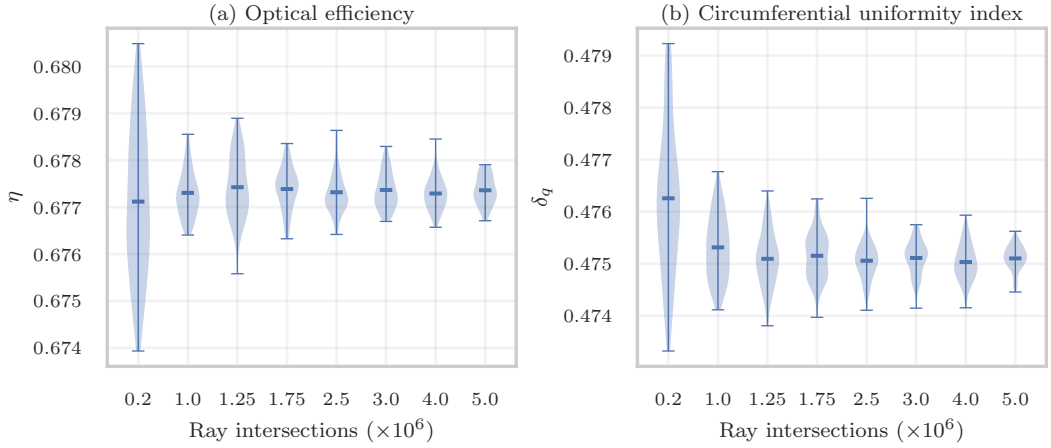

Figure 6.5: Convergence analysis concerning the number of ray intersections to be traced. It shows how the results of optical efficiency and circumferential uniformity index (both at normal incidence) vary in terms of the number of ray intersections. A total of 50 simulations were carried out for each value of desired intersections, considering pseudo random computation using the current clock time.

Therefore, based on the results shown in Figure 6.5, a density of 9413 ray intersections per square meter of aperture area ($1.25 \times 10^6/132.8$ m^2), and a seed number of 123 to ensure reproducible results, is then defined for all further simulations. Moreover, a minimum number of ray intersections of 2.0×10^5 is also considered to avoid simulations with few rays.

6.4 Results and discussion

6.4.1 Non-imaging optics secondaries

This section analyzes non-imaging designs proposed as secondary optics of the linear Fresnel solar concentrator. Thus, it compares CPC and CEC edge-ray designs [25] to geometries resulting from optimization routines that attribute decision variables to the secondary optic geometry that follows Oommen's formulation [22] of the CPC optic. Section 6.2 details the design of these optics. Two optimization studies use CPC geometry parameters as decision variables in the optimization routine: Cheng et al. [23] and Men et al. [24]. Both studies consider optical properties, sunshape model, and optical errors shown in Table 6.3.

Table 6.3: Optical settings considered by Cheng et al. [23] and Men et al. [24].

ρ_p	ρ_s	α	τ	Δ_{sun}	σ_t	σ_c
0.92	0.95	0.96	0.95	4.65	0.5	2.5

In the above table, Δ_{sun} stands for the half-width of a pillbox sunshape. ρ_p and ρ_s refers to the reflectivity of primary and secondary optics, respectively. α and τ refers to the absorption of transmission coefficients of the absorber tube and glass cover, respectively. σ_t and σ_c refers to the standard deviation of Gaussian profiles of the tracking and contour errors, respectively. The tracking error is only considered for the primary mirrors, and the contour error is considered for both primary and secondary reflectors.

The optimum geometry reported by Cheng et al. [23] for the case of a cylindrical primary field is hereafter denominated as Cheng's optic, and the corresponding geometric data is presented in Table 6.4. This geometry considers a distance between the absorber tube and outer cover radius of 0.0225 m. Therefore, $r_{gap} = r_a + 0.0225 + \Delta r_g$, where Δr_g was subjected to optimization within the range of [0.01, 0.1] [23]. The reported value for r_{gap} by Cheng et al. [23] is not feasible since it would give $\Delta r_g = -0.0125$ m. Thus, a minimum value of gap size is here considered for Cheng's optic, i.e., $\Delta r_g = 0.01$ m.

Table 6.4: Parameters of the optimum geometry reported by Cheng et al. [23], henceforth referred to as Cheng's optic. It was considered a glass cover thickness of 0.003 m.

n	W_p	w	d	R	r_a	r_{go}	r_{gap}	H_R	θ_a	θ_{max}
25	12.25	0.25	0.5	24.75	0.1	0.1225	0.1325	9.49	66.29°	183.69°

In Figure 6.6, the optimum geometry of the secondary optic reported by Cheng et al. [23] significantly deviates from the two edge-ray designs: CPC and CEC. Cheng's optic features a narrower aperture width and distinctly fails to align with the edge-rays originating from the primary field (green lines). Comparatively, the other two secondary optics – CPC and CEC – exhibit considerable similarity, differing mainly in their conic sections (macro focal parabola versus macro focal ellipse).

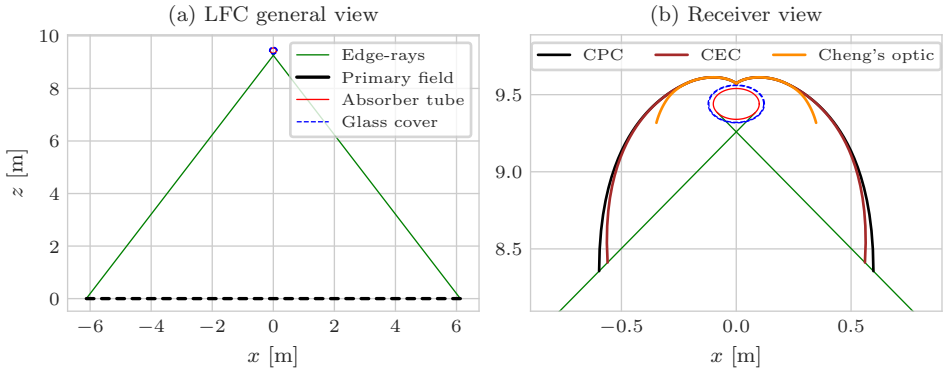

Figure 6.6: Linear Fresnel Collector optimum geometry reported by Cheng et al. [23] (see Table 6.4). It illustrates (a) the general view of the primary field, absorber tube, glass cover, and edge-rays – the uniform primary field is shown at a horizontal position; (b) a receiver view shows different secondary optics: CPC and CEC relate to edge-rays designs, and Cheng's optic refers to a reported optimum geometry [23].

Figure 6.7 presents the result of ray-tracing simulations for the optics depicted in Figure 6.6. Cheng's optic demonstrates superior optical efficiency compared to the edge-ray designs, as shown in Figure 6.7a. However, when evaluating circumferential flux uniformity and acceptance, Cheng's optic emerges as the least favorable design, as illustrated in Figure 6.7b and Figure 6.7c, respectively. These performance variations are consistent across the entire range of transversal incidences. It is worth noting that Cheng's optic was optimized solely to maximize annual efficiency and did not consider any other objectives.

Figure 6.8 presents the annual averaged values of the three metrics presented in Figure 6.7, showcasing CPC and CEC relative variations concerning Cheng's optic, with reference to TMY data from Jiexi County (N23.45°, E115.90°) [23]. The higher optical efficiency of Cheng's optic primarily stems from the shading caused by the receiver on the primary field: larger secondary optics, such as CEC and CPC, cast more shade for the same incidence.

Another factor impacting efficiency relates to h_s (refer to Figure 6.1), the height of the sec-

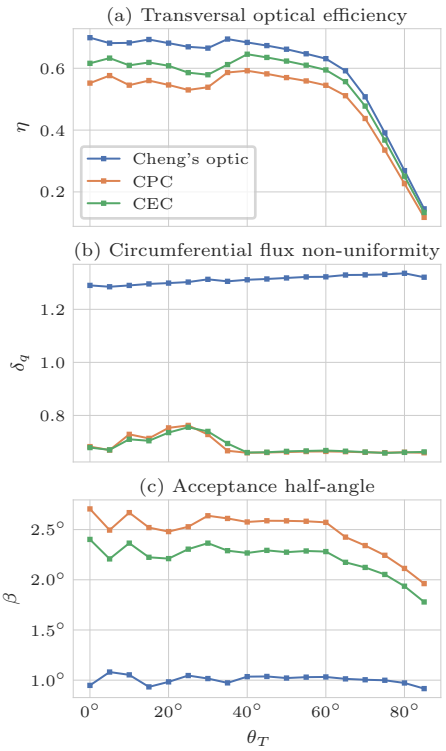

Figure 6.7: Results of (a) Transversal optical efficiency, (b) Circumferential uniformity index, and (c) Acceptance half-angle as functions of θ_T, the transversal incidence angle, for Cheng's optic and corresponding CPC and CEC edge-ray secondary optics (see Figure 6.6). The optimum geometry reported by Cheng et al. [23] is denominated as Cheng's optic (see Table 6.4).

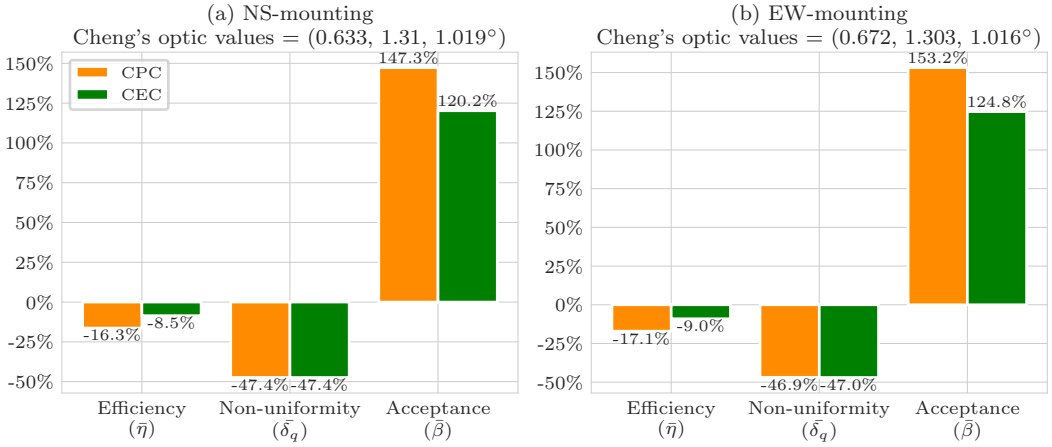

Figure 6.8: Annual average values of optical efficiency, non-uniformity index, and acceptance half-angle of CPC and CEC secondary optics as the relative difference to Cheng's optic (see Figure 6.6). Cheng's annual average metrics of efficiency, non-uniformity, and acceptance are (0.636, 1.309, 1.019°) and (0.673, 1.303, 1.016°) for NS and EW-mountings, respectively. Furthermore, it considers data from Jiexi County (N23.45°, E115.90°).

ondary optic: in Cheng's optic, more rays directly strike the absorber compared to the other two secondaries, as the aperture center is closer to the absorber, resulting in a lower average number of reflections. This phenomenon is evident in the circumferential flux uniformity, as depicted in Figure 6.7b: Cheng's optic exhibits markedly inferior performance. Regarding acceptance, Cheng's optic fares poorly (as shown in Figure 6.8), likely due to its smaller aperture size compared to the other two. However, aperture size alone does not entirely dictate acceptance results, as the differences between CPC and CEC are not as significant (as seen in Figure 6.6b), yet their acceptances vary (as shown in Figure 6.8). Thus, the match of the secondary optic profile with the primary optic also plays a crucial role in determining acceptance results.

The study conducted by Men et al. [24] is a multi-objective optimization aiming to simultaneously maximize annual surrogate models of optical efficiency and circumferential flux homogeneity. Consequently, the Pareto front of solutions was determined, which represents the trade-offs between the different objectives, where improving one objective can only be achieved at the expense of worsening at least one other objective. Then, the TOPSIS algorithm was used to select a set of 36 recommended geometries from the Pareto solutions. These recommended solutions are henceforth referred to as Men's optic, followed by the corresponding index number from the original work. For example, Men's optic #1 denotes the recommended solution indexed as 1 in their research.

Upon an initial analysis of these recommended geometries, it becomes clear that all of them refers to non-truncated CPC optics, given that $\theta_a + \theta_{max} = 270°$ for all cases. Among these recommended geometries, Men's optic #31 exhibits the highest disparity between edge-rays aperture angle and the CPC acceptance angle, θ_e and θ_a, respectively (see Figure 6.1): $\theta_a - \theta_e = 7.71°$. However, it is worth noting that this geometry is optimized for a location with a latitude of 75°, which lacks practical relevance. Therefore, for the purpose of this discussion, only considered locations with a latitude lower or equal than 45°are considered.

In this sense, Men's optic #15 is the one which shows the higher deviation: $\theta_a - \theta_e = 6.27°$. Its corresponding geometric data is presented in Table 6.5. In this case, a distance between absorber and outer cover radius of 0.0225 m, so that $r_{gap} = r_a + 0.0225 + \Delta r_g$, where Δr_g was optimized within the range of [0.01, 0.1] [24].

Table 6.5: Geometric parameters of an optimum configuration reported by Men et al. [24]. It shows the geometric parameters of recommended solution #15, denominated as Men's optic #15. A glass cover with a thickness of 0.003 m was considered.

n	W_p	w	d	R	r_a	r_{go}	r_{gap}	H_R	θ_a	θ_{max}	Latitude
25	31.43	0.71	1.28	47.14	0.05	0.075	0.11	14.95	52.81°	217.19°	[30°,45°)

In Figure 6.9, CPC and CEC secondary optics designed for Men's optic #15, based on the edge-rays principle, are also depicted. These two optics adhere to the minimum gap size: $r_{gap} = 0.0825$ m, meaning $\Delta r_g = 0.01$ m, which is the smallest value considered by Men et al. [24]. For this condition, interestingly, CPC and CEC edge-ray geometries essentially overlap and closely resemble each other. However, it's evident that Men's optic #15 does not match with the edge rays from the primary field, as illustrated in Figure 6.9a.

Figure 6.10 presents ray-tracing results for the optics in Figure 6.9a. The performance of CPC and CEC largely overlaps, aligning with expectations from their contour (refer to Figure 6.9a). Both of these optics outperform Men's optic #15 in terms of efficiency and acceptance results, although they are surpassed in flux uniformity – results for the whole range of transversal incidences.

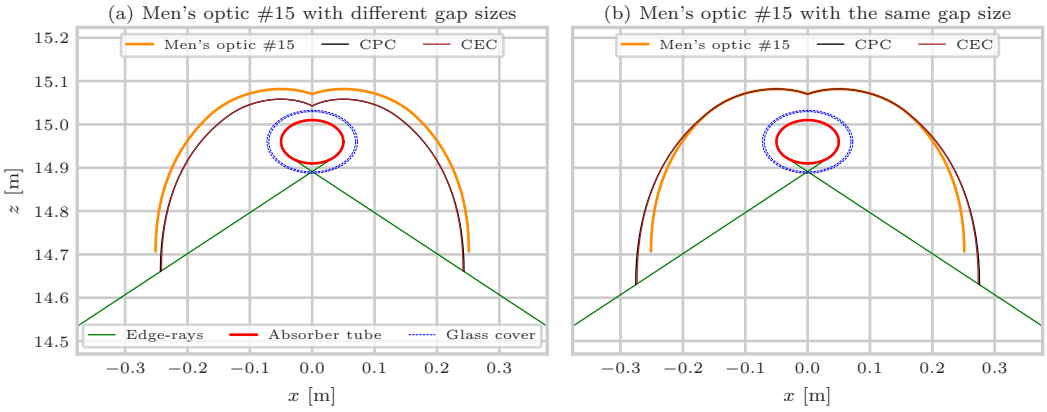

Figure 6.9: Receiver details of different secondary optics for Men's optic #15 (see Table 5). In Figure (a), CPC and CEC edge-ray designs have the minimum possible gap size ($r_{gap} = 0.0825$ m), a value lower than of Men's optic #15 ($r_{gap} = 0.11$ m). In Figure (b), CPC and CEC edge-ray designs have the same gap of Men's optic #15 ($r_{gap} = 0.11$ m).

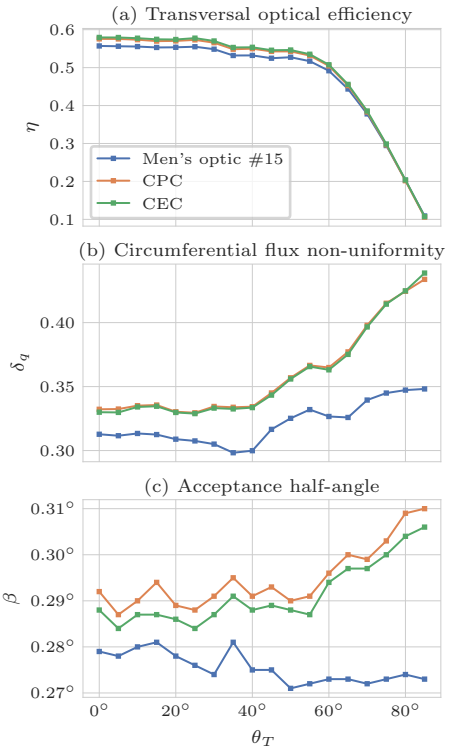

Figure 6.10: Results of (a) Transversal optical efficiency, (b) Circumferential uniformity index, and (c) Acceptance half-angle as functions of θ_T, the transversal incidence angle, for Men's optic #15 and corresponding cases with CPC and CEC edge-ray secondary optics, considering that edge-ray designs have the minimum possible gap size, as shown in Figure 6.9a.

In Figure 6.11, CPC and CEC annual average values of optical efficiency, non-uniformity index, and acceptance half-angle are presented as relative variations with respect to Men's optic #15. These calculations are conducted considering the TMY data from Evora (N38.53°, W8.00°) and the optical characterization data in Figure 6.10.

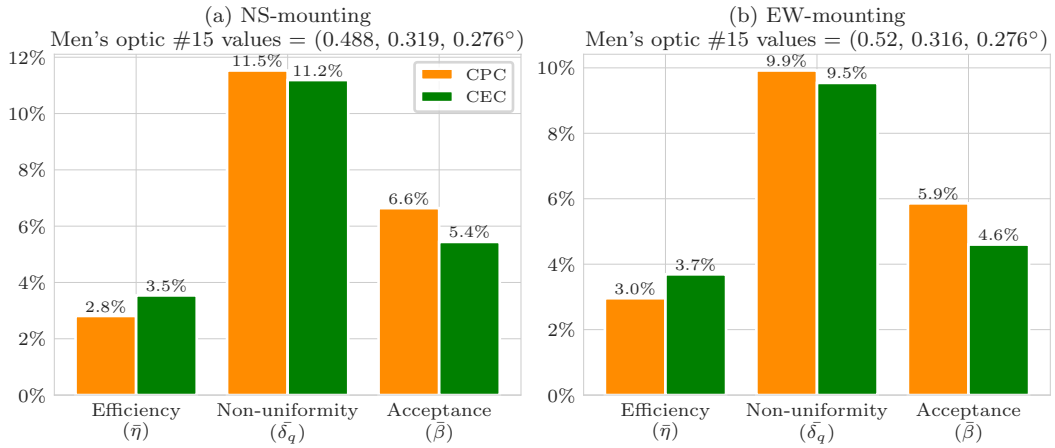

Figure 6.11: Annual average values of optical efficiency, non-uniformity index, and acceptance half-angle of CPC and CEC secondary optics as the relative difference to Men's optic #15 (see Figure 6.9a). It averages results from Figure 6.10, considering the TMY data from Evora (N38.53°, W8.0°). Men's optic #15 annual average metrics of (efficiency, non-uniformity, and acceptance) are (0.49, 0.319, 0.276°) and (0.522, 0.315, 0.276°) for NS and EW-mountings, respectively, and are considered as the base values.

In Figure 6.11, variations are not high as in the previous case (refer to Figure 6.8), aligning with the closer profiles shown in Figure 6.9a. In this scenario, the edge-ray designs exhibit higher efficiency and acceptance but demonstrate lower performance in flux uniformity, as indicated by the higher non-uniformity index. On the one hand, CPC and CEC optics feature smaller values for secondary optic aperture and gap, which helps in reducing optical losses and enhancing efficiency. Conversely, the higher value of h_s (refer to Figure 6.1) increases the average number of reflections and consequently reduces efficiency. Moreover, it becomes evident that the size of the secondary optic aperture has a lesser effect on acceptance compared to the optic profile: Men's optic #15 exhibits the lower average acceptance despite having the larger aperture. Additionally, while the gap size contributes to increased losses and reduced efficiency, it also contributes to improved flux uniformity.

In fact, when considering edge-ray designs with the same gap size as in Men's optic #15 (refer to Table 6.5), CPC and CEC optics align even more with it, as illustrated in Figure 6.9b: geometry profiles are now more closer to each other. Figure 6.12 shows metrics average values for the optics illustrated in Figure 6.9b. Efficiency and flux uniformity results are now closer. However, on the contrary, the acceptance differences are now more pronounced, driven by the larger apertures of the CPC and CEC secondaries compared to Men's optic #15 in addition to the already matching optic profile.

These previous finding highlight how edge-ray designs draw nearer to a Pareto solution of a bi-objective optimization problem considering a flux uniformity metric alongside an optical efficiency objective, as it can be seen from Cheng et al. [23] to Men et al. [24]. Indeed, the results in Figure 6.11 indicate that edge-ray designs are not dominated by Men's optic #15 (a Pareto solution) and can become even more closely aligned, as depicted in Figure 6.12, when the same gap radius is used for all secondary optics. Furthermore, edge-ray designs offer an additional advantage in acceptance, signifying higher tolerance to optical errors.

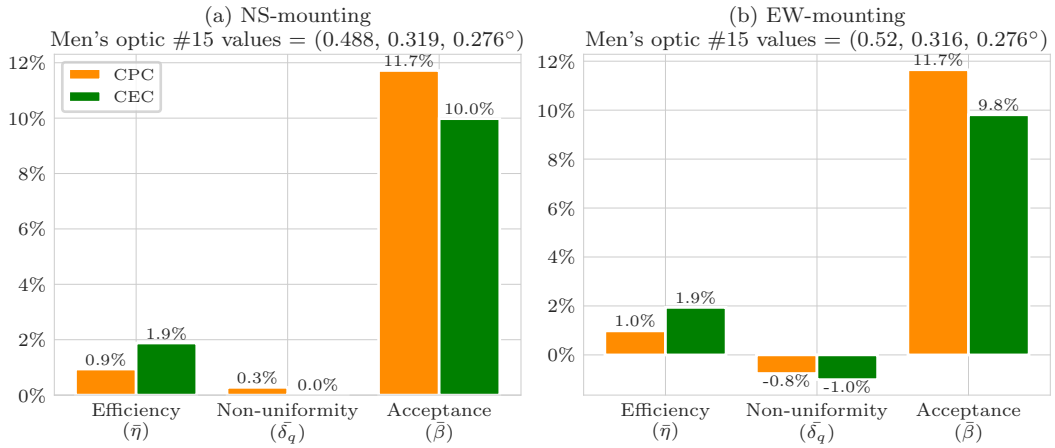

Figure 6.12: Annual average values of optical efficiency, non-uniformity index, and acceptance half-angle of CPC and CEC secondary optics as the relative difference to Men's optic #15 when design with the same gap size: $r_{gap} = 0.11$ m (see Figure 6.9b). It averages optical characterization results, considering the TMY data from Evora (N38.53°, W8.0°). Men's optic #15 annual average metrics of (efficiency, non-uniformity, and acceptance) are (0.49, 0.319, 0.276°) and (0.522, 0.315, 0.276°) for NS and EW-mountings, respectively, and are considered as the base values.

An intriguing observation from analyzing Men's recommended solutions is that although geometric parameters of the primary field vary within a reasonable range, the corresponding CPC geometry does not significantly deviate from an edge-ray. The case with the highest deviation, Men's optic #15, was here analyzed, where $\theta_a - \theta_e = 6.27°$. The case with the lowest difference is Men's optic #4, where $\theta_a - \theta_e = 0.46°$. Now, simulation results for the CPC edge-ray design and the reported optimum geometry practically overlap when they have the same r_{gap}, as shown in Figure 6.13b. Thus, only the gap size, denoted by r_{gap}, emerges as an important decision variable in the edge-ray design to balance efficiency, flux uniformity, and acceptance – a higher gap means lower efficiency but higher values of circumferential uniformity and acceptance.

Furthermore, considering the optimal geometries reported by Cheng et al. [23] and Men et al. [24], the previous results indicate that non-truncated (full open) CPC optics play a crucial role in achieving higher levels of circumferential flux uniformity. It is worth noting that the optimal geometries reported by Men et al. [24] comprise a subset of the Pareto front selected by the TOPSIS algorithm. Consequently, not all Pareto solutions were reported, implying that the CPC edge-ray designs might be part of the optimal solutions from the Pareto front but not selected by the TOPSIS.

6.4.2 Aplanatic optic comparison

Considering the aplanatic linear Fresnel geometry showed in Figure 6.3, CPC and CEC edge-ray optics were designed for a comparison analysis considering the data in Table 6.6

Table 6.6: Data regarding the aplanatic linear Fresnel analyzed by Souza et al. [16].

n	W_p	w	d	R	r_a	r_{gap}	H_R	σ_{sun}	ρ_p	ρ_s	α
12	2.094	0.166	var*	var**	0.012	0.214	2.142	9.0	0.95	0.95	0.95

In the above table, σ_{sun} stands for the standard deviation of a Gaussian sunshape; ρ_p and

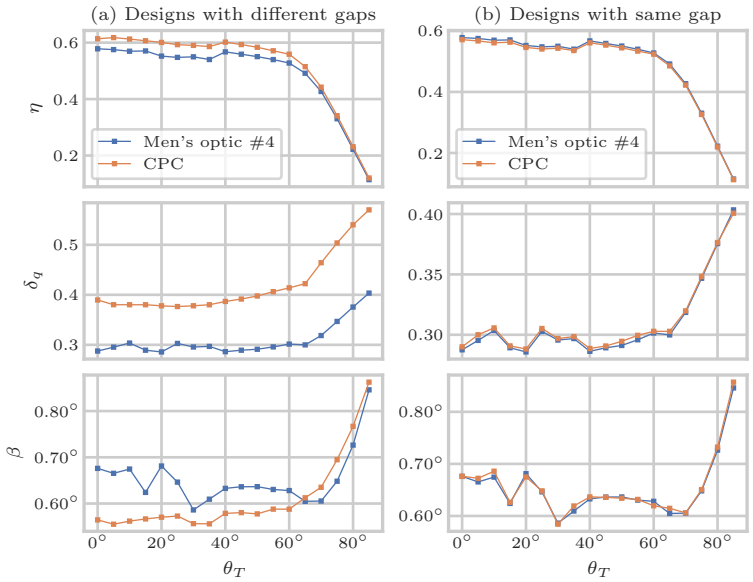

Figure 6.13: A comparison of Men's optic #4 and CPC edge-ray design for (a) the minimum gap radius and (b) the condition of the same gap radius. It shows simulation results of transversal optical efficiency (η), Circumferential non-uniformity index (δ_q), and Acceptance half-angle (β) as functions of θ_T, the transversal incidence angle.

ρ_s refers to the reflectivity of primary and secondary optics, respectively; α refers to the absorption coefficient of the absorber tube. For this matter, a gap size was considered so that $r_{gap}/r_a = 1.786$ – the ratio of outer cover radius and absorber radius in standard PTR®70 evacuated tubes [6] and $\Delta r_g = 0$. However, to follow Souza et al. [16], a glass cover was not included in the simulations.

Figure 6.14a shows a general view of the aplanatic LFC, and the edge-rays from the primary field to the absorber tube. As detailed in Figure 6.14b, the designed CPC and CEC optics are quite close, and both significantly diverge to the aplanat secondary. Moreover, the aplanat presents a larger aperture, as well as far bigger gap. It is important to highlight that whilst in CPC and CEC cases the tracking point is the secondary aperture center, the aplanatic case has a specific tracking procedure, as previously discussed regarding Fig. 4.

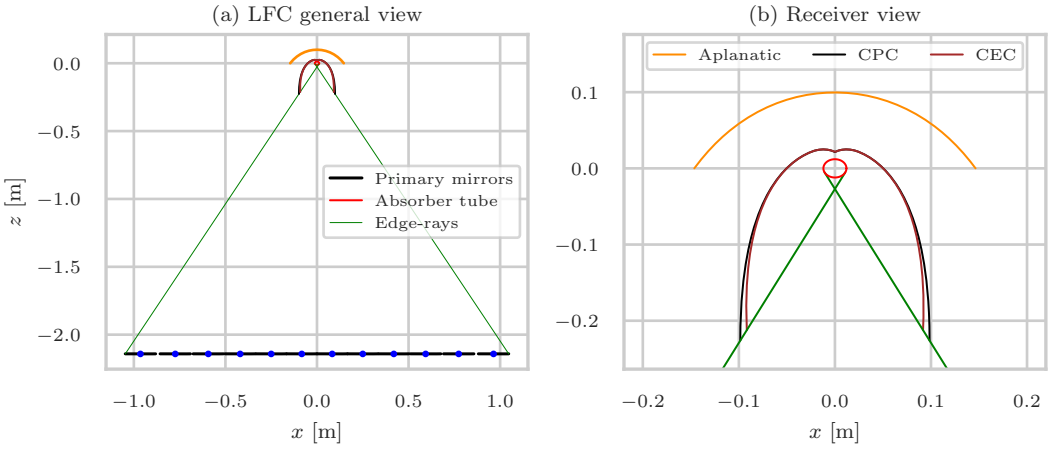

Figure 6.14: A comparison of the aplanatic linear Fresnel collector with CPC and CEC edge-ray secondary optics. It shows (a) the geometry general view and (b) the details of the receiver with the different secondary optics (CPC, CEC, and the aplanatic secondary).

Figure 6.15 presents simulation results for the optics shown in Figure 6.14. As seen, the CPC and CEC fairly surpass the aplanatic optic in terms of acceptance for the whole range of θ_T, but the CEC is superior also in terms of efficiency. These results indicate that average values for different locations only impact the magnitude of the differences but not in determining which secondary optic is better. On the other hand, flux uniformity results show that the best optic depends on θ_T. Furthermore, the data on CPC and CEC follow previous results: the first outperforms the latter in acceptance, while it is surpassed in efficiency and present approximately the same flux uniformity results.

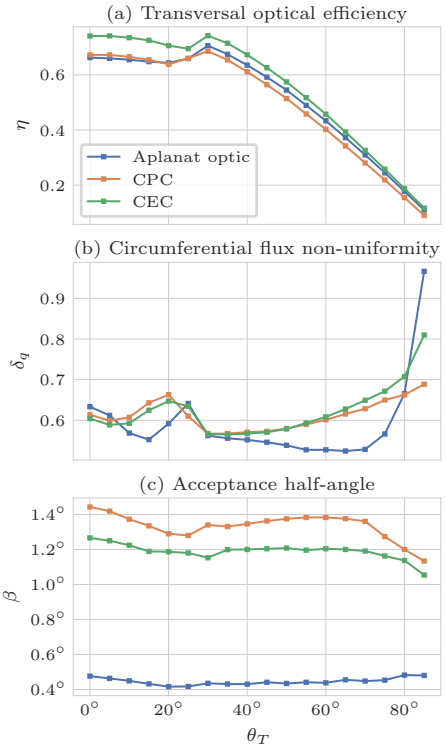

Figure 6.15: Results of (a) Transversal optical efficiency, (b) Circumferential uniformity index, and (c) Acceptance half-angle as functions of θ_T, the transversal incidence angle. It considers the case reported by Souza et al. [16] and secondary optic edge-ray designs (CPC and CEC) for the reported optimum aplanatic geometry.

Figure 6.16 displays the averaged values of the optical characterization data from Figure 6.15, utilizing TMY data for Evora (N38.53°, W8.0°). It is evident that the CPC optic exhibits a slight disadvantage in efficiency compared to the Aplanat optic (3.0% lower), while the CEC optical efficiency is nearly 8.0% higher. In this case of Evora, both CPC and CEC show higher levels of non-uniformity compared to the aplanatic, approximately 6.0% and 7.0%, respectively. Notably, both edge-rays optics demonstrate superior acceptance results, aligning with the finding from Figure 6.15.

Hence, the results depicted in Figure 6.16 shows that the aplanatic optic generally surpasses edge-ray designs only in terms of flux uniformity. In this scenario the specific tracking procedure proposed by Souza et al. [16] aligns primary mirrors with the aplanatic secondary optic, thereby ensuring that a larger portion of the absorber is illuminated. Qiu et al. [26] have demonstrated that employing a suitable aiming strategy can enhance flux uniformity without significantly sacrificing efficiency. Conversely, CPC and CEC edge-ray designs utilize the standard aiming strategy, complicating the illumination of the top of the absorber tube.

The evident advantage of CPC and CEC optics in acceptance implies a greater tolerance

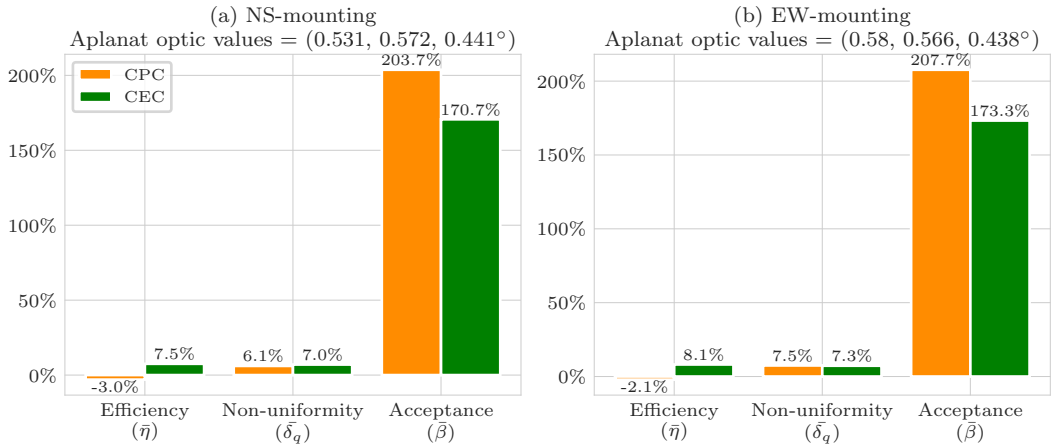

Figure 6.16: Relative differences in average values of optical efficiency, non-uniformity index, and acceptance half-angle for the optics shown in Figure 6.14. It averages results from Figure 6.15, considering the TMY data from Evora (N38.53°, W8.0°), and shows the relative differences between CPC and CEC secondaries to the Aplanatic optic (see Figure 6.14). The Aplanatic optic annual average metrics of {efficiency, non-uniformity, and acceptance} are {0.534, 0.572, 0.441°} and {0.584, 0.566, 0.438°} for NS and EW-mountings, respectively, and are considered as the base values.

to optical errors, which is a crucial factor in long-run operation and maintenance of solar concentrators. Furthermore, it is worth noting that edge-ray designs require only a single decision variable to be determined – the gap size (or radius), denoted as r_{gap}. This can even be simplified by opting for the minimum feasible gap. Hence, edge-rays designs represents a more straightforward and simpler approach.

On the contrary, the aplanatic linear Fresnel design analyzed here stems from a prior optimum search in the decision variable space involving s, k, and NA, as outlined by Souza et al. [16]. Consequently, any alteration in one parameter (e.g., the absorber tube radius) would lead to new optimum search for s, k, and NA, which is not the case with the edge-ray design method.

6.4.3 Further analysis on energy collection

The impact of a lower value of averaged annual efficiency, $\bar{\eta}$, on energy collection is direct since this metric represents how much of the incident energy is collected. However, flux non-uniformity, $\bar{\delta_q}$, and concentrator acceptance, $\bar{\beta}$, have impact on collector reliability and energy collection during long-term operation. Issues with flux uniformity can result in thermal stress that damages absorbers and may even lead to the failure of evacuated tubes, compromising the vacuum seal and causing higher thermal losses. Additionally, the heat transfer fluid can only absorb a maximum flux density without deteriorating its properties. The concentrator acceptance plays a significant role as continuous and long-run operation introduces errors on the optical system.

While the impact of lower uniformity on energy collection is evident, accurately quantifying the value is challenging without reliable operational and maintenance models and a metric for circumferential uniformity as a safety benchmark. On the other hand, a straightforward analysis demonstrates how lower acceptance mean a decrease in energy collection.

The overall optical error is here denominated by σ_o, and is computed by the convolution of

all errors [35]: $\sigma_o^2 = 4\sigma_t^2 + \sigma_s^2 + 4\sigma_c^2$. The overall error (e.g., refer to Table 6.3 and Table 6.6) considered for performance computations is a kind of an idealization as it is constant and do not vary in time to capture the long-run operational issues, i.e., annual analyzes considers a fixed value of σ_o. The operation introduces errors beyond those gathered in σ_o due to further tracking deviations, soiling leading to more non-specular reflection, misalignment related to erection, mechanical bending, and wear, among other factors. These additional errors are here represented by $\Delta\sigma_o$, and the final total optical error, σ_o^*, is then given by ${\sigma_o^*}^2 = \sigma_o^2 + \Delta\sigma_o^2$. Thus, $\Delta\sigma_o$ represents a measure of the deterioration of the optical system.

Figure 6.17 shows the impact of $\Delta\sigma_o$ on the annual averaged efficiency, $\bar{\eta}$, as $\Delta\sigma_o$ varies up to 25 mrad, for Cheng and the Aplanatic cases. Here, $\Delta\bar{\eta}$ stands for the relative difference of annual averaged efficiency of edge-rays designs to Cheng's (refer to Figure 6.6) and the Aplanatic (refer to Figure 6.14) optics. Thus, for example, in Figure 6.17a, for the CPC curve (in orange), $\Delta\bar{\eta} = (\bar{\eta}_{CPC} - \bar{\eta}_{Cheng})/\bar{\eta}_{Cheng}$.

Figure 6.17a shows that as $\Delta\sigma_o$ increases, $\Delta\bar{\eta}$ drops. Thus, as expected, CPC and CEC edge-ray designs present a higher tolerance to errors. Indeed, as the additional error achieves a value of 15 mrad, the CEC design has the same efficiency as Cheng's optic – 20 mrad for the CPC design. For conditions beyond these values, edge-ray designs have a higher value of annual averaged efficiency the Cheng's optic ($\Delta\bar{\eta} > 0$).

In the case of Figure 6.17b, the Aplanatic comparison, $\bar{\eta}$ drops as $\Delta\sigma_o$ increases. However, the values of $\Delta\sigma_o$ for which $\Delta\bar{\eta} = 0$ are now different. Indeed, the CEC starts with a higher efficiency ($\Delta\bar{\eta} > 0$), as expected from the data in Figure 6.16, and this difference increases with $\Delta\sigma_o$. For the CPC design, it has the same efficiency as the Aplanatic optic ($\Delta\bar{\eta} = 0$) at $\Delta\sigma_o = 5.0$ mrad, and higher efficiencies beyond it. These results agree with the data in Figure 6.16: since the Aplanatic optic has a far lower acceptance than CPC and CEC designs, it experiences a more pronounced reduction in the efficiency as the optical errors conditions increases.

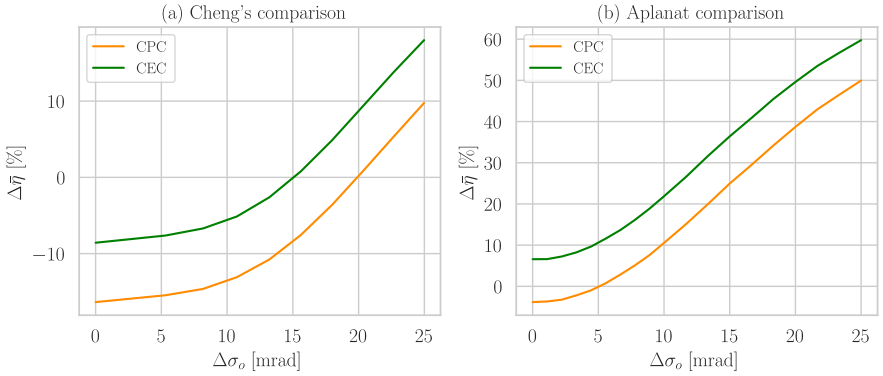

Figure 6.17: Relative difference of annual averaged efficiency, $\Delta\bar{\eta}$, as function of additional optical errors, $\Delta\sigma_o$. It shows the relative differences of CPC and CEC edge- rays to (a) Cheng's optic and (b) Aplanatic optics. In Figure (a), for the CPC curve (in orange), $\Delta\bar{\eta} = (\bar{\eta}_{CPC} - \bar{\eta}_{Cheng})/\bar{\eta}_{Cheng}$; in Figure (b), for the CEC, $\Delta\bar{\eta} = (\bar{\eta}_{CEC} - \bar{\eta}_{aplanatic})/\bar{\eta}_{aplanatic}$. This figure shows results for only an NS orientation, as the EW results are quite similar and are not presented here due to conciseness. The results presented in this figure are based on ray-tracing simulations carried out considering the optical settings defined in Table 6.3 and Table 6.6

From another perspective, what do additional optical errors mean in real operating conditions? Specifically, how much operating time results in an additional error of 5.0 mrad on the tracking system? How many millimeters of misalignment in the receiver position

correspond to an error of 20.0 mrad? Unfortunately, according to the author knowledge, there are no studies that provide a general correlation between these factors.

On the other hand, it is possible to run further simulations to assess the relation between an error in the receiver position (in both x and z axes – refer to Figure 6.6 and Figure 6.14) to the corresponding variation of annual optical efficiency. The ensuing results of these simulations are presented in Figure 6.18 for Cheng's and Aplanatic comparisons. In Figure 6.18a, in the case of the CEC curves (in green), $\Delta\bar{\eta} = (\bar{\eta}_{CEC} - \bar{\eta}_{Cheng})/\bar{\eta}_{Cheng}$.

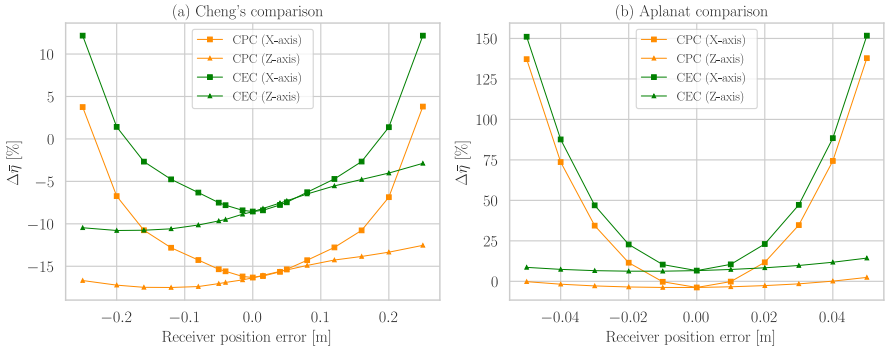

Figure 6.18: Relative difference of annual averaged efficiency, $\Delta\bar{\eta}$, as function of receiver position error in both x and z axes. It shows the relative differences of CPC and CEC edge-rays to (a) Cheng's optic and (b) Aplanat optics. In Figure (a), for the CPC curve (in orange), $\Delta\bar{\eta} = (\bar{\eta}_{CPC} - \bar{\eta}_{Cheng})/\bar{\eta}_{Cheng}$; in Figure (b), for the CEC, $\Delta\bar{\eta} = (\bar{\eta}_{CEC} - \bar{\eta}_{aplanatic})/\bar{\eta}_{aplanatic}$. This figure shows results for only an NS orientation, as the EW results are quite similar and are not presented here due to conciseness. The results presented in this figure are based on ray-tracing simulations carried out considering the optical settings defined in Table 6.3 and Table 6.6.

In general, Figure 6.18 shows that analyzed optics are far more sensitive to an error position in the x axis (horizontal) than in the z (vertical). In Figure 6.18a, misalignment in the x axis of 0.2 m introduces losses such that the annual efficiency of the CEC becomes higher than that of Cheng's optic ($\Delta\bar{\eta} > 0$), and values higher than it are needed for the CPC to become more efficient than Cheng's optic – a corresponding error position in the axis z does not produces the same effect. Conversely, an error position of 0.2 m does not seem a reasonable condition related to best practices of EPC (Engineering, Procurement, and Construction) companies.

In the case of the Aplanatic comparison, Figure 6.18b, the break-even values of error position ($\Delta\bar{\eta} = 0$) are significantly lower than that of Figure 6.18a, where a misalignment in the axis x higher than 0.01 m turns the CPC into a more efficient optic than the Aplanatic case – the CEC stars (error position of zero) being a more efficient case. Considering the error position in the z-axis, values above 0.04 m establishes a conditions for which the CPC is more efficient than the Aplanatic optic – these values are now closer to best practices of EPC companies.

In general, the results of this subsections illustrate how the higher tolerance to optical errors of edge-rays designs have a further impact on collector reliability and energy collection during long-term operation. Furthermore, this higher tolerance to errors means that using cheaper materials and manufacturing methods does not significantly impact the performance of CPC and CEC edge-ray designs. Consequently, despite their lower efficiency, edge-ray designs might be more cost-effective solutions, i.e., have lower cost of generated energy. Unfortunately, to the best of the authors' knowledge, there are no studies that provide models to relate materials and manufacturing methods to a metric of the resulting optical

errors and the concentrator cost, making this cost-energy assessment possible. Developing such models is, of course, beyond the scope of this work.

6.5 Conclusions

This work analyzes secondary optics for Linear Fresnel Collectors (LFCs) with a single absorber tube, and shows comparison based on averaged annual metrics of optical efficiency, flux uniformity, and acceptance angle, outputs of ray-tracing simulations and typical meteorological year hourly data.

The literature review indicates that the Compound Parabolic Concentrator (CPC) [22] is the main alternative – a winner optic in different comparison studies and under assessments including efficiency and flux uniformity. On the other hand, the Compound Elliptical Concentrator (CEC) [13] and a recently proposed Aplanatic Optic Concentrator (AOC) [16] emerged as secondaries never compared to the CPC. Moreover, CPC optimum geometries reported in a couple of studies [23, 24] were confronted to theoretical edge-ray designs [25] to better understand if the CPC geometry really needs to be subjected to optimization when used as an LFC secondary optic.

The results presented in Subsection 6.4.1 compares different non-imaging secondary optic designs. Regarding the difference between optimized CPC geometries and edge-ray designs, the developed results indicate that when optical efficiency is the sole objective to be maximized, as in Cheng et al. [23], these two design approaches strongly diverge: the inclusion of the CPC geometry in the set of decision variables to be optimized yields a concentrator with higher efficiency than the edge-ray design, but flux uniformity and acceptance are far lower.

In the case of a two-objective optimization based on optical efficiency and flux uniformity, as in the study conducted by Men et al. [24], results in Subsection 6.4.1 show that these two design approaches approximate more than in the case of the efficiency as the sole objective. First, an analysis of the optimum geometries reported by Men et al. [24] shows that all of them refer to non-truncated (full open) CPC optics – as it is done in the theoretical edge-ray design. Then, the practical case with the higher deviation in terms of CPC acceptance angle shows that even in this case the two design approaches yield similar secondary optics, and even more alike when designed with the same gap size. Indeed, the gap size emerges as an important decision variable to play with the trade-off between the optical efficiency, flux uniformity, and acceptance.

The approach of defining CPC geometric parameters as decision variables to be optimized by the search heuristic adds more decision variables to the optimization problem. On the contrary, the edge-rays design does not further complicate the optimization and even presents a clear advantage in the acceptance results. The results in Subsection 6.4.1 show that maximizing efficiency and flux uniformity yields a geometry close to an edge-ray design. Thus, a reasonable hypothesis is that the inclusion of an acceptance objective in the optimization routine would lead to edge-ray solutions for the CPC secondary optic – a subject for future research.

In Subsection 6.4.2, a comparison of the AOC and (CPC and CEC) edge-ray designs was presented. The results indicate that the AOC performs poorly in terms of acceptance, however, it presents higher flux uniformity than CPC and CEC and higher efficiency than the CPC. The aplanatic decision variables presented by Souza et al. [16] were optimized for a specific value of tube radius, so that a new value (e.g., the 0.035 mm of standard

evacuated tubes) would lead to a new search in the aplanatic design space. On the contrary, the edge-ray designs are analytical solutions, functions of the tube radius, and no further search is needed, simplifying the design problem.

Finally, the comparison results between CPC and CEC edge-ray designs shows that both optics relate to a trade-off between optical efficiency and acceptance, as represented by $\bar{\eta}$ and $\bar{\beta}$, respectively – the CPC presents the higher $\bar{\beta}$, whilst the CEC has higher $\bar{\eta}$. In terms of flux uniformity, as represented by $\bar{\delta}_q$, the optics do not significantly deviate. Furthermore, as the geometric concentration factor increases, the contour of CPC and CEC optics practically overlaps and, consequently, yield even closer performances.

References

[1] D. Feuermann and J. M. Gordon, "Analysis of a Two-Stage Linear Fresnel Reflector Solar Concentrator," *Journal of Solar Energy Engineering*, vol. 113, no. 4, pp. 272–279, 1991. DOI: 10.1115/1.2929973.

[2] P. Horta and T. Osório, "Optical Characterization Parameters for Line-focusing Solar Concentrators: Measurement Procedures and Extended Simulation Results," *Energy Procedia*, vol. 49, pp. 98–108, 2014. DOI: 10.1016/j.egypro.2014.03.011.

[3] G. C. Prasad, K. Reddy, and T. Sundararajan, "Optimization of solar linear Fresnel reflector system with secondary concentrator for uniform flux distribution over absorber tube," *Solar Energy*, vol. 150, pp. 1–12, 2017. DOI: 10.1016/j.solener.2017.04.026.

[4] S. Teske, J. Leung, L. Crespo, M. Bial, E. Dufour, and C. Richter, "Solar Thermal Electricity - Global Outlook 2016," European Solar Thermal Electricity Association (ESTELA), Tech. Rep., 2016. [Online]. Available: https://www.estelasolar.org/wp-content/uploads/2016/02/GP-ESTELA-SolarPACES_Solar-Thermal-Electricity-Global-Outlook-2016_Full-report.pdf.

[5] M. Collares-Pereira, D. Canavarro, and L. Guerreiro, "Linear Fresnel reflector (LFR) plants using superheated steam, molten salts, and other heat transfer fluids," in *Advances in Concentrating Solar Thermal Research and Technology*, M. J. Blanco and L. R. Santigosa, Eds., Cham: Elsevier, 2017, ch. 15, pp. 339–352. DOI: 10.1016/B978-0-08-100516-3.00015-0.

[6] RioGlass. "RECEIVER TUBES FOR LINEAR CSP (CONCENTRATED SOLAR POWER) APPLICATIONS." (2025), [Online]. Available: https://www.rioglass.com/en/our-products/hce-tubes (visited on 03/07/2025).

[7] F. Burkholder and C. Kutscher, "Heat Loss Testing of Schott's 2008 PTR70 Parabolic Trough Receiver," National Renewable Energy Laboratory (NREL), Golden, CO (United States), Tech. Rep., 2009. DOI: 10.2172/1369635.

[8] M. Cagnoli, D. Mazzei, M. Procopio, V. Russo, L. Savoldi, and R. Zanino, "Analysis of the performance of linear Fresnel collectors: Encapsulated vs. evacuated tubes," *Solar Energy*, vol. 164, pp. 119–138, 2018. DOI: 10.1016/j.solener.2018.02.037.

[9] R. Grena and P. Tarquini, "Solar linear Fresnel collector using molten nitrates as heat transfer fluid," *Energy*, vol. 36, no. 2, pp. 1048–1056, 2011. DOI: 10.1016/j.energy.2010.12.003.

[10] D. Canavarro, J. Chaves, and M. Collares-Pereira, "Simultaneous Multiple Surface method for Linear Fresnel concentrators with tubular receiver," *Solar Energy*, vol. 110, pp. 105–116, 2014. DOI: 10.1016/j.solener.2014.09.002.

[11] G. Zhu, "Development of an analytical optical method for linear Fresnel collectors," *Solar Energy*, vol. 94, pp. 240–252, 2013. DOI: 10.1016/j.solener.2013.05.003.

[12] S. Balaji, K. Reddy, and T. Sundararajan, "Optical modelling and performance analysis of a solar LFR receiver system with parabolic and involute secondary reflectors," *Applied Energy*, vol. 179, pp. 1138–1151, 2016. DOI: 10.1016/j.apenergy.2016.07.082.

[13] D. Canavarro, J. Chaves, and M. Collares-Pereira, "New dual asymmetric CEC linear Fresnel concentrator for evacuated tubular receivers," in *AIP Conference Proceedings*, vol. 1850, 2017, p. 040 001. DOI: 10.1063/1.4984397.

[14] A. Vouros, E. Mathioulakis, E. Papanicolaou, and V. Belessiotis, "On the optimal shape of secondary reflectors for linear Fresnel collectors," *Renewable Energy*, vol. 143, pp. 1454–1464, 2019. DOI: 10.1016/j.renene.2019.05.044.

[15] H. Ajdad, Y. Filali Baba, A. Al Mers, O. Merroun, A. Bouatem, and N. Boutammachte, "Particle swarm optimization algorithm for optical-geometric optimization of linear fresnel solar concentrators," *Renewable Energy*, vol. 130, pp. 992–1001, 2019. DOI: 10.1016/j.renene.2018.07.001.

[16] L. F. L. Souza, N. Fraidenraich, C. Tiba, and J. M. Gordon, "Linear aplanatic Fresnel reflector for practical high-performance solar concentration," *Solar Energy*, vol. 222, pp. 259–268, 2021. DOI: 10.1016/j.solener.2021.05.002.

[17] A. Ahmadpour, A. Dejamkhooy, and H. Shayeghi, "Optimization and modelling of linear Fresnel reflector solar concentrator using various methods based on Monte Carlo Ray–Trace," *Solar Energy*, vol. 245, pp. 67–79, 2022. DOI: 10.1016/j.solener.2022.09.006.

[18] H. Beltagy, "A secondary reflector geometry optimization of a Fresnel type solar concentrator," *Energy Conversion and Management*, vol. 284, p. 116 974, 2023. DOI: 10.1016/j.enconman.2023.116974.

[19] M. Hack, G. Zhu, and T. Wendelin, "Evaluation and comparison of an adaptive method technique for improved performance of linear Fresnel secondary designs," *Applied Energy*, vol. 208, pp. 1441–1451, 2017. DOI: 10.1016/j.apenergy.2017.09.009.

[20] R. Abbas, A. Sebastián, M. Montes, and M. Valdés, "Optical features of linear Fresnel collectors with different secondary reflector technologies," *Applied Energy*, vol. 232, pp. 386–397, 2018. DOI: 10.1016/j.apenergy.2018.09.224.

[21] R. Winston, J. C. Miñano, P. Benítez, W. T. Welford, J. C. Minano, and P. Benitez, *Nonimaging Optics*. Cambridge: Elsevier, 2005. DOI: 10.1016/B978-0-12-759751-5.X5000-3.

[22] R. Oommen and S. Jayaraman, "Development and performance analysis of compound parabolic solar concentrators with reduced gap losses – oversized reflector," *Energy Conversion and Management*, vol. 42, no. 11, pp. 1379–1399, 2001. DOI: 10.1016/S0196-8904(00)00113-8.

[23] Z. D. Cheng, X. R. Zhao, Y. L. He, and Y. Qiu, "A novel optical optimization model for linear Fresnel reflector concentrators," *Renewable Energy*, vol. 129, pp. 486–499, 2018. DOI: 10.1016/j.renene.2018.06.019.

[24] J. Men, X. Zhao, Z. Cheng, Y. Leng, and Y. He, "Study on the annual optical comprehensive performance of linear Fresnel reflector concentrators with an effective multi-objective optimization model," *Solar Energy*, vol. 225, pp. 591–607, 2021. DOI: 10.1016/j.solener.2021.07.051.

[25] J. Chaves, *Introduction to Nonimaging Optics*, 2nd Edition. New York: CRC Press, 2016. DOI: 10.1201/b18785.

[26] Y. Qiu, M. J. Li, K. Wang, Z. B. Liu, and X. D. Xue, "Aiming strategy optimization for uniform flux distribution in the receiver of a linear Fresnel solar reflector using a multi-objective genetic algorithm," *Applied Energy*, vol. 205, pp. 1394–1407, 2017. DOI: 10.1016/j.apenergy.2017.09.092.

[27] J. Ma, C.-L. Wang, Y. Zhou, and R.-D. Wang, "Optimized design of a linear Fresnel collector with a compound parabolic secondary reflector," *Renewable Energy*, vol. 171, pp. 141–148, 2021. DOI: 10.1016/j.renene.2021.02.100.

[28] Y. Qiu, Y. L. He, Z. D. Cheng, and K. Wang, "Study on optical and thermal performance of a linear Fresnel solar reflector using molten salt as HTF with MCRT and FVM methods," *Applied Energy*, vol. 146, pp. 162–173, 2015. DOI: 10.1016/j.apenergy.2015.01.135.

[29] E. T. Gomes, N. Fraidenraich, O. C. Vilela, C. A. Oliveira, and J. M. Gordon, "Aplanats and analytic modeling of their optical properties for linear solar concentrators with tubular receivers," *Solar Energy*, vol. 191, pp. 697–706, 2019. DOI: 10.1016/j.solener.2019.08.037.

[30] R. Abbas and J. Martínez-Val, "Analytic optical design of linear Fresnel collectors with variable widths and shifts of mirrors," *Renewable Energy*, vol. 75, pp. 81–92, 2015. DOI: 10.1016/j.renene.2014.09.029.

[31] T. Wendelin, A. Dobos, and A. Lewandowski, "SolTrace: A Ray-Tracing Code for Complex Solar Optical Systems," National Renewable Energy Laboratory (NREL), Golden, CO (United States), Tech. Rep., 2013. DOI: 10.2172/1260924.

[32] A. Santos, "soltracepy: a Python module for the fast implementation of SolTrace ray-tracing simulations," *Zenodo*, 2023. DOI: 10.5281/zenodo.10439687.

[33] W. F. Holmgren, C. W. Hansen, and M. A. Mikofski, "Pvlib python: A python package for modeling solar energy systems," *Journal of Open Source Software*, vol. 3, no. 29, p. 884, 2018. DOI: 10.21105/joss.00884.

[34] I. Reda and A. Andreas, "Solar position algorithm for solar radiation applications," *Solar Energy*, vol. 76, no. 5, pp. 577–589, 2004. DOI: 10.1016/j.solener.2003.12.003.

[35] A. Rabl, *Active Solar Collectors and Their Applications*. New York: Oxford University Press, 1985. [Online]. Available: https://shorturl.at/oGLX6.

Nomenclature

Abbreviations

AOC	Aplanatic Optic Concentrator
CEC	Compound Elliptical Concentrator
CPC	Compound Parabolic Concentrator
DNI	Direct Normal Irradiance
EW	East-West
LFC	Linear Fresnel Collector
NS	North-South
TMY	Typical Meteorological Year

Latin Letters

$\mathbf{F}_1$,$\mathbf{F}_2$	Edge-points of the primary field	
$\mathbf{T}_1$,$\mathbf{T}_2$	Edge-points of the absorber tube	
A_{abs}	Absorber tube surface area	[m^2]
A_{net}	Primary field mirror (net) area	[m^2]
d	The distance between centers of two neighboring primary mirrors	[m]
h_s	Secondary optic height from the tube center	[m]
H_R	Absorber tube height above the primary field	[m]
k	Aplanatic optic design parameter	[-]
L	concentrator length (in the longitudinal direction)	[m]
n	Number of mirrors in the primary field	[-]
NA	Aplanatic optic design parameter	[-]
N_{bins}	Number of circumferential bins in which the absorber is divided	[-]
N^a_{rays}	Number of absorbed rays	[-]
q_i	Flux density in the circumferential bin of index i	[W/m^2]
q_{ray}	Power carried by each light ray	[W]
Q_{abs}	Absorbed flux in the receiver	[W]
r_a	Absorber tube radius	[m]
r_{gap}	The gap radius	[m]
r_{go}	Outer cover radius	[m]
R	Primary mirror curvature radius	[m]
s	Aplanatic optic design parameter	[-]
w	Primary mirror width	[m]
W_a	Aplanatic primary optic aperture width	[m]
W_p	Primary field aperture width	[m]
W_s	Secondary optic aperture width	[m]

Greek Letters

α	Absorptivity of the absorber tube	[-]
β	LFC optic acceptance half-angle	[degrees]
$\bar{\beta}$	Annual average value of β	[degrees]
δ_q	Circumferential flux non-uniformity index	[-]
$\bar{\delta_q}$	Annual average value of δ_q	[-]
η	LFC optical efficiency	[-]
$\bar{\eta}$	Annual average value of η	[-]
θ_a	CPC optic acceptance half-angle	[degrees]
θ_e	Angular aperture defined by the intersection of edge-rays	[degrees]
θ_{max}	Maximum opening angle of a CPC secondary optic	[degrees]
θ_L	Longitudinal incidence angle	[degrees]
θ_T	Transversal incidence angle	[degrees]

μ_q	Average flux density at the absorber	[W/m^2]
ρ_p	Primary reflectors reflectivity	[-]
ρ_s	Secondary reflector reflectivity	[-]
σ_c	Standard deviation of a Gaussian contour error distribution	[mrad]
σ_o	Standard deviation of the overall Gaussian error distribution	[mrad]
σ_q	Standard deviation of the circumferential flux distribution	[W/m^2]
σ_s	Standard deviation of a Gaussian specular error distribution	[mrad]
σ_{sun}	Standard deviation of a Gaussian sunshape distribution	[mrad]
σ_t	Standard deviation of a Gaussian tracking error distribution	[mrad]
Δr_g	Distance between glass outer cover and secondary optic: $r_{gap} - r_{go}$	[m]
Δ_{sun}	Half-width of a pillbox sunshape distribution	[mrad]
$\Delta\bar{\eta}$	Relative difference of annual optical efficiency	[-]

Indices

h	Hour index
i	General counting index
j	General counting index

Chapter 7

On optimum designs[†]

Abstract

This chapter investigates the optimal design of linear Fresnel collectors using a two-objective optimization strategy aimed at maximizing annual energy efficiency while minimizing the specific direct cost of the solar field. The analysis then compares Pareto-optimal solutions for non-uniform designs (where geometric parameters such as width, shift, and radius vary) with solutions for variable radius configurations (constant width and shift). Additionally, the study evaluates whether the curvature radius can be effectively decoupled from other optimization parameters. The results in this paper show that non-uniform designs generally provide greater cost-effectiveness, particularly in certain regions of the objective space. While some regions show negligible differences between configurations, others distinctly favor non-uniform designs, although the differences are not significant and are reduced as the number of mirrors in the primary field increases. Furthermore, an analysis through dimensionless parameters highlights clear trends among the Pareto solutions. The investigation also reveals that predefined curvature radius criteria, such as the sun reference or Iparraguirre's model, yield outcomes nearly identical to optimization-based solutions for both uniform and non-uniform configurations. Consequently, curvature radius can be decoupled from other design parameters, significantly reducing computational complexity without compromising performance. The insights presented are valuable for advancing cost-effective designs of linear Fresnel collectors. Nevertheless, the conclusions rely on a simplified cost model, highlighting the need for more comprehensive cost modeling. However, developing such detailed models remains challenging due to limited operational data stemming from the low commercial maturity of the linear Fresnel technology.

Keywords: Linear Fresnel Collector; Optical analysis; Geometric optimization.

[†]A. V. Santos, D. Canavarro, P. Horta, and M. Collares-Pereira, "On optimum designs of linear Fresnel solar collectors," Under review, *Solar Energy*, 2025.

7.1 Introduction

The model presented in Figure 2.3 describe all parameters needed to define a geometric configuration of a linear Fresnel collector. For a particular absorber, the general decision vector describing a configuration is given by $\hat{x} = \{n, \{w_1, m_1, R_1\}, ..., \{w_n, m_n, R_n\}, H_R, z_s, W_s\}$, where w, m, and R stands for the width, position, and curvature radius of the n primary mirrors in the field. Moreover, H_R denotes the receiver height above the primary field, and z_s and W_s are shape function and aperture width of the secondary optic. In short, the design problem relates to find a decision vector, $\hat{x}^*$, which yields an optimal performance.

The literature on the optimum design of linear Fresnel collectors (LFCs) comprises studies that analyze particular optical losses and propose design criteria on how to calculate some decision variables [1–7]. It also comprises studies that take the approach of an optimization problem [8–14], where decision variables, constraints, and objective functions are defined, and parametric analysis [8], gradient-based methods [9] or computational intelligence tools [10–14] are used as search heuristics to determine optimum set of variables.

In general, results from these works are not in accordance, and the comparison is not easy: the dimensions (sizing) vary due to different applications and constraints. They comprise different primary field configurations (uniform and non-uniform); single [9, 11, 12] and multi-objective [10, 14] approaches defined by a wide range of objective functions based on different metrics [2, 10–12] and cost models [6, 9, 10]; performance computations comprise instantaneous [13], daily [10, 12, 15], and annual [2, 6, 8, 9, 11, 14] analyses.

Nevertheless, dimensionless parameters can be defined to be used as a comparison basis and, thus, different works can be confronted. One parameter is the filling factor: $\pi_1 = \sum w_i / W_p$, where i is an index to count for each mirror in the primary field ($i = \{1, 2, ..., n\}$) and W_p stands for the primary field width. π_1 is a packing measure of the primary field: a higher filling factors means denser fields. Another is the shape factor, π_2, here defined as $\pi_2 = W_p / 2H_R$, used to represent an overall proportionality metric width and height of the concentrator. The last, π_3, is the pitch factor, defined by the pitch-to-width ratio, so that $\pi_3 = s/w$, where s denotes for the distance (or pitch) between neighboring primary mirrors, only meaningful for uniform configurations of width ($w_i = w$) and shift ($s_i = s$).

A summary of reported optimum parameters are presented in Table 7.1. As it shows, the aforementioned parameters vary significantly among the different studies. It is reasonable to consider that such variability is caused by the different locations and orientations [8, 14] since the frequency distribution of incidence angles and the corresponding available sunlight change with these two factors. Furthermore, different optimization objectives also lead to different optimum geometries, as highlighted by Montes et al. [2]. Although no generalization can be assumed from the literature data presented in Table 7.1, some important lessons can be learned from those works.

The majority of studies deal with uniform primary fields (all mirrors have the same width and curvature radius, and are evenly spaced) [8, 11, 12, 14, 15]. Normally, studies that tackle non-uniform configurations does it by an analytical pre-design [1, 3–5] in which some variables are calculated based on design criteria and only few of them are optimized by the search heuristic – a strategy to reduce the number of variables and simplify the problem.

Table 7.1: Dimensionless parameters reported on the linear Fresnel collector optimal designs. In the "Configuration" column, C and V refer to constant and variable geometric settings, respectively, and W, S, and R refer to width, shift, and radius of primary mirrors, respectively – thus, C-W stands for constant width, while V-R stands for variable radius. In the "Orientation" column, NS and EW refer to North-South and East-West, respectively. CBC refers to parameters that cannot be calculated due to missing data in the original paper. Moreover, $\pi_1 = \sum w_i/W_p$, $\pi_2 = W_p/2H_R$, and $\pi_3 = s/w$.

Reference	**Location**	**Orientation**	**Configuration**	π_1	π_2	π_3
Nixon and Davies [6]	E72.65°, N23.22°	NS	C-W & V-S & C-R	0.647	0.865	var
Montes et al. [2]	E2.36°, N37.11°	NS	C-W & C-S & V-R	0.720	1.000	1.405
Sharma et al. [8]	E76.95°, N8.48°	NS	C-W & C-S & C-R	0.616	1.160	1.65
		EW		0.826	0.865	1.22
	E72.63°, N23.07°	NS		0.581	1.229	1.75
		NS		0.728	0.982	1.39
	W1.6°, N38.27°	NS		0.548	1.305	1.86
		EW		0.623	1.147	1.63
Boito and Grena [9]	Not reported	NS	C-W & C-S & C-R	0.832	1.502	1.21
			C-W & V-S & C-R	0.836	1.497	var
			C-W & C-S & V-R	0.828	1.603	1.127
Moghimi et al. [10]	Do not apply	Do not apply	V-W & V-S & V-R	0.829	1.661	var
Cheng et al. [11]	E115.90°, N23.45°	EW	C-W & C-S & C-R	0.968	0.718	1.034
Ajdad et al. [12]	W8.0°, N31.62°	NS	C-W & C-S & C-R	0.510	0.649	2.000
			C-W & C-S & C-R	0.786	0.639	1.297
Ahmadpour et al. [15]	E48°18', N38°12'	Not reported	C-W & C-S & C-R	CBC	CBC	CBC
López-Núñez et al. [13]	W99.23°, N18.54°	Not reported	C-W & V-S & C-R	CBC	CBC	var

Evidence suggest that primary field with non-uniform configurations of width and shift do not significantly increase energy collection [3–5, 9]. Some results [1, 3–5] are based on an analytical pre-design, which constrains the search space and might lead to local optima (biased) results. Another [9] used the cost-energy ratio as the objective function to be minimized, transforming a two-objective problem (cost and efficiency) into a single objective one – a strategy that can lead to only a single Pareto solution and difficults a more general assessment. On the one hand, it is striking that different studies through different approaches have found that these non-uniform designs do not have a significant impact on performance in comparison to the uniform design. On the other hand, most of these studies do not include an economic model and only consider energy collection [3–5]. A previous work [7] verified that the collected energy per unit of reflective area was lower for their non-uniform shift proposition. Only Boito and Grena [9] have included a cost model, but a rather simple and linear one. Thus, a reasonable research question to be further investigated rises:

- are non-uniform designs of width and shift more cost-effective than variable-radius designs (with constant width and shift)?

Regarding the curvature radius design of the primary mirrors, the different studies concerning the optimal radius [1, 3–5, 16], outlined in Chapter 5, holds a fundamental underlying hypothesis that, of course, might not be true and should be verified: they assume the curvature radius as a decoupled variable that can be optimized in a step after other geometric parameters (such as mirrors widths and pitches, receiver height, among others) – only Boito and Grena [9] include the curvature radius in the optimization routine with the other decision variable – their results indicate that different configurations of curvature radius (uniform or non-uniform) have a meager impact on the other geometric parameters. Then, the following research question is established:

- can the curvature radius be decoupled from other decision variables in design optimization?

To address these questions, this study adopts a multi-objective optimization approach, focusing on energy efficiency and cost, as optical, thermal, and economic components are crucial for evaluating overall performance and can even present a cost-benefit trade-off. Accordingly, the structure of this chapter is as follows. It starts by outlining the methodology, defining decision variables, performance models, and objective functions that link a specific geometric configuration to key metrics, such as annual useful energy efficiency and the direct specific cost of the linear Fresnel collector. Then, its introduces the evolutionary algorithm used to solve the global optimization problem. Section 7.5 presents the results and discusses each of the previously defined research questions. Lastly, Section 7.6 presents the conclusions and suggests directions for future research.

7.2 Geometric model and decision variables

Figure 2.3 presents a geometric model for the standard Linear Fresnel Collector (LFC). Therefore, the same nomenclature as defined in Subsection 2.1.3 is used in this chapter. Among all these geometric parameters some are considered as decision variables to be optimized, while others are defined by constraints of the problem.

The context of solar thermal electricity application refers to high-temperature heat generation (> 400 °C), and the use evacuated tubes [17] is a practical constrain due to its low

thermal losses under such conditions [18, 19]. Commercial availability imposes a restriction on the size of these tubes, and, here, the 70 mm diameter evacuated tube is defined as the absorber element – the smallest option, which leads to higher concentration and lower thermal losses. The geometric characteristic of this tube are presented in Table 7.2: r_a refers to the absorber tube radius, while r_{go} and r_{gi} stands for the outer and inner glass cover radius, respectively.

Table 7.2: Evacuated tube geometric characteristics [17]. r_a refers to the absorber tube radius, while r_{go} and r_{gi} stands for the outer and inner glass cover radius, respectively.

r_a [m]	r_{go} [m]	r_{gi} [m]
0.035	0.0625	0.0595

The receiver considered in this chapter also comprises an edge-ray CEC (Compound Elliptical Concentrator) secondary optic. It has the lowest possible gap between the optic and the absorber – that is, the cusp point touches the outer glass cover of the absorber tube. This CEC geometry is a consequence of the other parameters and does not add new parameters to the model shown in Figure 2.3. Moreover, this edge-ray CEC design yields a secondary optic that simultaneously maximizes efficiency, flux uniformity, and tolerance to optical errors, as demonstrated in Chapter 6. Thus, the aim of this chapter concerns mainly the primary field and receiver position.

By considering these constraints regarding the receiver, the design of a linear Fresnel collector relates to the definition of the following geometric parameters: width, position, and curvature radius (w, m, and R, respectively) of the n primary mirrors, and the receiver height (H_R). In this sense, a non-uniform configuration is defined by the following decision vector: $\hat{x} = \{n, \{w_1, m_1, R_1\}, ..., \{w_n, m_n, R_n\}, H_R\}$, which involves $3n+2$ decision variables. A uniform configuration is defined by $\hat{x} = \{n, w, s, R, H_R\}$, which has only five decision variables. Of course, it is also possible to consider uniform and non-uniform settings for only particular parameters such as w and R, for example. Moreover, a symmetric design also leads to a significant reduction in the number of geometric parameters to be defined.

7.3 Performance models

The performance of a linear Fresnel collector can be evaluated under three aspects. One is the optical component, which represents the energetic input on the system. The thermal aspect evaluate the production of useful heat by assessing the thermal losses, while the economical aspect gives a metric of the cost of produced energy. Here, the power block computations that account for the heat-to-electricity conversion are not considered because it would be a common factor among all different configurations.

Energy efficiency computations must consider an annual time frame to account for all incident solar irradiation at a particular location. To reduce the total computation time of ray-tracing simulations other authors have define surrogate models for an annual analysis: Abbas and Martínez-Val [5] compute only twelve representative days (the 21st of each month); Cheng et al. [11] and Men et al. [14] have considered four representative days (solstices and equinoxes); others simply consider a daily average [10, 12, 15], or just instantaneous values [13]. Here, an actual annual analysis is carried out.

7.3.1 Energy Efficiency model

Here, the useful energy efficiency is calculated by a steady-state model that accounts for the absorbed energy (optical input) above a threshold of flux intensity on the absorber sufficient to overcome thermal losses. This analysis is based on hourly averages to compute the annual yield.

To this end, the optical behavior of a particular configuration is computed by the analytical method developed in Chapter 3, which computes the flux at the aperture of the CEC secondary optic. Since all LFC configurations analyzed in this work have the same type of secondary, it is assumed that the CEC does not play a role on the differences of useful efficiency produced by two different configurations, and the flux at the aperture is enough to determine the one which has a higher yield. This optical model computes the efficiency for a particular incidence direction based on transversal and longitudinal incidence angles, θ_T and θ_L, respectively. The optical characterization determines the efficiency for an incidence range in which $\theta_L \in [0°, 85°]$ and $\theta_T \in [-85°, 85°]$ or asymmetric primary fields or $\theta_T \in [0°, 85°]$ for symmetric cases. At θ_L or θ_T equals to 90°, the efficiency is set to zero. The annual analysis is based on hourly data of a typical meteorological year taken from the PVGIS application program interface [20]. For each of the 8760 hours of the year, sun azimuth and zenith are calculated by a solar position algorithm [21] and then converted to transversal and longitudinal incidence angles, θ_T and θ_L, respectively.

In this chapter, the Energy Collection Factor, ECF, as shown in Equation 7.1, is the metric used to represent the amount of useful energy efficiency produced by a particular geometric configuration, in the meaning that $\mathrm{ECF} = \mathrm{ECF}(\hat{x})$.

$$\mathrm{ECF} = \frac{\sum_{h=1}^{8760} \left[\eta_T(\theta_T^h)\eta_L(\theta_{LS}^h) I_b^h \cdot A_{net} - I_{min} \cdot A_{abs}\right]^+}{\eta_0 \sum_{h=1}^{8760} I_b^h \cdot A_{net}} \tag{7.1}$$

In Equation 7.1, the optical efficiency for a particular incidence direction is computed by the factorized approach, and a better approximation is achieved by using θ_{LS}, the longitudinal-solar incidence angle, as detailed in Section 2.3. As such, the terms η_T and η_L stands for the transversal and longitudinal optical efficiencies of this factorized approach, respectively, while η_0 is the optical efficiency at normal incidence. Moreover, this optical analysis considers conditions of sunshape and optical errors as shown in Table 7.3.

Table 7.3: Models of sunshape and optical errors considered for the optical analysis of a linear Fresnel geometric configuration.

	Sunshape	**Optical errors**
Profile	Pillbox	Gaussian
Size	4.65 mrad	5.0 mrad

In the yield model shown in Equation 7.1, the thermal losses are included by I_{min} and the positive sign (+). The first represents a threshold of flux intensity, which together with the latter means that only the flux at the absorber above a particular threshold is computed as useful heat. The terms A_{net} and A_{abs} represent mirror and absorber areas of the linear Fresnel configuration. Furthermore, I_b stands for the direct normal (or beam) irradiance, and h is an index that ranges for each of the 8760 hours of the year.

Abbas et al. [4] argues for $I_{min} = 25.0$ kW/m^2 to reach temperatures higher than 400 °C, but this data comes from studies that account for non-evacuated receivers, which implies considerable higher thermal losses. For an evacuated receiver operating at temperatures of 560 °C, modelling and experimental works [18, 22, 23] indicate thermal losses per unit of absorber surface up to 5.0 kW/m^2 for a 70 mm diameter absorber tube. Thus, the computations in this chapter considers $I_{min} = 5.0$ kW/m^2 – the absorber flux intensity threshold necessary to overcome thermal losses and produce useful heat.

7.3.2 Cost model

A geometric cost model relates parameters shown in Figure 2.3 to a metric of the direct specific cost of the linear Fresnel concentrator, Γ, given in units of €/m^2 of mirror aperture area. Therefore, Γ is a function of the geometric settings, and one can write $\Gamma = \Gamma(\hat{x})$.

The functional relationship used in this work for Γ follows the equations proposed by Mertins [24], but in a more generalized formulation to include variations of the decision vector other than the simple uniform configuration. Mertins' model was also used in the work carried out by Moghimi et al. [10] but with a modification to account for a multi-tube receiver.

Here, Γ is given by Equation 7.2, where c_m, c_g, c_e, and c_r refers to mirror, gap, elevation, and receiver cost factors, respectively. Moreover, w and g stands for the width and gap of a primary mirror, respectively, H_R is the receiver height, and i is an index used to range for all n mirrors in the primary field.

$$\Gamma = \frac{\sum_{i=1}^{n} c_{m,i} + \sum_{i=1}^{n-1} c_{g,i} \cdot g_i + c_e \cdot (H_R + 4.0) + c_r}{\sum_{i=1}^{n} w_i} \tag{7.2}$$

To develop the cost factors that comprise Γ, Mertins [24] used empirical data from the SOLARMUNDO project, scale relationships, and logarithmic averages to project values of c_m, c_g, c_e, and c_r at a target size.

The mirror cost factor, c_m, represents the cost of the mirror per unit of length, and accounts for the reflective material, driving motors, tracking system, controllers, assembly, etc. Then, for a mirror width w, the corresponding mirror cost factor c_m is calculated as shown in Equation 7.3, where w_0 and c_{m0} are the reference size and cost, respectively, and f_m is the scale factor, as given in Table 7.4.

$$c_m = c_{m0} \left(\frac{w}{w_0} \right)^{f_m} \tag{7.3}$$

The gap cost factor, c_g, represents the cost of the distance between two mirrors per unit of length. It relates to the distance between two neighbor mirrors when they are in a horizontal position. It is reasonable to assume that a higher gap increases cost as its uses more structuring material. For a gap g, the cost factor c_g is determined by Equation 7.4, where g_0 and c_{g0} are the reference size and cost, respectively, and f_g is the corresponding scale factor, as shown in Table 7.4.

$$c_g = c_{g0} \left(\frac{g}{g_0} \right)^{f_g} \tag{7.4}$$

Table 7.4: Mirror and gap cost factors [24].

c_{m0}	30.5 €/m	c_{g0}	11.5 €/m^2
w_0	0.5 m	g_0	0.01 m
f_m	1	f_g	1

The elevation cost factor, c_e, relates with the receiver mounting at a height H_R above the primary field. It is given per unit of length and unit of elevation, thus in €/m^2. It follows a similar approach than in the cases of c_m and c_g, but based on the absorber tube diameter, d_a, and a variable scale factor, f_e, also a function of d_a, as in shown in Equation 7.5. The reference size and elevation cost factor reported by Mertins [24] are for a tube diameter of 0.219 m and a cost of 19.8 €/m^2, respectively.

$$c_e = 19.8 \text{ €/m}^2 \left(\frac{d_a}{0.219 \text{ m}} \right)^{f_e(d_a)} \tag{7.5}$$

f_e is calculated as given by Equation 7.6, a logarithmic average of the three elevation subsystems shown in Table 7.5, where k is an index to range for all these subsystems.

$$f_e = \frac{\ln \left[\sum_k \left(\frac{c_{e,k}}{19.8 \text{ €/m}^2} \right) \left(\frac{d_a}{0.219 \text{ m}} \right)^{f_{e,k}} \right]}{\ln \left(\frac{d_a}{0.219 \text{ m}} \right)} \tag{7.6}$$

Table 7.5: Reference costs and scaling factors of elevation subsystems [24].

Elevation subsystem	$f_{e,k}$	$c_{e,k}$ [€/m^2]
Construction	1.4	14.2
Transportation	1	0.9
Assembly	1	4.6

The receiver cost factor, c_r, relates with the absorber tube, coatings, welding and construction, assembly and transportation. It is given per unit of length, thus in €/m. As in the case of c_e, it considers d_a as the scaling parameter and also a variable scale factor, as shown in Equation 7.7. The reference size and receiver cost factor reported by Mertins [24] are for a tube diameter of 0.219 m and a cost of 654.0 €/m, respectively.

$$c_e = 654.0 \text{ €/m} \left(\frac{d_a}{0.219 \text{ m}} \right)^{f_r(d_a)} \tag{7.7}$$

f_r is calculated as given by Equation 7.8, a logarithmic average of the three receiver subsystems shown in Table 7.6, where k is an index to range for all these subsystems.

$$f_e = \frac{\ln \left[\sum_k \left(\frac{c_{r,k}}{654.0 \text{ €/m}} \right) \left(\frac{d_a}{0.219 \text{ m}} \right)^{f_{r,k}} \right]}{\ln \left(\frac{d_a}{0.219 \text{ m}} \right)} \tag{7.8}$$

Table 7.6: Reference costs and scaling factors of receiver subsystems [24].

Receiver subsystem	$f_{r,k}$	$c_{r,k}$ [€/m]
Absorber tube	2.0	116.2
Selective coating	0.9	56.6
Welding	0.7	116.4
Construction	1.4	136.5
Transportation and packing	0.6	26.4
Assembly	0.6	112.6

The mathematical models from Equations 7.2 to 7.8 were implemented in Python and yield the exact same cost as reported by Mertins [24] for a reference case: 99.2 €/m^2.

It is important to highlight some aspects regarding this cost model. Γ is a metric of the solar field specific direct cost, a component of the engineering procurement and construction costs. Thus, it does not include other factors such as land, site preparation, storage, power block, among others that sums up the power plant Capital Expenditures (CAPEX) [25]. The influence of the curvature radius (values and non-uniform configurations) on Γ is not included. On the one hand, usually $R \gg w$ and mirrors are almost flat, leading to negligible additional cost due to the use of more reflective material (which occurs in parabolic trough collectors). On the other hand, some additional steps in the manufacturing process of bent mirrors [26] can indeed lead to increase in costs. Moreover, non-uniform configurations regarding w and R can have an influence on the Operational Expenditures (OPEX) due to the need of more spare parts, which are not included here. In this sense, the presented cost model assumes negligible effects on OPEX, an assumption that might not be true. However, further analysis of how non-uniform configurations affect CAPEX and OPEX lies beyond the scope of this work.

Lastly, the reported values are from 2009 and should be corrected by inflation. However, from a comparison point-of-view, the functional relationships within the model are more important than the current monetary values. For this reason, the base values of this model were not corrected up to today's inflation.

7.4 Optimization approach

7.4.1 Problem definition

Considering the performance metrics presented in Section 7.3, the aim is to find a decision vector which simultaneously yields the highest ECF and lowest Γ; that is, the objectives are to find maximum efficiency and minimum cost. This optimization problem is defined in Equation 7.9, where ECF and Γ are the objective functions that relates the performance of a geometric configuration defined by the decision vector $\hat{x}$.

$$\begin{cases} \max & \text{ECF}(\hat{x}) \\ \min & \Gamma(\hat{x}) \end{cases} \tag{7.9}$$

A general decision vector $\hat{x} = \{n, \{w_1, m_1, R_1\}, ..., \{w_n, m_n, R_n\}, H_R\}$ corresponds to a full non-uniform configuration and its size is a function of n, the number of mirrors comprising the primary field. Usually in the literature [3, 4, 9, 11, 14], n is fixed and the other parameters are decision variables to be optimized by the search heuristic since find the optimum $\hat{x}$ with changing number of decision variables is a quite hard task. Here, two sizes of primary fields are addressed: $n = 12$ and $n = 25$.

As reported by many works [4, 5, 8, 27], the East-West (EW) orientation have a lower annual efficiency than the North-South (NS) case. For this reason, only the NS orientation is considered in this chapter, and geometric configurations are assumed to be symmetric, so that, for example, $\{w_1, m_1, R_1\} = \{w_n, -m_n, R_n\}$. Moreover, it is easier to work with the gap, g, as a decision variable instead of mirror position or shift (m or s), as it makes unnecessary to account for feasible solutions that must obey a shift large enough for two neighboring mirrors to not collide. Then, $\hat{x}$ is a function of w, g, R, and H_R, where these variables are subjected to bounds as given by Table 7.7.

Table 7.7: Decision variables bounds for the optimization search.

H_R [m]	w [m]	g [m]	R [m]
$[4.0, 20.0]$	$[0.2, 2.0]$	$[0.0, 2.0]$	$[0.0, 100.0]$

For this matter, different configurations of primary field must be defined in order to address the research questions established in Section 7.1. First, the NUN case refers to a full non-uniform setting, where each mirror has particular values of w, g, and R, and all of them are subjected to the optimization routine. The VAR refers to the case of a primary field in which mirrors have constant values of width and gap (w and g) but with a variable radius (R), and all of them are subjected to the optimization routine. The NUN-sunRef is denominated by a non-uniform configuration in which w and g are subjected to optimization but R is calculated as given by the sun reference criteria [3]. UN defines a full uniform configuration, a geometric setting in which the primary field is defined by constant values of w, g, and R, all of them are subjected to the optimization routine. The UN-IpaRef stands for a configuration in which the primaries have constant values of w, g, and R, but only the first two are subjected to the optimization routine, while R is calculated by the criteria proposed by Pulido-Iparraguirre et al. [26].

Moreover, computations for ECF vary depending on a selected location since the annual distribution of beam irradiance and incidence angles change from one place to another. In this work, Evora (Portugal) is considered for the calculations, though it can be replicate to any other location. Evora general data is presented in Table 7.8.

Table 7.8: Location data for the selected site used to useful energy efficiency computations. Hourly data of a typical meteorological year is taken from the PVGIS application program interface [20] for the years between 2006 and 2016. For each of the 8760 hours of the year, sun azimuth and zenith are calculated by a solar position algorithm [21] and then converted to transversal and longitudinal incidence angles, θ_T and θ_L, respectively.

Location	Latitude	Longitude	$\sum I_b$
Evora (Portugal)	38.53°	-8.0°	2229.2 kWh $\cdot$ m^{-2} $\cdot$ yr^{-1}

7.4.2 Search algorithm

The problem defined in Equation 7.9 relates to an unconstrained multi-objective optimization [28, 29]. Both ECF and Γ must be simultaneously optimized, and instead of a single optimum decision vector, $\hat{x}^*$, a set of optimal solutions, $\{\hat{x}_1^*, ..., \hat{x}_N^*\}$, the so-called Pareto solutions, should be determined to represent the trade-off between objectives. In this context, evolutionary algorithms, as are stochastic population-based methods, are a proven strategy to determine the Pareto front of optimum solutions [30].

In this chapter, the evolutionary algorithm starts by generating a random population of N_{pop} individuals – each individual is a candidate solution defined by a decision vector. This population is evaluated and the corresponding fitnesses are defined by the objective functions (ECF and Γ). An offspring of N_{pop} individuals (children) is produced from the population by parents (mate) selection, followed by crossover and mutation. From the poll of individuals given by the union of population and offspring (size $2N_{pop}$), N_{pop} individuals are selected (survivors selection) to form a new population, to then produce a new offspring and so on [31, 32]. This cycle repeats itself until a stopping criterion is satisfied, and the Pareto solutions are then sorted from the final population. A flow diagram of this evolutionary process is presented in Figure 7.1.

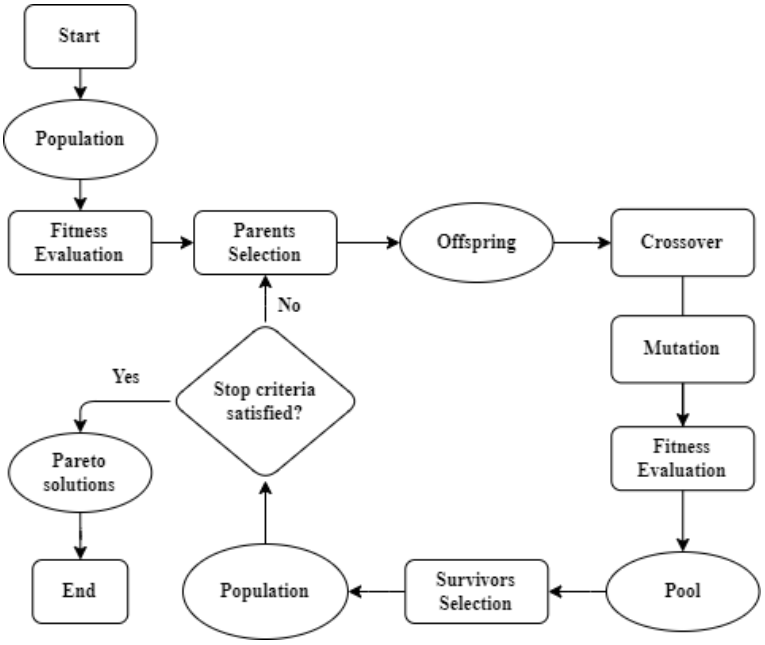

Figure 7.1: Evolutionary procedure used as the multi-objective search heuristic. It starts by generating a random population of N_{pop} individuals – each individual is a candidate solution defined by a decision vector. This population is evaluated and the corresponding fitnesses are defined by the objective functions (ECF and Γ). An offspring of N_{pop} individuals (children) is produced from the population by parents (mate) selection, followed by crossover and mutation. From the poll of individuals given by the union of population and offspring (size $2N_{pop}$), N_{pop} individuals are selected (survivors selection) to form a new population, to then produce a new offspring and so on [31, 32]. This cycle repeats itself until a stopping criteria is satisfied, and the Pareto solutions are then sorted from the final population.

This evolutionary search heuristic was implemented based on the DEAP (Distributed Evolutionary Algorithm in Python) framework [33, 34]. An individual (candidate solution) is coded as a list of real numbers between 0 and 1 (genes) and is decoded to the decision variable space (subjected to the bounds shown Table 7.7) to fitness evaluation. The selection mech-

anisms are based on dominance and crowding distance following the elitist Non-dominated Sorted Genetic Algorithm (NSGA-II) [35].

A solution B dominates another solution C if B is not worse than C in all objectives and B is strictly better than C in at least one objective. If neither B dominates C nor C dominates B, they are considered non-dominated. NSGA-II sorts the population into non-dominated fronts to rank solutions. The first non-dominated front consists of solutions that are not dominated by any other solution in the population – these are given rank 1. The second front (rank 2) holds individuals that are only dominated by those in the first front, and subsequent fronts contain solutions that are dominated by previous ones. The crowding-distance is a metric used to maintain diversity in the population by estimating the density of solutions surrounding a particular individual. It quantifies how close a solution is (in the objective space) to its neighbors within a non-dominated front. Therefore, high crowding distance means that a solution is in a sparse region (likely to be selected), while low crowding distance means that the solution is in a dense region (less chance of being selected).

Parents selection considers a tournament of two individuals randomly selected from the population. First, they are compared based on dominance – wins the individual which dominates the other, i.e., the one with the lowest rank. If they are non-dominated, wins the individual with higher crowding distance. Survivor selection is based on a combination of non-dominated sorting and crowding distance to ensure both convergence and diversity. First, individuals in the pool (population and offspring) are ranked into non-dominated fronts, where solutions in lower-ranked fronts (better Pareto-optimal solutions) are prioritized for selection. If the number of individuals in selected fronts exceeds the population size, the last front is sorted based on crowding distance, which measures how isolated a solution is in objective space. Solutions with higher crowding distance are preferred to maintain diversity. This ensures that the next generation retains high-quality and well-distributed solutions along the Pareto front.

Due to the computational cost of ECF evaluations, $N_{pop} = 200$ and the stopping criteria is a number of 400 (four hundred) generations, divided into two steps of 200 generations, each one with different settings of the same evolutionary operators: two-point crossover and (zero mean) Gaussian mutation. As shown in Table 7.9, there are probabilities for both crossover and mutation to take place, and σ_{mu} refers to the standard deviation of the Gaussian mutation operator. The first 200 generations runs with the evolutionary operator eoA, while the last 200 generations runs with eoB.

Table 7.9: Operators used in the evolutionary loop. A total of 400 generations is divided into two steps of 200 generations each. The first 200 generations runs with the evolutionary operator eoA, while the last 200 generations runs with eoB. In this table, σ_{mu} refers to the standard deviation of the (zero mean) Gaussian mutation operator.

Evolutionary operator	Crossover probability	Mutation probability	σ_{mu}
eoA	0.8	0.4	0.2
eoB	0.5	0.25	0.1

Further details about NSGA-II can be found in the works by Deb [30] and Eiben and Smith [32], while DEAP documentation has more information on the evolutionary operators.

7.5 Results and discussion

7.5.1 Non-uniform configuration analysis

Results from previous works [3–5, 9] highlighted that the non-uniform configuration might not be cost-effective, as it yields a slightly higher efficiency than a variable radius design but may imply more costs, which leads to a reasonable question: is the non-uniform design (NUN) more cost-effective than the variable-radius (VAR) case? To this end, this section presents a comparison of NUN and VAR optimum geometries.

Figure 7.2 shows a comparison of optimal solutions for optimization problem defined in Section 7.4, considering cases where the primary field is composed of (a) $n = 12$ and (b) $n = 25$ mirrors. As seen, the Pareto fronts clearly show a trade-off between efficiency (ECF) and cost (Γ) – as efficiency increases, costs rise significantly, showing an asymptotic behavior in all cases. The red dashed lines indicate the maximum efficiency, $\text{ECF}^{\max}$, and minimum cost, $\Gamma^{\min}$, achieved within each case. Therefore, many solutions have quite the same cost but with slightly increasing efficiencies; other solutions have practically the same efficiency but with highly increasing costs; then, there are solutions presenting a smoother trade-off between these asymptotic cases.

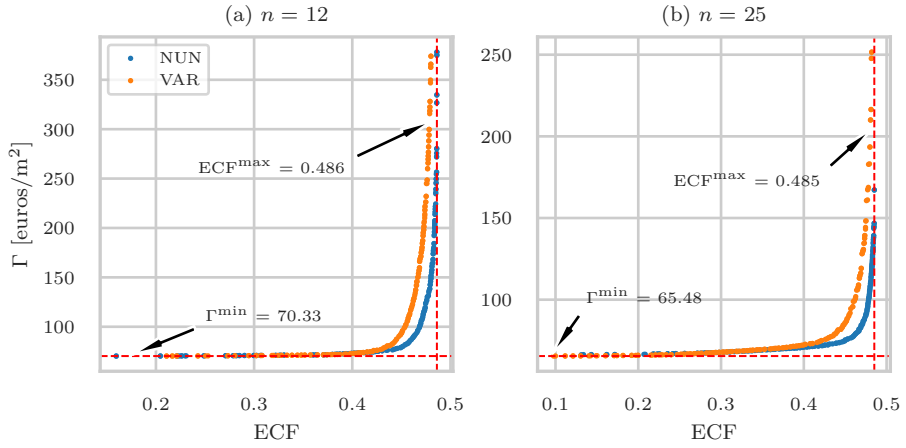

Figure 7.2: Pareto Fronts of optimal solutions for non-uniform and variable radius designs. It considers geometries for primary fields with different number of mirrors: (a) $n = 12$ and (b) $n = 25$, and annual efficiency computations for Evora and an absorber flux threshold of $I_{min} = 5.0$ kW/m^2. Blue dots represent non-uniform design, while the orange ones represent variable radius designs.

In general, Figure 7.2 shows that NUN (blue points) and VAR (orange points) configurations have similar trends. Previous works [3–5, 9] have found a meager difference between non-uniform and variable radius designs, as it is shown in Figure 7.2 for a wide region of the objective space. However, this figure also shows that in a region, for a particular value of efficiency, non-uniform designs have a lower cost than variable radius designs (or a higher efficiency for a reference cost). Moreover, these results indicate that the difference between non-uniform and variable radius is more noticeable for a primary field with fewer mirrors, and as the number of mirrors increases, the benefit of the fully non-uniform design diminishes.

In short, results in Figure 7.2 indicate that non-uniform designs are more cost-effective solutions, however, the performance difference is reduced as the number of mirrors in the primary field increases. In the theoretical limit case of a large number ($n \to \infty$) of tiny mirrors ($w \to \mathrm{d}w$), there would be no differences between these configurations.

Figure 7.3 provides a geometric perspective of the Pareto solutions in Figure 7.2 by plotting two dimensionless parameters: filling factor, $\pi_1 = \sum w_i/W_p$, and shape factor, $\pi_2 = W_p/2H_R$. Each point corresponds to a different geometric configuration, meaning that a direct comparison between solutions is complex, especially for non-uniform designs where mirror parameters vary individually. Despite this complexity, the scatter plots reveal two clear trends that apply to both configurations: a set of trivial solutions where π_1 is approximately 1, and a more structured trend for the remaining data points.

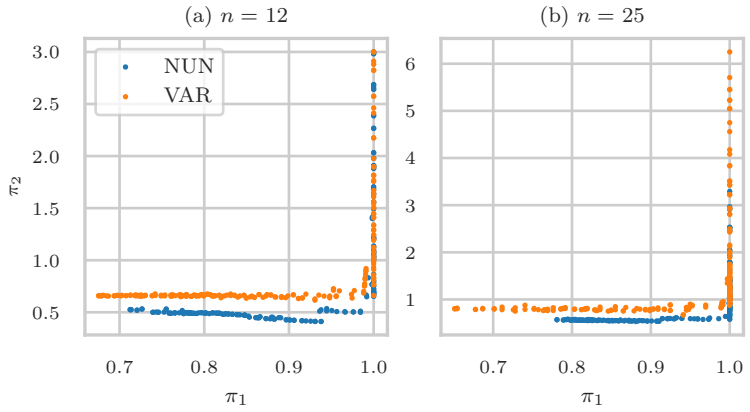

Figure 7.3: Dispersion plots of dimensionless parameters showing the correlation between filling (π_1) and shape (π_2) factors, for primary fields with (a) $n = 12$ and (b) $n = 25$. It considers $\pi_1 = \sum w_i/W_p$ and $\pi_2 = W_p/2H_R$, while each dot represents one Pareto solution shown in Figure 7.2.

The trivial solutions, where $\pi_1 \approx 1$, result from primary fields with minimal spacing between mirrors ($g \approx 0$). In these cases, π_2 varies significantly, reaching extreme values, particularly in the variable radius configuration. When disregarding these high π_1 cases, a second trend emerges, showing that the shape factor tends to remain below an upper bound, specifically $\pi_2 < 1$. Additionally, the results indicate that for comparable π_1 values, the variable radius design generally exhibits higher π_2 values than the non-uniform cases. This suggests that while allowing radius variation provides flexibility, it also leads to larger primary field width relative to receiver height, which could introduce practical design constraints.

To understand how dimensionless parameters influence the Pareto solutions, Figure 7.4 presents scatter plots relating efficiency (ECF) and cost (Γ) to geometric characteristics for the case $n = 12$. As observed in Figures 7.4a and 7.4d, efficiency and cost generally decrease as π_1 increases. However, when π_1 approaches 1, Γ stabilizes while ECF continues to decline. This trend reflects the behavior observed in Figure 7.2a, where these trivial solutions ($g \approx 0$) lead to an asymptotic horizontal limit. The trivial cases for variable radius configurations correspond to a pitch factor, $\pi_3 = s/w$, so that $\pi_3 = 1$, as shown in Figures 7.4c and 7.4f. Additionally, as s/w increases, both ECF and Γ increase, indicating that designs with larger pitch-to-width ratios tend to be more efficient but also more expensive.

The shape factor, π_2 , impacts efficiency and cost in distinct ways. Figure 7.4b illustrates that the first decreases as the shape factor increases, meaning that more elongated fields relative to receiver height negatively affect optical performance. However, the relationship between π_2 and cost is more complex, as seen in Figure 7.4e. There are two obvious trends: one set of solutions shows small variations in π_2 but significant cost differences, which correspond to the vertical asymptotic trend observed in Figure 7.2a. Another set of solutions maintains nearly constant costs while π_2 increases, representing the horizontal asymptotic behavior seen in Figure 7.2a. This suggests that while some geometric variations lead to notable cost changes, others have minimal impact, depending on how mirror proportions

are optimized relative to field layout.

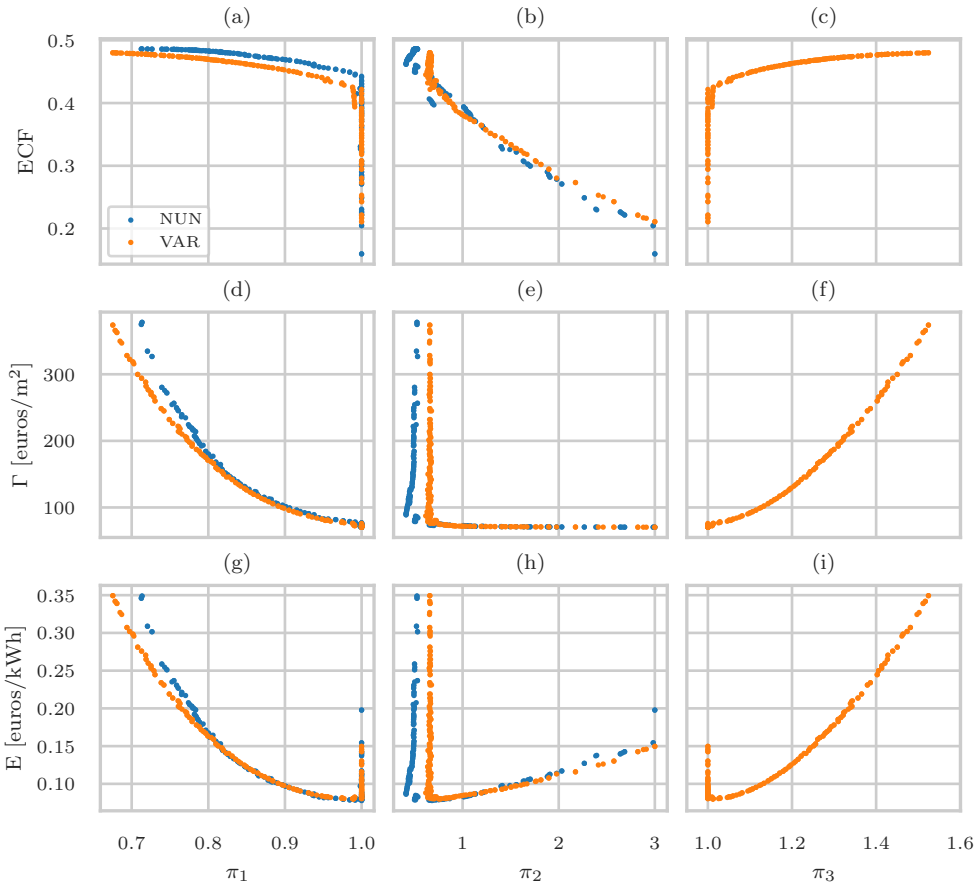

Figure 7.4: Dimensionless parameters versus objective functions for both non-uniform and variable radius designs for primary fields with $n = 12$ mirrors. It shows how π_1, π_2, and π_3 affects efficiency (ECF), figures (a), (b), and (c), and cost (Γ) of Pareto solutions, figures (d), (e), and (f). It also shows how parameters affect the specific cost of energy, $\mathrm{E} = \Gamma/(\mathrm{ECF} \cdot \sum I_b)$, so that E is given in units of €/kWh, figures (g), (h), and (i).

Furthermore, considering now a metric for the specific cost of energy, $\mathrm{E} = \Gamma/(\mathrm{ECF} \cdot \sum I_b)$, Figure 7.4 shows that π_1, π_2 , and π_3 affect E similarly as Γ. That is, E decreases as π_1 increases, and the opposite occur as π_3 and π_2 increase. Minimum values of E in Figure 7.4 are 0.078 and 0.08 €/kWh for NUN and VAR configurations, respectively, meaning that the full non-uniform case (NUN) yields a specific cost of energy 2.56% lower than the variable radius configuration (VAR). This result agrees well with the impact of non-uniform settings regarding width and shift found by Boito and Grena [9] for an analogous metric.

Overall, these results highlight that increasing π_1 leads to cost reductions but with efficiency penalties, particularly for trivial solutions. The pitch factor, $\pi_3 = s/w$, directly influences both objectives, with higher values leading to more efficient but expensive configurations. Meanwhile, the shape factor, π_2, primarily affects efficiency, with cost dependencies varying across different design configurations. These insights reinforce the need for careful optimization of geometric parameters to balance cost and efficiency.

7.5.2 Curvature radius analysis

The currently approaches to design the curvature radius of primary mirrors [3, 4, 16], shown in Chapter 5, have an underlying assumption that such decision variable can be optimized in a step after the others (w, s, H_R). This assumption leads to the question: can the curvature radius be decoupled of other decision variables in design optimization?

To verify such a hypothesis, Figure 7.5 presents a Pareto front comparison between two non-uniform configurations. One (NUN) have all primary mirror parameters (w, g, and R) subjected to optimization. The other configuration (NUN-sunRef) is similar to the first one but now the curvature radius (R) is determined by the sun reference criterion [3] instead of being subject to optimization. Results are presented for two sizes of primary fields, (a) $n = 12$ and (b) $n = 25$, following a similar structure to the previous case. These results show that the two configurations produce nearly identical Pareto fronts, for primary fields with 12 and 25 mirrors, Figures 7.5a and 7.5b, respectively, suggesting that determining the curvature radius by the sun reference criterion does not substantially alter the cost-efficiency trade-off.

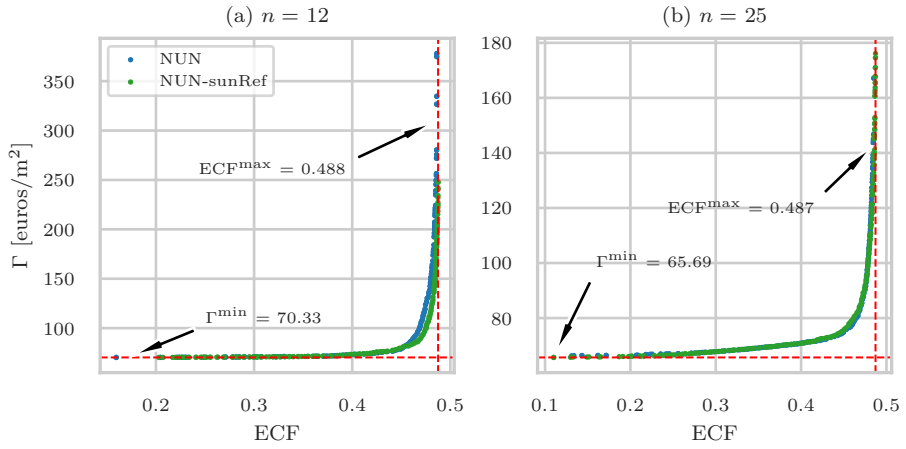

Figure 7.5: Pareto Fronts of optimal solutions for two non-uniform configurations: the NUN refers to the case where all primary mirror parameters (width, gap, and radius) are optimized and NUN-sunRef considers the curvature radius by the sun reference criterion instead of subjected to the optimization algorithm. The figure considers geometries for primary fields where (a) $n = 12$ and (b) $n = 25$, annual efficiency computations for Evora, and an absorber flux threshold of $I_{min} = 5.0$ kW/m^2.

On the other hand, while the objective space analysis provides insights into the trade-offs between efficiency and cost, it does not reveal how different design variables contribute to these optimal solutions. In this sense, Figure 7.6 presents the frequency distribution of decision variables for all Pareto solutions in Figure 7.5a ($n = 12$), comparing the NUN and NUN-sunRef configurations and providing insights into the distribution of key geometric parameters. It reveals strong similarities between NUN and NUN-sunRef configurations. The observed frequency trends highlight that design parameters remain across both configurations while maintaining comparable performance. These results highlight the effectiveness of the sun reference criterion in approximating optimized solutions.

This curvature design analysis can also be done regarding uniform configurations. As previously stated, the UN case defines a full uniform configuration, in which all decision variables (w, g, and R) are subjected to the optimization routine. The UN-IpaRef stands for a uniform configuration in which R is calculated by the criteria proposed by Pulido-Iparraguirre et al. [26] instead of subjected to the optimization routine. The comparison between UN and

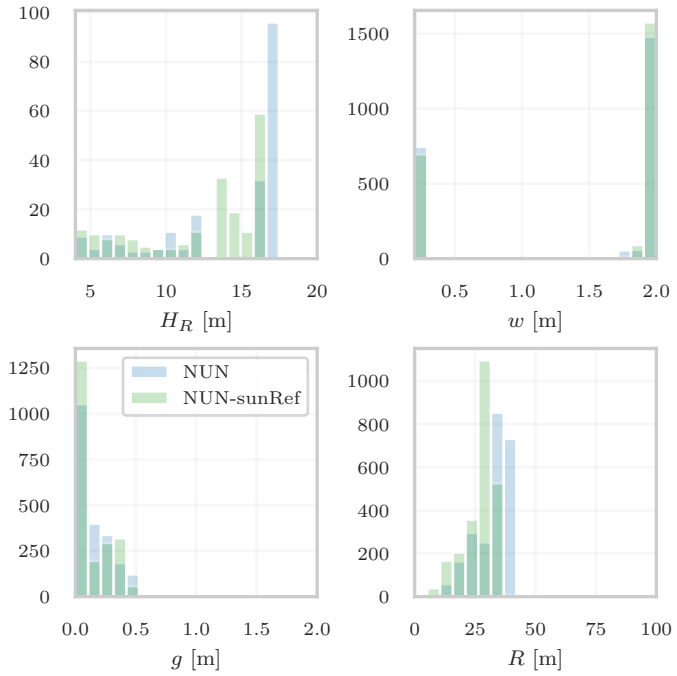

Figure 7.6: Frequency distribution of decision variables for all Pareto solutions of NUN (blue) and NUN-sunRef (green) configurations, for the case in which $n = 12$ mirrors. The histograms present terms of receiver height (H_R), mirror width (w), mirror gap (g), and curvature radius (R).

UN-IpaRef is presented in Figure 7.7. These results shows that the two configurations produce nearly identical Pareto fronts, for primary fields with 12 and 25 mirrors, Figures 7.7a and 7.7b, respectively, suggesting that determining the curvature radius by Iparraguirre's criterion does not substantially alter the cost-efficiency trade-off.

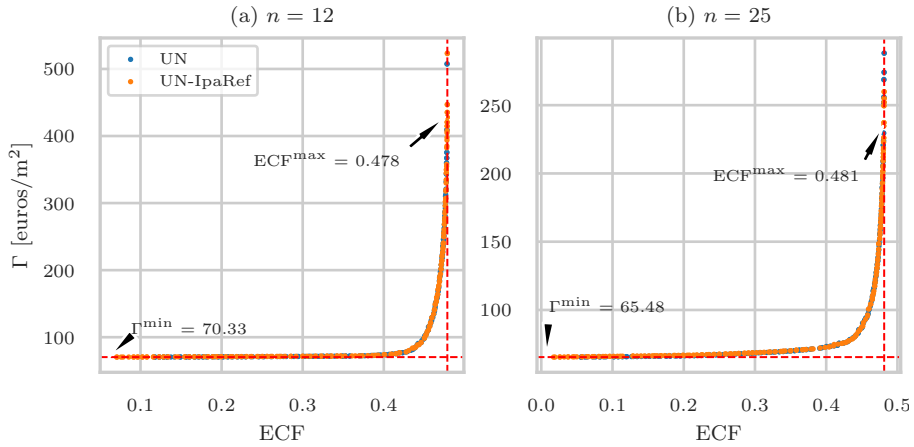

Figure 7.7: Pareto Fronts of optimal solutions for two uniform configurations: the UN refers to the case where all primary mirror parameters (width, gap, and radius) are optimized and UN-IpaRef considers the curvature radius by Pulido-Iparraguirre's [26] criterion instead of subjected to the optimization algorithm. The figure considers geometries for primary fields where (a) $n = 12$ and (b) $n = 25$, annual efficiency computations for Evora, and an absorber flux threshold of $I_{min} = 5.0$ kW/m^2.

Regarding to the design space, Figure 7.8 shows that UN and UN-IpaRef designs produce Pareto solutions with similar frequency distribution of geometric parameters. The higher

differences are seen for the curvature radius R. Nevertheless, these differences does not have a major impact on performance, as both designs yield the same Pareto front. Of course, some small differences can be attributed to the stochastic nature NSGA-II in determining the decision variables of candidate solutions.

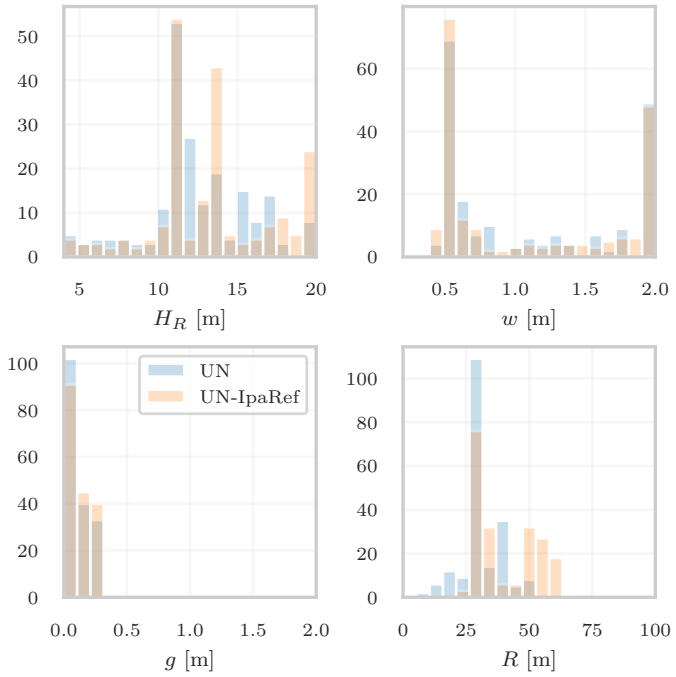

Figure 7.8: Frequency distribution of decision variables for all Pareto solutions of UN (blue) and UN-IpaRef (orange) configurations, for the case in which $n = 12$ mirrors. The histograms present terms of receiver height (H_R), mirror width (w), mirror gap (g), and curvature radius (R).

In short, the results presented in this section corroborates the hypothesis that the curvature radius can be decoupled from the optimization routine. This statement implicates in simplifying the linear Fresnel design problem, as a lower number of decision variables can be used without converging to local optimal solutions.

7.6 Conclusions

This chapter addressed the optimal design problem for linear Fresnel collectors by employing a two-objective optimization approach. The optimization was based on maximizing annual energy efficiency, while minimizing the specific direct cost of the solar field. The analysis compared Pareto-optimal solutions of different design configurations, particularly evaluating the cost-effectiveness of non-uniform designs (varying width, shift, and radius) relative to variable radius configurations (constant width and shift), and exploring whether the curvature radius can be effectively decoupled from other design variables.

The results obtained demonstrate that non-uniform designs can indeed be more cost-effective solutions. In certain regions of the objective space, differences between Pareto solutions for these two configurations are minimal, even excluding trivial cases. However, other regions indicate a clear cost advantage for non-uniform designs over variable radius cases. Additionally, Pareto solutions display considerable geometric diversity but also reveal identifiable trends when evaluated through dimensionless parameters.

The analysis of curvature radius suggests that predefined design criteria on non-uniform and uniform configurations (such as sun reference or Iparraguirre's model) yield solutions nearly identical to those obtained via optimization. Thus, curvature radius can effectively be decoupled from other optimization variables without significantly compromising performance. Given the computational demands associated with optimization routines, these criteria represent practical alternatives for determining the curvature radius of mirrors while preserving optimal cost-performance.

It is worth noting that, by definition, Pareto solutions show the trade-off between the objectives, meaning that all of them are somehow equivalent and there is no single optimal solution. Therefore, the selection of a single case of a Pareto front ultimately depend on the user's choices, criteria, and considerations, and on what they value most. The results presented in this work provide insights into this design problem, establishing boundaries and limits but do not definitively determining the "best" solution.

Additionally, it should be noted that the findings and discussions in this paper rely on the simplified cost model outlined in Section 7.3. This model excludes considerations such as the impact of curvature radius on cost and does not quantify the effect of various non-uniform configurations on capital and operational expenditures. Consequently, alternative cost models might yield different conclusions regarding the established research questions.

References

[1] R. Abbas, M. J. Montes, M. Piera, and J. M. Martínez-Val, "Solar radiation concentration features in Linear Fresnel Reflector arrays," *Energy Conversion and Management*, vol. 54, no. 1, pp. 133–144, 2012. DOI: 10.1016/j.enconman.2011.10.010.

[2] M. J. Montes, C. Rubbia, R. Abbas, and J. M. Martínez-Val, "A comparative analysis of configurations of linear Fresnel collectors for concentrating solar power," *Energy*, vol. 73, pp. 192–203, 2014. DOI: 10.1016/j.energy.2014.06.010.

[3] R. Abbas and J. Martínez-Val, "Analytic optical design of linear Fresnel collectors with variable widths and shifts of mirrors," *Renewable Energy*, vol. 75, pp. 81–92, 2015. DOI: 10.1016/j.renene.2014.09.029.

[4] R. Abbas and J. Martínez-Val, "A comprehensive optical characterization of linear Fresnel collectors by means of an analytic study," *Applied Energy*, vol. 185, pp. 1136–1151, 2017. DOI: 10.1016/j.apenergy.2016.01.065.

[5] R. Abbas, M. Valdés, M. Montes, and J. Martínez-Val, "Design of an innovative linear Fresnel collector by means of optical performance optimization: A comparison with parabolic trough collectors for different latitudes," *Solar Energy*, vol. 153, pp. 459–470, 2017. DOI: 10.1016/j.solener.2017.05.047.

[6] J. Nixon and P. Davies, "Cost-exergy optimisation of linear Fresnel reflectors," *Solar Energy*, vol. 86, no. 1, pp. 147–156, 2012. DOI: 10.1016/j.solener.2011.09.024.

[7] A. V. Santos, D. Canavarro, and M. Collares-Pereira, "The gap angle as a design criterion to determine the position of linear Fresnel primary mirrors," *Renewable Energy*, vol. 163, pp. 1397–1407, 2021. DOI: 10.1016/j.renene.2020.09.017.

[8] V. Sharma, J. K. Nayak, and S. B. Kedare, "Effects of shading and blocking in linear Fresnel reflector field," *Solar Energy*, vol. 113, pp. 114–138, 2015. DOI: 10.1016/j.solener.2014.12.026.

[9] P. Boito and R. Grena, "Optimization of the geometry of Fresnel linear collectors," *Solar Energy*, vol. 135, pp. 479–486, 2016. DOI: 10.1016/j.solener.2016.05.060.

[10] M. Moghimi, K. Craig, and J. Meyer, "Simulation-based optimisation of a linear Fresnel collector mirror field and receiver for optical, thermal and economic performance," *Solar Energy*, vol. 153, pp. 655–678, 2017. DOI: 10.1016/J.SOLENER.2017.06.001.

[11] Z. D. Cheng, X. R. Zhao, Y. L. He, and Y. Qiu, "A novel optical optimization model for linear Fresnel reflector concentrators," *Renewable Energy*, vol. 129, pp. 486–499, 2018. DOI: 10.1016/j.renene.2018.06.019.

[12] H. Ajdad, Y. Filali Baba, A. Al Mers, O. Merroun, A. Bouatem, and N. Boutammachte, "Particle swarm optimization algorithm for optical-geometric optimization of linear fresnel solar concentrators," *Renewable Energy*, vol. 130, pp. 992–1001, 2019. DOI: 10.1016/j.renene.2018.07.001.

[13] O. A. López-Núñez, J. A. Alfaro-Ayala, J. J. Ramírez-Minguela, J. M. Belman-Flores, and O. A. Jaramillo, "Optimization of a Linear Fresnel Reflector Applying Computational Fluid Dynamics, Entropy Generation Rate and Evolutionary Programming," *Renewable Energy*, vol. 152, pp. 698–712, 2020. DOI: 10.1016/j.renene.2020.01.105.

[14] J. Men, X. Zhao, Z. Cheng, Y. Leng, and Y. He, "Study on the annual optical comprehensive performance of linear Fresnel reflector concentrators with an effective multi-objective optimization model," *Solar Energy*, vol. 225, pp. 591–607, 2021. DOI: 10.1016/j.solener.2021.07.051.

[15] A. Ahmadpour, A. Dejamkhooy, and H. Shayeghi, "Optimization and modelling of linear Fresnel reflector solar concentrator using various methods based on Monte Carlo Ray–Trace," *Solar Energy*, vol. 245, pp. 67–79, 2022. DOI: 10.1016/j.solener.2022.09.006.

[16] P. Boito and R. Grena, "Optimal focal length of primary mirrors in Fresnel linear collectors," *Solar Energy*, vol. 155, pp. 1313–1318, 2017. DOI: 10.1016/j.solener.2017.07.079.

[17] RioGlass. "RECEIVER TUBES FOR LINEAR CSP (CONCENTRATED SOLAR POWER) APPLICATIONS." (2025), [Online]. Available: https://www.rioglass.com/en/our-products/hce-tubes (visited on 03/07/2025).

[18] F. Burkholder and C. Kutscher, "Heat Loss Testing of Schott's 2008 PTR70 Parabolic Trough Receiver," National Renewable Energy Laboratory (NREL), Golden, CO (United States), Tech. Rep., 2009. DOI: 10.2172/1369635.

[19] M. Cagnoli, D. Mazzei, M. Procopio, V. Russo, L. Savoldi, and R. Zanino, "Analysis of the performance of linear Fresnel collectors: Encapsulated vs. evacuated tubes," *Solar Energy*, vol. 164, pp. 119–138, 2018. DOI: 10.1016/j.solener.2018.02.037.

[20] W. F. Holmgren, C. W. Hansen, and M. A. Mikofski, "Pvlib python: A python package for modeling solar energy systems," *Journal of Open Source Software*, vol. 3, no. 29, p. 884, 2018. DOI: 10.21105/joss.00884.

[21] I. Reda and A. Andreas, "Solar position algorithm for solar radiation applications," *Solar Energy*, vol. 76, no. 5, pp. 577–589, 2004. DOI: 10.1016/j.solener.2003.12.003.

[22] M. Shokrnia, M. Cagnoli, R. Grena, A. D'Angelo, M. Lanchi, and R. Zanino, "Comparative Techno-Economic Analysis of Parabolic Trough and Linear Fresnel Collectors with Evacuated and Non-Evacuated Receiver Tubes in Different Geographical Regions," *Processes*, vol. 12, no. 11, p. 2376, 2024. DOI: 10.3390/pr12112376.

[23] M. Cagnoli, M. Shokrnia, and R. Zanino, "Analisi delle prestazioni termiche di ricevitori con coating selettivi a bassa emissività applicati a tubi ricevitori evacuati operanti fino a 550 ° C," ENEA (Italian National Agency for New Technologies, Energy and Sustainable Economic Development), Tech. Rep., 2020. [Online]. Available: https://www2.enea.it/it/Ricerca_sviluppo/documenti/ricerca-di-sistema-elettrico/adp-mise-enea-2019-2021/solare-termodinamico/report-rds_ptr_2020_262.pdf.

[24] M. Mertins, "Technische und wirtschaftliche Analyse von horizontalen Fresnel Kollektoren," Ph.D. dissertation, University of Karlsruhe, 2009.

[25] T. Hirsch, E. Yildiz, F. Hustig-Diethelm, S. Heide, and J. Kretschmann, "CSP Bankability Project Report Draft: Draft for an Appendix O – Cost Structures to the SolarPACES Guideline for Bankable STE Yield Assessment," 2017. [Online]. Available: https://shorturl.at/57MDO.

[26] D. Pulido-Iparraguirre, L. Valenzuela, J.-J. Serrano-Aguilera, and A. Fernández-García, "Optimized design of a Linear Fresnel reflector for solar process heat applications," *Renewable Energy*, vol. 131, pp. 1089–1106, 2019. DOI: 10.1016/j.renene.2018.08.018.

[27] N. Kincaid, G. Mungas, N. Kramer, M. Wagner, and G. Zhu, "An optical performance comparison of three concentrating solar power collector designs in linear Fresnel, parabolic trough, and central receiver," *Applied Energy*, vol. 231, pp. 1109–1121, 2018. DOI: 10.1016/J.APENERGY.2018.09.153.

[28] M. J. Kochenderfer and T. A. Wheeler, *Algorithms for optimization*. Cambridge: MIT Press, 2019. [Online]. Available: https://algorithmsbook.com/optimization/.

[29] J. R. R. A. Martins and A. Ning, *Engineering Design Optimization*. Cambridge University Press, 2021. DOI: 10.1017/9781108980647.

[30] K. Deb, *Multi-Objective Optimization using Evolutionary Algorithms*. New York: John Wiley & Sons, 2001. [Online]. Available: http://tiny.cc/pby4xz.

[31] K. De Jong, *Evolutionary Computation: A Unified Approach*. Cambridge: The MIT Press, 2006. [Online]. Available: https://mitpress.mit.edu/books/evolutionary-computation.

[32] A. Eiben and J. Smith, *Introduction to Evolutionary Computing* (Natural Computing Series), 2nd Ed. Berlin, Heidelberg: Springer Berlin Heidelberg, 2015. DOI: 10.1007/978-3-662-44874-8.

[33] F. A. Fortin, F. M. De Rainville, M. A. Gardner, M. Parizeau, and C. Gagńe, "DEAP: Evolutionary algorithms made easy," *Journal of Machine Learning Research*, vol. 13, pp. 2171–2175, 2012.

[34] F.-M. De Rainville, F.-A. Fortin, M.-A. Gardner, M. Parizeau, and C. Gagné, "DEAP: A Python Framework for Evolutionary Algorithms," in *Proceedings of the fourteenth international conference on Genetic and evolutionary computation conference companion - GECCO Companion '12*, New York, New York, USA: ACM Press, 2012. DOI: 10.1145/2330784.2330799.

[35] K. Deb, S. Agrawal, A. Pratap, and T. Meyarivan, "A Fast Elitist Non-dominated Sorting Genetic Algorithm for Multi-objective Optimization: NSGA-II," in *CEUR Workshop Proceedings*, vol. 1133, 2000, pp. 849–858. DOI: 10.1007/3-540-45356-3_83.

Nomenclature

Abbreviations

CEC	Compound Elliptical Concentrator	
DEAP	Distributed Evolutionary Algorithm in Python	
ECF	Energy Collection Factor	[-]
EW	East-West	

LFC	Linear Fresnel Collector
NS	North-South
NSGA-II	Elitist Non-dominated Sorted Genetic Algorithm

Latin Letters

A_{abs}	Absorber tube surface area	[m^2]
A_{net}	Concentrator mirror (reflective) aperture area	[m^2]
c_e	Elevation cost factor	[€/m^2]
c_g	Gap cost factor	[€/m^2]
c_m	Mirror cost factor	[€/m]
c_r	Receiver cost factor	[€/m]
d_a	Absorber tube diameter: $d_a = 2r_a$	[m]
g	Gap between two neighboring mirrors	[m]
H_R	Receiver height	[m]
I_{min}	Flux intensity threshold at the absorber	[W/m^2]
m	Horizontal (x-axis) position of a primary mirror	[m]
n	Number of mirrors in a primary field	[-]
N_{pop}	Number of individuals in a population	[-]
r_a	Evacuated tube absorber radius	[m]
r_{go}	Evacuated tube glass cover outer radius	[m]
r_{gi}	Evacuated tube glass cover inner radius	[m]
R	Curvature radius of a primary mirror	[m]
s	Shift (distance between center points) between two neighboring mirrors	[m]
w	Primary mirror width	[m]
W_p	Primary field width	[m]
$\hat{x}$	Decision vector	

Greek Letters

Γ	Direct specific cost of a linear Fresnel solar field	[€/m^2]
θ_L	Longitudinal incidence angle	[°]
θ_{LS}	Longitudinal-solar incidence angle	[°]
θ_T	Transversal incidence angle	[°]
σ_{mu}	Standard deviation of the (zero mean) Gaussian mutation operator	[-]
π_1	Filling factor of a linear Fresnel configuration: $\pi_1 = \sum w_i / W_p$	[-]
π_2	Shape factor of a linear Fresnel configuration: $\pi_2 = W_p / 2H_R$	[-]
π_3	Pitch factor of a linear Fresnel configuration: $\pi_3 = s/w$	[-]

Indexes

h	hour index

i	General counting index for the mirrors in a primary field
k	General counting index

Chapter 8

Conclusions

8.1 Findings and contributions

This thesis addressed the geometric design problem of linear Fresnel collectors within the context of solar thermal electricity production. The adopted strategy was to decompose this complex problem into smaller, focused sub-problems, each guided by specific research questions that navigated through an already extensive and well-established body of literature. The research covered four main topics: (i) optical modeling methods, (ii) the curvature of primary mirrors, (iii) secondary optics design, and (iv) optimal geometric configurations. The main goal was to provide advances on the state of the art by filling key gaps in the literature related to these topics.

In Chapter 3, an analytical optical method was developed to evaluate optical losses in linear Fresnel collectors. This method demonstrated that simplified, non-stochastic models could yield fast and accurate results, comparable to those from ray-tracing simulations. This contribution provides a reliable surrogate tool for design optimization, reducing the reliance on computationally expensive simulations.

Chapter 4 focused on the shape of the primary mirrors. It was shown that cylindrical mirrors are practically indistinguishable from parabolic ones – the theoretically ideal shape – under a wide range of design conditions, when viewed from the receiver's perspective. This chapter introduced a new comparison metric, addressing a methodological gap in the literature. It explains why previous studies have shown similar performance between cylindrical and parabolic shapes and simplifies the design process by eliminating the need to choose between them. As cylindrical mirrors are easier to define and cheaper to manufacture, they emerge as the practical default.

In Chapter 5, a comparison of design approaches for determining the curvature radius of primary mirrors was presented, focusing on uniform (same radius for all mirrors) and non-uniform (each mirror has a particular radius value) configurations. The results show that simple, closed-form equations can yield near-optimal performance for both configurations. While the uniform approach results in slightly lower efficiency, its acceptance loss is significantly higher. These findings add empirical evidence – via numerical experiments – that validate the use of straightforward equations over computationally expensive optimization routines, thereby streamlining the design process.

Although the Compound Parabolic Concentrator (CPC) is widely regarded in the literature

as the best secondary optic, some unresolved issues remained. Chapter 6 addressed these by demonstrating that optimized and edge-ray CPC-based designs converge when optimizing for both optical efficiency and flux uniformity. It also showed that the edge-ray designs of CPC and Compound Elliptical Concentrator (CEC) closely overlap at high geometric concentration ratios, leading to comparable performance. Moreover, CPCs and CECs display a trade-off between efficiency and tolerance to optical errors, with the CPC being more tolerant and the CEC slightly more efficient. Overall, this chapter provides new insights into the trade-offs and convergence of secondary optics and reinforces the edge-ray design as a fast and effective tool that simplifies the design task.

Chapter 7 explored optimal geometric configurations with respect to efficiency and solar field cost. The findings showed that non-uniform designs – where primary mirrors differ in width, shift, and curvature – can be more cost-effective than simpler configurations, but only in a specific region of the design space. Importantly, results support the hypothesis that the curvature radius can be decoupled from the optimization process and calculated a priori using the tools introduced in earlier chapters. This insight significantly simplifies the optimization problem by reducing the number of decision variables.

In summary, while the literature on linear Fresnel collector design is extensive, it is often fragmented and case-specific, with limited generalization. This thesis contributions comprise a set of cohesive, evidence-based tools and findings that address key knowledge gaps, promote general design principles, and simplify the design process across multiple fronts.

8.2 Implications

The contributions of this thesis extend beyond academic advancement, as it also offers practical tools and strategies for the design and optimization of linear Fresnel collectors in real-world applications. By providing simplified yet robust design procedures and methods, the findings enables engineers and designers to make informed decisions without the need for extensive computational resources.

The demonstrated equivalence between cylindrical and parabolic mirrors, as well as the validation of simple curvature radius equations, can streamline manufacturing processes and reduce costs. The insights on secondary optics and optimal configurations present a valuable foundation for integrated design, balancing efficiency, flux uniformity, and tolerance to tracking and manufacturing errors. The identification of the edge-ray design as a fast, effective design method opens the door for automated design tools that incorporate these principles, making advanced collector design more accessible to a wider audience.

8.3 Limitations

The findings and methods presented in this thesis are subject to certain limitations, which arise from inherent factors in the modeling approach, methodological choices, and necessary assumptions made to define the research scope. These limitations should be considered when interpreting the results and assessing their relevance to real-world applications.

First, several results rely predominantly on ray-tracing simulations and analytical models to perform optical evaluations. Although these tools are effective in isolating and analyzing specific design aspects, they do not fully account for real-world uncertainties such as mechanical deformations, material aging, and installation imperfections, even when employing

tools validated through experimental results, such as SolTrace [1, 2].

Within this context, the optical method developed in Chapter 3 computes the flux at flat target, which is interpreted as the aperture of a secondary optic. The assessments presented in Chapters 5 and 7 assume that the fraction of this aperture flux that actually reaches the absorber does not vary as the incidence changes. That is, the average number of reflections and transmissions in the receiver does not significantly varies with the transversal and longitudinal incidence angles. Although there are evidences pointing this assumption as a reasonable one [3–6], this simplification constitute an important modeling approach used to conduct the research presented in this thesis.

Second, performance models assume idealized conditions, including steady-state analysis, typical meteorological year data, and constant optical properties. Similarly, sunshape and optical error models employed remained fixed throughout comparative studies. These simplifications are justified within the context of the analyses conducted in this thesis and are essential to isolate geometric effects. However, they restrict the understanding of long-term performance under variable conditions. For example, circumsolar radiation changes with time, and optical properties vary with incidence angle and time (due to degradation and soiling). Therefore, the calculated annual performance values should not be directly compared or extrapolated to real-world facilities.

Third, the cost model employed in the evaluation of optimal geometric designs (Chapter 7) is simplified and intended for relative comparisons. Although based on empirical data from a real-world experimental facility [7], it does not account for further impacts of non-uniform settings, nor curvature radius, on capital and operational expenditures. Similarly, it does not include potential variability in labor, logistics, or component pricing across different regions or scales of deployment. As such, the conclusions regarding cost-effectiveness are indicative but not prescriptive.

Fourth, this thesis is developed considering the context solar thermal electricity, which imposes the constraint of a receiver comprising an evacuated tube as the absorber element. In the context of other applications [8–12] where an absorber other than a single tube is used, which could comprise a different evaluation of thermal losses and other secondary optics, the ensuing conclusions might lead to different paths to the ones presented here.

Despite these limitations, this thesis provides a solid foundation for future research and application, offering methods and insights that can be built upon and validated in experimental or real-world contexts.

8.4 Future research directions

Looking ahead, the results of this work and the limitations discussed previously suggest several directions for future research.

The optical method developed in Chapter 3 could be extended to incorporate other types of receivers, such as tilted flat absorbers or alternative tubular configurations. Additionally, this method could be adapted to accommodate other designs of primary field, including the etendue-matched approach proposed by Chaves and Collares-Pereira [13]. Another valuable improvement would be replacing the linear integration method with an approach that determines the flux distribution, such as the projection method developed by Sánchez-González and Santana [14]. Developing a generalized, fast, and accurate optical evaluation tool is a key step for assessing the cost-effectiveness of linear Fresnel collectors.

Expanding and refining cost modeling methodologies should be pursued. Given the wide variety of potential configurations in linear Fresnel concentrating technology, creating a robust cost model that accurately accounts for the influence of different geometric parameters and configurations on capital and operational expenditures would significantly strengthen conclusions regarding their economic viability of these geometric solutions. However, the limited availability of empirical data due to the relatively small number of existing utility-scale linear Fresnel power plants poses a considerable challenge to this task.

Exploring the applicability of the methodologies and findings beyond the specific context of systems with evacuated tube receivers is another promising avenue. Investigating alternative absorber configurations, or broader applications – such as industrial process heat or thermochemical processes – could unveil new opportunities for optimization and innovation. Such research would also contribute additional empirical data, which is essential for advancing this relatively immature concentrating technology.

Finally, while the thesis focuses on simplifying the design process through analytical tools and empirical insights, it does not fully integrate these tools into a comprehensive automated design pipeline. Future work could explore the implementation of these methods into user-friendly software platforms to enhance their practical usability by engineers and designers.

Addressing these research directions would further enhance the practical applicability and robustness of the developed methodologies, ensuring continued progress toward more reliable, cost-effective, and efficient solar thermal energy solutions.

References

[1] T. Wendelin, A. Dobos, and A. Lewandowski, "SolTrace: A Ray-Tracing Code for Complex Solar Optical Systems," National Renewable Energy Laboratory (NREL), Golden, CO (United States), Tech. Rep., 2013. DOI: 10.2172/1260924.

[2] C. S. Turchi, M. Boyd, D. Kesseli, P. Kurup, M. S. Mehos, T. W. Neises, P. Sharan, M. J. Wagner, and T. Wendelin, "CSP Systems Analysis - Final Project Report," National Renewable Energy Laboratory (NREL), Golden, CO (United States), Tech. Rep., 2019. DOI: 10.2172/1513197.

[3] V. Sharma, J. K. Nayak, and S. B. Kedare, "Effects of shading and blocking in linear Fresnel reflector field," *Solar Energy*, vol. 113, pp. 114–138, 2015. DOI: 10.1016/j.solener.2014.12.026.

[4] G. Zhu, "New adaptive method to optimize the secondary reflector of linear Fresnel collectors," *Solar Energy*, vol. 144, pp. 117–126, 2017. DOI: 10.1016/j.solener.2017.01.005.

[5] M. Hack, G. Zhu, and T. Wendelin, "Evaluation and comparison of an adaptive method technique for improved performance of linear Fresnel secondary designs," *Applied Energy*, vol. 208, pp. 1441–1451, 2017. DOI: 10.1016/j.apenergy.2017.09.009.

[6] A. Vouros, E. Mathioulakis, E. Papanicolaou, and V. Belessiotis, "On the optimal shape of secondary reflectors for linear Fresnel collectors," *Renewable Energy*, vol. 143, pp. 1454–1464, 2019. DOI: 10.1016/j.renene.2019.05.044.

[7] M. Mertins, "Technische und wirtschaftliche Analyse von horizontalen Fresnel Kollektoren," Ph.D. dissertation, University of Karlsruhe, 2009.

[8] M. Romero and J. González-Aguilar, "High-flux/high-temperature solar thermal conversion: technology development and advanced applications," *Renewable Energy and Environmental Sustainability*, vol. 1, p. 26, 2016. DOI: 10.1051/rees/2016011.

[9] F. J. Sepúlveda, M. T. Miranda, I. Montero, J. I. Arranz, F. J. Lozano, M. Matamoros, and P. Rodríguez, "Analysis of Potential Use of Linear Fresnel Collector for Direct Steam Generation in Industries of the Southwest of Europe," *Energies*, vol. 12, no. 21, p. 4049, 2019. DOI: 10.3390/en12214049.

[10] A. Resch and R. Höller, "Optical Modelling of a Linear Fresnel Concentrator for the Development of a Spectral Splitting Concentrating Photovoltaic Thermal Receiver," *Energies*, vol. 16, no. 14, p. 5373, 2023. DOI: 10.3390/en16145373.

[11] G. Papakokkinos, A. C. Montenon, P. Petrou, and M. Papadimitriou, "Synergy between biogas and concentrating solar thermal - case study of a dairy industry in Cyprus," in *3rd International Conference on Energy Transition in the Mediterranean Area (SyNERGY MED)*, IEEE, 2024, pp. 1–5. DOI: 10.1109/SyNERGYMED62435.2024.10799306.

[12] V. Palladino, M. Di Somma, C. Cancro, W. Gaggioli, M. De Lucia, M. D'Auria, M. Lanchi, F. Bassetti, C. Bevilacqua, S. Cardamone, F. Nana, F. M. Montagnino, and G. Graditi, "Innovative Industrial Solutions for Improving the Technical/Economic Competitiveness of Concentrated Solar Power," *Energies*, vol. 17, no. 2, p. 360, 2024. DOI: 10.3390/en17020360.

[13] J. Chaves and M. Collares-Pereira, "Etendue-matched two-stage concentrators with multiple receivers," *Solar Energy*, vol. 84, no. 2, pp. 196–207, 2010. DOI: 10.1016/j.solener.2009.10.022.

[14] A. Sánchez-González and D. Santana, "Solar flux distribution on central receivers: A projection method from analytic function," *Renewable Energy*, vol. 74, pp. 576–587, 2015. DOI: 10.1016/j.renene.2014.08.016.

Nomenclature

Abbreviations

CEC	Compound Elliptical Concentrator
CPC	Compound Parabolic Concentrator

Appendix A

Auxiliary functions

This appendix presents a comprehensive collection of the auxiliary functions and equations that are utilized throughout this thesis. These auxiliary functions play a crucial role in developing and analyzing the mathematical models presented in this work.

By consolidating them into a single appendix, the aim is to provide readers with a convenient and readily accessible reference for these fundamental mathematical tools. This collection includes a wide range of functions, from basic mathematical operations to functions specifically designed to address the unique requirements of the research. Each function is accompanied by a concise description and, where necessary, its derivation or source reference.

The direction vectors for x, y, and z axes of a right-handed coordinate system are given by $\vec{I}_x$, $\vec{I}_y$, $\vec{I}_z$, respectively, as shown in Equation A.1, where I_3 stands for the 3×3 identity matrix.

$$\{\vec{I}_x, \vec{I}_y, \vec{I}_z\} = I_3 \tag{A.1}$$

The function sign(x) function is defined as shown in Equation A.2.

$$\text{sign}(x) = \begin{cases} -1, & \text{if } x < 0 \\ 0, & \text{if } x = 0 \\ 1, & \text{if } x > 0 \end{cases} \tag{A.2}$$

The function ang calculates the angle between vectors $\vec{u}$ and $\vec{v}$ as given by Equation A.3. It yields an angle in the interval $[0, \pi]$.

$$\text{ang}(\vec{u}, \vec{v}) = \cos^{-1}\left(\frac{\vec{u} \cdot \vec{v}}{|\vec{u}||\vec{v}|}\right) \tag{A.3}$$

The matrices that represent basic rotations regarding the x, y, and z axes of a right-handed coordinate system are shown in Equation A.4.

$$\begin{gathered} R_x(\theta) = \begin{bmatrix} 1 & 0 & 0 \\ 0 & \cos\theta & -\sin\theta \\ 0 & \sin\theta & \cos\theta \end{bmatrix} \\ R_y(\theta) = \begin{bmatrix} \cos\theta & 0 & \sin\theta \\ 0 & 1 & 0 \\ -\sin\theta & 0 & \cos\theta \end{bmatrix} \quad R_z(\theta) = \begin{bmatrix} \cos\theta & -\sin\theta & 0 \\ \sin\theta & \cos\theta & 0 \\ 0 & 0 & 1 \end{bmatrix} \end{gathered} \tag{A.4}$$

Equation A.5 presents a reflection function, where vector $\vec{u}$ is transformed by a normal vector $\vec{n}$. This function follows Zhu's [1] so that if u points up, its reflection also points up.

$$\text{reft}(\vec{u}, \vec{n}) = 2(\vec{u} \cdot \vec{n})\vec{n} - \vec{u} \tag{A.5}$$

The intersection between a straight line defined by a point $\mathbf{P}$ and a vector $\vec{v}$ and a plane defined by a point $\mathbf{Q}$ and a normal vector $\vec{n}$ is then given by Equation A.6 [2].

$$\text{islp}(\mathbf{P}, \vec{v}, \mathbf{Q}, \vec{n}) = \mathbf{P} + \frac{(\mathbf{Q} - \mathbf{P}) \cdot \vec{n}}{\vec{v} \cdot \vec{n}} \vec{v} \tag{A.6}$$

The function angpn calculates the angle between vectors $\vec{u}$ and $\vec{v}$, in the range $[-\pi, \pi]$, considering if $\vec{v}$ is on a positive (counter-clockwise) or negative (clockwise) rotation around the normal vector $\vec{n}$ with respect to $\vec{u}$, where $\vec{u}$ and $\vec{v}$ lie in a plane defined by $\vec{n}$ as shown in Equation A.7.

$$\text{angpn}(\vec{u}, \vec{v}, \vec{n}) = \text{sing}(\vec{u} \times \vec{v} \cdot \vec{n}) \cdot \text{ang}(\vec{u}, \vec{v}) \tag{A.7}$$

References

[1] G. Zhu, "Development of an analytical optical method for linear Fresnel collectors," *Solar Energy*, vol. 94, pp. 240–252, 2013. DOI: 10.1016/j.solener.2013.05.003.

[2] J. Chaves, *Introduction to Nonimaging Optics*, 2nd Edition. New York: CRC Press, 2016. DOI: 10.1201/b18785.

Appendix B

Sunlight modeling

B.1 Incidence direction

The Sun direction is defined by an $\{x, y, z\}$ vector denominated $\vec{S}$ that can be defined in two different coordinate systems. One is the Global Coordinate System (GCS), an inertial reference system attached to the Earth's surface such that X_G points to the East, Y_G points North, and Z_G points Zenith, as shown in Figure B.1.

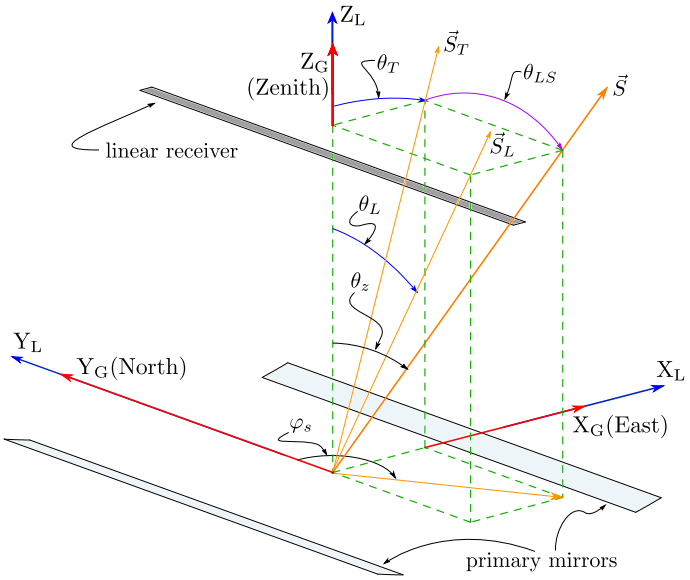

Figure B.1: The direction of the incidence sunlight, denominated as $\vec{S}$. The figure illustrates two XYZ coordinate systems, referenced by the corresponding subscripts: G denotes the GCS, illustrated in red, is attached to Earth's surface; L denotes the LCS, shown in blue, is attached to the concentrator aperture plane. Moreover, the figure shows the decomposition of $\vec{S}$ in different planes, as well as the corresponding angles that are formed.

Considering this GCS, $\vec{S}$ is then represented as ${}^{G}\vec{S}$ and is a function of sun zenith and azimuth angles, θ_z and φ_s, respectively, since both angles are defined in the GCS.

θ_z is the angle between $\vec{S}$ and the zenithal direction; φ_s is the angle between the projection of ${}^{G}\vec{S}$ in the horizontal plane and the North so that $0 \leq \varphi_s \leq 2\pi$. This definition of φ_s

differs from the one presented in some textbooks (westward from the South direction) [1, 2], but it follows the definitions of a solar position algorithm [3].

From Figure B.1, one can derive a direct expression for ${}^{\mathrm{G}}\vec{S}$ as a function of θ_z and φ_s, as Equation B.1 shows.

$$ {}^{\mathrm{G}}\vec{S}(\theta_z, \varphi_s) = \begin{bmatrix} \sin\theta_z \, \sin\varphi_s \\ \sin\theta_z \, \cos\varphi_s \\ \cos\theta_z \end{bmatrix} \tag{B.1} $$

In addition, an LCS attached to the concentrator aperture is also shown in Figure B.1 and is defined as follows:

- The transversal plane is the ZX plane, and angles in such a plane are defined as positive or negative regarding a correspondent rotation around the Y-axis.
- The longitudinal plane is the YZ plane, and angles in such a plane are defined as positive or negative regarding a correspondent rotation around the X-axis.

In this LCS, $\vec{S}$ is represented by ${}^{\mathrm{L}}\vec{S}$ and its projections in the transversal and longitudinal planes are $\vec{S}_T$ and $\vec{S}_L$, respectively. The transversal and longitudinal incidence angles are θ_T and θ_L, respectively, i.e., the angles that $\vec{S}_T$ and $\vec{S}_L$ make with the Z-axis, as shown in Figure B.1.

Considering these definitions regarding the LCS, ${}^{\mathrm{L}}\vec{S}$ can be obtained by two sequential rotations of the direction vector of the Z axis, as

$$ {}^{\mathrm{L}}\vec{S} = R_y\left(\theta_T\right) \cdot R_x\left(\theta_{LS}\right) \cdot \vec{I}_z, \tag{B.2} $$

where $\vec{I}_z = \{0, 0, 1\}$ is the direction vector of the Z axis, R_x and R_y represents the basic rotation matrices around the X and Y axes, as defined in Equation A.4, and θ_{LS} is the so-called longitudinal solar angle, defined as the projection of θ_L in the plane defined by $\vec{S}$ and $\vec{S}_T$, as given by Equation B.3.

$$ \theta_{LS} = \tan^{-1}\left(\tan\theta_L \cos\theta_T\right) \tag{B.3} $$

Thus, Equation B.2 can be expanded to give ${}^{\mathrm{L}}\vec{S}$ as an explicit function of both θ_T and θ_L, as shown in Equation B.4.

$$ {}^{\mathrm{L}}\vec{S}(\theta_T, \theta_L) = \frac{1}{\sqrt{\tan^2\theta_L \cos^2\theta_T + 1}} \begin{bmatrix} \sin\theta_T \\ -\cos\theta_T \tan\theta_L \\ \cos\theta_T \end{bmatrix} \tag{B.4} $$

The case presented in Figure B.1 is denominated as the North-South (NS) orientation (or NS-mounting): the longitudinal axis of the concentrator is aligned with the NS direction. In this situation, GCS and LCS are fully aligned and

$$ {}^{\mathrm{L}}\vec{S} = I_3 \cdot {}^{\mathrm{G}}\vec{S}, \tag{B.5} $$

where I_3 represents the 3×3 identity matrix. Therefore, it is easy to derive expressions for θ_T and θ_L as functions of θ_z and φ_s, as shown in Equation B.6.

$$ \begin{aligned} \theta_T &= \tan^{-1}\left(\tan\theta_z \sin\varphi_s\right) \\ \theta_L &= \tan^{-1}\left(\tan\theta_z \cos\varphi_s\right) \end{aligned} \tag{B.6} $$

Figure B.1 and Equation B.6 show relations for the case of an NS and horizontal plane mounting. Nevertheless, this could not be the case. Two factors can modify the alignment between these two coordinate systems: an azimuthal rotation of the concentrator aperture plane, here defined by an angle ψ, and a tilt of the concentrator regarding the horizontal plane, here defined as β.

The tilt β is a complicated assembly rarely used in utility-scale solar fields. Due to this fact, the displacement from the horizontal plane is not considered here. However, the azimuthal displacement defined by ψ is simpler to assemble and analyze, as shown in Figure B.2.

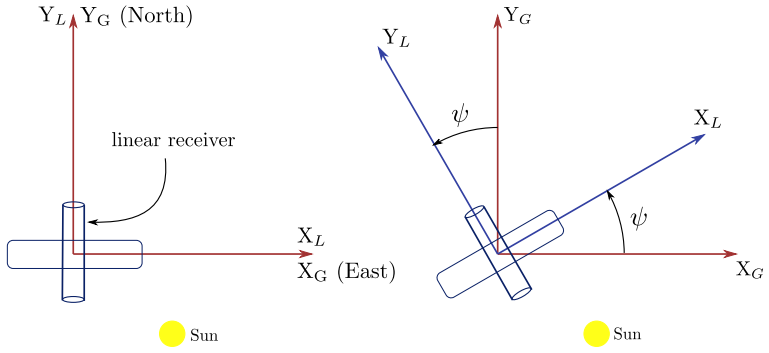

Figure B.2: Details of the Global Coordinate System (superscript G) and Local Coordinate System (superscript L) axes after an azimuthal displacement ψ of the concentrator in the horizontal plane.

Then, ${}^{\mathrm{L}}\vec{S}$ relates to ${}^{\mathrm{G}}\vec{S}$ as defined in Equation B.7, where R_z is the basic rotation matrix regarding the Z-axis, as defined in Equation A.4.

$$ {}^{\mathrm{L}}\vec{S} = R_z\left(\psi\right) \cdot {}^{\mathrm{G}}\vec{S} \tag{B.7} $$

Expanding the matrix production of Equation B.7, a closed-form vector equation for ${}^{\mathrm{L}}\vec{S}$ is then shown in Equation B.8.

$$ {}^{\mathrm{L}}\vec{S} = \begin{bmatrix} \cos\psi \sin\theta_z \sin\varphi_s - \sin\psi \sin\theta_z \cos\varphi_s \\ \sin\psi \sin\theta_z \sin\varphi_s + \cos\psi \sin\theta_z \cos\varphi_s \\ \cos\theta_z \end{bmatrix} = \begin{bmatrix} \sin\theta_z \sin(\varphi_s - \psi) \\ \sin\theta_z \cos(\varphi_s - \psi) \\ \cos\theta_z \end{bmatrix} \tag{B.8} $$

As expected, when $\psi = 0$, ${}^{\mathrm{L}}\vec{S} = {}^{\mathrm{G}}\vec{S}$ and θ_T and θ_L are given by Equation B.6. Considering that an East-West (EW) orientation (also referred to as EW-mounting) is when $\psi = -\pi/2$, ${}^{\mathrm{L}}\vec{S}$ is then calculated as shown in Equation B.9.

$$ {}^{\mathrm{L}}\vec{S} = \begin{bmatrix} \sin\theta_z \cos\varphi_s \\ -\sin\theta_z \sin\varphi_s \\ \cos\theta_z \end{bmatrix} \tag{B.9} $$

Thus, θ_T and θ_L are calculated as shown in Equation B.10.

$$ \begin{aligned} \theta_T &= \tan^{-1}\left(\tan\theta_z \cos\varphi_s\right) \\ \theta_L &= \tan^{-1}\left(-\tan\theta_z \sin\varphi_s\right) \end{aligned} \tag{B.10} $$

Therefore: $\{\theta_T^{\mathrm{EW}}, \theta_L^{\mathrm{EW}}\} = \{\theta_L^{\mathrm{NS}}, -\theta_T^{\mathrm{NS}}\}$, where the superscripts NS and EW refers to North-South and East-West orientations, respectively. This result is easily seen in Figure B.2.

B.2 Radiance distribution

B.2.1 Overview

Interpreting sunlight as a set of parallel rays, straight lines representing their path in the optical system – a collimated sunlight model – is very common in many situations. However, this approach is not accurate when dealing with high-concentration solar collectors since it does not account for the well-known radiance distribution of extraterrestrial radiation and the effects of atmospheric scattering, and neither offers the proper approach to model the interactions of sunlight with real surfaces.

Thermal radiation heat transfer theory states that the radiation emitted by a surface, such as the Sun, is directional. It also has a spectral nature, but this property is omitted here since this discussion refers to radiometric quantities integrated over all wavelengths [4].

The radiance, L, is the radiometric quantity that holds the directional properties of emitted radiation. It is defined as the radiant energy per unit of time (the radiant flux, $\mathrm{d}\Phi$) emitted per unit of solid angle, $\mathrm{d}\Omega$, and per unit of area, $\mathrm{d}A$, perpendicular to a direction given by given by ξ and φ, as shown in Figure B.3 [5]. In this sense, L has units of $\mathrm{W/m^2 \cdot sr}$ and Φ has units of $\mathrm{W/m^2}$.

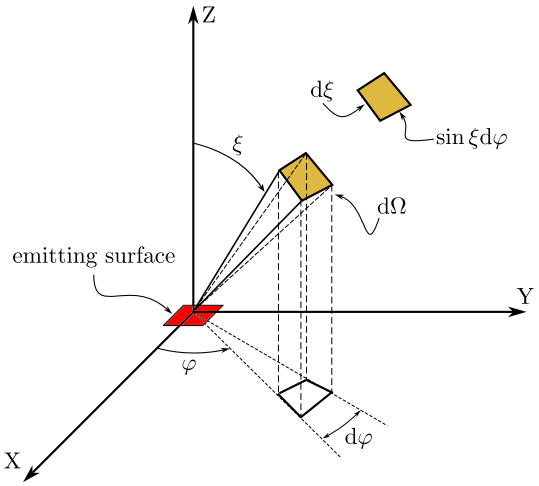

Figure B.3: Radiant flux, $\mathrm{d}\Phi$, confined within in a small solid angle, $\mathrm{d}\Omega$, in a direction given by angles ξ and φ. Adapted from Howell et al. [4].

The total (hemispherical) radiant flux emitted can be calculated by the integration of the radiance profile, as shown in Equation B.11.

$$\Phi = \int_0^{2\pi} \int_0^{\pi/2} L(\xi, \varphi) \sin\xi \cos\xi \mathrm{d}\xi \mathrm{d}\varphi \tag{B.11}$$

B.2.2 Sunshape

In the context of solar energy engineering, the directional nature of the radiant energy emitted by the Sun is of utmost importance to optimize solar energy utilization in high-concentration applications.

As viewed from the Earth's surface, the Sun is not a point but comprehends a small angular

aperture, as illustrated in Figure B.4. Considering typical values of sun radius, $R_{sun} = 0.695 \times 10^9$ m, and the average Sun-Earth distance, $A_0 = 1.496 \times 10^{11}$ m, the Sun subtends a disk whose radius is $\theta_\delta = 4.65$ mrad. This value is calculated from the simple geometrical relation shown in Figure B.4, but astronomic measurements established a value for the disk radius between 4.6496 and 4.6498 mrad [6]. Thus, considering the angular extent of the Sun disk as $\theta_\delta = 4.65$ mrad is a reasonable assumption.

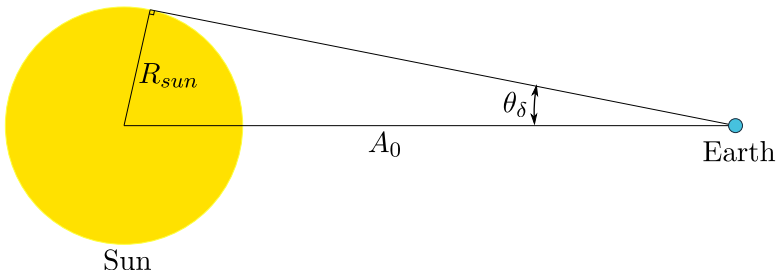

Figure B.4: Sun-Earth astronomic relations. From Earth's surface, the Sun has a finite size that subtends a half-angle θ_δ, also called solar disk angular radius, a relation between Sun's radius, R_{sun} and its average distance to Earth, A_0.

The radiance distribution within the solar disk is governed by the phenomenon known as limb-darkening. This effect arises from variations in the Sun's temperature distribution and results in the center of the disk appearing brighter than its edges. When sunlight enters Earth's atmosphere, it undergoes forward scattering by tiny suspended particles, giving rise to an emitting region located beyond the disk called the circumsolar region, which forms an aureole that extends up to an angular radius referred to as θ_Δ [7, 8].

Measurements of solar radiance distribution [7, 8] indicate that radiance values decrease exponentially in the circumsolar region, and values for $\xi > 100\,\text{mrad}$ are negligible. Consequently, $\sin\xi \approx \xi$ and $\cos\xi \approx 1$. Furthermore, a reasonable assumption is to consider an azimuthal symmetry, so that $L(\xi^*, \varphi)$ is constant for $\varphi \in [0, 2\pi]$.

In this sense, the total radiant flux emitted by the Sun can be calculated as given by Equation B.12[1], where the radiance distribution is now represented by ϕ, the so-called sunshape: an azimuthally averaged profile, function of only ξ, as defined in Equation B.13 [9].

$$\Phi = 2\pi \int_0^{\pi/2} \phi(\xi)\xi \mathrm{d}\xi \tag{B.12}$$

By definition, $\phi(\xi)$ is given in units of $\mathrm{W/m^2 \cdot sr}$ but an usual way is to present it as a normalized function so that $\phi(0) = 1$, or even as a Probability Density Function (PDF) so that $\int \phi(\xi)\xi \mathrm{d}\xi = 1$.

$$\phi(\xi) = \frac{1}{2\pi} \int_0^{2\pi} L(\xi, \varphi)\, \mathrm{d}\varphi \tag{B.13}$$

As mentioned, the scattering effects that create the circumsolar region are related to the local atmospheric conditions of particulates, composition, and clouds. Thus, the actual sunshape profile and the amount of circumsolar energetic flux are also functions of local conditions.

Nevertheless, Buie et al. [10] have proposed a normalized averaged model of sunshape that is not locally dependent but only a function of a single parameter. It is derived from a statistical analysis of radiance profile measurements from the databases described by Noring et al. [7]

[1] Although the integration limit is set to $\pi/2$, ϕ vanishes for $\xi > 100\,\text{mrad}$. Thus, it only indicates the integration of the sunshape for the whole domain of ξ. Another common value used is simply $\xi = \infty$.

and Neumann et al. [8]. Buie's model is a piece-wise function with two sub-functions: one that rules the radiance distribution over the disk and the other for the circumsolar region, as shown in Equation B.14.

$$\phi(\xi) = \begin{cases} \dfrac{\cos(0.326\xi)}{\cos(0.308\xi)}, & \text{for } \xi \leq \theta_\delta \\ e^{\kappa}\xi^{\gamma}, & \text{for } \theta_\delta < \xi \leq \theta_\Delta \end{cases} \tag{B.14}$$

In Equation B.14, κ and γ are coefficients that are functions of the circumsolar ratio χ, as given by Equation B.15.

$$\begin{aligned} \kappa &= 0.9\ln(13.5\chi)\chi^{-0.3} \\ \gamma &= 2.2\ln(0.52\chi)\chi^{0.43} - 0.1 \end{aligned} \tag{B.15}$$

The CSR, denominated by χ in Equation B.15, is defined as the ratio between the irradiance within the circumsolar region and the total irradiance (disk and circumsolar), as given by Equation B.16, where θ_δ and θ_Δ are extensions of the disk and aureole, respectively.

$$\chi = \frac{\displaystyle\int_{\theta_\delta}^{\theta_\Delta} \phi(\xi)\xi \mathrm{d}\xi}{\displaystyle\int_{0}^{\theta_\Delta} \phi(\xi)\xi \mathrm{d}\xi} \tag{B.16}$$

The analysis carried-out by Buie et al. [10] to derive this sunshape model considers that δ_Δ is 43.6 mrad to follow the angular aperture of most common and commercial pyrheliometers used in DNI measurements, so that Equation B.14 is applied up to this aureole extension.

Buie's model, Equation B.14, follows empirical data to rule a quite meager radiance variation over the sun disk. Then, a simpler and usual model to represent a clear sky condition is to neglect circumsolar radiation and assume a uniform PDF for the radiance distribution over the disk: the pillbox sunshape [11, 12]. In this case, the distribution is characterized by a single parameter, Δ_{sun}, the half-width of the distribution, as given by Equation B.17. Usually, $\Delta_{sun} = 4.65$ mrad to fit the disk size.

$$\phi(\xi) = \begin{cases} 1, & \text{for } \xi \leq \Delta_{sun} \\ 0, & \text{otherwise} \end{cases} \tag{B.17}$$

Another simple approach to model the radiance distribution is to consider a Gaussian sunshape [13, 14]. In this case, σ_{sun} is the standard deviation of the Gaussian distribution and fully defines the model.

Figure B.5 illustrates the above mentioned of profiles: Buie's model, pillbox, and Gaussian. It shows how normalized functions ($\phi(0) = 1$) vary with ξ, the radial displacement from the center of the sun ($\xi = 0$). As seen from this figure, the pillbox model assumes no circumsolar radiation, but fairly represents the disk region. The Gaussian profile has a poor model for the disk, although it includes circumsolar irradiation. In general, both are simplifications for the empirical-based model proposed by Buie et al. [10].

The models illustrated in Figure B.5 are defined by different parameters (χ, Δ_{sun}, σ_{sun}). However, a direct comparison can be evaluated through the Root Mean Square (RMS) width of the corresponding PDF distribution, a more convenient metric to evaluate the dispersion than by the parameters that define each model [1]. The RMS width relates to the second central moment, the variance of the distribution [15]. In this context of sun radiance distribution, Equation B.12 states that the corresponding PDF, $f(\xi)$, of a sunshape $\phi(\xi)$ is

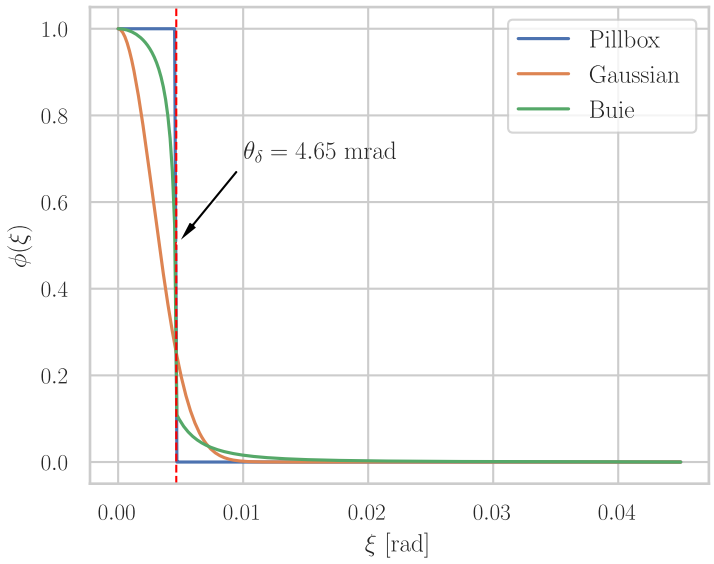

Figure B.5: A comparison of normalized sunshape profiles. It shows Buie, pillbox, and Gaussian sunshape profiles for: $\chi = 0.25$, $\Delta_{sun} = 4.65$ mrad, and $\sigma_{sun} = 2.8$ mrad. The vertical red dashed line represents the sun disk radius, θ_δ, at 4.65 mrad. Of course, due to the radial symmetry, $\phi(\xi) = \phi(-\xi)$.

$f(\xi) = \phi(\xi)\xi$. Therefore, the variance and RMS width of a radial sunshape ϕ, V_{sun} and δ_{sun}, respectively, are then given by Equation B.18.

$$\mathrm{V}_{sun} = \delta_{sun}^2 = \frac{\int_0^\infty \phi(\xi)\xi^3 \mathrm{d}\xi}{\int_0^\infty \phi(\xi)\xi \mathrm{d}\xi} \tag{B.18}$$

Thus, if ϕ is a Gaussian function of standard deviation σ_{sun}, then $\delta_{sun} = \sigma_{sun}\sqrt{2}$; if ϕ is a pillbox function of half-width Δ_{sun}, then $\delta_{sun} = \Delta_{sun}/\sqrt{2}$.

B.2.3 Optical errors

Solar concentration technologies use mirrors that actively track the apparent motion of the Sun to properly collect the incident sunlight. Optical error is a concept used to comprise imperfections of a real solar concentrating system. Overall, it leads to reflected sunlight missing the receiver, reducing concentration and energy collection [1].

Perfect specular reflection is a simplification. Due irregularities, the reflected sunlight on a surface does not follow what is stated by Snell's law. Reflective materials have roughness (microscopic irregularities) that deviates a reflected ray from the theoretical direction, which cause scattering and define the specular error [16]. Due to macroscopic effects, the surface shape does not conform the ideal (designed) profile and the actual normal vector at the surface deviates from the expected direction, defining the contour error [17]. Such deviations occur continuously at each point of the surface, so that their characterization constitutes a problem of defining the proper statistical distribution [18].

As shown in Figure B.6, the deviation of a vector $\vec{v}$ from the main direction can be described using radial (ϵ) and azimuthal (α) angular displacements. Early experimental studies [16,

17] measured deviations in reflected rays and normal vectors to characterize specular and contour errors, respectively. The results reveal two key findings: (1) azimuthal deviations follow a uniform Probability Density Function (PDF) over $\alpha \in [0, 2\pi]$, indicating a radial symmetry, and (2) radial deviations ϵ are described by a Gaussian distribution. Consequently, specular and contour errors can each be fully characterized by a single parameter, σ_s and σ_c, respectively, representing the standard deviations of the Gaussian distributions for radial deviations.

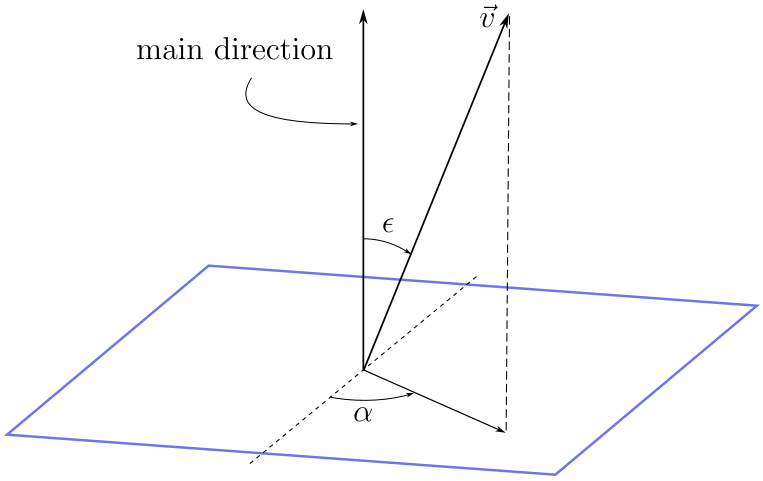

Figure B.6: The deviation of a vector $\vec{v}$ from a main direction. $\vec{v}$ is defined by radial and azimuthal angular displacements, ϵ and α, respectively, where α lies in a plane normal to the main direction.

Figure B.7 illustrates the effects of specular and contour errors on an incident ray $\vec{S}$ reflected as $\vec{v}_n$ from a surface with normal vector $\vec{n}$. In the case of specular error (Figure B.7a), the standard deviation σ_s determines the probability that the reflected ray lies within the solid angle defined by $\vec{v}_n$ and ϵ. Conversely, for contour error (Figure B.7b), the standard deviation σ_c determines the probability that the actual normal vector lies within the solid angle defined by $\vec{n}$ and ϵ. This deviation in the normal vector causes the reflected ray to shift by 2ϵ [18, 19], a useful but conservative geometric relation that overestimate the effects of normal vector displacement on the reflected ray deviation [20]. Then, σ_c determines the probability that the reflected ray lies within a solid angle defined by $\vec{v}_n$ and 2ϵ.

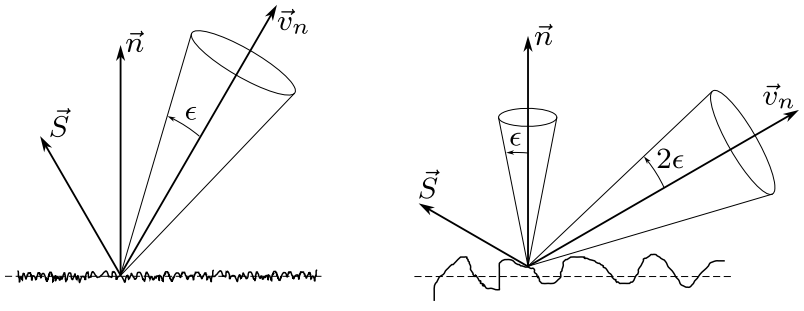

(a) Specular error (b) Contour error

Figure B.7: The effect of (a) specular and (b) contour optical errors. An incident ray $\vec{S}$ is reflected as $\vec{v}_n$ in a surface with normal vector $\vec{n}$. A deviation ϵ in the normal vector causes a displacement of 2ϵ in the reflected ray. Adapted from Bonanos [19].

Therefore, both specular and contour errors represent deviations per solid angle increment [21] and correspond to distributions which are analogous to the sun radiance distribution

(sunshape) described in Equations B.12 and B.13, with a profile ϕ characterizing the corresponding Gaussian functions and RMS widths following Equation B.18.

Other source of errors also occur in a solar concentrating system. Tracking and displacement errors in solar refer to inaccuracies in aligning the components of the optical system with the position of the sun. Tracking errors occur when the mechanism fails to perfectly follow the sun's apparent motion across the sky. These errors are typically caused by mechanical inaccuracies as imperfections in the components, such as motors, gears, or sensors; control system errors due to poor calibration, delays, or errors in algorithms that compute the sun's position; external factors such as environmental conditions, such as wind or vibrations, which destabilize the tracking structure. Displacement errors refer to misalignment of the optical components relative to their designed position or orientation within the optical system. These errors are typically due to assembly inaccuracies due to mispositioning or misalignment of mirrors and receivers during installation; structural deformations by bending or warping of the support structure caused by thermal expansion, wind loads, or mechanical stress; misalignments due to slight angular or positional offsets in individual reflectors.

Thus, tracking errors involve misalignment in real-time sun tracking, while displacement errors are related to static misalignments within the optical system. Although these errors should be conceptually treated in a different way as specular and contour errors, for long time averages they can be defined in terms of a Probability Density Function (PDF) [1]. In this case, usually a Gaussian distribution is assumed [1, 19], so that σ_t and σ_d are then the standard deviations associated with the tracking and displacement errors, respectively.

B.2.4 Effective source

In a real solar concentrator, several effects cause a ray to deviate from its ideal direction: non-collimated sunlight (sunshape), the actual shape of the concentrator does not follow the desired profile (contour error), non-specular reflection (specular error), imperfect tracking (tracking error), and misalignment between the concentrator and the receiver (displacement error). Radiance is conserved after perfect specular reflection [22], and the sunshape profile would still be a property of the reflected sunlight even in an perfect optical system.

As referred before, sunshape and optical errors are characterized by Probability Density Functions (PDFs). In a specular reflection, an incident ray $\vec{S}$ is reflected as $\vec{v}_n$ in a surface with normal vector $\vec{n}$. The sunshape rule the probability of $\vec{S}$ to be within a particular solid angle. Then, optical errors deviates $\vec{v}_n$ from the specular direction, and the corresponding PDFs rule the probability of the reflected ray to lie within a particular solid angle.

Figure B.8 illustrates this specular reflection defined by $\vec{S}$, $\vec{v}_n$, and $\vec{n}$. It also shows incident (in orange) and reflected (in green) beams. The first is defined by the main direction $\vec{S}$ and the PDF which characterize the sunshape, radially symmetric in a plane normal to $\vec{S}$, the sun plane (dashed orange circle), and with orthogonal axes given by $\vec{\theta}_x$ and $\vec{\theta}_y$. Similarly, the reflected beam is defined by $\vec{v}_n$, whose PDF is radially symmetric in the image plane (dashed green circle) defined by orthogonal axes $\vec{\theta}_u$ and $\vec{\theta}_v$. Of course, the probability of a ray having radial deviations from main directions, ξ and ϵ, is directly connected with the fraction of total flux contained within the solid angle defined by such deviations.

The effective source is the concept used to represent sunshape and optical errors in a single distribution, as from the receiver perspective it does not matter which error deviates a ray from its ideal direction [1]. From probability theory, the composition random variables defined by PDFs (here rays deviations) is given by the convolution of the individual distributions. However, the total variance is the sum of the individual variances [15], and the

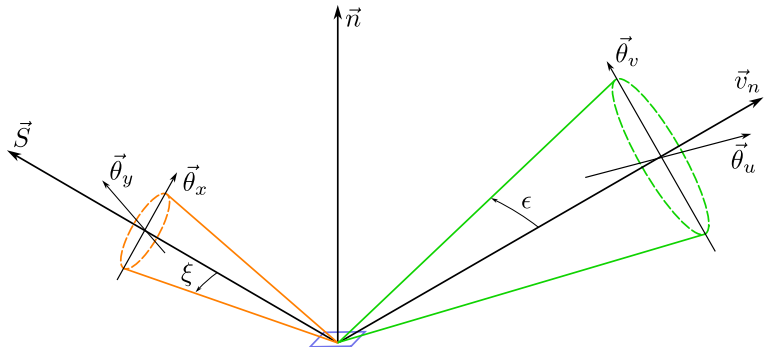

Figure B.8: Specular reflection of an incident ray $\vec{S}$. It is reflected as $\vec{v}_n$ in a surface with normal vector $\vec{n}$. The sunshape rule the probability of $\vec{S}$ to be within a particular solid angle, which defines the incident beam (in orange). Then, optical errors deviates $\vec{v}_n$ from the specular direction, and the corresponding PDFs rule the probability of the reflected ray to lie within a particular solid angle, defining the reflected beam (in green).

Root Mean Square (RMS) width of the effective source, δ_{es}, is then given by Equation B.19.

$$\delta_{es}^2 = \delta_{sun}^2 + \delta_s^2 + 4\delta_c^2 + \delta_t^2 + \delta_d^2 \tag{B.19}$$

In the above equation, the terms in the right hand side refer (from the left to right) to the RMS widths of sunshape, specular error, contour error, tracking error, and displacement error, respectively. The contribution of the contour error, δ_c, is multiplied by 4 in Equation B.19 since a displacement ϵ in the normal vector cause a 2ϵ shift in the reflected ray, as detailed before in Subsection B.2.3, as all other terms are described considering the reflected ray deviation. For linear Fresnel collectors, the tracking error contribution should be replaced by $4\delta_t^2$ for the same reason [1]. Generally, the composition of all beam spread sources other than the sunshape defines the overall optical error, denominated by δ_{opt}, so that Equation B.19 is rewritten as:

$$\delta_{es}^2 = \delta_{sun}^2 + \delta_{opt}^2. \tag{B.20}$$

Therefore, the Probability Density Function (PDF) which characterizes the reflected beam in Figure B.8 is the effective source profile, hereafter denominated by ϕ_{es}. Although Equation B.19 gives an overall measure of the dispersion of ϕ_{es}, its functional relationship, $\phi_{es}(\epsilon)$, is only obtained by the convolution of those individual PDFs. On the other hand, the central limit theorem states that as the number of independent distributions increase, the convoluted profile becomes Gaussian regardless of the individual profiles [1, 15]. Indeed, it is only the sunshape contribution in Equation B.19 that is not assumed as Gaussian, however, results from Pettit et al. [23] highlight that ϕ_{es} can be fairly represented by a Gaussian profile for $\delta_{es} \geq 2\delta_{sun}$.

In ray-tracing simulations, convolution is computed through the sampling procedure of the algorithm. Rays are generated having the direction given by the sun position, and angular deviations are sampled following the sunshape inverse Cumulative Density Function (CDF). When rays hit surfaces, specular reflection determines the ideal direction of reflected rays, and angular deviations are sampled from the overall surface error inverse CDF to modify the ideal direction of reflected rays. Thus, ray-tracing should consider a large number of rays so that the frequency distribution of these angular deviations approximates to the original PDF. Details about this procedure can be found in the work by Wang et al. [21].

B.2.5 Linear integration

The sunshape is a radiance model with radial symmetry, as defined from Equations B.11 to B.13. As shown in Figure B.8, the incident beam defines the sun plane over which the radial displacements from the sun direction are used to determine the total irradiance. Figure B.9 illustrates how the radiance model of Equation B.12 is radially integrated over elementary units of irradiance, $\mathrm{d}\Phi$. This is why this model is also called a radial sunshape model [1].

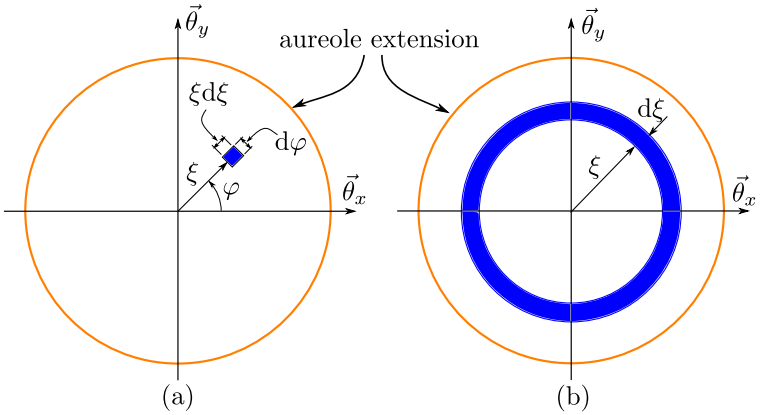

Figure B.9: Radial sunshape integration. It illustrates a top view of the sun plane for (a) general case of an elementary solid angle $\mathrm{d}\Omega = \xi \mathrm{d}\varphi \mathrm{d}\xi$, and (b) when radial symmetry is assumed — the integration over variable ξ is done by adding the disks with $\mathrm{d}\Omega = 2\pi\xi\mathrm{d}\xi$. Axes $\vec{\theta}_x$ and $\vec{\theta}_y$ define the sun plane as one perpendicular to the sun vector, $\vec{S}$. The aureole extension is intentionally oversized for clarity.

Similarly, the effective source profile, ϕ_{es}, which characterizes the reflected beam, has also a radial symmetry. Thus, this radial source is integrated by the model of Equation B.12 and follows the same approach as shown in Figure B.9b. Consequently, variance and RMS width of ϕ_{es}, V_ϕ and δ_ϕ, are then calculated as by Equation B.18.

Bendt et al. [24] proposed a linear integration to compute the intercepted flux in parabolic trough collectors with a tubular absorber, a procedure later detailed by Rabl [1], arguing that integration over orthogonal directions is more appropriate due to the longitudinal symmetry of linear concentrators. The total (hemispherical) irradiance in the reflected beam is then calculated as shown in the below equation [1]:

$$\Phi = \int_{-\infty}^{+\infty} \zeta(\theta)\mathrm{d}\theta, \tag{B.21}$$

where ζ is the linear integration function, or linear source, given in units of $\mathrm{W/m^2 \cdot rad}$. For a linear source ζ as presented in Equation B.21, the variance and RMS width, V_ζ and δ_ζ, respectively, are then calculated by Equation B.22.

$$V_\zeta = \delta_\zeta^2 = \frac{\displaystyle\int_{-\infty}^{+\infty} \zeta(\theta)\theta^2 \mathrm{d}\theta}{\displaystyle\int_{-\infty}^{+\infty} \zeta(\theta)\mathrm{d}\theta} \tag{B.22}$$

The issue now is how to derive the relation between ζ and ϕ_{es}. Figure B.10 shows the elementary solid angle for a integration over orthogonal directions $\vec{\theta_u}$ and $\vec{\theta_v}$ of the image plane of the reflected beam.

From Figure B.10, it is clear that $\epsilon^2 = \theta_u^2 + \theta_v^2$, and that the total irradiance can be calculated

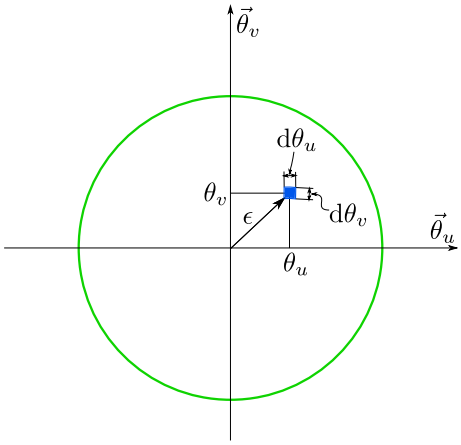

Figure B.10: Effective source radiance profile integration for bidirectional distribution function. It shows the image plane and a integration based in two orthogonal directions $\vec{\theta}_u$ and $\vec{\theta}_v$, so that the elementary solid angle is $d\Omega = d\theta_v d\theta_v$. The reflected beam extension is intentionally oversized for clarity.

as shown in Equation B.23, where μ stands for a bidirectional effective source distribution function.

$$\Phi = \int_{-\infty}^{\infty}\int_{-\infty}^{\infty} \mu(\theta_u, \theta_v) d\theta_u d\theta_v \tag{B.23}$$

Then, the variance of effective source distribution function in terms of the bidirectional function is given by:

$$V_\phi = \frac{\int_{-\infty}^{\infty}\int_{-\infty}^{\infty} \mu(\theta_u, \theta_v) d\theta_u d\theta_v \epsilon^2}{\int_{-\infty}^{\infty}\int_{-\infty}^{\infty} \mu(\theta_u, \theta_v) d\theta_u d\theta_v}. \tag{B.24}$$

Since $\epsilon^2 = \theta_u^2 + \theta_v^2$, the V_ϕ is rewritten as:

$$V_\phi = \frac{1}{\Phi}\left(\int_{-\infty}^{\infty}\int_{-\infty}^{\infty} \mu(\theta_x, \theta_v) d\theta_v \theta_u^2 d\theta_u + \int_{-\infty}^{\infty}\int_{-\infty}^{\infty} \mu(\theta_u, \theta_v) d\theta_u \theta_v^2 d\theta_v\right). \tag{B.25}$$

The above equation can be further simplified by replacing the first integrals, considering that $\zeta_v(\theta_u) = \int_{-\infty}^{\infty} \mu(\theta_u, \theta_v) d\theta_v$ and $\zeta_u(\theta_v) = \int_{-\infty}^{\infty} \mu(\theta_u, \theta_v) d\theta_u$. Geometrically, Figure B.11 illustrate the meaning of this integrals: they represent linear integrations to construct elementary units of irradiance over orthogonal directions, where ζ_u and ζ_v are functions integrating the bidirectional distribution μ over axes $\vec{\theta}_u$ and $\vec{\theta}_v$, respectively.

Then, V_ϕ is now rewritten as:

$$V_\phi = \frac{1}{\Phi}\left(\int_{-\infty}^{\infty} \zeta_v(\theta_u)\theta_u^2 d\theta_u + \int_{-\infty}^{\infty} \zeta_u(\theta_v)\theta_v^2 d\theta_v\right), \tag{B.26}$$

which by using Equation B.22 can simplified to:

$$V_\phi = V_u + V_v. \tag{B.27}$$

Due to the radial symmetry of the effective source radiance function, ϕ_{es}, a rotation of the reference frame $\{\vec{\theta}_u, \vec{\theta}_v\, \vec{v}_n\}$ around $\vec{v}_n$ will not change anything. Thus, there are no preferential directions for axes $\vec{\theta}_u$ and $\vec{\theta}_v$, so that $\zeta_v(\theta_u) = \zeta_u(\theta_v) = \zeta(\theta)$ and $V_u = V_v = V_\zeta$. Therefore,

$$\delta_\phi = \sqrt{2}\delta_\zeta. \tag{B.28}$$

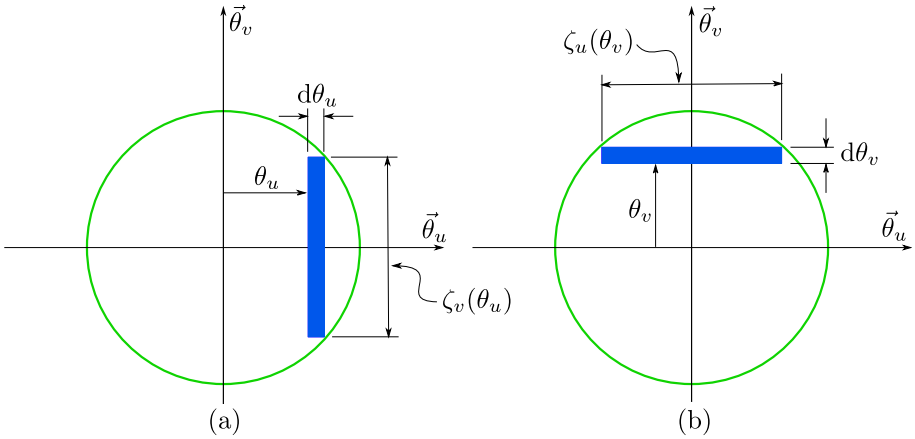

Figure B.11: Geometric interpretation of the construction of functions (a) $\zeta_v(\theta_u)$ and (b) $\zeta_u(\theta_v)$. They represent the length of the elementary rectangle used to integrate the radiance distribution function. The reflected beam extension is intentionally oversized for clarity.

Equation B.28 shows a relation between radial and linear sources. It was first presented by Rabl [1] without a detailed explanation, and used to state that "*the sun appears smaller to a line-focus collector than to a point-focus*". Although quite simple, it does not hold any information on how to transform the radial source, ϕ_{es}, into a linear one, ζ, but just an overall factor between dispersion measures; that is, it does not yield what type of functional expressions one should consider to construct a linear source from the radial one.

In this sense, Equations B.18, B.22, and B.28, can be used to determine the proper value of δ_ζ accordingly a pre-defined linear source profile. For example, a pillbox radial source ϕ_{es} of half-width Δ_ϕ will correspond to a linear pillbox source ζ of half-width Δ_ζ, so that $\Delta_\zeta = \sqrt{3}\Delta_\phi/2$; a radial Gaussian source of standard deviation σ_ϕ will correspond to a linear Gaussian source of standard deviation σ_ζ, which are related by $\sigma_\zeta = \sigma_\phi$. However, when the actual profile of the source does not follow an analytical function (e.g., a Buie sunshape convoluted with Gaussian errors), it is unclear how to proceed. Nevertheless, a Gaussian approximation is a usual and simple approach, so that $\sigma_\zeta = \delta_\phi/\sqrt{2}$.

References

[1] A. Rabl, *Active Solar Collectors and Their Applications*. New York: Oxford University Press, 1985. [Online]. Available: https://shorturl.at/oGLX6.

[2] S. A. Kalogirou, *Solar Energy Engineering*, 2nd Ed. London: Elsevier, 2014. DOI: 10.1016/C2011-0-07038-2.

[3] I. Reda and A. Andreas, "Solar position algorithm for solar radiation applications," *Solar Energy*, vol. 76, no. 5, pp. 577–589, 2004. DOI: 10.1016/j.solener.2003.12.003.

[4] J. R. Howell, M. P. Mengüç, and R. Siegel, *Thermal radiation heat transfer*. Boca Raton: CRC Press, 2016. DOI: 10.1201/b18835.

[5] F. L. Pedrotti, L. M. Pedrotti, and L. S. Pedrotti, *Introduction to Optics*, 3rd Edition. Cambridge University Press, 2017. DOI: 10.1017/9781108552493.

[6] S. Puliaev, J. L. Penna, E. G. Jilinski, and A. H. Andrei, "Solar diameter observations at Observatório Nacional in 1998-1999," *Astronomy and Astrophysics Supplement Series*, vol. 143, no. 2, pp. 265–267, 2000. DOI: 10.1051/aas:2000180.

[7] J. E. Noring, D. F. Grether, and A. J. Hunt, "Circumsolar Radiation Data: The Lawrence Berkeley Laboratory Reduced Data Base, Final Subcontract Report," National Renewable Energy Laboratory (NREL), Golden, CO (United States), Tech. Rep., 1991. DOI: 10.2172/6125786.

[8] A. Neumann, A. Witzke, S. A. Jones, and G. Schmitt, "Representative terrestrial solar brightness profiles," *Journal of Solar Energy Engineering, Transactions of the ASME*, vol. 124, no. 2, pp. 198–204, 2002. DOI: 10.1115/1.1464880.

[9] P. Blanc, B. Espinar, N. Geuder, C. Gueymard, R. Meyer, R. Pitz-Paal, B. Reinhardt, D. Renné, M. Sengupta, L. Wald, and S. Wilbert, "Direct normal irradiance related definitions and applications: The circumsolar issue," *Solar Energy*, vol. 110, pp. 561–577, 2014. DOI: 10.1016/j.solener.2014.10.001.

[10] D. Buie, A. Monger, and C. Dey, "Sunshape distributions for terrestrial solar simulations," *Solar Energy*, vol. 74, no. 2, pp. 113–122, 2003. DOI: 10.1016/S0038-092X(03)00125-7.

[11] Z. D. Cheng, X. R. Zhao, Y. L. He, and Y. Qiu, "A novel optical optimization model for linear Fresnel reflector concentrators," *Renewable Energy*, vol. 129, pp. 486–499, 2018. DOI: 10.1016/j.renene.2018.06.019.

[12] J. Men, X. Zhao, Z. Cheng, Y. Leng, and Y. He, "Study on the annual optical comprehensive performance of linear Fresnel reflector concentrators with an effective multi-objective optimization model," *Solar Energy*, vol. 225, pp. 591–607, 2021. DOI: 10.1016/j.solener.2021.07.051.

[13] G. Zhu, "Development of an analytical optical method for linear Fresnel collectors," *Solar Energy*, vol. 94, pp. 240–252, 2013. DOI: 10.1016/j.solener.2013.05.003.

[14] M. Moghimi, K. Craig, and J. Meyer, "Simulation-based optimisation of a linear Fresnel collector mirror field and receiver for optical, thermal and economic performance," *Solar Energy*, vol. 153, pp. 655–678, 2017. DOI: 10.1016/J.SOLENER.2017.06.001.

[15] G. Cowan, *Statistical data analysis*. Oxford: Oxford University Press, 1998. [Online]. Available: https://www.sherrytowers.com/cowan_statistical_data_analysis.pdf.

[16] R. B. Pettit, "Characterization of the reflected beam profile of solar mirror materials," *Solar Energy*, vol. 19, no. 6, pp. 733–741, 1977. DOI: 10.1016/0038-092X(77)90036-6.

[17] G. Johnston, "On the Analysis of Surface Error Distributions on Concentrated Solar Collectors," *Journal of Solar Energy Engineering*, vol. 117, no. 4, pp. 294–296, 1995. DOI: 10.1115/1.2847843.

[18] T. Cooper and A. Steinfeld, "Derivation of the Angular Dispersion Error Distribution of Mirror Surfaces for Monte Carlo Ray-Tracing Applications," *Journal of Solar Energy Engineering*, vol. 133, no. 4, pp. 1–4, 2011. DOI: 10.1115/1.4004035.

[19] A. M. Bonanos, "Error analysis for concentrated solar collectors," *Journal of Renewable and Sustainable Energy*, vol. 4, no. 6, p. 063 125, 2012. DOI: 10.1063/1.4768546.

[20] H. Lee, "The geometric-optics relation between surface slope error and reflected ray error in solar concentrators," *Solar Energy*, vol. 101, pp. 299–307, 2014. DOI: 10.1016/j.solener.2013.12.035.

[21] Y. Wang, D. Potter, C. A. Asselineau, C. Corsi, M. Wagner, C. Caliot, B. Piaud, M. Blanco, J. S. Kim, and J. Pye, "Verification of optical modelling of sunshape and surface slope error for concentrating solar power systems," *Solar Energy*, vol. 195, pp. 461–474, 2020. DOI: 10.1016/j.solener.2019.11.035.

[22] J. Chaves, *Introduction to Nonimaging Optics*, 2nd Edition. New York: CRC Press, 2016. DOI: 10.1201/b18785.

[23] R. B. Pettit, C. N. Vittitoe, and F. Biggs, "Simplified Calculational Procedure for Determining the Amount of Intercepted Sunlight in an Imaging Solar Concentrator," *Journal of Solar Energy Engineering*, vol. 105, no. 1, pp. 101–107, 1983. DOI: 10.1115/1.3266335.

[24] P. Bendt, A. Rabl, H. W. Gaul, and K. A. Reed, "Optical analysis and optimization of line focus solar collectors," National Renewable Energy Laboratory (NREL), Golden, CO (United States), Tech. Rep., 1979, p. 75. DOI: 10.2172/5746400.

Nomenclature

Abbreviations

CSR	Circumsolar Ratio
GCS	Global Coordinate System
LCS	Local Coordinate System
NS	North-South
EW	East-West
PDF	Probability Density Function
CDF	Cumulative Density Function
RMS	Root Mean Square

Latin Letters

A_0	Average Earth-Sun distance
L	Radiance distribution function
R_{sun}	Sun radius
R_x, R_y, R_z	Basic rotation matrices
V_ϕ	Variance of the effective source radial distribution defined by ϕ_{es}
$\vec{I}_x, \vec{I}_y, \vec{I}_z$	Direction vectors of an xyz right-handed coordinate system
$\vec{n}$	Normal vector to a surface
$\vec{S}$	Incident sunlight direction vector
$\vec{S}_L$	Projection of $\vec{S}$ in the longitudinal plane
$\vec{S}_T$	Projection of $\vec{S}$ in the transversal plane
$\vec{v}$	A generic vector
$\vec{v}_n$	Reflected ray direction

Greek Letters

α	Azimuthal deviation of a vector regarding a main direction
ϕ	Radial sunshape profile function

ϕ_{es}	Radial effective source distribution function
Φ	Total (hemispherical) radiant flux
φ_s	Sun azimuth angle
θ_L	Longitudinal incidence angle
θ_{LS}	Longitudinal-solar incidence angle
θ_T	Transversal incidence angle
θ_z	Sun zenith angle
θ_δ	Sun disk radius
θ_Δ	Sun aureole radius
ψ	Azimuthal displacement from the horizontal plane
σ_c	Standard deviation of a contour error Gaussian distribution
σ_s	Standard deviation of a specular error Gaussian distribution
σ_t	Standard deviation of a tracking error Gaussian distribution
ξ	Radial displacement from the Sun center
φ	Azimuthal displacement from the Sun center
Δ_{sun}	Half-width of a Pillbox sunshape
σ_{sun}	Standard deviation of a Gaussian sunshape
χ	Circumsolar Ration (CSR)
ϵ	Radial deviation of a vector regarding a main direction
κ, γ	Buie's sunshape model fitting coefficients
δ_ϕ	RMS width of the effective source radial distribution defined by ϕ_{es}

Superscripts

G	Refers to a point or vector represented in the Global Coordinate System (GCS)
L	Refers to a point or vector represented in the Local Coordinate System (LCS)

UNIVERSIDADE DE ÉVORA
INSTITUTO DE INVESTIGAÇÃO
E FORMAÇÃO AVANÇADA

Contactos:
Universidade de Évora
Instituto de Investigação e Formação Avançada — IIFA
Palácio do Vimioso | Largo Marquês de Marialva, Apart. 94
7002 - 554 Évora | Portugal
Tel: (+351) 266 706 581
Fax: (+351) 266 744 677
email: iifa@uevora.pt